THE UNIVERSITY OF CHICAGO

AQUEOUS PROTON STRUCTURES AND DYNAMICS OBSERVED WITH NONLINEAR INFRARED SPECTROSCOPY

A DISSERTATION SUBMITTED TO

THE FACULTY OF THE DIVISION OF THE PHYSICAL SCIENCES

IN CANDIDACY FOR THE DEGREE OF

DOCTOR OF PHILOSOPHY

DEPARTMENT OF CHEMISTRY

BY

WILLIAM BRANDON CARPENTER

CHICAGO, ILLINOIS

AUGUST 2020

Contents

List of Figures

.

List of Tables

Acknowledgments

The work in this thesis would not have been possible without the support from multiple people. First, I want to thank my advisor, Andrei Tokmakoff, for being a thoughtful and patient mentor. Andrei was intentional about my development as a young scientist, and his advice helped me productively channel my enthusiasm for doing research. He taught me how to think carefully about scientific problems, how to take leadership on a project, and how to clearly express my findings through written and oral presentation. Andrei is an approachable advisor, and I highly value that I could be honest with him about any problem. Finally, Andrei has served as a role model who leads pioneering science and keeps a cool head despite the pressures of research.

I also owe a significant share of my scientific development to my lab mates in the Tokmakoff group. The senior group members helped me feel welcome in the group and taught me the intricacies of nonlinear spectroscopy. I'm thankful to have great friends in Lukas Whaley-Mayda and Chi-Jui Feng, and I'll fondly remember our taquería runs, summer learning sessions, and late-night discussions on the office couch. As well, they both pushed me to think clearly about the scientific problem at hand. I have also enjoyed learning from my colleagues in the Big Lab. In additional to being hard-working and clever scientists, their enthusiasm, humor, and aesthetic made the office a welcoming and collaborative environment. I want to additionally thank Lukas, Chi-Jui, and Paul Sanstead for careful readings and feedback on Chapters 2 and 3 of this thesis.

I am immensely privileged to have worked as a member of the Water Lab. Luigi De Marco, Joe Fournier, and Rajib Biswas guided and encouraged me as a junior student, and Joe's physical intuition for tough problems set a high bar as I learned how to interpret raw data. Nick Lewis and John Hack also pushed me to be the best scientist I could be. Nick is a thoughtful mentor and lab mate who showed me what it means to set high standards for myself as an experimentalist. John's

curiosity, patience, and experimental skill made working with him effortless, and he is going to achieve in lab what seemed unreachable only a few short years ago. I'm also highly encouraged by our newest lab member, Melissa Bodine. Even from the short amount of time we worked together, Melissa has displayed significant talent in the lab and I'm excited to see what discoveries she makes in her graduate career. I've additionally enjoyed working with Bogdan Dereka, especially our recent remote discussions during quarantine. Bogdan also has a remarkable wealth of chemical intuition that leads to fascinating research. Finally, I want to thank the Water Lab for the immense amount of time and thought dedicated to reading and editing many rough drafts over the years. They taught me how to craft a scientific argument and make it presentable to the research community. I am particularly grateful to Nick, John, Bogdan, and Melissa for their feedback on Chapters 1, 3, and 5 in this thesis.

Friends and colleagues outside of lab have been a source of support throughout graduate school. There are too many graduate students to name who have volunteered in the chemistry department, but I am grateful for their dedication to fostering a welcoming chemistry community. My friends and colleagues in Artifice and GRIT have taught me about how to make science a more equitable endeavor, and I look forward to hearing about their future work. I also owe Dr. Britni Ratliff for mentoring me in effective chemistry teaching and providing a supportive learning environment. I want to thank my friends at Learn Scuba Chicago who helped me feel at home in Chicago and keep perspective. Finally, Kade Head-Marsden, Cat Triandafillou, and Alek Durumeric have been some of my closest friends in Chicago. By talking with my friends, I learned that I was not alone in the struggles of graduate school and that I could overcome many of those challenges. They also held me to regular exercise, which was crucial for blowing off steam and keeping an optimistic attitude.

I also would not have made it this far without the support from my family. My parents Anne and Philip have always been enthusiastic and curious about the latest developments on my project and were a great source of encouragement while writing this thesis. My brother George has always shared fascinating electronics projects to engage my curiosity and taught me about design, both of which have been useful in my research career. I lastly want to thank my partner Dr. Audrey Han for her unwavering support over the last few years, particularly while I wrote this thesis under quarantine. Even though we were separated by distance for most of my time in graduate school, I could always call her and relax at the end of a long day.

Funding

I want to thank the U.S. Department of Energy, Office of Basic Energy Sciences for their generous support towards my degree and the work that is presented in this thesis.

Abstract

The aqueous proton is one of the fundamental species of aqueous chemistry, but a clear picture of its structure and transport dynamics have eluded chemists for over a century. This arises from the complex interactions with the rapidly fluctuating hydrogen bond (H-bond) network in water, generating a distribution of structures that can interconvert on femtosecond-picosecond timescale. As a result, there is currently an intense debate on the structure of the aqueous proton, typically described in terms of the limiting gas-phase structures, the Eigen cation $H_3O^+(H_2O)_3$ and the Zundel complex $H_5O_2^+$. Additionally, acidic solutions display anomalously high conductivity, described in terms of Grotthuss diffusion where a series of small hydrogen displacements result in the rapid flow of net charge along a H-bonded "water wire." Despite the advances of molecular dynamics simulations, there have been few experiments that can directly probe the structural fluctuations and ultrafast dynamics involved in proton diffusion. Additionally, the vibrational spectrum lacks distinct vibrational peaks, instead displaying a continuum of absorption spanning 1000-3200 cm^{-1}. The work in this thesis harnesses recent technological developments in nonlinear IR spectroscopy to assign the vibrational features in the continuum, correlate them to instantaneous structures, and track their evolution during proton transfer.

This thesis presents the most comprehensive 2D IR dataset to date of the aqueous proton. All of the vibrations of the aqueous proton complex show off-diagonal cross peaks with each other, which reveals that these modes all belong to the same molecular complex versus distinct Eigen and Zundel species in solution. Along with high-level anharmonic calculations, the polarization-sensitive 2D IR spectrum provides reliable assignments for the vibrations of the aqueous proton complex. The broad feature at 1200 cm^{-1} shows a distinctive anharmonicity pattern due to the stretching motion of the shared proton in Zundel-like instantaneous configurations. The nuclear

potential for this vibration is sensitive to the confinement by two solvating waters and asymmetry from the solvation environment. This vibration is strongly coupled to the concerted flanking bending vibrations at 1750 cm^{-1} and the O–H stretches of the flanking waters at 3100 cm^{-1}. The continuous absorption from 2000-3000 cm^{-1} arises from hydronium O–H stretches in instantaneous Eigen-like configurations which are broadened by a distribution of H-bond strengths to the solvation environment. There is also a large distribution of complexes in between the Eigen and Zundel extremes which appear spectrally similar to Zundel-like complexes, but show breadth like the Eigen vibrational response. Cross peaks between Eigen-like and Zundel-like vibrations at the earliest waiting times support the theory that the aqueous proton is a "fluxional complex" that rapidly fluctuates between instantaneous Zundel-like and Eigen-like configurations.

The polarization anisotropy decay of flanking bending modes reveals a 2.5 ps timescale due to proton transfer that rotates the aqueous proton complex. Arrhenius analysis reveals that the barrier for this process is 2.4 kcal/mol, consistent with temperature-dependent measurements of proton transfer measured with other techniques. The anisotropy barrier and timescale are both sensitive to the concentration of the acid and the identity of the counterion. Additionally, this timescale grows monotonically, yet nonlinearly with the viscosity of the solution. These all point to a proton transfer mechanism that depends on the collective rearrangement of the H-bond network. In situations where the barrier decreases, we find that the proton transfer rate also slows down. With Eyring analysis, we conclude that there are entropic penalties associated with proton transfer at high concentrations, arising from obstructed proton transfer pathways and hindered H-bond reorganization. These measurements reveal the complex behavior of proton transport in water and provide necessary data to benchmark molecular dynamics simulations of this process.

Chapter 1

Introduction

1.1 Aqueous Acid Chemistry

Aqueous acids are one of the cornerstone species in chemistry. In our day-to-day experience, acidic solutions corrode metals or produce a sour taste in food. We devote multiple weeks teaching acid-base equilibrium in our general chemistry courses, starting with the seemingly simple dissociation of a strong acid in water.[1] We also commonly invoke proton transfer as a mechanistic step in chemical reactions. Solution acidity, typically measured on the pH scale, can catalyze chemical reactions,[2–4] serving as a source and sink of free protons. In cellular biology, the flow of aqueous protons couples a chemical potential gradient across a membrane to the generation of adenosine triphosphate via ATP synthase.[5] Acid chemistry is also connected to some of the grand environmental challenges of the twenty-first century. Acid rain from SO_x emissions[6] and ocean acidification associated with global climate change[7] is responsible for various forms of ecological damage. On the other hand, acidic solutions are also a key ingredient for low-emission hydrogen fuel cell technology, which efficiently converts chemical energy stored in H_2 covalent bonds into electrical energy as a current of protons and electrons.[8]

Alchemists and chemists have attempted to describe and control the properties of acids for over a millennium. In the ninth century, Arabic scholars documented procedures for isolating strong acids and provided the first written record of *aqua regia*, the mixture of hydrochloric and

nitric acids that dissolves gold.[9] In 1777, Antoine Lavoisier proposed the first atomistic description of acidity, mistakenly identifying it with oxygen (Greek for "sour maker") instead of hydrogen.[10] The definition of an acid has been updated multiple times since then, due to the efforts of Justus Liebig in 1832,[11] Svante Arrhenius in 1887,[12] Brønsted and Lowry independently in 1923,[13,14] and G.N. Lewis also in 1923.[15] This attention reveals the core role acid-base chemistry plays in chemical systems and the desire for chemists to understand its behavior. The long years of study and application of aqueous acid chemistry would suggest that we had a fairly solid grasp of structure of the aqueous proton and its transport through water.

However, as with many microscopic phenomena, reality is much more complicated. At first, the aqueous proton is typically written as $H^+(aq)$, but it is also frequently written as the hydronium ion H_3O^+, which acknowledges that a polar water molecule is so strongly attracted to the bare proton that they form a covalent bond. This concept is important, but the confidence with which it is presented in a general chemistry course implies the chemical formula has been determined quantitatively. In reality, this is an immensely challenging task, and there is currently a highly active debate amongst physical chemists about the arrangement of a proton and its nearest waters. Because the aqueous complex in question includes water, the normally reliable "solute" and "solvent" labels are less distinct than in other electrolyte solutions. Ambiguity on the structure of the aqueous proton therefore introduces uncertainty in our understanding of how it participates in chemical reactions.

Proton transport in water also behaves distinctly from other aqueous electrolytes. It has been appreciated since the mid-nineteenth century that the conductivity of acidic solutions is approximately five times larger than in comparable electrolyte solutions, despite a similar quantity of dissociated charges.[16] This suggests that the standard diffusion models do not accurately

describe proton diffusion.[17] Instead, a model invoking ideas from Theodore von Grotthuss suggests that many individual hydrogens undergo small displacements along a "water wire," which results in the rapid *net* flow of charge despite the relatively slow diffusion of aqueous electrolytes. While the conceptual underpinning of this model is widely accepted, there are a multitude of competing theories for proton transport from molecular dynamics simulations, and experimental observation of these molecular-scale details is missing. In this thesis, I will present my contributions toward answering questions on aqueous proton structure and transport. However, in order to place this work into context, I will first present in this introduction a summary of the properties of pure water, followed by a survey of the research to date on the aqueous proton.

1.2 Structural and Dynamical Properties of Liquid Water

In order to understand acidity in aqueous solution, it is necessary to discuss the physical chemistry of water. Water's behavior determines the outcomes of multiple processes on Earth on scales spanning many orders of magnitude. Liquid water covers 71% of the surface area of the planet, giving Earth the appearance of a "pale blue dot" from space.[18] The movement of water shapes Earth's geography, climates, and weather patterns. Water also plays a central role in biology, from single-celled microbes to complex plant and animal life. Yet despite our day-to-day familiarity with liquid water, it is a remarkable medium from the perspective of its molecular properties.

Liquid water is a system of associated H_2O molecules, which together, behave distinctly from individual molecules as a result of hydrogen bonding (H-bonding). A single gas-phase water molecule is a bent molecule with average H–O–H angle of 104.5° and O–H bond lengths of 0.957 Å.[19] The highly electronegative oxygen atom is spatially separated from the weakly

electronegative hydrogen, generating a static dipole moment of 1.855 Debye for an isolated molecule.[20] The polarity of a water molecule allows electrostatic interactions with other dipoles (including other water molecules) and ions such as H^+. Beyond simple electrostatics, water molecules also form H-bonds amongst themselves, directional non-covalent associations between the H atom on one water with the lone pair electrons on the oxygen of another water. There is a quantum mechanical component to this interaction, where $0.04e$ of electronic charge transfers from the H-bond donor to the lone pair on the acceptor, which stabilizes a water dimer over two monomers by 3.15 kcal/mol.[21,22] The energy of a H-bond is approximately one tenth the energy of a typical covalent bond, meaning that a H-bond can join two water molecules but also break from thermal fluctuations ($k_BT \approx 0.59$ kcal/mol at room temperature). Compared to similar simple molecular liquids like liquid methane or ammonia, water has been described as possessing many "anomalous" properties such as high boiling point and viscosity because of its ability to form relatively strong H-bonds. In larger collections of water molecules, such as in trimers, tetramers, and in the liquid, H-bonds between multiple water molecule can stabilize or destabilize each other as many-body interactions.[21,23–26] Many-body effects contribute approximately 20% of the total stabilization in water clusters,[21,24] and recent water models incorporating many-body effects have accurately modeled many of liquid water's physical properties.[26]

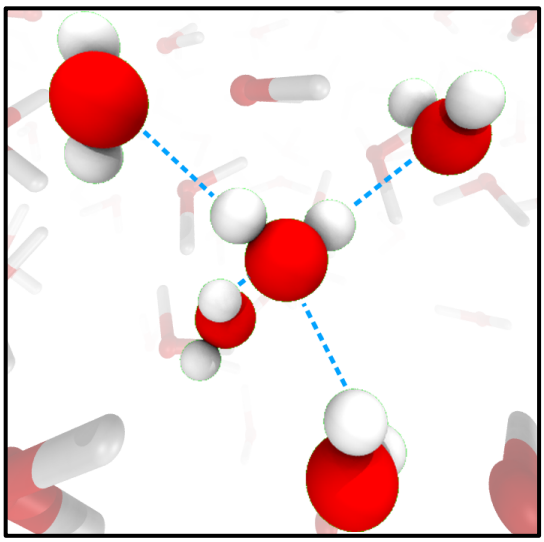

Figure 1.1: A water molecule and its four H-bonding partners in the liquid phase. The central water molecule donates two H-bonds to the top to waters and receives two H-bonds from the bottom two waters. The four surrounding water molecules are roughly arranged at the corners of a tetrahedron.

Liquid water's remarkable properties are the result of a continuous interplay between stabilizing H-bond interactions and stochastic thermal fluctuations. In standard conditions, a single water molecule forms four H-bonds on average (Fig. 1.1), donating two and receiving two H bonds to waters in a roughly tetrahedral arrangement. The tetrahedral arrangement imparts a local order, but thermal fluctuations distort tetrahedrality, break H-bonds, and scramble any long-range spatial correlations. For the liquid, defining what constitutes a H-bond has received much scholarly attention.[27] Various levels of sophistication have been invoked, ranging from simple geometric cut-offs[28] to degree of charge transfer from electronic structure calculations.[24] One of the most common is the Luzar-Chandler criteria, where the O···O distance between two waters is within 3.5 Å (corresponding to the first minimum of the oxygen-oxygen pair correlation function) and the donor-acceptor O-H···O angle is more than 150°.[28] Despite its simplicity, this definition is somewhat arbitrary since H-bonds in the liquid are highly varied, from short and strong ($R_{OO} \approx$ 2.7 Å, $E_{HB} \approx$ 4 kcal/mol) to long and weak ($R_{OO} >$ 3.0 Å, $E_{HB} <$ 3 kcal/mol). The strength of H-

bonds to solutes can also widely vary, depending on the nature of the solute-solvent interaction. We will see that H-bonds involving the excess proton are particularly strong due to the high charge density on a bare proton.[29]

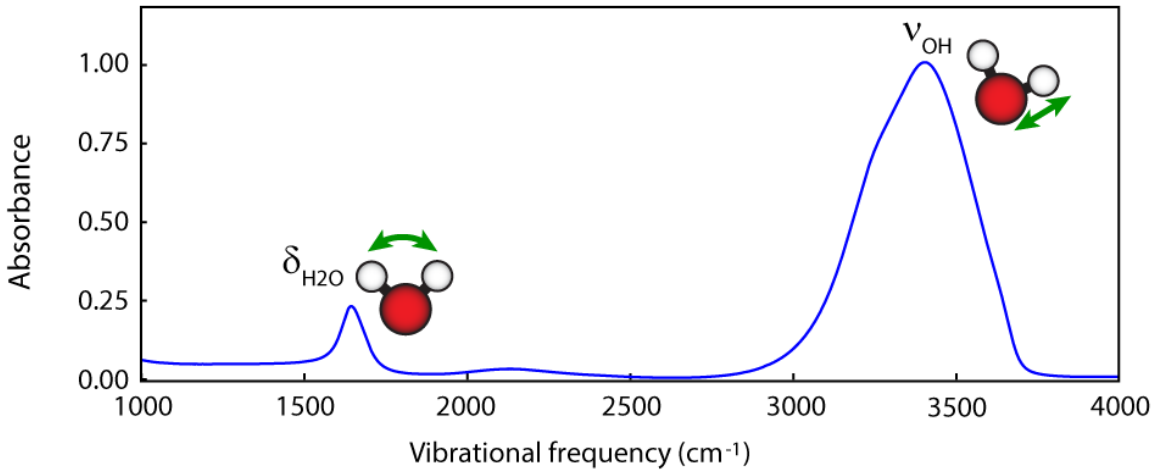

Figure 1.2: The FTIR spectrum of liquid water.

The infrared spectrum of liquid water is a highly sensitive reporter of the distribution of H-bonding configurations (Fig. 1.2). The O–H stretch vibration is an intense and broad feature peaked at 3400 cm^{-1} and the H–O–H bend is a weaker and narrower feature centered at 1650 cm^{-1}. The 500 cm^{-1} breadth of the O–H stretch feature is due in part to its sensitivity to various local H-bonding environments, an example of inhomogeneous broadening.[30] Because an H-bond transfers electronic charge to a neighboring water, the effective force constant of the O–H stretch vibration of the H-bond donor lowers and the frequency redshifts, in accordance with Badger's Rule.[31] In isotopically dilute HOD in D_2O, the O–H stretch frequency anticorrelates linearly with R_{OO} ($R^2 = 0.77$), and this correlation increases to $R^2 = 0.98$ when frequency is compared against the liquid's collective electric field at the H position in the direction of R_{OH}.[32,33] The shoulder at 3250 cm^{-1} in H_2O arises from anharmonic mixing between the O–H stretch and the H–O–H bend overtone,[34,35] resulting in a phenomenon known as Fermi resonance where the intensity of the

overtone is enhanced and the two features split.[36] Finally, the increased charge transfer with H-bond strength amplifies the O–H vibrational transition dipole and the intensity of the corresponding O–H stretches.[37]

Beyond reporting on the distribution of H-bonding configurations, the IR spectrum of the O–H stretch also contains signatures of H-bond fluctuation dynamics. In response to environmental fluctuations such as H-bond distortion or rupture, the frequency of a single O–H oscillator can shift stochastically in a process known as spectral diffusion.[38] It has been appreciated for the better part of a century that H-bond rupture events occur on the ps timescale,[39] but direct measurements of these dynamics have only been realized in the last couple decades.[40–48] Low-energy distortions cause the O–H stretch frequency to fluctuate much more rapidly, on the timescale of the vibrational period (~10 fs for the O-H stretch). The rapid scrambling of the vibrational coherences of an ensemble of O–H stretches induces destructive interference between them in a process known as dephasing. Rapid relaxation of excited O–H stretches (~250 fs lifetime in H_2O[34]) also decays the vibrational oscillation. The decay of the coherent oscillation from dephasing and excited state relaxation results in homogeneous broadening in the frequency domain. A linear IR spectrum is incapable of disentangling contributions of homogeneous broadening, inhomogeneous broadening, and spectral diffusion, but nonlinear spectroscopic experiments have been key to disentangling these contributions and observing the ultrafast H-bonding dynamics in water.

Some of the earliest measurements of H-bonding dynamics recorded the frequency fluctuations of the O–H stretch of dilute HOD in D_2O.[33,43] In these experiments, Fecko *et al.* generated 45-fs IR laser pulses centered at 3400 cm^{-1} with 300 cm^{-1} bandwidth at full width half maximum, which could excite the full bandwidth of the O–H stretch. They employed vibrational

echo peak shift measurements, a nonlinear spectroscopic technique which measured the frequency correlation function $C(\tau) = \langle \delta\omega(\tau)\delta\omega(0) \rangle$ of the O–H stretch frequency fluctuation $\delta\omega$ using three ultrafast pulses. From these measurements, they found multiple distinct timescales associated with H-bond fluctuations: a large 50-fs decorrelation due to hindered rotations (librations), a 170-fs recurrence in frequency correlation due to O···O oscillations, and a 1.2-ps timescale due to collective H-bond reorganization events.

Subsequently, the Loparo *et al.*[43] used polarization-selective transient absorption to measure the O–H stretch polarization anisotropy decay $r(\tau) = \frac{2}{5}\langle P_2[\hat{\mu}(\tau)\cdot\hat{\mu}(0)]\rangle$, where P_2 is the second Legendre polynomial of the O–H stretch dipole reorientation at time τ after initial excitation. In HOD/D_2O, the O–H stretch anisotropy decayed biexponentially, with one 50-fs timescale due to librations and a 3-ps timescale due to H-bond reorientation. The ps timescale differs between $C(\tau)$ and $r(\tau)$ since the anisotropy measures the second Legendre polynomial of the orientational relaxation, not the relaxation timescale itself. Later temperature-dependent analysis of these correlation functions revealed a shared barrier of 3.7 kcal/mol, indicating the common underlying process of collective H-bond reorganization for these picosecond dynamics.[49] These relaxations also show non-Arrhenius kinetics, revealing that H-bond relaxation occurs over a rough potential energy surface with a distribution of energy scales.[50,51]

Two-dimensional infrared (2D IR) spectroscopy has more recently been an invaluable tool for spectrally correlating various H-bonding motifs with fs time resolution. A 2D IR spectrum (Fig. 1.3) is a two-dimensional frequency plot which correlates vibrational frequencies excited by a pump laser and the frequencies detected as the change of absorption of a probe laser pulse separated by a waiting time τ_2. Along the diagonal reside oppositely signed doublets comprised by positive ground state bleaches (GSB) and negative excited state absorptions (ESA) shifted in

detection frequency due to anharmonicity of the vibrational potential. Cross peak doublets off the diagonal indicate anharmonic coupling between different vibrational modes. The 2D IR lineshape decomposes the inhomogeneous and homogeneous broadening contributions to the linear IR lineshape as diagonal and antidiagonal breadth, respectively.[44,46] Detailed discussions of 2D spectroscopy theory and experimental implementation will be presented in Chapters 2 and 3, respectively.

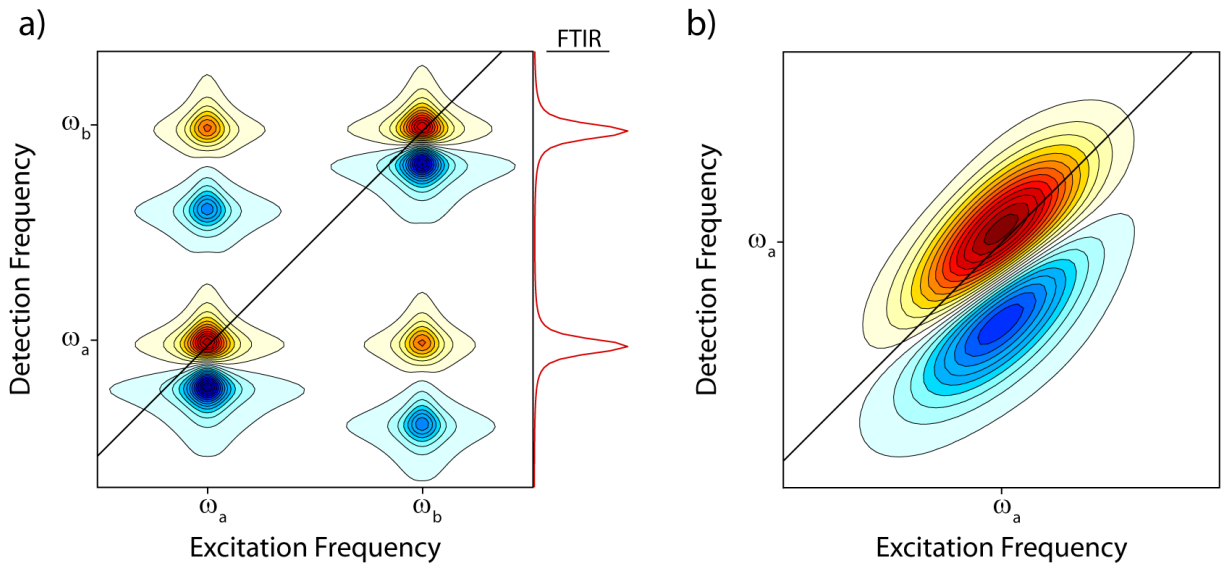

Figure 1.3: Model 2D IR spectra. (a) A model 2D IR spectrum for two coupled vibrations. Positive bleach features are shown in yellow, and negative induced absorption features are in blue. (b) The 2D IR spectrum of an inhomogeneously broadened peak, elongated along the diagonal.

The 2D IR lineshape of the O–H stretch of HOD in D_2O decomposes different origins of spectral broadening and elucidates molecular details of H-bond breaking dynamics. The GSB is elongated along the diagonal at the earliest measurable waiting times ($\tau_2 \leq 100$ fs) due to inhomogeneous broadening from the distribution of H-bonding environments. The peak is also "pear-shaped," where the higher frequencies display larger antidiagonal width than the lower frequencies. This width indicates fast frequency fluctuation kinetics of weakly H-bonded O–H

oscillators, and comparison with MD simulations demonstrates that weakened or broken H-bonds only persist for < 200 fs between stable H-bonded configurations, rather than persisting as meta-stable dangling H-bonds in the bulk.[44] Further experiments and modeling demonstrated that H-bond exchange events occur via a large-angle jump diffusion mechanism between sets of H-bonding partners.[42,48,52]

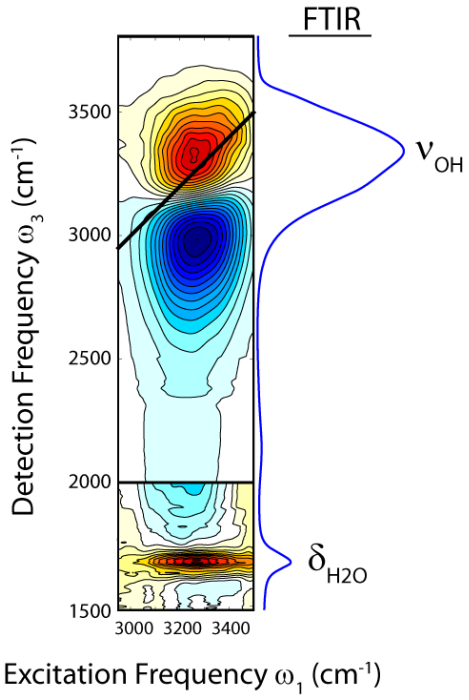

Figure 1.4: The 2D IR spectrum of the H_2O O–H stretch.

While studies on isotopically dilute water have been useful for studying H-bond dynamics, 2D IR spectroscopic studies of pure H_2O have demonstrated that the O–H stretch is best described as a highly anharmonic vibrational exciton delocalized over multiple water molecules. The τ_2 = 100 fs 2D IR surface of H_2O (Fig. 1.4) shows a broad GSB feature, and an exceedingly broad ESA spanning detection frequencies from 3100 to below 1500 cm^{-1}.[34,53] The broad ESA reflects the extreme vibrational anharmonicity of the vibrational exciton introduced by H-bonding and the distribution of vibrational potential shapes in various collective H-bonding configurations.

Additionally, a cross peak bleach appears at detection frequency 1650 cm^{-1}, which indicates anharmonic coupling between the O-H stretch and H-O-H bend. Spectral modelling has predicted that the O-H stretch delocalizes over approximately twelve local O-H stretch modes,[54] but this number could vary depending on local density of oscillators of similar frequency. H-bonding configurations corresponding to the wings of the O-H stretch band appear to be more localized, whereas configurations near the 3400 cm^{-1} peak maximum are more delocalized.[34]

Delocalization of the O-H stretch also results in fast relaxation dynamics, pushing the limit of experimental time resolution. The frequency correlation function $C(\tau)$ decays on a 170 fs timescale[34] and the transient absorption anisotropy $r(\tau)$ decays on an 80 fs timescale, both an order of magnitude faster than the observed timescales in isotopically dilute HOD in D_2O.[34,55] These timescales reflect transient coupling and vibrational energy transfer between oscillators instead of physical H-bonding fluctuations. The lifetime of the first vibrational excited state decreases to 250 fs (compared to 700 fs in HOD/D_2O[43]) due to the excitonic coupling between O–H oscillators and efficient deposition of energy into collective low-frequency modes. In contrast to the cascading stretch-to-bend relaxation mechanism seen in HOD/D_2O,[56] the O–H stretch in pure H_2O is directly coupled to low-frequency modes and can simultaneously relax via multiple parallel channels. The ultrafast deposition in energy produces a transient signal that grows in on an 800 fs timescale known as the hot ground state (HGS). This signal is isotropic in water and appears similar to the temperature difference spectrum in neat water, but the HGS is far from equilibrium and cannot be regarded as a temperature increase of the sample. The HGS appears like a thermal increase because the ultrafast and equilibrium processes involve increased kinetic energy, which weaken H-bonds and thus blueshifts O-H stretches. The delocalization and extreme anharmonicity of water vibrations will be discussed in more detail in Chapter 4, a study of the δ_{H2O} bending mode.

The H-bonding structure and dynamics of liquid water give rise to its many fascinating properties. They introduce local order in the system, but are weak enough to distort and even break on the ultrafast timescale. Nonlinear IR spectroscopy has proven to be useful to learn about the dynamics of pure water and aqueous solutions,[57,58] which naturally lends it to studying the aqueous proton's structure and H-bonding dynamics. The properties of this species are heavily influenced by the aqueous environment, and the development of nonlinear spectroscopic methods have introduced many tools for detailed study. To understand the context of the experiments and modeling presented in this thesis, I now present a review of the key studies that have shaped the discussion on the aqueous proton and the remaining open questions.

1.3 Foundational Studies of the Aqueous Proton: Early Conceptions of Structure and Charge Transport

The first recorded studies of aqueous proton structure and transport date back to the nineteenth century. While studying the conductivity of electrolyte solutions in 1853, von Hittorf measured an unusually high conductivity in acidic and basic solutions, on the order of five times larger than in similar monovalent salt solutions.[16] Without a framework for describing the molecular structure of aqueous solutions, this mysterious observation went unexplained. The first proposal on the structure of the acidic species in solution came in 1899, where Collie and Tickle proposed that oxygen could form an oxonium species OH_3^+,[59] whose extended valency compared to water was proposed to be analogous to the relationship between ammonia and ammonium.

In a foundational paper in 1933, Bernal and Fowler published the first detailed theoretical study on the structure and diffusion of aqueous protons.[17] In order to make headway on the problem, they also discovered various structural properties of pure water, such as water's bent

structure and formation of a tetrahedral H-bond network. With a structural model in place, they concluded that the hydronium molecule had to be trigonal pyramidal to be effectively incorporated into water's tetrahedral H-bond network. However, they reasoned that an intact H_3O^+ could not be the primary diffusing species because of the drastic difference in mobility between H^+ and NH_4^+ (32.5×10^{-4} and 6.7×10^{-4} $cm^2/V\cdot s$, respectively). Interestingly, they observed that the anomalous mobility disappeared in dry HF, but returned upon the addition of water. Their central conclusion was therefore that "an $(OH_3)^+$ ion in sufficiently close contact with a water molecule OH_2 need not retain its extra proton but can transfer it to the other molecule…. Indeed, these ideas are of venerable antiquity for we really do little more than resuscitate in modern dress the idea of Grottius' chains." It was in Bernal and Fowler's work that the Grotthuss mechanism of proton transport was postulated, while Grotthuss's original hypothesis in 1806 was to explain the electrolysis of pure water under an applied voltage.[60]

Beyond the Grotthuss transfer mechanism, Bernal and Fowler proposed other important mechanistic details of aqueous proton transfer. They expected that the proton transfer would be barrierless when H_3O^+ and another water were in close proximity, but the barrier would rise as the two species separated, which was later demonstrated computationally with *ab initio* molecular dynamics simulations.[61–63] From the symmetry of the system, they expected that the proton would be equally likely found on either of the two waters, and an external electric field would break this symmetry, which Zundel and Metzger supported with experiments decades later.[64]

Subsequent experimental study put Bernal and Fowler's ideas of proton hopping on more quantitative footing. By analyzing the temperature-dependent "excess mobility," corrected for a hydrodynamic contribution to the proton mobility, Gierer and Wirtz[65] derived a proton transfer barrier of 2.4 kcal/mol in 1949 using Eyring's recent rederivation of activation free energy.[66] They

found that the excess mobility was only present in H-bonding solvents, which led them to conclude that proton hopping only occurs over H-bonds. They further found that the barrier was the same in acidic DCl solutions within experimental error, indicating that the rate-limiting step was due to motion of the heavy atoms.[67] They proposed this step was hydronium reorientation due to H-bonds breaking and reforming on a timescale of ~10^{-11} s.

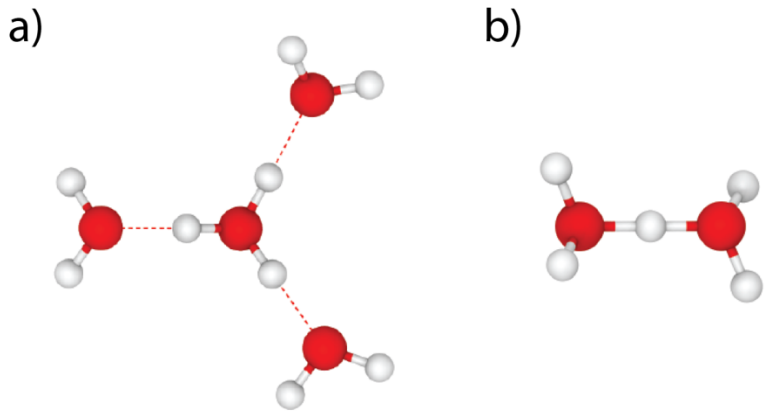

Figure 1.5: The a) Eigen and b) Zundel cations.

The present-day debate has been framed by the mid-century experimental studies by Manfred Eigen and Georg Zundel. By comparing the molar heats of solvation in acid and salt solutions, Wicke, Eigen, and Ackermann concluded that the H_3O^+ species was solvated like other monovalent cations like Li^+ and Na^+.[68] Subsequent analysis by mass spectrometry revealed a maximum at m/z = 73, indicating equilibrium stability of the $H_9O_4^+$ species.[3] This latter species, now known as the Eigen cation, is known by the tight solvation of hydronium by three equivalent waters (Fig. 1.5a). Continuous near-IR absorption was also observed from 1.4-2.2 μm, which the authors attributed to fluctuation of delocalized charge within the complex. Eigen modified Gierer and Wirtz's structural reorganization hypothesis to account for the $H_9O_4^+$ species, arguing that while the proton was free to move within the complex, proton transfer occurred by H-bond reorganization from the environment.[68]

To explain a continuous Raman scattering spectrum of aqueous acid solutions, Zundel and Metzger published an argument in 1968 in favor of a hydrated proton complex, $H_5O_2^+$, involving just two waters (Fig. 1.5b). In an experiment with polystyrene sulfonic acid films in a humidity cell, they found that the aqueous proton's signature continuum appeared with at least two waters per sulfonic acid group, implying that the aqueous proton required only two waters for solvation. They interpreted the lack of temperature dependence of continuum intensity as resulting from a freely fluctuating central proton in a double-minimum potential. The barrier was proposed to be small enough that the proton could quantum mechanically tunnel across. The proton, being free to diffuse along this potential, was thus proposed to be highly polarizable and sensitive to the fluctuations of the electric field from the solvation environment, resulting in a broad distribution of energy-level shifts responsible for the continuous absorption spectrum. While this motif involves a proton flanked by two waters, the authors argued that the complex would be asymmetric due to asymmetries in the solvation environment. Zundel and Metzger also embraced Gierer and Wirtz's structural diffusion ideas, and noted that the $H_9O_4^+$ moiety was not a necessary component for describing proton transfer.[64]

The first inference of picosecond proton transfer kinetics came from NMR linewidth analysis in 1961. With ^{17}O NMR spectroscopy, Meiboom interpreted NMR linewidths in terms of chemical exchange between H_3O^+ and H_2O and recovered a time constant of 1.5 ps, which is on the order of the H-bond reorganization timescale in pure water and predicts a proton hopping distance of 2.8 Å, the average H-bond length in H_2O.[69] While this time constant is on a reasonable scale, its derivation relied on assumptions about the molecular geometry that are still up for debate. Despite this, this numerical value is used as the point of reference for simulation studies on proton transfer.[70–73] Subsequent Arrhenius analyses of temperature-dependent NMR spectra recovered

observed barriers in the range of 2.4-2.8 kcal/mol, consistent with Gierer and Wirtz.[74–76] As with the original NMR experiment, the molecular details that determine the barrier have yet to be understood.

1.4 Structural Insight from Gas-Phase IR Spectroscopy of Hydrated Proton Clusters

Vibrational spectroscopy of gas-phase protonated water clusters provided an opportunity to study the Eigen and Zundel cations without complications from solvation fluctuations in the aqueous phase. The first IR spectrum of the gas-phase Eigen cation was measured by Schwarz in 1977, revealing an intense and broad peak at 2660 cm^{-1} from hydronium O–H stretches. The 860 cm^{-1} redshift compared to water demonstrated the extreme H-bonds within the cation.[77] These IR spectra also demonstrated that the gas-phase cation was C_{3v}-symmetric with the hydronium oxygen at the apex of a trigonal pyramid. In 1989, Yeh *et al.* measured the bare Zundel cation spectrum in the O–H stretch region above 3000 cm^{-1}.[78] They found that the O–H splitting pattern revealed a C_2-symmetric Zundel cation with an evenly shared central proton, while the H_2-tagged Zundel species contained an excess proton shifted by 0.1 Å away from the center. Comparison with electronic structure calculations found a 0.4 kcal/mol barrier between these two Zundel cation geometries,[79] indicating a relatively flat-bottomed proton potential well. Subsequent high-resolution rovibrational spectra revealed tunneling splittings caused by large-amplitude, low-frequency internal motions, revealing that the gas-phase Zundel ion is flexible even at low temperature.[80]

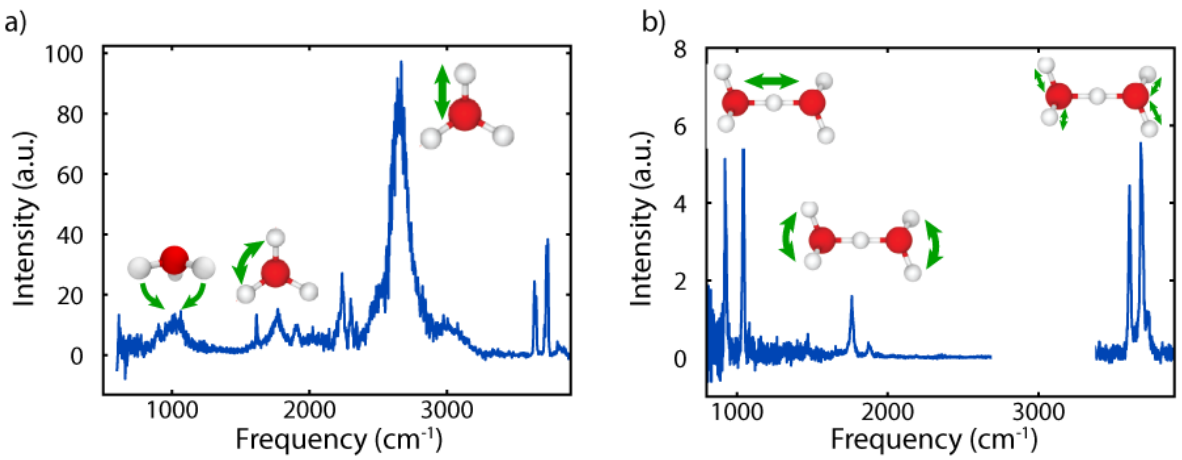

Figure 1.6: IR predissociation spectra of the (a) D_2-tagged Eigen and (b) Ne-tagged Zundel cations with normal mode cartoons for the main features. In (a), only the central H_3O^+ of the Eigen cation is shown for simplicity. Data are from Refs. 85 and 83, respectively.

While early gas-phase studies were technologically limited to the O–H stretch region above 3000 cm^{-1}, broadband IR spectroscopic studies in the early 2000s uncovered other key vibrational features that distinguish the Eigen and Zundel motifs (Fig. 1.6). The first broadband IR spectrum of the bare $H_5O_2^+$ showed a complicated peak pattern between 1000 and 1600 cm^{-1} due to anharmonic coupling,[81,82] but the Ne-tagged predissociation spectrum of the Zundel cation was simplified to a doublet at 970 and 1080 cm^{-1} from a Fermi resonance between the asymmetric shared proton stretch with a combination band of low-frequency modes.[83] Joint experimental and theoretical study by Headrick *et al.* extended the predissociation method to a series of clusters $H^+(H_2)_{n=2-11}$, setting the standard for broadband vibrational spectra for the Eigen and Zundel cations.[84] In the Eigen cation,[85] the key features are the intense and broad 2665 cm^{-1} peak due to the hydronium asymmetric O-H stretch mode, the hydronium in-plane bend at 1760 cm^{-1}, and a weak umbrella mode at 1045 cm^{-1}. The symmetric and asymmetric stretches of the first shell waters appear as two sharp peaks at 3600 cm^{-1} and 3720 cm^{-1}, respectively. For the Zundel cation,[83] the main features are an intense and sharp asymmetric proton stretch at 1080 cm^{-1}, an out-

of-phase coupled flanking water bend at 1770 cm^{-1}, and flanking water symmetric and asymmetric O-H stretches between 3400 and 3700 cm^{-1}. The O–H stretch frequencies associated with the excess proton shifted across the 1000-3200 cm^{-1} region with varying hydration number, indicating its extreme sensitivity to local environment. Further work measured a continuous absorption spectrum of the $H^+(H_2O)_{28}$ cluster, a hydronium-capped water cage. The presence of the continuum was used as evidence to suggest that the aqueous spectrum could be entirely described within the Eigen framework.[86]

Gas-phase experiments on these model systems have contributed greatly to our intuition for the spectral features of various protonated hydration complexes, but there are important differences between the aqueous bulk and large gas-phase clusters. First, the minimum energy configuration of the $H^+(H_2O)_{28}$ cluster places the H_3O^+ on the outside of the cluster due to the oxygen's reduced charge density,[87,88] whereas in bulk water, hydration will be more isotropic, and a weak H-bond can be donated to this site.[70,89] More importantly, cluster spectra were recorded at 10K, whereas aqueous acid species at 300K ($k_BT \approx 200$ cm^{-1}) will experience much larger thermal fluctuations and excitations of low-frequency modes. The resulting sub-Å configurational fluctuations distort the solvation environment away from ideal symmetry and blur the distinction between Eigen-like and Zundel-like configurations. Distinct Eigen and/or Zundel motifs have been observed in the gas phase, in crystalline HCl hydrates,[90] and in protonated ice,[91,92] but not in solution. Quantitative assessment of the effects of an aqueous environment has required sophisticated molecular modeling to connect to spectroscopy.

1.5 Molecular Details of Aqueous Proton Structure and Diffusion

1.5.1 Different Assignments within the Continuous IR Spectrum of the Aqueous Proton

In contrast to the sharp features from the smallest clusters, the aqueous IR absorption spectrum is a continuum of absorption spanning 1000-3000 cm^{-1} (Fig. 1.7). This broad spectrum eludes straightforward interpretation as there are no sharp characteristic peaks to assign to molecular vibrations. Subtraction of the water background from the acid spectrum demonstrates that there are local maxima in the acid continuum, but these features each span hundreds of wavenumbers. In particular, there is a broad feature at 1200 cm^{-1}, a feature at 1750 cm^{-1} which appears like a shoulder of the water bend, a continuum spanning the 2000-3000 cm^{-1} region, and finally another local maximum around 3000 cm^{-1}. Comparing to the gas-phase spectra, the features at 1200 cm^{-1}, 1750 cm^{-1}, and 3000 cm^{-1} have been proposed to correspond to the shared proton stretch, flanking bend, and flanking stretch modes of aqueous Zundel-like species,[93–95] but they have also been assigned to the umbrella mode, protonated bend, and O-H stretch modes, respectively, of Eigen-like species.[86] By decomposing the spectrum based on geometric configuration and accounting for solution fluctuations, molecular dynamics simulations have made important first steps connecting experimental observables to molecular details. However, because the IR spectral assignments are still debated, many of these details have yet to be verified by measurements.

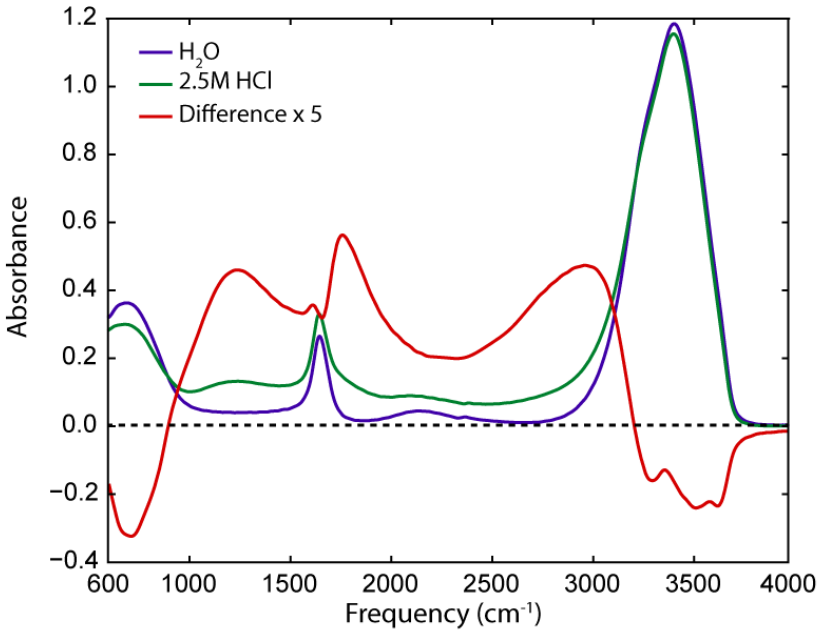

Figure 1.7: The linear IR spectrum of 2.5M HCl in water.

One approach to simulate the linear IR spectrum is by relating the IR spectrum to the Fourier transform of the dipole time autocorrelation function (Eq. 2.24). This requires long trajectories (at least 100 ps) for the autocorrelation function to converge, and simulations of the excess proton must be able to break and form chemical bonds during proton transfer events. To satisfy these requirements, multi-state empirical valence bond (MS-EVB) models were developed for simulating the aqueous proton.[89,96–99] In these simulations, the state of the aqueous proton is represented as a linear combination of different chemical bonding patterns which form an approximate basis for the ground state nuclear potential energy surface. For each time step, relative weights of the bonding patterns are computed based on the nuclear configuration and the *ab initio* potential energy surface of a small system such as the protonated water tetramer.[96,100] This approach allows for states where the proton is localized on a single hydronium, shared between two waters in a Zundel-like configuration, or delocalized over four waters in the Eigen complex.

Kim *et al.* utilized the MS-EVB model of the excess proton to perform the first simulation of the IR spectrum of the aqueous excess proton.[97] In this study, they found that the contribution to the total dipole from electronic charge was necessary to replicate the continuum, and this charge delocalized over approximately six water molecules. This result supported Eigen's hypothesis that fluctuations of delocalized electronic charge produced IR continuum absorption, instead of Zundel's polarizable shared proton. Further iterations of the MS-EVB model improved the correspondence to experiment,[89,101] but the dipole autocorrelation approach could not be reliably decomposed based on aqueous proton geometry.

An alternative approach for modeling the IR spectrum involves extracting small clusters (typically $H^+(H_2O)_6$) from aqueous proton simulations and calculating the frequencies and intensities of the resulting normal modes. With this approach, the clusters can be partitioned by geometric characteristics to collected statistically averaged spectra from Eigen-like and Zundel-like configurations.[89,97,101] Multiple studies[97,101,102] found that Zundel-like configurations produced features at 1200 cm^{-1}, 1800 cm^{-1}, and 3100 cm^{-1} due to oscillations of the shared proton, flanking bending motions, and flanking O-H stretches, similar to gas-phase vibrations. The continuum between 2000 and 3000 cm^{-1}, by contrast, arose from the variety of H-bond strengths in the dynamically distorted Eigen complex. These gave first indications of qualitative assignments but differences between the calculated and experimental IR lineshapes left uncertainty in these assignments.

In a recent experimental and computational study by Biswas *et al.*, it was revealed that the normal modes delocalize substantially, involving waters out to the second solvation shell.[102] Additionally, decomposition by normal mode character uncovered substantial mixing between stretching, bending, and umbrella modes, suggesting strong anharmonic mixing between

vibrational modes. Because of the strongly anharmonic nuclear potential of the aqueous proton, harmonic frequency positions were not accurate, but the trends were crucial for developing intuition on the types of vibrations that were present in various regions of the proton continuum. These studies demonstrated that anharmonicity of the nuclear potential would be a necessary component for understanding the spectroscopy, but treating anharmonicity appropriately requires significantly higher computational expense.

Most recently, *ab initio* studies on the aqueous proton have analyzed the IR spectrum with physically intuitive models beyond the traditional Eigen/Zundel paradigm. Incorporating *ab initio* molecular dynamics, spectral simulation, and IR spectroscopy,[103] it was argued that the shared proton stretching mode constituted a broad band spanning 1000-1500 cm^{-1}, whereas flanking water O–H stretches spanned 2000-3000 cm^{-1}. Additionally, nuclear quantum effects rendered the small proton stretch barrier essentially irrelevant, which blurred the distinction between Eigen-like and Zundel-like geometries in solution. The authors concluded that the aqueous excess proton complex could be described as somewhat Zundel-like, but asymmetric due to solvation environment in the spirit of Zundel and Metzger's original picture.[64] In another study employing *ab initio* simulations,[104] the IR spectrum was decomposed by a H-bond asymmetry coordinate which described the solvation environment around the excess proton. In this framework, symmetric configurations displayed the proton stretch oscillation, but their analysis pointed to oscillations out of the O–H···O axis, resembling more of an O–H–O bending motion.

These different methods for modeling the linear IR spectrum have provided multiple possibilities for its interpretation. However, this means that at this time, there is still significant uncertainty with respect to the vibrational assignments, let alone how the spectrum reports on the distributions of aqueous proton configurations. Does the 1200 cm^{-1} feature correspond to Zundel-

like shared proton stretch, O–H–O bending, or Eigen-like umbrella motion? Is the 1750 cm^{-1} feature due to bending modes, or are they strongly H-bonded Eigen O–H stretches? Is the continuum between 2000-3000 cm^{-1} due to Eigen O-H stretching, Zundel flanking stretching, or charge oscillations delocalized over the Eigen complex? The difficulty in interpreting the IR spectrum arises not only from the various assignments and the distribution of configurations, but also because these vibrations are highly anharmonic and strongly mixed with each other and surrounding water vibrations. For the experimentalist, putting these assignments on firm footing is the first step to studying the molecular details of proton transfer in solution. Chapters 6 and 7 address both the linear and the nonlinear IR spectroscopy of the aqueous proton to provide some insight on these questions.

1.5.2 Various Proposed Mechanisms of Proton Transport Dynamics

The first microscopic examinations of the Grotthuss mechanism for proton transfer occurred in the mid-1990s with the advent of *ab initio* molecular dynamics (AIMD) simulations, followed soon after by multi-state empirical valence bond (MS-EVB) simulations. Because ultrafast IR spectroscopy was relatively new during this time, simulation studies dominated the discussion on the aqueous proton. One key challenge in simulating proton transfer dynamics is to appropriately treat the covalent bond exchange needed for proton hopping. AIMD treats bonding as quantum mechanical electron density, which is calculated based on nuclear coordinates and is used to generate forces on the nuclei for the next time step.[105] There is debate regarding the accuracy of AIMD simulations, however, because they are sensitive to density functional choices and the "fictitious" electron mass which both introduce artifacts like slow aqueous dynamics and overstructured hydration geometries.[106] MS-EVB simulations, on the other hand, can handle larger

systems and longer trajectories by using an approximate representation of the electronic states which allows fluctuations between different bonding topologies.[96] However, as an effectively classical simulation technique, it also cannot entirely reproduce the structural correlations of water.[89] Simulations and analyses of the excess proton have grown increasingly sophisticated over the last couple decades, but are based in these two methods. The following theoretical studies have proposed many new mechanistic details and shaped our current conception of aqueous proton transfer, most of which remain untested by experiment.

AIMD simulations of the aqueous proton depicted the aqueous proton as a dynamical complex, fluctuating on the fs timescale, rather than discrete Eigen and Zundel motifs.[106] The first simulation of $H^+(aq)$ came from Tuckerman *et al.* in 1995, where they found about 60% of configurations associated with $H_9O_4^+$ configurations and 40% Zundel-like configurations. However, they found significant fluctuations of the proton between two waters, but these "proton rattling" motions did not result in proton transfer. The identities of Eigen-like and Zundel-like groupings were further blurred upon the discovery of a "special pair" formed in Eigen species between hydronium and one distinctly close solvation water. The barrier between Eigen-like and Zundel-like configurations was found to be small, only ~ 0.6 kcal/mol ($\approx k_BT$), and was further reduced to < 0.15 kcal/mol when the proton was treated quantum mechanically.[61] However, they stressed that the excess proton potential had to be considered in at least two dimensions, since extension of R_{OO} resulted in an increased barrier, consistent with Bernal and Fowler's proposal.[17] These studies have presented a sophisticated picture of aqueous proton dynamics, but details as seemingly straightforward as the relative population of Eigen-like and Zundel-like geometries have not been verified by experimental measurements.

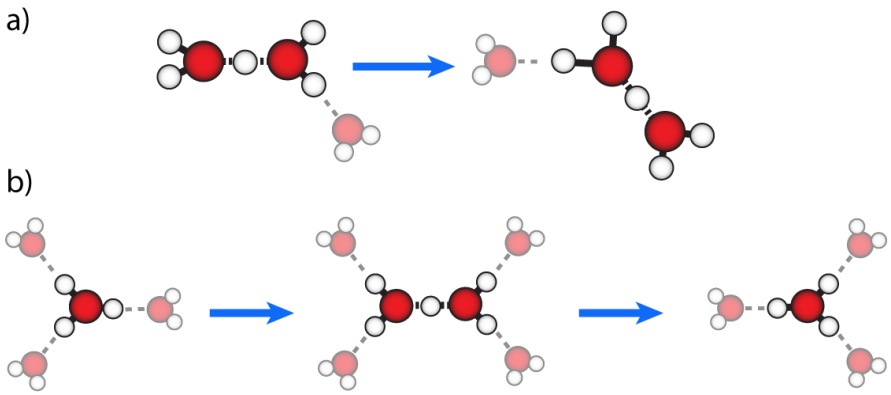

Figure 1.8: Schematics of the proposed (a) Zundel-Zundel and (b) Eigen-Zundel-Eigen proton transfer mechanisms in water.

MS-EVB studies have been utilized to collect statistics in proton hopping events, leading to conflicting proton transport mechanisms. One of the earliest MS-EVB studies arose from Vuilleumier and Borgis, advocating a Zundel-Zundel proton transfer mechanism (Fig. 1.8a), whose prevalence was enhanced with quantized H nuclei.[99] However, Schmitt and Voth soon afterward argued that their method for incorporating charge transfer and proton quantization over-estimated the fraction of Zundel-like species, and in response they developed a different MS-EVB model for describing the excess proton.[96] Early MS-EVB studies from Lapid *et al.*[107] produced a proton diffusion barrier of 2.7 kcal/mol, in good agreement with experiment[67,74] and argued in favor of an Eigen-Zundel-Eigen proton transfer mechanism (Fig. 1.8b).[108] From their trajectories they recovered an average Zundel lifetime of only ~370 fs, implying that the Zundel complex was a transition state between two Eigen configurations stabilized by 0.9 kcal/mol.[89,98] They also found that proton transfer events occurred with H-bond reorganization in the second solvation shell of the reactant hydronium, as suggested before by Agmon.[29,108] Recently, however, a study from Xu and Meuwly developed a multi-state reactive molecular dynamics (MS-RMD) model which limited bias from empirical parameters in the MS-EVB technique. They found similar success as

previous studies in reproducing experimental pair correlation functions, but with a Zundel complex stabilized compared to the Eigen by ~1 kcal/mol and suggested a predominant Zundel-Zundel proton transfer mechanism requiring involvement from two solvation shells.[88] Conflicting proton transfer mechanisms have been deduced despite using similar methods, which highlights how sensitive these models are to initial assumptions.

One of the central mechanistic hypotheses from Voth and Agmon's MS-EVB simulations is the importance of a sub-100 fs process known as the "special pair dance."[109] In this process, a central hydronium experiences fast fluctuations in special pair identity amongst its solvating waters, which decorrelates its initial solvation geometry. Each "special pair" water flanking the excess proton is three-coordinated, on average, with R_{OO} = 2.5 Å, appearing as distorted Zundel-like configuration. But because the identity of the central hydronium persisted past the 40 fs fluctuation timescale, Voth and Agmon argued that the Eigen species is the foundational aqueous species, and the special pair dance reflects the delocalization of electronic charge as Eigen hypothesized.[3,68] The authors argued that the special pair dance mechanism was necessary to recover the fast diffusion coefficient of the excess proton, but this mechanism has not been studied by other groups in detail. Due to the characteristic 40 fs timescale, verifying the special pair dance has remained out of reach for experiment.

To distinguish fast proton rattling from successful proton transfer events, Berkelbach *et al.* uncovered a "pre-solvation" proton transfer mechanism driven by collective H-bond reorganization events.[70] In this mechanism (Fig. 1.9), the typically "hydrophobic" lone pair on hydronium transiently accepts a water H-bond, becoming four-coordinated, while the same fluctuation breaks a H-bond on an adjacent water, creating a solvation environment favorable for the excess proton to exchange sites. This process was found to occur on a 1.7 ps timescale,

consistent with the earlier NMR experiments from Meiboom.[69] Comparing H-bond rupture and formation events, the authors argued that these two process happened as a concerted H-bond jump reorganization event, rather than as a two-step process. The pre-solvation mechanism has become widely accepted,[63,89,104,106,110,111] but experiments have yet to observe this mechanism. Recent AIMD studies of the IR spectrum suggest that there may be spectroscopic markers of the weak H-bond donated to H_3O^+, which may provide a way to directly observe pre-solvation dynamics.[104]

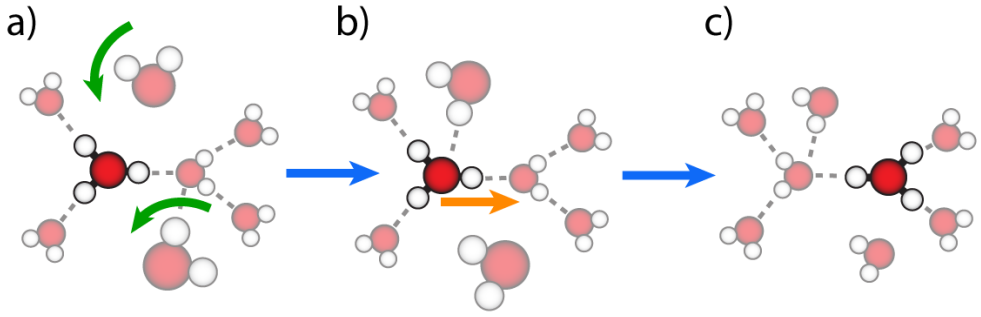

Figure 1.9: A schematic of the pre-solvation mechanism for proton transport. (a) A concerted H-bond reorganization event introduces a fourth H-bond to hydronium and breaks an accepted H-bond by a first shell water. (b) The proton is pushed away from the over-coordinated hydronium, and pulled towards the undercoordinated water, resulting in (c) a new hydronium species.

In the last decade, new results from Hassanali *et al.* indicate that aqueous proton transfer may occur over a hierarchy of energy, length, and time scales, pushing back on the paradigm of individual, stepwise proton hops.[63] In their simulations, they found multi-exponential proton transfer kinetics associated with sub-100fs, concerted proton transfer bursts over many waters and proton traps that persist for multiple ps, known as the "burst-rest" mechanism. This finding suggests that sub-100 fs dynamics could involve long length scales, not just the localized rattling of the proton between two waters as previously assumed. They also found that proton transfer bursts occurred via collective O···O compression and were facilitated by the multiple parallel H-bonding "water wires" emanating from the excess proton. The variety of H-bonding topologies in

solution, including wire and ring motifs, meant that proton transfer could occur with a distribution of energy barriers, similar to the multiple energy scales involved in H-bond reorganization in pure water.[51] Inclusion of nuclear quantum effects amplified solution fluctuations, increased hydrophilicity of hydronium, and amplified the fraction of Zundel-like configurations, all increasing the likelihood of proton transfer events.[110] A later analysis of AIMD trajectories by Tse *et al.* found that water H-bond donation to hydronium was correlated with burst events, connecting burst-rest dynamics with the presolvation mechanism.[111]

The above discussion demonstrates that the majority of our current understanding of proton transfer comes from simulation studies, but there are many competing theories. There is currently debate over whether proton transfer occurs via the Eigen-Zundel-Eigen mechanism, between two Zundel-like species, or if it occurs via a concerted transfer between more than two waters. While proton transfer has traditionally been described as step-wise, recent simulations of the pre-solvation mechanism suggest that concerted H-bond reorganization events drive proton transfer, even if the transfer occurs stepwise between two waters. The dynamics are thought to occur over multiple orders in time, from sub-100 fs rattling, special pair dancing, or concerted transfer events, to multi-ps H-bond reorganization or proton trapping timescales. Much of the remaining uncertainty arises from the variety of the models used for study without connection to measurements. Opposing conclusions, such as the role of Eigen-like or Zundel-like configurations, can arise from similar models, depending on the choices for describing the nuclear potential or if the proton is treated quantum mechanically or not. Ultrafast IR spectroscopic experiments, with femtosecond time resolution and structural sensitivity, are uniquely suited to test these hypotheses.

1.6 Ultrafast Infrared Spectroscopy: Recent Experimental Probes of Structure and Dynamics

While investigations on the aqueous proton have been dominated by gas-phase experiments and aqueous phase simulations, recent advances in 2D IR spectroscopy have made important contributions towards the study of aqueous proton structure. In 2015, Thämer *et al.* employed 2D IR spectroscopy with broadband IR detection to reveal a cross peak between the features at 3200 and 1750 cm^{-1}, respectively, indicative of strong anharmonic coupling between the presumed flanking stretching and bending modes of Zundel-like species. The cross peak appeared to blue-shift in excitation frequency on a 480 fs timescale, demonstrating a growing correlation with bulk water. This timescale set a lower bound for successful proton transfer and challenged the previous conclusion that the Zundel species was a transition state with 370 fs lifetime.[107]

Clear evidence of the Zundel complex in bulk solution came from another 2D IR study by Dahms *et al.*[112] The 2D IR spectrum of the 1200 cm^{-1} diagonal in aqueous medium revealed an unusual inverted anharmonicity pattern, where the ESA appeared at higher detection frequency than the GSB. This signature was the hallmark of the Zundel species in solution, since Zundel's conception of the shared proton potential with confining walls implies a relatively large $|1\rangle \rightarrow |2\rangle$ energy gap. Within the bandwidth of their pump and probe pulses, the feature appeared homogeneously broadening, which was interpreted as arising from fast and large-amplitude electric field fluctuations about a symmetric Zundel motif. The bandwidth of the pulse was much narrower than the breadth of this feature, however, which means that the experiment could not capture any potential inhomogeneous broadening from a distribution of solvation environments. This study also only studied a small region along the 2D IR diagonal and did not address the possible assignment of this feature as Eigen-like umbrella modes. The rich information housed in

2D IR cross peaks has not yet been collected but would provide much-needed clarity on the spectrum of the aqueous proton.

A transient absorption study by Bakker and Woutersen made the first measurements of proton rattling in solution.[113] This was accomplished with isotopically dilute H in deuterated 5M DCl solution, where the lone proton could fluctuate between participation in Eigen-like and Zundel-like geometries. Their measurements involved a two-color experiment, where they pumped the supposedly Eigen-like O–H stretch at 2800 cm^{-1} and probed the transient response at 3300 cm^{-1}, argued to be due to flanking O-H stretches in Zundel-like geometries. They recovered an exponentially decaying signal with a timescale of 120 fs, which is consistent with the fast timescale expected for proton rattling, but is too fast for the type of irreversible proton transfer that is responsible for the anomalously high conductivity of the excess proton.

A more recent study by Yuan *et al.* employed a methyl thiocyanate (MeSCN) vibrational probe to observe proton transfer in highly concentrated HCl solutions.[71] By measuring the chemical exchange timescale between proton-coordinated and water-coordinated SCN and comparing with *ab initio* simulations, the authors were able to arrive at a proton transfer timescale extrapolated to 1.6 ps in the dilute limit, consistent with earlier NMR measurements.[69] The similarity of the proton transfer timescale to H-bond reorganization timescales in water supported a picture of concerted H-bond rearrangement driving proton transfer, but relied on using a molecular probe at high HCl concentrations (>10M HCl) rather than directly observing the proton transfer between water molecules at a more reasonable acid concentration.

These first 2D IR studies on the aqueous proton demonstrate the potential to answer some long-standing questions regarding the structure of the aqueous proton and the dynamics of proton transfer, but there is much more work to be done. As mentioned earlier, the vibrational assignments

across the continuum is uncertain, which impedes attempts to make physical interpretations from spectroscopic data. This uncertainty could be mitigated with stringent benchmarks provided by ultrafast 2D IR spectroscopy, but studies so far have only examined a small subset of the full 2D IR spectrum. Ultrafast IR spectroscopy is also well-suited to test the many dynamical hypotheses proposed by molecular dynamics simulations. A direct experimental measurement of proton transfer between waters has not been measured. The foundational NMR kinetic experiments have measured an apparent 2.4 kcal/mol proton transfer barrier, but the interpretation of this value in terms of a molecular process is missing.

In this thesis, I will present spectroscopic measurements that directly probe the structure and the dynamics of the aqueous proton. With the help of high-level anharmonic vibrational calculations, I will present reliable assignments of the features along the continuum that are consistent with experiment. The assignments are corroborated by new polarization-resolved 2D IR measurements spanning the entire mid-IR, which provide detailed information about the nuclear motions of the aqueous proton complex, their anharmonic couplings, and their mutual orientational relationships. I will then use the anharmonic vibrational calculations to analyze the 2D IR spectrum, which directly assigns vibrational fingerprints to molecular geometries over a distribution of aqueous-phase configurations in solution. Finally, I will present a direct measurement of Grothuss proton transfer in solution with TA spectroscopy and analyze the variation of the kinetics and energy barriers by solution composition to improve our understanding of the molecular mechanism of proton transfer. These analyses provide a reliable foundation for IR spectroscopic studies of the aqueous proton and provide the opportunity for future experiments to directly observe new aspects of proton transfer.

1.7 Thesis Outline

This introduction has provided a brief summary of the knowledge obtained to date on the aqueous proton, but it also demonstrates that there is still much to learn. This thesis will present the work undertaken to gain clarity on aqueous proton structures and proton transport dynamics using linear and nonlinear infrared spectroscopy.

Chapter 2 presents the theory behind linear and nonlinear IR spectroscopy. This chapter will not be exhaustive but will provide the framework necessary to read and interpret these experiments. In particular, this chapter will discuss linear IR spectroscopy, 2D IR spectroscopy, and transient absorption anisotropy decay, and an introduction to the anharmonic vibrational calculations used to interpret aqueous proton spectra.

Chapter 3 contains information on the spectrometer used in these experiments. In the last five years, we have expanded our capabilities in being able to pump across the entire mid-IR. This chapter will present the recent successes and remaining challenges for carrying out these experiments.

Chapter 4 presents a study of the liquid water bend with 2D IR spectroscopy. This study expands upon the discussion of the spectroscopy of pure water in Section 1.2, with additional measurements and a more thorough discussion of excitonic character of H_2O vibrational modes. These findings provide an important backdrop for understanding aqueous acid spectroscopy.

Chapter 5 will present a comprehensive collection of linear and nonlinear IR spectroscopic data on strong acid solutions. This chapter contains spectra excited and detected across the mid-IR, making this the most comprehensive collection of 2D IR spectra of the aqueous proton to date. Spectra as a function of various parameters such as concentration, temperature, and counterion identity are included as appendices to demonstrate their effects on the spectra.

Chapter 6 will present a computational study undertaken to dissect the linear IR spectrum of the aqueous proton. With high-level anharmonic calculations on 800 aqueous configurational snapshots, it has been feasible to reliably assign the different regions of the continuum to anharmonic modes with different vibrational character and cluster geometry. These assignments will play a key role in interpreting the nonlinear IR spectrum.

Chapter 7 will present the second part of the computational study from Chapter 6, interpreting the 2D IR spectrum of the aqueous proton with the aid of high-level anharmonic calculations. I present the 2D IR spectral signatures of various geometric sub-ensembles and assess how they can be related to experiments. These results demonstrate that inclusion of Zundel-like species is necessary to explain the 2D cross peak pattern.

Finally, Chapter 8 will present the results of transient absorption experiments which reveal microscopic details on the Grotthuss proton transfer mechanism in solution. In particular, I have observed reorientation of the aqueous proton complex caused by irreversible proton transfer. These kinetics are probed by the flanking bending modes of predominantly Zundel-like configurations at 1750 cm^{-1}, which are strongly coupled to the proton stretching mode at 1200 cm^{-1}. These experiments involve temperature and counterion dependence, which demonstrate competing enthalpic and entropic effects on the proton transfer barrier.

1.8 References

(1) Oxtoby, D. W.; Gillis, H. P.; Butler, L. J. *Principles of Modern Chemistry*, 8th ed.; Cengage Learning: Boston, MA, 2016.

(2) Whipple, D. T.; Kenis, P. J. A. Prospects of CO_2 Utilization via Direct Heterogeneous Electrochemical Reduction *J. Phys. Chem. Lett.* **2010**, *1*, 3451.

(3) Eigen, M. Proton Transfer, Acid-Base Catalysis, and Enzymatic Hydrolysis. Part I: Elementary Processes *Angew. Chemie Int. Ed. English* **1964**, *3*, 1.

(4) Agmon, N.; Bakker, H. J.; Campen, R. K.; Henchman, R. H.; Pohl, P.; Roke, S.; Thämer, M.; Hassanali, A. Protons and Hydroxide Ions in Aqueous Systems *Chem. Rev.* **2016**, *116*, 7642.

(5) Junge, W.; Nelson, N. ATP Synthase *Annu. Rev. Biochem.* **2015**, *84*, 631.

(6) Schindler, D. W. Effects of acid rain on freshwater ecosystems *Science* **1988**, *239*, 149.

(7) Talmage, S. C.; Gobler, C. J. Effects of past, present, and future ocean carbon dioxide concentrations on the growth and survival of larval shellfish *Proc. Natl. Acad. Sci. U. S. A.* **2010**, *107*, 17246.

(8) Yan, L.; Hu, Y.; Zhang, X.; Yue, B. Applications of NMR Techniques in the Development and Operation of Proton Exchange Membrane Fuel Cells *Annu. Reports NMR Spectrosc.* **2016**, *88*, 149.

(9) İhsanoğlu, E.; Research Centre for Islamic History, A. *Cultural contacts in building a universal civilisation : Islamic contributions*; O.I.C. Research Centre for Islamic History, Art and Culture (IRCICA), 2005.

(10) Parks, G. D.; Mellor, J. W. *Mellor's Modern Inorganic Chemistry*, 6th ed.; Longmans, Green and Co: London, 1939.

(11) Wöhler; Liebig. Untersuchungen über das Radikal der Benzoesäure *Ann. der Pharm.* **1832**, *3*, 249.

(12) Arrhenius, S. Über die Dissociation der in Wasser gelösten Stoffe *Z. Phys. Chem.* **1887**, *1*, 631.

(13) Brönsted, J. N. Einige Bemerkungen über den Begriff der Säuren und Basen *Recl. des Trav. Chim. des Pays-Bas* **1923**, *42*, 718.

(14) Lowry, T. M. The uniqueness of hydrogen *J. Soc. Chem. Ind.* **1923**, *42*, 43.

(15) Lewis, G. N. *Valence and the Structure of Atoms and Molecules*; Noyes, W. A., Ed.; The Chemical Catalog Company: New York, NY, 1923.

(16) Hittorf, W. On the migration of ions during electrolysis *Pogg. Ann.* **1853**, *89*, 177.

(17) Bernal, J. D.; Fowler, R. H. A theory of water and ionic solution, with particular reference to hydrogen and hydroxyl ions *J. Chem. Phys.* **1933**, *1*, 515.

(18) United States Geographical Survey. How Much Water is There on Earth? https://www.usgs.gov/special-topic/water-science-school/science/how-much-water-there-earth?qt-science_center_objects=0#qt-science_center_objects (accessed Apr 11, 2020).

(19) Császár, A. G.; Czakó, G.; Furtenbacher, T.; Tennyson, J.; Szalay, V.; Shirin, S. V.; Zobov, N. F.; Polyansky, O. L. On equilibrium structures of the water molecule *J. Chem.*

Phys. **2005**, *122*, 214305.

(20) Lovas, F. J. Microwave spectral tables II. Triatomic molecules *J. Phys. Chem. Ref. Data* **1978**, *7*, 1445.

(21) Hankins, D.; Moskowitz, J. W.; Stillinger, F. H. Water molecule interactions *J. Chem. Phys.* **1970**, *53*, 4544.

(22) Rocher-Casterline, B. E.; Chng, L. C.; Mollner, A. K.; Reisler, H. Communication: Determination of the bond dissociation energy (D_0) of the water dimer, $(H_2O)_2$, by velocity map imaging *J. Chem. Phys.* **2011**, *134*, 211101.

(23) Tainter, C. J.; Pieniazek, P. A.; Lin, Y. S.; Skinner, J. L. Robust three-body water simulation model *J. Chem. Phys.* **2011**, *134*, 184501.

(24) Fanourgakis, G. S.; Xantheas, S. S. Development of transferable interaction potentials for water. V. Extension of the flexible, polarizable, Thole-type model potential (TTM3-F, v. 3.0) to describe the vibrational spectra of water clusters and liquid water *J. Chem. Phys.* **2008**, *128*, 074506.

(25) Wang, Y.; Bowman, J. M. Towards an ab initio flexible potential for water, and post-harmonic quantum vibrational analysis of water clusters *Chem. Phys. Lett.* **2010**, *491*, 1.

(26) Reddy, S. K.; Straight, S. C.; Bajaj, P.; Huy Pham, C.; Riera, M.; Moberg, D. R.; Morales, M. A.; Knight, C.; Gotz, A. W.; Paesani, F. On the accuracy of the MB-pol many-body potential for water: Interaction energies, vibrational frequencies, and classical thermodynamic and dynamical properties from clusters to liquid water and ice *J. Chem. Phys.* **2016**, *145*, 194504.

(27) Kumar, R.; Schmidt, J. R.; Skinner, J. L. Hydrogen bonding definitions and dynamics in liquid water *J. Chem. Phys.* **2007**, *126*, 204107.

(28) Luzar, A.; Chandler, D. Effect of environment on hydrogen bond dynamics in liquid water *Phys. Rev. Lett.* **1996**, *76*, 928.

(29) Agmon, N. Hydrogen bonds, water rotation and proton mobility *J. Chim. Phys.* **1996**, *93*, 1714.

(30) Boyer, M. A.; Marsalek, O.; Heindel, J. P.; Markland, T. E.; McCoy, A. B.; Xantheas, S. S. Beyond Badger's Rule: The Origins and Generality of the Structure–Spectra Relationship of Aqueous Hydrogen Bonds *J. Phys. Chem. Lett.* **2019**, *10*, 918.

(31) Badger, R. M. A relation between internuclear distances and bond force constants *J. Chem. Phys.* **1934**, *2*, 128.

(32) Eaves, J. D.; Tokmakoff, A.; Geissler, P. L. Electric Field Fluctuations Drive Vibrational Dephasing in Water. *J. Phys. Chem. A* **2005**, *109*, 9424.

(33) Fecko, C. J.; Eaves, J. D.; Loparo, J. J.; Tokmakoff, A.; Geissler, P. L. Ultrafast Hydrogen-Bond Dynamics in the Infrared Spectroscopy of Water. *Science* **2003**, *301*, 1698.

(34) De Marco, L.; Fournier, J. A.; Thämer, M.; Carpenter, W.; Tokmakoff, A. Anharmonic exciton dynamics and energy dissipation in liquid water from two-dimensional infrared spectroscopy *J. Chem. Phys.* **2016**, *145*, 094501.

(35) Kananenka, A. A.; Skinner, J. L. Fermi resonance in OH-stretch vibrational spectroscopy of liquid water and the water hexamer *J. Chem. Phys.* **2018**, *148*, 244107.

(36) Monecke, J. Theory of Fermi Resonances in Raman and Infrared Spectra *J. Raman Spectrosc.* **1987**, *18*, 477.

(37) Schmidt, J. R.; Corcelli, S. A.; Skinner, J. L. Pronounced non-Condon effects in the ultrafast infrared spectroscopy of water. *J. Chem. Phys.* **2005**, *123*, 044513.

(38) Kubo, R. In *Fluctuation, Relaxation and Resonance in Magnetic Systems*; Ter Haar, D., Ed.; Oliver & Boyd: Edinburgh, 1962; pp 23–68.

(39) Hall, L. The origin of ultrasonic absorption in water *Phys. Rev.* **1948**, *73*, 775.

(40) Fecko, C. J.; Loparo, J. J.; Roberts, S. T.; Tokmakoff, A. Local Hydrogen Bonding Dynamics and Collective Reorganization in Water: Ultrafast Infrared Spectroscopy of HOD/D$_2$O. *J. Chem. Phys.* **2005**, *122*, 54506.

(41) Nicodemus, R. A.; Ramasesha, K.; Roberts, S. T.; Tokmakoff, A. Hydrogen Bond Rearrangements in Water Probed with Temperature-Dependent 2D IR *J. Phys. Chem. Lett.* **2010**, *1*, 1068.

(42) Ramasesha, K.; Roberts, S. T.; Nicodemus, R. A.; Mandal, A.; Tokmakoff, A. Ultrafast 2D IR Anisotropy of Water Reveals Reorientation During Hydrogen-Bond Switching. *J. Chem. Phys.* **2011**, *135*, 54509.

(43) Loparo, J.; Fecko, C.; Eaves, J.; Roberts, S.; Tokmakoff, A. Reorientational and Configurational Fluctuations in Water Observed on Molecular Length Scales. *Phys. Rev. B* **2004**, *70*, 180201.

(44) Eaves, J. D.; Loparo, J. J.; Fecko, C. J.; Roberts, S. T.; Tokmakoff, A.; Geissler, P. L. Hydrogen Bonds in Liquid Water are Broken Only Fleetingly. *Proc. Natl. Acad. Sci. U. S. A.* **2005**, *102*, 13019.

(45) Asbury, J. B.; Steinel, T.; Kwak, K.; Corcelli, S. A.; Lawrence, C. P.; Skinner, J. L.; Fayer, M. D. Dynamics of water probed with vibrational echo correlation spectroscopy. *J. Chem. Phys.* **2004**, *121*, 12431.

(46) Steinel, T.; Asbury, J. B.; Zheng, J.; Fayer, M. D. Watching Hydrogen Bonds Break: A Transient Absorption Study of Water. *J. Phys. Chem. A* **2004**, *108*, 10957.

(47) Asbury, J. B.; Steinel, T.; Fayer, M. D. Vibrational Echo Correlation Spectroscopy Probes of Hydrogen Bond Dynamics in Water and Methanol. *J. Lumin.* **2004**, *107*, 271.

(48) Ji, M.; Odelius, M.; Gaffney, K. J. Large angular jump mechanism observed for hydrogen bond exchange in aqueous perchlorate solution. *Science* **2010**, *328*, 1003.

(49) Nicodemus, R. A.; Corcelli, S. A.; Skinner, J. L.; Tokmakoff, A. Collective Hydrogen Bond Reorganization in Water Studied with Temperature-Dependent Ultrafast Infrared Spectroscopy *J. Phys. Chem. B* **2011**, *115*, 5604.

(50) Ohmine, I.; Saito, S. Water Dynamics: Fluctuation, Relaxation, and Chemical Reactions in Hydrogen Bond Network Rearrangement *Acc. Chem. Res.* **1999**, *32*, 741.

(51) Ohmine, I. Liquid Water Dynamics: Collective Motions, Fluctuation, and Relaxation *J. Phys. Chem.* **1995**, *99*, 6767.

(52) Laage, D.; Hynes, J. T. A molecular jump mechanism of water reorientation *Science* **2006**, *311*, 832.

(53) Ramasesha, K.; De Marco, L.; Mandal, A.; Tokmakoff, A. Water vibrations have strongly mixed intra- and intermolecular character *Nat. Chem.* **2013**, *5*, 935.

(54) Auer, B. M.; Skinner, J. L. IR and Raman spectra of liquid water: theory and interpretation. *J. Chem. Phys.* **2008**, *128*, 224511.

(55) Paarmann, A.; Hayashi, T.; Mukamel, S.; Miller, R. J. D. Nonlinear response of vibrational excitons: Simulating the two-dimensional infrared spectrum of liquid water *J. Chem. Phys.* **2009**, *130*, 204110.

(56) Lindner, J.; Vöhringer, P.; Pshenichnikov, M. S.; Cringus, D.; Wiersma, D. A.; Mostovoy, M. Vibrational relaxation of pure liquid water *Chem. Phys. Lett.* **2006**, *421*, 329.

(57) Park, S.; Fayer, M. D. Hydrogen bond dynamics in aqueous NaBr solutions. *Proc. Natl. Acad. Sci. U. S. A.* **2007**, *104*, 16731.

(58) Fournier, J. A.; Carpenter, W.; De Marco, L.; Tokmakoff, A. Interplay of Ion–Water and Water–Water Interactions within the Hydration Shells of Nitrate and Carbonate Directly Probed with 2D IR Spectroscopy *J. Am. Chem. Soc.* **2016**, *138*, 9634.

(59) Collie, J. N.; Tickle, T. LXVI. - The salts of dimethylpyrone, and the quadrivalence of oxygen *J. Chem. Soc. Trans.* **1899**, *75*, 710.

(60) de Grotthuss, C. J. T. Sur la decomposition de l'eau et des corps qu'elle tient en dissolution à l'aide de l'electricité galvanique *Ann. Chim.* **1806**, *58*, 54.

(61) Marx, D.; Tuckerman, M. E.; Hutter, J.; Parrinello, M. The nature of the hydrated excess proton in water *Nature* **1999**, *397*, 601.

(62) Marx, D. Proton Transfer 200 Years after von Grotthuss: Insights from Ab Initio Simulations *Chem. Phys. Chem* **2006**, *7*, 1848.

(63) Hassanali, A.; Giberti, F.; Cuny, J.; Kühne, T. D.; Parrinello, M. Proton transfer through the water gossamer. *Proc. Natl. Acad. Sci. U. S. A.* **2013**, *110*, 13723.

(64) Zundel, G.; Metzger, H. Energiebänder der tunnelnden Überschuß-Protonen in flüssigen Säuren. Eine IR-spektroskopische Untersuchung der Natur der Gruppierungen $H_5O_2^+$ *Z. Phys. Chem.* **1968**, *58*, 225.

(65) Gierer, A.; Wirtz, K. Anomalous Mobility of H^+ and OH^- Ions *J. Chem. Phys.* **1949**, *17*, 745.

(66) Glasstone, S.; Laidler, K. J.; Eyring, H. *The Theory of Rate Processes*; McGraw-Hill: New York, NY, 1941.

(67) Gierer, A.; Wirtz, K. Proton and deuteron transfer over hydrogen bridges as cause of conductivity effects *J. Phys. Chem.* **1952**, *56*, 914.

(68) Wicke, E.; Eigen, M.; Ackermann, T. Über den Zustand des Protons (Hydroniumions) in wäßriger Lösung *Z. Phys. Chem. (N. F)*. **1954**, *1*, 340.

(69) Meiboom, S. Nuclear Magnetic Resonance Study of the Proton Transfer in Water *J. Chem. Phys.* **1961**, *34*, 375.

(70) Berkelbach, T. C.; Lee, H. S.; Tuckerman, M. E. Concerted Hydrogen-Bond Dynamics in the Transport Mechanism of the Hydrated Proton: A First-Principles Molecular Dynamics Study *Phys. Rev. Lett.* **2009**, *103*, 238302.

(71) Yuan, R.; Napoli, J. A.; Yan, C.; Marsalek, O.; Markland, T. E.; Fayer, M. D. Tracking Aqueous Proton Transfer by Two-Dimensional Infrared Spectroscopy and ab Initio Molecular Dynamics Simulations *ACS Cent. Sci.* **2019**, *5*, 1269.

(72) Fischer, S. A.; Gunlycke, D. Analysis of Correlated Dynamics in the Grotthuss Mechanism of Proton Diffusion *J. Phys. Chem. B* **2019**, acs. jpcb.9b02610.

(73) Fischer, S. A.; Dunlap, B. I.; Gunlycke, D. Correlated dynamics in aqueous proton diffusion *Chem. Sci.* **2018**, *9*, 7126.

(74) Luz, Z.; Meiboom, S. The Activation Energies of Proton Transfer Reactions in Water *J. Am. Chem. Soc.* **1964**, *86*, 4768.

(75) Pfeifer, R.; Hertz, H. G. Activation Energies of the Proton-exchange Reactions in Water Measured with the 1 H-NMR Spin Echo Technique *Berichte Der Bunsengesellschaft Fur Phys. Chemie* **1990**, *94*, 1349.

(76) Loewenstein, A.; Szoke, A. The Activation Energies of Proton Transfer Reactions in Water *J. Am. Chem. Soc.* **1962**, *84*, 1151.

(77) Schwarz, H. A. Gas phase infrared spectra of oxonium hydrate ions from 2 to 5 μ *J. Chem. Phys.* **1977**, *67*, 5525.

(78) Yeh, L. I.; Okumura, M.; Myers, J. D.; Price, J. M.; Lee, Y. T. Vibrational spectroscopy of the hydrated hydronium cluster ions $H_3O^+ \cdot (H2O)_n$ (n= 1, 2, 3) *J. Chem. Phys.* **1989**, *91*, 7319.

(79) Xie, Y.; Remington, R. B.; Schaefer, H. F. The protonated water dimer: Extensive theoretical studies of $H_5O_2^+$ *J. Chem. Phys.* **1994**, *101*, 4878.

(80) Yeh, L. I.; Lee, Y. T.; Hougen, J. T. Vibration-Rotation Spectroscopy of the Hydrated Hydronium Ions $H_5O_2^+$ and $H_9O_4^+$ *J. Mol. Spectrosc.* **1994**, *164*, 473.

(81) Asmis, K. R.; Pivonka, N. L.; Santambrogio, G.; Brümmer, M.; Kaposta, C.; Neumark, D. M.; Wöste, L. Gas-phase infrared spectrum of the protonated water dimer. *Science* **2003**, *299*, 1375.

(82) Vendrell, O.; Gatti, F.; Meyer, H.-D. Full dimensional (15-dimensional) quantum-dynamical simulation of the protonated water dimer. II. Infrared spectrum and vibrational dynamics *J. Chem. Phys.* **2007**, *127*, 184303.

(83) Hammer, N. I.; Diken, E. G.; Roscioli, J. R.; Johnson, M. A.; Myshakin, E. M.; Jordan, K. D.; McCoy, A. B.; Huang, X.; Bowman, J. M.; Carter, S. The vibrational predissociation spectra of the $H_5O_2^+ \cdot RG_n$(RG=Ar,Ne) clusters: Correlation of the solvent perturbations in the free OH and shared proton transitions of the Zundel ion *J. Chem. Phys.* **2005**, *122*, 244301.

(84) Headrick, J. M.; Diken, E. G.; Walters, R. S.; Hammer, N. I.; Christie, R. A.; Cui, J.; Myshakin, E. M.; Duncan, M. A.; Johnson, M. A.; Jordan, K. D. Spectral Signatures of Hydrated Proton Vibrations in Water Clusters *Science* **2005**, *308*, 1765.

(85) Wolke, C. T.; Fournier, J. A.; Dzugan, L. C.; Fagiani, M. R.; Odbadrakh, T. T.; Knorke, H.; Jordan, K. D.; McCoy, A. B.; Asmis, K. R.; Johnson, M. A. Spectroscopic snapshots of the proton-transfer mechanism in water *Science* **2016**, *354*, 1131.

(86) Fournier, J. A.; Wolke, C. T.; Johnson, M. A.; Odbadrakh, T. T.; Jordan, K. D.; Kathmann, S. M.; Xantheas, S. S. Snapshots of Proton Accommodation at a Microscopic Water Surface: Understanding the Vibrational Spectral Signatures of the Charge Defect in Cryogenically Cooled $H^+(H_2O)_{n=2-28}$ Clusters *J. Phys. Chem. A* **2015**, *119*, 9425.

(87) Iyengar, S. S.; Petersen, M. K.; Day, T. J. F.; Burnham, C. J.; Teige, V. E.; Voth, G. A. The properties of ion-water clusters. I. the protonated 21-water cluster *J. Chem. Phys.* **2005**, *123*, 084309.

(88) Xu, Z.-H.; Meuwly, M. Multistate Reactive Molecular Dynamics Simulations of Proton Diffusion in Water Clusters and in the Bulk *J. Phys. Chem. B* **2019**, *123*, 9846.

(89) Biswas, R.; Tse, Y. L. S.; Tokmakoff, A.; Voth, G. A. Role of Presolvation and

Anharmonicity in Aqueous Phase Hydrated Proton Solvation and Transport *J. Phys. Chem. B* **2016**, *120*, 1793.

(90) Devlin, J. P.; Sadlej, J.; Hollman, M.; Buch, V. Solvation stages of HCl and HBr in crystalline phases with methanol and small ethers: Acid-ether cluster complexes in amorphous and crystal phases *J. Phys. Chem. A* **2004**, *108*, 2030.

(91) Kobayashi, C.; Saito, S.; Ohmine, I. Mechanism of fast proton transfer in ice: Potential energy surface and reaction coordinate analyses *J. Chem. Phys.* **2000**, *113*, 9090.

(92) Drechsel-Grau, C.; Marx, D. Collective proton transfer in ordinary ice: local environments, temperature dependence and deuteration effects *Phys. Chem. Chem. Phys.* **2017**, *19*, 2623.

(93) Kalish, N. B.-M.; Shandalov, E.; Kharlanov, V.; Pines, D.; Pines, E. Apparent Stoichiometry of Water in Proton Hydration and Proton Dehydration Reactions in CH_3CN/H_2O Solutions *J. Phys. Chem. A* **2011**, *115*, 4063.

(94) Dahms, F.; Costard, R.; Pines, E.; Fingerhut, B. P.; Nibbering, E. T. J.; Elsaesser, T. The Hydrated Excess Proton in the Zundel Cation $H_5O_2^+$: The Role of Ultrafast Solvent Fluctuations *Angew. Chemie - Int. Ed.* **2016**, *55*, 10600.

(95) Thämer, M.; De Marco, L.; Ramasesha, K.; Mandal, A.; Tokmakoff, A. Ultrafast 2D IR spectroscopy of the excess proton in liquid water *Science* **2015**, *350*, 78.

(96) Schmitt, U. W.; Voth, G. A. The computer simulation of proton transport in water *J. Chem. Phys.* **1999**, *111*, 9361.

(97) Kim, J.; Schmitt, U. W.; Gruetzmacher, J. A.; Voth, G. A.; Scherer, N. E. The vibrational spectrum of the hydrated proton: Comparison of experiment, simulation, and normal mode analysis *J. Chem. Phys.* **2002**, *116*, 737.

(98) Wu, Y.; Chen, H.; Wang, F.; Francesco Paesani, A.; Voth, G. A. An Improved Multistate Empirical Valence Bond Model for Aqueous Proton Solvation and Transport† *J. Phys. Chem. B* **2007**, *112*, 467.

(99) Vuilleumier, R.; Borgis, D. Transport and spectroscopy of the hydrated proton: A molecular dynamics study *J. Chem. Phys.* **1999**, *111*, 4251.

(100) Knight, C.; Voth, G. A. The curious case of the hydrated proton *Acc. Chem. Res.* **2012**, *45*, 101.

(101) Xu, J.; Zhang, Y.; Voth, G. A. Infrared spectrum of the hydrated proton in water *J. Phys. Chem. Lett.* **2011**, *2*, 81.

(102) Biswas, R.; Carpenter, W.; Fournier, J. A.; Voth, G. A.; Tokmakoff, A. IR spectral assignments for the hydrated excess proton in liquid water *J. Chem. Phys.* **2017**, *146*, 154507.

(103) Daly, C. A.; Streacker, L. M.; Sun, Y.; Pattenaude, S. R.; Hassanali, A. A.; Petersen, P. B.; Corcelli, S. A.; Ben-Amotz, D. Decomposition of the Experimental Raman and Infrared Spectra of Acidic Water into Proton, Special Pair, and Counterion Contributions *J. Phys. Chem. Lett.* **2017**, *8*, 5246.

(104) Napoli, J. A.; Marsalek, O.; Markland, T. E. Decoding the spectroscopic features and time scales of aqueous proton defects *J. Chem. Phys.* **2018**, *148*, 222833.

(105) Car, R.; Parrinello, M. Unified approach for molecular dynamics and density-functional theory *Phys. Rev. Lett.* **1985**, *55*, 2471.

(106) Hassanali, A. A.; Cuny, J.; Verdolino, V.; Parrinello, M. Aqueous solutions: State of the art in ab initio molecular dynamics *Phil. Trans. R. Soc. A* **2014**, *372*.

(107) Lapid, H.; Agmon, N.; Petersen, M. K.; Voth, G. A. A bond-order analysis of the mechanism for hydrated proton mobility in liquid water *J. Chem. Phys.* **2005**, *122*, 014506.

(108) Agmon, N. The Grotthuss mechanism *Chem. Phys. Lett.* **1995**, *244*, 456.

(109) Markovitch, O.; Chen, H.; Izvekov, S.; Paesani, F.; Voth, G. A.; Agmon, N. Special pair dance and partner selection: elementary steps in proton transport in liquid water. *J. Phys. Chem. B* **2008**, *112*, 9456.

(110) Giberti, F.; Hassanali, A. A.; Ceriotti, M.; Parrinello, M. The Role of Quantum Effects on Structural and Electronic Fluctuations in Neat and Charged Water *J. Phys. Chem. B* **2014**, *118*, 13226.

(111) Tse, Y. L. S.; Knight, C.; Voth, G. A. An analysis of hydrated proton diffusion in ab initio molecular dynamics *J. Chem. Phys.* **2015**, *142*, 014104.

(112) Dahms, F.; Fingerhut, B. P.; Nibbering, E. T. J.; Pines, E.; Elsaesser, T. Large-amplitude transfer motion of hydrated excess protons mapped by ultrafast 2D IR spectroscopy *Science* **2017**, *357*, 491.

(113) Woutersen, S.; Bakker, H. J. Ultrafast Vibrational and Structural Dynamics of the Proton in Liquid Water *Phys. Rev. Lett.* **2006**, *96*, 138305.

Chapter 2

Theoretical Background for Nonlinear Spectroscopy and Anharmonic Vibrational Calculations

2.1 Introduction

To perform two-dimensional infrared (2D IR) and transient absorption (TA) measurements on the structure and dynamics of the aqueous proton complex, we need a framework for understanding these experiments. This chapter presents a summary of the main results of these techniques to orient the reader before presenting the data. While central mathematical results are presented in this chapter, an additional aim is to provide some physical insights for those who are less familiar with the formalism. The topics in this chapter include light-matter interaction in the condensed phase, linear absorption, coherent third-order signals and 2D IR spectra, and orientational measurements via polarization anisotropy. These selected topics are key to the conclusions regarding the aqueous proton in this thesis, but inevitably there are other topics relating to nonlinear spectroscopy that were not included that the reader can explore if interested.[1–8]

For interpreting the experimental spectra of the aqueous proton, I collaborated with Dr. Qi Yu and Prof. Joel Bowman at Emory University, who specialize in quantum-mechanical vibrational calculations of highly anharmonic gas-phase clusters. As will be presented in Chapters 6 and 7, their calculations on hydrated proton clusters have provided a firm footing for assigning vibrational

modes of the aqueous proton complex. Their method, vibrational self-consistent field/virtual configuration interaction (VSCF/VCI), can treat highly anharmonic systems with multi-mode coupling on high-dimensional nuclear potential energy surfaces. Despite its high computational expense, VSCF/VCI is necessary for modeling the aqueous proton due to the large anharmonicity of each mode and strong coupling with other vibrational modes, as seen in the experimental 2D IR spectrum (Chapter 5). To introduce the reader to the method, I have included a summary to highlight some of the underpinnings of VSCF/VCI and why they are useful for studying the aqueous proton. Bear in mind that I am not an expert in the technique, so the discussion will not be too technical. Instead, I hope this may serve as a resource for experimentalists who may be interested in learning about the technique and applying it to new systems in the future.

2.2 Time-Domain Spectroscopy and the Response Function

Spectroscopic experiments are physically possible because light and matter interact with each other. Despite the fact that molecules are orders of magnitude smaller than the wavelength of light, the way a beam of light changes after interacting with a sample is directly connected to its molecular behavior. This ability to directly interrogate a microscopic system is what makes spectroscopy valuable for observing molecular dynamics.

To begin, we treat light as an oscillating electric field $\mathbf{E}(\mathbf{r},t)$ described in terms of its position $\mathbf{r}$ and time t, where bolded terms indicate vector quantities. We can consider the simple case where $\mathbf{E}(\mathbf{r},t)$ is a transverse plane wave with angular frequency ω, propagating in the direction of the wavevector $\mathbf{k}$:

$$\mathbf{E}(\mathbf{r},t) = E_0 \exp[-i\omega t + \mathbf{k}\cdot\mathbf{r}] + \text{c.c.} \tag{2.1}$$

An electric field traveling through a dielectric medium displaces the bound positive and negative charges of the medium (e.g. nuclei and electrons), inducing a collective dipole called the polarization $\mathbf{P}(\mathbf{r},t)$. This acts as a source term coupling the light and matter in Maxwell's equations, written here in Gaussian units:

$$\nabla^2\mathbf{E}(\mathbf{r},t)-\frac{1}{c^2}\frac{\partial^2\mathbf{E}(\mathbf{r},t)}{\partial t^2}=\frac{4\pi}{c^2}\frac{\partial^2\mathbf{P}(\mathbf{r},t)}{\partial t^2}, \tag{2.2}$$

where c is the speed of light in vacuum. Using Eq. 2.1 for $\mathbf{E}(\mathbf{r},t)$, it can be shown that $\mathbf{P}(\mathbf{r},t)$ also takes a plane wave form whose phase is shifted by a factor of $\pi/2$.[1]

The oscillatory nature of the electric field generates a collection coherently oscillating induced dipoles, which in turn generate their own oscillating electric field. In most situations, there is a linear relationship between the amplitude of the electric field and the resulting polarization. However, for large electric field amplitudes ($E_0 > 1$ V/Å),[9] the incident field is comparable to the ambient electric field experienced by the electrons in the medium, driving them from equilibrium in a way that scales nonlinearly with $\mathbf{E}(\mathbf{r},t)$. The polarization can be expanded by the order of nonlinearity, written in the frequency domain as

$$\begin{aligned}\mathbf{P}(\omega)&=\mathbf{P}^{(1)}(\omega)+\mathbf{P}^{(2)}(\omega)+\mathbf{P}^{(3)}(\omega)+\ldots\\&=\chi^{(1)}\mathbf{E}(\omega)+\chi^{(2)}\mathbf{E}^2(\omega)+\chi^{(3)}\mathbf{E}^3(\omega)+\ldots\end{aligned} \tag{2.3}$$

where $\chi^{(1)}$ is the linear susceptibility and $\chi^{(i)}$ for $i > 1$ are the i^{th}-order nonlinear susceptibilities.[10] Experimental access to nonlinear polarization was made achievable with the development of pulsed lasers,[11] and manifests as nonlinear optical phenomena like second harmonic generation (SHG) or 2D IR spectroscopy.

To retrieve the molecular information from the nonlinear polarization, it is necessary to build a framework to connect microscopic and macroscopic quantities. Because nonlinear optical

experiments are conducted with ultrashort laser pulses, it is natural to employ a time-domain treatment of the evolving polarization. The following semi-classical approach describes how a quantum system responds to a classical electric field. The dynamics of the material system is described in terms of its evolving density matrix $\hat{\rho}(t)$, which is a useful quantity for characterizing an ensemble of quantum states.

The dynamics of a system's density matrix is described by the quantum Liouville equation:

$$\frac{d}{dt}\rho(t) = -\frac{i}{\hbar}\Big[H(t), \rho(t)\Big], \tag{2.4}$$

where $\hat{H}(t)$ is the Hamiltonian for the system. In linear response theory, the interaction between the density matrix with the incident electric field is treated as a small perturbation $\hat{V}(t)$, such that

$$H(t) = H_0(t) + V(t), \tag{2.5}$$

with $\hat{H}_0(t)$ as the Hamiltonian of the system at equilibrium. The light-matter interaction term reflects the coupling between the material dipole, written as the quantum operator $\boldsymbol{\mu}$, and the field:

$$V(t) = -\boldsymbol{\mu} \cdot \mathbf{E}(t). \tag{2.6}$$

This expression invokes the electric dipole approximation, neglecting weaker higher-order terms such as coupling to electric quadrupoles. This is a reasonable approximation for bulk-sensitive third-order spectroscopy, but is less reliable for surface-sensitive second-order techniques.[12,13]

We transform our representation to the interaction picture of quantum mechanics to describe the action of quantum operators at specific times. An operator $A(t)$ is transformed by applications of the unitary time propagator $U(t)$:

$$A_I(t) = U^{\dagger}(t)\, A(t) U(t) \tag{2.7}$$

where $U(t) = \exp[-iH_0 t/\hbar]$ is the time propagator under the equilibrium Hamiltonian and $U^{\dagger}(t)$ is its adjoint. Rewriting Eq. 2.4 in the interaction picture and integrating over time yields a solution for the density matrix:

$$\rho_I(t) = \rho_0 - \frac{i}{\hbar}\int_{t_0}^{t} \mathrm{d}t_1 \left[V_I(t_1), \rho_I(t_1)\right], \tag{2.8}$$

where ρ_0 is the equilibrium density matrix at initial time t_0. The presence of $V_I(t)$ in the commutator reflects that the evolution of the density matrix away from equilibrium is caused by the perturbation rather than the equilibrium portion of the Hamiltonian.

Within a small perturbation regime, the right-hand side of Eq. 2.8 can be iteratively plugged in for $\rho_I(t_1)$, which results in an expansion for the density matrix in terms of the order of the perturbation:

$$\rho_I(t) = \sum_{n=0}^{\infty} \rho_I^{(n)}(t), \tag{2.9}$$

where

$$\rho_I^{(n)}(t) = \left(\frac{i}{\hbar}\right)^n \int_{t_0}^{t} \mathrm{d}t_n \int_{t_0}^{t_n} \mathrm{d}t_{n-1} \ldots \int_{t_0}^{t_2} \mathrm{d}t_1 \left[V_I(t_n), \left[V_I(t_{n-1}), \left[\ldots, \left[V_I(t_1), \rho_0\right]\right]\right]\right], \tag{2.10}$$

where $t_n \geq t_{n-1} \geq \ldots \geq t_1 \geq t_0$.[1]

In connection to the classical picture presented in Eq. 2.2, the polarization is the ensemble average of the dipole operator, which can be calculated as a trace:

$$\mathbf{P}(t) = \langle \boldsymbol{\mu}_I(t) \rangle = \mathrm{Tr}\{\boldsymbol{\mu}_I(t)\rho_I(t)\}. \tag{2.11}$$

The nonlinear terms of the polarization expansion in Eq. 2.3 are directly related to the respective terms in the density matrix in Eq. 2.10. We can evaluate for the nonlinear polarization of order n by plugging in Eqs. 2.9 and 2.10 into Eq. 2.11, substituting in Eq. 2.6 for $V(t)$, which yields

$$\mathbf{P}^{(n)}(t)=\left(\frac{i}{\hbar}\right)^{n}\int_{t_0}^{t}\mathrm{d}t_n\int_{t_0}^{t_n}\mathrm{d}t_{n-1}...\int_{t_0}^{t_2}\mathrm{d}t_1\mathbf{E}_n(t_n)\mathbf{E}_{n-1}(t_{n-1})...\mathbf{E}_1(t_1)\mathrm{Tr}\left\{\boldsymbol{\mu}_I(t_n),\left[\boldsymbol{\mu}_I(t_{n-1}),...,\left[\boldsymbol{\mu}_I(t_1),\rho_0\right]\right]\right\}. \quad (2.12)$$

We change variables from absolute times t_i to time intervals τ_i, since intervals between pulses are actually under our control in the experiment. We send $t_1 = 0$ and define intervals τ_k as

$$\begin{aligned}\tau_1&=t_2-t_1\\ \tau_2&=t_3-t_2\\ &\vdots\\ \tau_k&=t_{k+1}-t_k.\end{aligned} \quad (2.13)$$

This results in the final expressions for the nonlinear polarization and response function:

$$\mathbf{P}^{(n)}(t)=\int_0^{\infty}\mathrm{d}\tau_n\int_0^{\infty}\mathrm{d}\tau_{n-1}...\int_0^{\infty}\mathrm{d}\tau_1\mathbf{E}(t-\tau_n)\mathbf{E}(t-t_n-t_{n-1})...\mathbf{E}(t-\tau_n-...-\tau_1)R^{(n)}(\tau_1,\tau_2,...,\tau_n) \quad (2.14)$$

and

$$R^{(n)}(\tau_n,\tau_{n-1},...,\tau_1)=\left(\frac{i}{\hbar}\right)^{n}\mathrm{Tr}\left\{\left[\boldsymbol{\mu}_I(\tau_n+...+\tau_1),\left[\boldsymbol{\mu}_I(\tau_{n-1}+...+\tau_1),...,\left[\boldsymbol{\mu}_I(\tau_1),\boldsymbol{\mu}_I(0)\right]\right]\right]\rho_0\right\}\prod_{k=1}^{n}\theta(\tau_k). \quad (2.15)$$

In Eq. 2.15, time ordering has been maintained with the Heaviside step functions $\theta(\tau_k)$. Additionally, we took advantage of the cyclic permutability of the trace to write $R^{(n)}$ as a trace of nested dipole commutators over the equilibrium density matrix.

There is important physical insight in the form of the response function and the polarization. First, the response function, is invariant to translation in time, i.e. it is stationary. Second, the Heaviside functions in the response function constrain it to be causal, which implies that material system cannot respond until irradiated by the driving electric fields. This response is described as a trace over the dipole commutator, which is related to quantum time correlation functions for the dipole operator. Finally, the response function is equal to the polarization if all electric fields can be described by δ functions. In reality, though, our electric fields have a finite

temporal width which influences the measured polarization. Eqs. 2.16 and 2.17 are the general equations necessary for describing the resulting nonlinear polarization after excitation by an arbitrary number of intense laser pulses. To illustrate the behavior of the response function, we discuss the specific case of linear response $R^{(1)}(\tau)$ before delving into third-order spectroscopy.

2.3 Linear Spectroscopy in the Time Domain

As an introduction, we examine the linear cases of Eqs. 2.16 and 2.17 to highlight key behaviors of the response function that apply to third-order nonlinear spectroscopy. We start by presenting the expressions for the linear polarization and response function:

$$P^{(1)}(t) = \int_0^\infty E(t-\tau) R^{(1)}(\tau) \mathrm{d}\tau \tag{2.16}$$

and

$$R^{(1)}(\tau) = \frac{i}{\hbar} \mathrm{Tr}\left\{[\mu_I(\tau), \mu_I(0)]\rho_0\right\}\theta(\tau). \tag{2.17}$$

For this discussion, we will treat all quantities as scalars. Eq. 2.16 states that the polarization is a convolution of the response function with the incident electric field. In the linear regime, the polarization also propagates in the same direction as the field. Both of these properties are useful in the linear case, but are not necessarily true in the nonlinear regime. In Eq. 2.17, the response function is given as the quantum mechanical trace of the dipole commutator over the equilibrium density matrix, with a Heaviside function $\theta(\tau)$ to ensure causality. By expanding the commutator in Eq. 2.17 and treating the trace over ρ_0 as an ensemble average, the response becomes equal to a difference of time correlation functions (TCFs) of the dipole operator:

$$\begin{aligned}\mathrm{Tr}\left\{[\mu_I(\tau),\mu_I(0)]\rho_0\right\} &= \left\langle \mu_I(\tau)\cdot\mu_I(0)\right\rangle - \left\langle \mu_I(0)\cdot\mu_I(\tau)\right\rangle \\ &= \left\langle \mu_I(\tau)\cdot\mu_I(0)\right\rangle - \left\langle \mu_I(\tau)\cdot\mu_I(0)\right\rangle^* \\ &= 2\mathrm{Im}\left\{\left\langle \mu_I(\tau)\cdot\mu_I(0)\right\rangle\right\},\end{aligned} \tag{2.18}$$

where the asterisk denotes the complex conjugate. This result is an example of the Onsager regression hypothesis and the fluctuation-dissipation theorem: the system's response to a weak macroscopic perturbation is linearly related to its microscopic fluctuations at equilbrium.[5]

To get a more concrete description of the linear response function, we can evaluate it in the eigenstate basis of the system. Starting from Eq. 2.18,

$$\begin{aligned}\left\langle \mu_I(\tau)\mu(0)\right\rangle &= \sum_a P_a \left\langle a\middle|\mu_I(\tau)\mu_I(0)\middle|a\right\rangle \\ &= \sum_a P_a \left\langle a\middle|U^\dagger(\tau)\mu U(\tau)\mu\middle|a\right\rangle \\ &= \sum_{a,b} P_a \left\langle a\middle|U^\dagger(\tau)\mu U(\tau)\middle|b\right\rangle\left\langle b\middle|\mu\middle|a\right\rangle \\ &= \sum_{a,b} P_a \left\langle a\middle|e^{iE_a\tau/\hbar}\mu e^{-iE_b\tau/\hbar}\middle|b\right\rangle\left\langle b\middle|\mu\middle|a\right\rangle \\ &= \sum_{a,b} P_a \left|\mu_{ba}\right|^2 e^{-i\omega_{ba}\tau}.\end{aligned} \tag{2.19}$$

In the above equations, P_a is the Boltzmann factor for the equilibrium occupation probability of state $|a\rangle$, μ_{ba} is the transition dipole matrix element for the $|a\rangle \rightarrow |b\rangle$ transition with frequency $\omega_{ba} = (E_b - E_a)/\hbar$. Eq. 2.19 reveals that the phase of the dipole TCF oscillates under the equilibrium Hamiltonian, weighted by the equilibrium probabilities of the initial states $|a\rangle$. There are also two transition dipole factors, one for each dipole in the correlation function. The complex conjugate of $\left\langle \mu_I(\tau)\mu(0)\right\rangle$ contains the same oscillatory information, but evolves with opposite phase. Plugging Eq. 2.19 into Eq. 2.18 to evaluate the linear response in Eq. 2.17 yields

$$R^{(1)}(\tau) = \frac{2}{\hbar}\sum_{a,b} P_a \left|\mu_{ba}\right|^2 \sin(\omega_{ba}\tau)\theta(\tau). \tag{2.20}$$

The linear response function can be expressed as a sum of sine functions, which reflects that at initial time, the response must be zero and then gains amplitude as result of the perturbation. Additionally, the response function is real-valued as expected for a quantum mechanical observable.

In most realistic liquid-phase systems, there is a separation of system and bath coordinates, which result in a modification of Eq. 2.18. We include a lineshape function $F^{ab}(\tau)$, which characterizes the frequency fluctuations that dampen the coherence between $|a\rangle$ and $|b\rangle$, a process known as dephasing due to the interaction between system and bath degrees of freedom.[1,2,4,8] We can incorporate $F^{ab}(\tau)$ into the response function with terms such as

$$R^{ab}(\tau) = P_a \,|\, \mu_{ba} \,|^2 \sin(\omega_{ba} t) F^{ab}(\tau) \theta(\tau) \tag{2.21}$$

If the frequency fluctuations are fast compared to the timescale of the measurement, $F^{ab}(\tau)$ can be modeled with an exponential decay with rate Γ. In addition to dephasing, other contributions influence the decay of the response function, such as energy relaxation, rotational motion, and effects from inhomogeneous broadening. These various contributions cannot be separated with linear spectroscopy but can each be independently measured with third-order nonlinear spectroscopy.[4] Eq. 2.21 has also assumed the vibrational Condon approximation where the dipole amplitude is independent of the nuclear coordinate. This approximation is reasonable in many weakly anharmonic systems but fails for hydrogen-bonded vibrations like the O–H stretch in liquid water.[14]

Finally, we want to connect the time-domain response to a linear absorption spectrum in the frequency domain. Eq. 2.2 states that $P(\omega) = \chi^{(1)}(\omega) E(\omega),$ where $\chi^{(1)}$ is a complex quantity, $\chi^{(1)}(\omega) = \chi'(\omega) + i\chi''(\omega)$. The real and imaginary parts of the susceptibility correspond to

dispersion and absorption, respectively. From Eq. 2.16, the linear polarization is a convolution of the response and the electric field, equivalent to multiplication in the frequency domain, which implies that the response and the susceptibility are related by a Fourier transform:

$$\chi^{(1)}(\omega) = \int_{-\infty}^{\infty} R^{(1)}(\tau) e^{i\omega\tau} \mathrm{d}\tau. \tag{2.22}$$

To satisfy detailed balance, the population prefactors in Eq. 2.21 can be related to each other, which also relates $\langle \mu_I(\tau)\mu(0) \rangle$ with its complex conjugate. This results in a more direct relationship between $\chi^{(1)}$ and $\langle \mu_I(\tau)\mu(0) \rangle$:

$$\chi^{(1)}(\omega) = \frac{1}{\hbar}\left(1 - e^{-\beta\hbar\omega}\right) \int_{-\infty}^{\infty} \langle \mu_I(\tau)\mu(0) \rangle e^{i\omega\tau} \, \mathrm{d}\tau. \tag{2.23}$$

The imaginary part of Eq. 2.23 is related to the linear absorption of the system, which is given by

$$\alpha(\omega) = \frac{4\pi\omega}{c} \chi''(\omega). \tag{2.24}$$

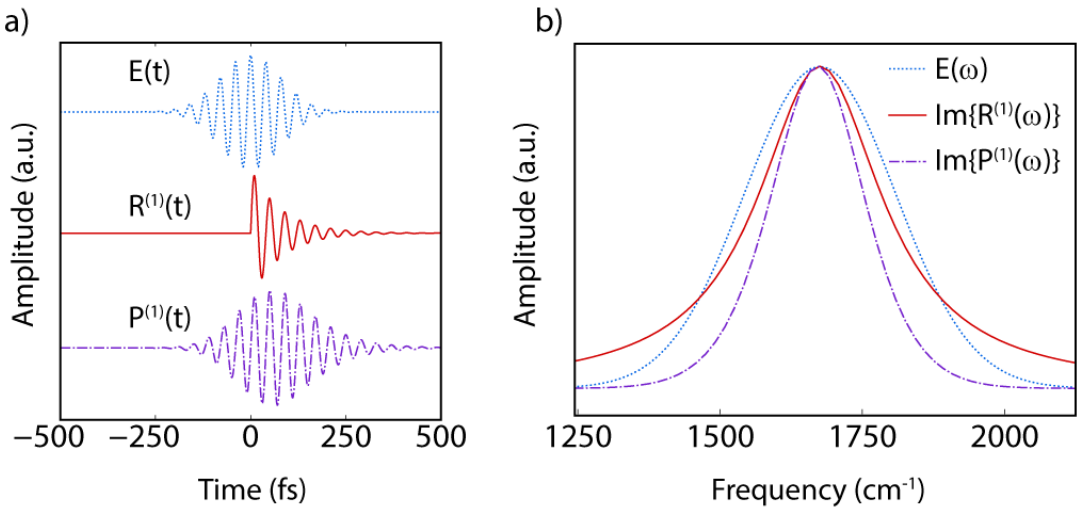

Figure 2.1: The amplitudes of a model mid-IR electric field E, linear response $R^{(1)}$ function, and linear polarization $P^{(1)}$ in the (a) time domain and (b) frequency domain. Parameters for the model are included in the main text.

In Fig. 2.1a, we show the results of a simple time-domain calculation with a transform-limited Gaussian electric field pulse (ω_0 = 1666 cm^{-1}, τ_p = 200 fs FWHM), response function according to Eq. 2.21 with exponentially decaying lineshape function (ω_{ba} = 1666 cm^{-1}, Γ = 0.0125 fs^{-1}), and polarization according to Eq. 2.16. The polarization decays more slowly in time than the response, but inherits the response's $\pi/2$ phase shift relative to the driving field. Fourier transformation of these functions produces the spectra of the electric field, response, and the resulting polarization (Fig. 2.1b). The imaginary components of the response and the polarization both show absorptive lineshapes. The electric field is narrower in bandwidth than the response, and the polarization is spectrally narrowed compared to the full response due to the bandwidth limits of the electric field.

2.4 Third-Order IR Spectroscopy

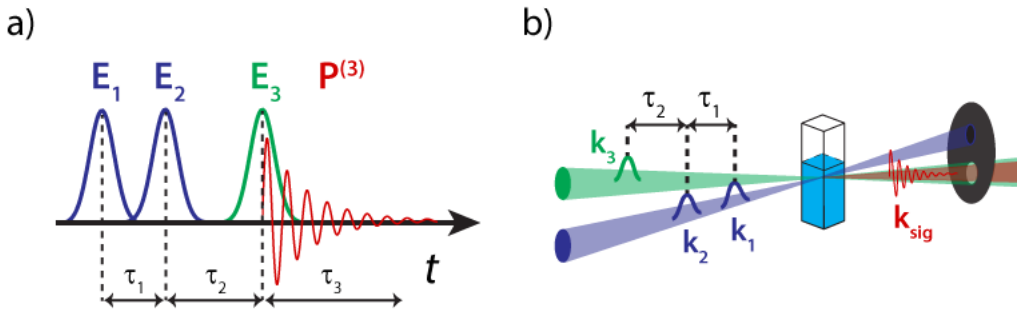

Figure 2.2: The pulse sequence of a 2D IR experiment arranged (a) in time and (b) in space.

Many of the properties of the linear response generalize to the third-order nonlinear response, but the interaction of the system with three fields provides access to many new details about the system. This section will provide an overview of the key features of third-order infrared spectroscopy to lay the groundwork for reading a 2D IR spectrum. To begin, the third-order polarization $\mathbf{P}^{(3)}$ is generated when three ultrafast IR pulses interact with the sample. In time, the

electric fields $\mathbf{E}_1$, $\mathbf{E}_2$, and $\mathbf{E}_3$ are separated by time intervals τ_1 and τ_2, and the nonlinear signal radiates over τ_3 (Fig. 2.2a). Spatially, our experiments are in the pump-probe geometry, where $\mathbf{E}_1$ and $\mathbf{E}_2$ (known as the pump pulses) are collinear and cross with the probe pulse $\mathbf{E}_3$ (Fig. 2.2b). Frequently, the electric fields $\mathbf{E}_i$ are indicated by their wavevectors $\mathbf{k}_i$, as labelled in Fig. 2.2b. As will soon be shown, the nonlinear polarization propagates collinearly with the probe. This is because the phase relationship between the pulses determines the spatial direction of the nonlinear signal, in a process known as phase matching.

The polarization and response function can be written down from Eqs. 2.16 and Eq. 2.17 as

$$\mathbf{P}^{(3)}(t) = \int_0^\infty \int_0^\infty \int_0^\infty \mathrm{d}\tau_3 \, \mathrm{d}\tau_2 \, \mathrm{d}\tau_1 \mathbf{E}_3(t-\tau_3-\tau_2-\tau_1)\mathbf{E}_2(t-\tau_2-\tau_1)\mathbf{E}_1(t-\tau_1)R^{(3)}(\tau_1,\tau_2,\tau_3) \tag{2.25}$$

and

$$R^{(3)}(\tau_3,\tau_2,\tau_1) = \left(\frac{i}{\hbar}\right)^3 \mathrm{Tr}\left\{\left[\boldsymbol{\mu}_I(\tau_3+\tau_2+\tau_1),\left[\boldsymbol{\mu}_I(\tau_2+\tau_1),[\boldsymbol{\mu}_I(\tau_1),\boldsymbol{\mu}_I(0)]\right]\right]\rho_0\right\}\theta(\tau_1)\theta(\tau_2)\theta(\tau_3). \tag{2.26}$$

Similar to the linear response function $R^{(1)}(\tau)$, the third-order response function is evaluated by taking the trace over ρ_0 of nested dipole commutators, with Heaviside functions in τ_1-τ_3 for causality. Expanding out the commutators reveals that there are eight components to the response function, but half are complex conjugates of the other four:

$$R^{(3)}(\tau_3,\tau_2,\tau_1) = \sum_{n=1}^{4} R_n^{(3)}(\tau_1,\tau_2,\tau_3) - R_n^{(3)*}(\tau_1,\tau_2,\tau_3). \tag{2.27}$$

The four terms $R_n^{(3)}(\tau_3,\tau_2,\tau_1)$ correspond to different four-point dipole TCFs with distinct phase evolution dynamics in the density matrix. With a procedure similar to Eq 2.19, one can evaluate the pathway in terms of four eigenstates $|a\rangle$, $|b\rangle$, $|c\rangle$, and $|d\rangle$:[4]

$$R_1^{(3)}(\tau_3,\tau_2,\tau_1) = \sum_{a,b,c,d} P_a \mu_{cd}\mu_{bc}\mu_{ab}\mu_{da} \exp(-i\omega_{dc}\tau_3 - i\omega_{db}\tau_2 - i\omega_{da}\tau_1) F_1^{abcd}(\tau_3,\tau_2,\tau_1) \quad (2.28)$$

$$R_2^{(3)}(\tau_3,\tau_2,\tau_1) = \sum_{a,b,c,d} P_a \mu_{cb}\mu_{dc}\mu_{ba}\mu_{ad} \exp(-i\omega_{bc}\tau_3 + i\omega_{db}\tau_2 + i\omega_{da}\tau_1) F_2^{abcd}(\tau_3,\tau_2,\tau_1) \quad (2.29)$$

$$R_3^{(3)}(\tau_3,\tau_2,\tau_1) = \sum_{a,b,c,d} P_a \mu_{cb}\mu_{ba}\mu_{dc}\mu_{ad} \exp(-i\omega_{bc}\tau_3 + i\omega_{ca}\tau_2 + i\omega_{da}\tau_1) F_3^{abcd}(\tau_3,\tau_2,\tau_1) \quad (2.30)$$

$$R_4^{(3)}(\tau_3,\tau_2,\tau_1) = \sum_{a,b,c,d} P_a \mu_{ab}\mu_{bc}\mu_{cd}\mu_{da} \exp(-i\omega_{ba}\tau_3 - i\omega_{ca}\tau_2 - i\omega_{da}\tau_1) F_4^{abcd}(\tau_3,\tau_2,\tau_1). \quad (2.31)$$

These terms share similar important features to the linear response function in Eq. 2.21. The intensities of each term are weighted by the equilibrium probability P_a of occupying $|a\rangle$ and four transition dipole factors for the four dipoles in the correlation function. Next, the complex exponentials indicate that the phases of the response pathways oscillate over the three time intervals. Because they are oscillations between the eigenstates of the system, these oscillations indicate phase evolution under the equilibrium Hamiltonian H_0. This reflects that after interacting with each pulse, the equilibrium Hamiltonian propagates the system. The complex exponential terms contain phase evolution mixtures that can proceed in the positive or negative direction during each time interval, depending on the eigenstates involved and the interaction of light with the bra or ket sides of the density matrix. Finally, the lineshape functions $F_n^{abcd}(\tau_3,\tau_2,\tau_1)$ characterize the decay of oscillations with each time interval, which leads to a multidimensional lineshape in the frequency domain.

The different correlation functions $R_n^{(3)}(\tau_3,\tau_2,\tau_1)$ indicate the allowable transitions within the density matrix, but the nonlinear polarization depends on which transitions are actually resonant with the incident electric fields. According to Eq. 2.1, an electric field can be written as the sum of two complex exponentials, but only one of these terms will be resonant with the

oscillations in the response function. The other term will oscillate rapidly with a form such as $\exp(-2i\omega\tau)$ and mostly cancel itself out after integration, contributing little to the overall polarization. This leads to the rotating wave approximation for evaluating the polarization, where nonresonant components of the electric field are removed from the calculation of $\mathbf{P}^{(3)}(t)$. This phase relationship influences the spatial behavior of the polarization as well, because the polarization of the medium forms an oscillating spatial pattern. This pattern forms a spatial grating which only allows generation of $\mathbf{P}^{(3)}(t)$ in a particular phase-matched direction with wavevector $\mathbf{k}_{sig} = \mathbf{k}_1 \pm \mathbf{k}_2 \pm \mathbf{k}_3$, where the signs depend on the phase of the interaction with the density matrix.

The rotating wave approximation leads to a diagrammatic representation of the interaction of light with the four correlation functions of Eqs. 2.28-2.31 (Fig. 2.3),[1] where a unique set of interactions is known as a Liouville pathway. Each row corresponds to an element of the density matrix, starting below with the equilibrium state $|a\rangle\langle a|$ and time proceeding up the ladder. Resonant electric fields are depicted as arrows labelled by their wavevector $\mathbf{k}_i$, interacting with either the bra or the ket side of the density matrix depending on the sign of the oscillation in the response correlation function. Arrows pointing into the ladder correspond to absorption of light, whereas arrows pointing out correspond to stimulated emission. Left-pointing arrows indicate a negative wavevector for determining the phase matching condition for the pathway, whereas right-pointing arrows indicate positive wavevector. For example, absorption on the bra side and stimulated emission on the ket side both denote a negative wavevector. The total sign for a given pathway can either be positive or negative, which lead to oppositely signed signals in third order nonlinear spectroscopy. This is distinct from linear absorption spectroscopy where the signal is always positive, and reflects the sign accumulated within the nested commutator in Eq. 2.26. The sign of a particular pathway is determined by taking -1 to the power of the number of bra-side interactions.

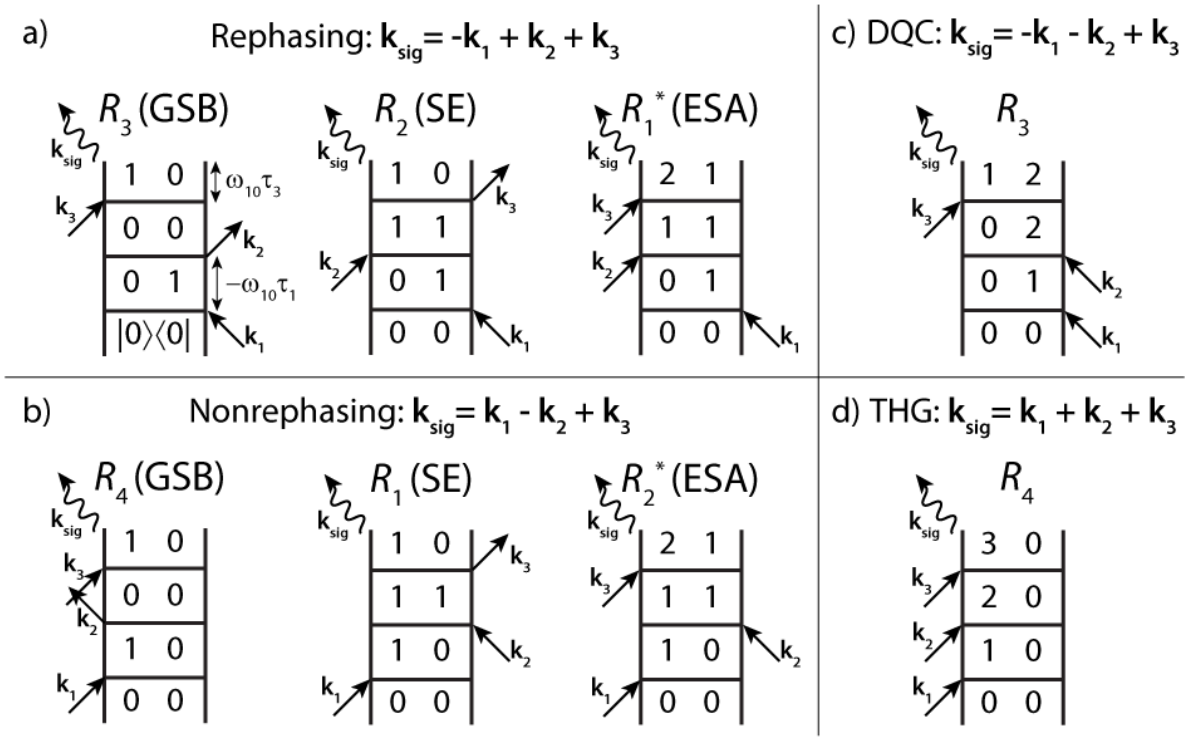

Figure 2.3: Four double-sided ladder diagrams representing various possible Liouville pathways from the four response correlation functions in Eqs. 2.28-2.31. Three common (a) rephasing and (b) nonrephasing pathways for a three-level system corresponding to the physical processes of ground state bleaching (GSB), stimulated emission (SE), and excited state absorption (ESA). Asterisks on ESA pathways denote that the complex conjugates of the response correlations are shown, corresponding to a reflection over the ladder in the diagram. (c) A double-quantum coherence (DQC) pathway. (d) A third-harmonic generation (THG) pathway.

The ladder diagrams visualize the evolving state of the density matrix over each time interval. After an interaction, if the two sides of the density matrix are in different states, then the density matrix is said to be in a coherence and its phase evolves with the difference frequency between the two states. The first interaction always generates a coherence, such that τ_1 is frequently called the coherence time. After a second interaction, the bra and ket sides are frequently equal, forming a population which on its own does not show coherent oscillations. Excited state population relaxation is frequently measured over τ_2, and τ_2 is historically called the waiting time

after pump-probe experiments. However, coherent oscillations can be present during τ_2 if multiple eigenstates are excited within the bandwidth of the pulse. The third interaction with the probe pulse puts the system in another coherence which evolves during τ_3. Finally, the fourth interaction represents taking the trace over the density matrix rather than excitation by a light pulse, and leaves the density matrix in a population.

The pathways in Fig. 2.3 are grouped by their phase evolution. Rephasing (RP) pathways are those where phase evolution during τ_1 is counteracted by phase evolution of opposite sign during τ_3, and the phase matching condition is $\mathbf{k}_{sig} = -\mathbf{k}_1 + \mathbf{k}_2 + \mathbf{k}_3$. This leads to phenomena like photon echoes[15,16] and contributes to measurement of inhomogeneous broadening in nonlinear spectroscopy.[4] Nonrephasing (NR) pathways are characterized by phase evolution of the same sign in both τ_1 and τ_3, resulting in $\mathbf{k}_{sig} = -\mathbf{k}_1 + \mathbf{k}_2 + \mathbf{k}_3$. The double quantum coherence (DQC) pathways involve the same phase evolution in τ_1 and τ_2, and is less common in nonlinear spectroscopy. Finally, in third harmonic generation (THG), the system absorbs three photons of frequency ω and emits a photon of frequency 3ω. For 2D IR experiments, we will only concern ourselves with the rephasing and nonrephasing pathways.

We illustrate the rephasing and nonrephasing pathways with a ground state bleach (GSB) signal for a two-level system with ground state $|0\rangle$ and excited state $|1\rangle$. The GSB rephasing 2D IR pathway (R_3 in Fig. 2.3a) begins with an absorption of $\mathbf{k}_1$ on the bra side, followed by stimulated emission (SE) by $\mathbf{k}_2$ on the bra side, absorption of $\mathbf{k}_3$ on the ket side, and the nonlinear signal radiating in the direction $\mathbf{k}_s = -\mathbf{k}_1 + \mathbf{k}_2 + \mathbf{k}_3$. For the model in Fig. 2.4a, the time-domain response was calculated from Eq. 2.30, assuming impulsive excitation and a two-dimensional decaying exponential for the lineshape function $F_3(\tau_1, 0, \tau_3)$.[4] Fourier transforming the response over both τ_1 and τ_3 generates the 2D IR spectrum expressed in terms of frequencies ω_1 and ω_3 (Fig. 2.4a). In

general, the 2D IR spectrum is complex-valued, but normally the real component is kept because it leads to more easily interpretable signals. The peak is centered at (ω_1, ω_3) = (ω_{10}, ω_{10}), which are the frequencies of the phase evolutions in τ_1 and τ_3, respectively. Because the phase evolution in τ_1 has negative sign in RP pathways (Fig. 2.3a), the rephasing spectrum is actually reflected over ω_1 from the $\omega_1 < 0$ region of the spectrum. The 2D IR spectrum shows a phase twist in two dimensions, characterized by alternating positive and negative features due to taking the real part of the 2D Fourier transform. There is a corresponding GSB nonrephasing pathway (Fig. 2.3b) whose 2D IR spectrum (Fig. 2.4b) is also centered at (ω_1, ω_3) = (ω_{10}, ω_{10}), but the phase twist is rotated by $\pi/2$ due to the different phase relationships in the NR pathway.

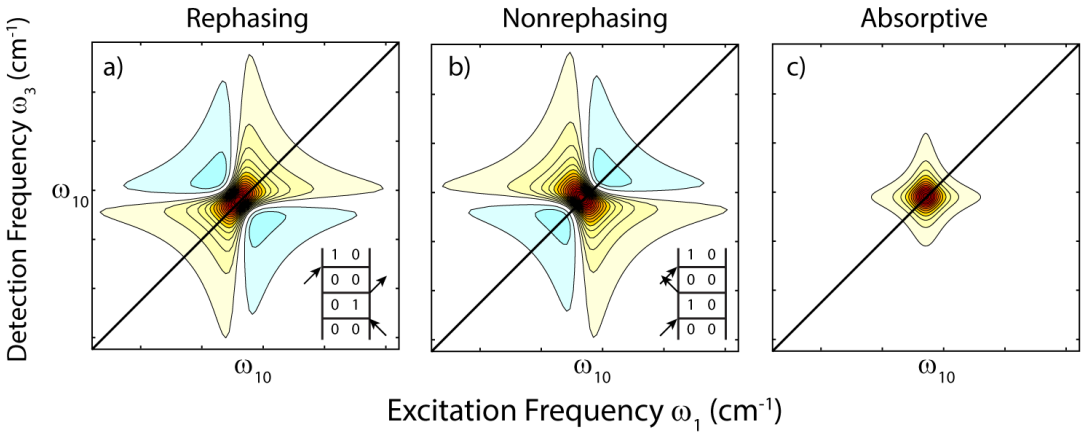

Figure 2.4: The (a) rephasing, (b) nonrephasing, and (c) absorptive 2DIR spectra for a model ground state bleach (GSB) of a two-level system. The spectrum in (c) is the sum of the spectra in (a) and (b).

Adding the rephasing and nonrephasing spectra produces an absorptive 2D Lorentzian lineshape centered at (ω_1, ω_3) = (ω_{10}, ω_{10}) (Fig. 2.4c), cancelling out the dispersive components of the rephasing and nonrephasing signals. Additionally, the absorptive resonance is much narrower, which improves separation between multiple features in a 2D IR spectrum. Except for the model rephasing and nonrephasing spectra in Fig. 2.4, all model and experimental 2D IR spectra shown

in this thesis are absorptive. Experimentally, obtaining absorptive spectra occurs automatically in the pump-probe geometry, where $\mathbf{k}_1$ and $\mathbf{k}_2$ are collinear with each other and crossed with $\mathbf{k}_3$. Both the rephasing and nonrephasing pathways are phase matched along the direction of the probe ($\mathbf{k}_{sig} = \mathbf{k}_3$, Fig. 2.2b) since $\mathbf{k}_1 = \mathbf{k}_2$. Because ω_1 is related to the time delay between the pump pulses $\mathbf{k}_1$ and $\mathbf{k}_2$, we call ω_1 the excitation frequency, whereas $\mathbf{k}_{sig}$ is measured with the probe and ω_3 is called the detection frequency. From this perspective, the 2D IR spectrum can be viewed as a two-dimensional conditional frequency distribution, where one measures the probability of detecting signal at ω_3 given excitation at ω_1.

A 2D IR spectrum more commonly shows a doublet along the diagonal (Fig. 2.5a), rather than a single positive peak, arising from different possible pathways upon excitation at $\omega_1 = \omega_{10}$. In addition to the two RP and NR GSB pathways, there are two stimulated emission (SE) pathways centered at $(\omega_1, \omega_3) = (\omega_{10}, \omega_{10})$ (Fig. 2.3), which also are positively signed and have the same amplitude as the GSB pathways. The negative feature (shown in blue in Fig. 2.5) is due to an excited state absorption (ESA) from $|1\rangle \rightarrow |2\rangle$. This feature is present because the excitation pulses can place the system in the excited state population $|1\rangle\langle 1|$, which can be excited by the probe to $|1\rangle\langle 2|$. This pathway oscillates in τ_3 with the difference frequency ω_{21}, resulting in a peak at $\omega_3 = \omega_{21}$. For an experiment in the pump-probe geometry, the positive and negative peaks can be interpreted as positive or negative changes in transmission, respectively, because of excitation from the pump pulses at ω_{10}. Bleaching and SE result in more light reaching detector, appearing like positive signal, whereas ESA results in induced absorption of $\mathbf{k}_3$ which appears like negative signal at $\omega_3 = \omega_{21}$. For a weakly anharmonic system such as this, the intensity of the ESA is $\mu_{21}^2\mu_{10}^2 \approx 2\mu_{10}^4$, which is equal in amplitude to the sum of the GSB and SE pathways.

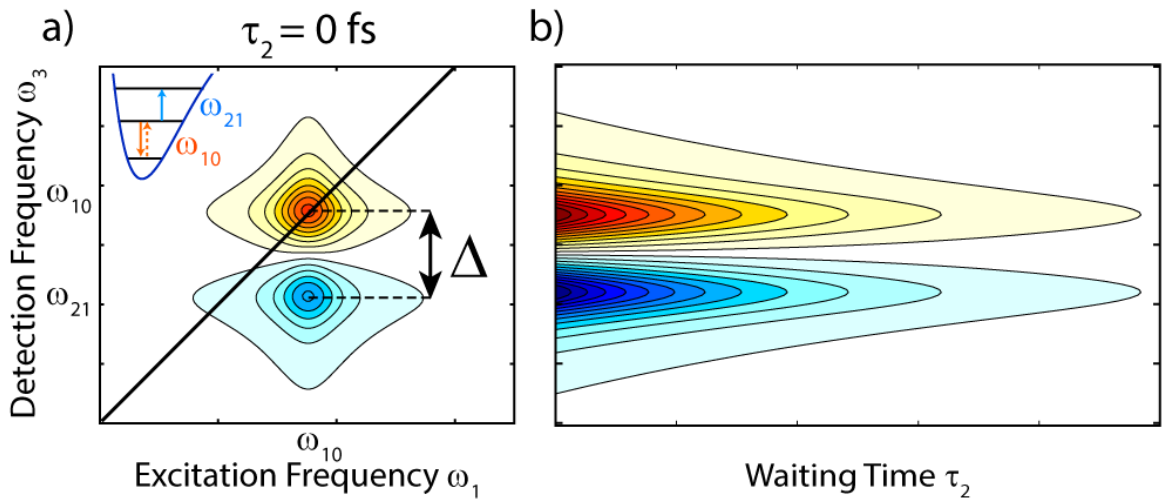

Figure 2.5: Third-order response for a model weakly anharmonic vibration. (a) Absorptive 2DIR spectrum, with a schematic potential in the top left corner indicating the ω_{10} and ω_{21} transitions. The dashed orange arrow indicates the GSB pathway, the solid orange arrow indicates SE, and the solid blue arrow indicates ESA. (b) The TA spectrum for the doublet, showing its relaxation with waiting time.

The ESA peak is separated from the GSB peaks due to the anharmonicity of the nuclear potential, characterized by the anharmonic splitting parameter Δ. Since the amplitude of the positive and negative peaks are approximately equal, if the system were perfectly harmonic ($\Delta = 0$) then the positive and negative features would cancel. Therefore, the 2D IR spectrum is observable precisely because the system is anharmonic. This is a useful property because the access to the second excited state provides information on the shape of the nuclear potential which cannot be accessed otherwise.

The isotropic TA spectrum tracks the kinetics of this doublet in τ_2 (Fig. 2.5b). This spectrum plots the change of the amplitude of the diagonal doublet in ω_3 with waiting time τ_2. TA spectroscopy is another type of third-order spectroscopy where the excitation pulses arrive at the sample simultaneously, i.e. $\tau_1 = 0$ fs. According to the projection slice theorem, the TA signal at a particular τ_2 is equivalent to the projection of the 2D IR spectrum onto the ω_3 axis, which means

that a TA spectrum measures the same response as the 2D IR spectrum, but without ω_1 resolution. Despite the loss of ω_1 information, the experimental benefit comes from the ability to quickly collect data over a range of waiting times without needing to also step through τ_1. This is particularly convenient for sensitive signals like polarization anisotropy decay (Section 2.5), which require a lot of averaging to attain a reasonable signal-to-noise ratio.

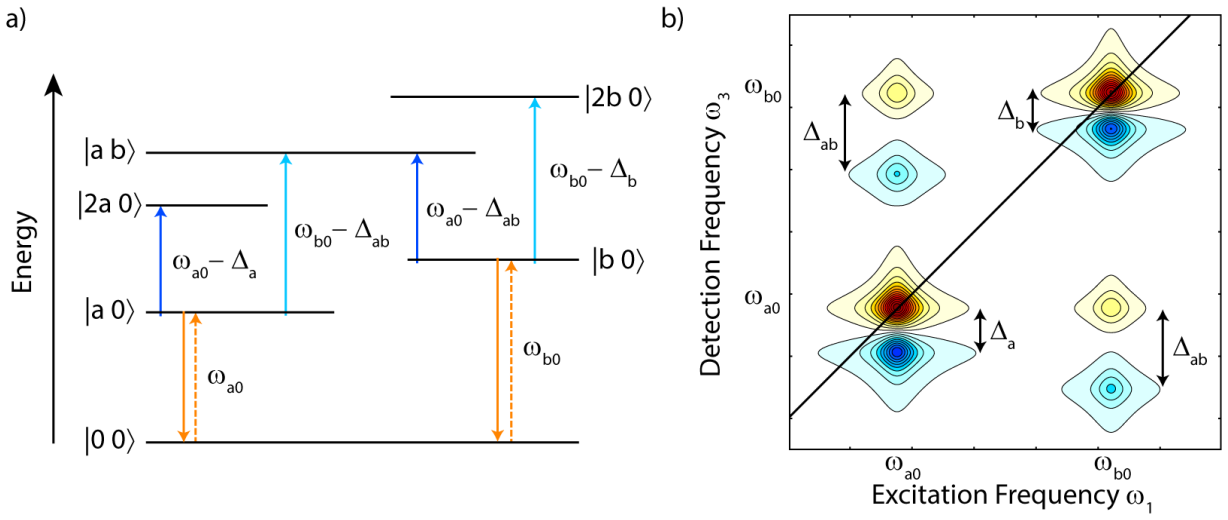

Figure 2.6: (a) A six-level system between two coupled modes. GSB transitions are indicated by dashed orange arrows, and SE is indicated by solid orange arrows. ESAs into overtones are indicated in blue, and the ESA transitions into the combination band are colored in cyan. (b) The absorptive 2DIR spectrum of the two coupled modes.

In addition to the diagonal doublets, the 2D IR spectrum visualizes the anharmonic coupling between two vibrations $|a\rangle$ and $|b\rangle$ in the form of off-diagonal cross peaks. In Fig 2.6a, we show a model 6-level system involving these two states. In addition to the first excited states $|a\rangle$ and $|b\rangle$ and their overtones $|2a\rangle$ and $|2b\rangle$, the combination band $|a\ b\rangle$ is also accessible. The 2D IR spectrum of these vibrations (Fig. 2.6b) shows two doublets on the diagonal for each of these features, with two additional doublets off the diagonal due to the coupling between $|a\rangle$ and $|b\rangle$. Each cross peak consists of a bleach feature, which can be interpreted as population depletion

from a shared ground state between two vibrations. The accompanying negative signal arises from either the $|a\rangle \rightarrow |ab\rangle$ or $|b\rangle \rightarrow |ab\rangle$ transitions. Like along the diagonal, the doublet is separated in ω_3 by an anharmonicity constant Δ_{ab}. If the system were harmonic, the cross peak would vanish. Additionally, if two fundamental transitions are uncorrelated, such as if they belong to different molecules, cross peaks will not appear. Therefore, a cross peak pattern can serve as a two-dimensional vibrational fingerprint for a single species in a mixture.

In general, there is rich information content in 2D IR spectra because of its access to anharmonicity, but the presence of anharmonicity doesn't say much on its own. For one, no realistic molecular systems are actually purely harmonic, but rather described as either weakly or strongly anharmonic. Additionally, the origin of anharmonicity can come from a variety of sources related to the molecular geometry, electronic structure, or environment. For well-behaved systems like cold gas-phase clusters, the nuclear potential energy surface can be calculated with high accuracy using high-level quantum mechanical calculations and fit to high-order polynomials in terms of the complex's vibrational coordinates.[17,18] For instance, hydrogen bonding provides an attractive interaction between donor and acceptor molecules which dramatically alters the shape of the donor D-H stretch potential and results in a strongly anharmonic vibration.[19] Beyond anharmonicity, the presence of 2D IR cross peaks demonstrates that the nuclear potential is not just anharmonic, but multidimensional. Physically, this reflects the fact that the eigenstates of two coupled vibrations are mixed with each other, and displacement in one nuclear coordinate induces motion in the other. In the case of the aqueous proton, the potential is both strongly anharmonic and highly multidimensional, which requires a high-level treatment to calculate the vibrational response. The VSCF/VCI method (Section 2.6) is the method of choice for this system because of its ability to handle complicated potential energy surfaces.

2.5 Polarization Resolution in Nonlinear Spectroscopy

2.5.1 Anisotropy Decay of One Transition Dipole

An additional capability of nonlinear spectroscopy is the ability to follow orientational diffusion of transition dipoles, as they are vector quantities that couple to the polarization vectors of the electric fields. In this section, polarization refers to the unit vector aligned to the transverse direction of an electric field instead of the polarization dipole of the sample. In an isotropic medium like liquid water, transition dipoles are randomly oriented, but a subset is selected by the excitation pulses and the orientation is tracked by the interaction with the probe pulse. The pulses will all be linearly polarized along the *X*, *Y*, or *Z* directions in the lab frame of reference. With third-order experiments, all quantities are ensemble averaged, so the final measurement tracks an orientational time correlation function that decays with τ_2. This correlation function includes mechanistic information such as molecular reorientation due to fluctuations in the solution.

To start, the response correlation functions $R_n^{(3)}$ from Eqs. 2.28-2.31 are modified with orientational response prefactors $Y_{IJKL}^{abcd}(\tau_3,\tau_2,\tau_1)$:

$$R_n^{(3)}(\tau_3,\tau_2,\tau_1) = \sum_{IJKL}\sum_{abcd} Y_{IJKL}^{abcd}(\tau_3,\tau_2,\tau_1) R_n^{abcd}(\tau_3,\tau_2,\tau_1). \tag{2.32}$$

$Y_{IJKL}^{abcd}(\tau_3,\tau_2,\tau_1)$ is a tensor quantity which accounts for orientational averaging for four dipoles that interact with four electric fields. Initially, we will consider the interaction of a single dipole $\hat{\mu}$ vector with the four fields, where the circumflex indicates that $\hat{\mu}$ is a unit vector. The indices *I, J, K,* and *L* each correspond to one of the lab frame coordinates *X, Y,* or *Z*, while $\hat{\mu}$ resides in its molecular frame of reference with coordinate axes *a, b,* and *c* (Fig. 2.7). For convenience, $\hat{\mu}$ is chosen to lie along the *a* axis, so that the relevant tensor elements to evaluate are Y_{IJKL}^{aaaa}.

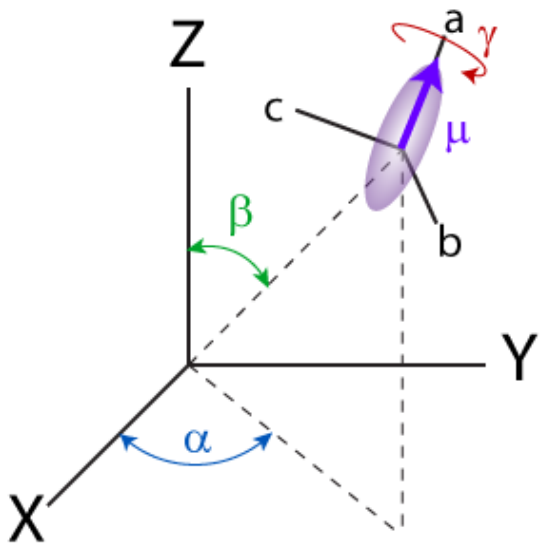

Figure 2.7: A Schematic relating the lab frame (*X,Y,Z*) to the molecular frame (*a,b,c*) by the orientation $\Omega = (\alpha, \beta, \gamma)$. The vibrational dipole $\hat{\mu}$ is aligned with axis *a*.

In general, Y_{IJKL}^{aaaa} can have $3^4 = 81$ tensor elements, but only four are nonzero due to the spatial symmetries of isotropic medium, and the nonlinear susceptibility tensor $\chi_{IJKL}^{(3)}$ inherits these symmetries.[10] Rotational symmetry implies that only three tensor elements are independent and are related to the fourth:

$$Y_{ZZZZ}^{aaaa} = Y_{ZZYY}^{aaaa} + Y_{YZYZ}^{aaaa} + Y_{ZYYZ}^{aaaa}. \tag{2.33}$$

As indicated by Fig. 2.7, the *Z* direction can be taken to be vertical while *Y* is horizontal, but rotational symmetry of the medium means that these definitions can be interchanged and produce the same results.

For experiments in the pump-probe geometry, it is only necessary to evaluate Y_{ZZZZ}^{aaaa} and Y_{ZZYY}^{aaaa}. To evaluate Y_{ZZZZ}^{aaaa}, we must orientationally average over four dipole interactions with the field polarized along *Z*, each interaction taking the form of a dot product between unit vectors. For

each interaction, the lab and molecular frames are related by an orientation $\Omega_i(\alpha, \beta, \gamma)$, where α, β, and γ correspond to a sequence of three Euler angle rotations. The averaging requires the isotropic orientational probability density $P(\Omega_0) = 1/8\pi^2$ for the random intitial oriention of $\hat{\mu}$. For $\tau_1 = \tau_2 = \tau_3 = 0$,

$$\begin{aligned} Y_{ZZZZ}^{aaaa}(0,0,0) &= \int d\Omega_3 \int d\Omega_2 \int d\Omega_1 \int d\Omega_0 P(\Omega_0)(\hat{\mu}_a \cdot \hat{Z})^4 \\ &= \frac{1}{8\pi^2} \int_0^{2\pi} d\alpha \int_0^{\pi} \sin\beta \, d\beta \int_0^{2\pi} d\gamma \cos^4\beta \\ &= \frac{1}{5}. \end{aligned} \tag{2.34}$$

$Y_{ZZZZ}^{aaaa} = 1/5$ means that an ensemble of randomly oriented dipoles interacting with four simultaneous fields will respond with 1/5 the amplitude it would if they were all fixed parallel to *Z*. For Y_{ZZYY}^{aaaa}, we average over two interactions with *Z*-polarized fields and two *Y*-polarized fields:

$$\begin{aligned} Y_{ZZYY}^{aaaa}(0,0,0) &= \int d\Omega_3 \int d\Omega_2 \int d\Omega_1 \int d\Omega_0 P(\Omega_0)(\hat{\mu}_a \cdot \hat{Z})^2 (\hat{\mu}_a \cdot \hat{Y})^2 \\ &= \frac{1}{8\pi^2} \int_0^{2\pi} d\alpha \int_0^{\pi} \sin\beta \, d\beta \int_0^{2\pi} d\gamma \cos^2\beta \cdot \sin^2\beta \cdot \sin^2\gamma \\ &= \frac{1}{15}. \end{aligned} \tag{2.35}$$

The value for the ZZYY response is less than ZZZZ by a factor of three, indicating that the initial two interactions selectively excite molecules with a component in the *Z* direction, which are less likely to have a large component in the *Y* direction.

Experimentally, we can measure the Y_{ZZZZ}^{aaaa} and Y_{ZZYY}^{aaaa} tensor elements with two types of measurements. In the first measurement, $\mathbf{k}_1$, $\mathbf{k}_2$, $\mathbf{k}_3$, and $\mathbf{k}_{sig}$ are all polarized in the *Z* direction, whereas in the second measurement $\mathbf{k}_1$ and $\mathbf{k}_2$ are *Z*-polarized and $\mathbf{k}_3$ and $\mathbf{k}_{sig}$ are *Y*-polarized. The polarization anisotropy *r* between the ZZZZ and ZZYY experiments is defined as

$$r = \frac{S_{ZZZZ} - S_{ZZYY}}{S_{ZZZZ} + 2S_{ZZYY}}, \tag{2.36}$$

where S_{ZZZZ} and S_{ZZYY} refer to either TA or 2D IR spectra measured with the respective polarization schemes. According to Eq. 2.32, the nonlinear signal for a single pathway is directly proportional to its orientational averaging tensor element. Therefore, at early waiting time,

$$r \propto \frac{Y^{aaaa}_{ZZZZ} - Y^{aaaa}_{ZZYY}}{Y^{aaaa}_{ZZZZ} + 2Y^{aaaa}_{ZZYY}} = \frac{2}{5}, \tag{2.37}$$

which is the maximum possible anisotropy value for a single pathway. This result neglects the effects of interfering signals or signal modulations due to coherences in τ_2. In Fig. 2.8a and 2.8b, we show the relative amplitudes of the model 2D IR diagonal doublet from Fig. 2.5 in the ZZZZ and ZZYY polarization schemes, displaying a 3:1 intensity ratio. As is necessary for evaluating the polarization anisotropy for a measured spectrum, the predicted orientational response incorporates all of the rephasing and nonrephasing GSB, SE, and ESA pathways necessary to describe the doublet. In Fig. 8, it was assumed that the transition dipoles for all of these pathways were parallel, which is true in the harmonic limit, but breaks down with increasing anharmonicity.[20]

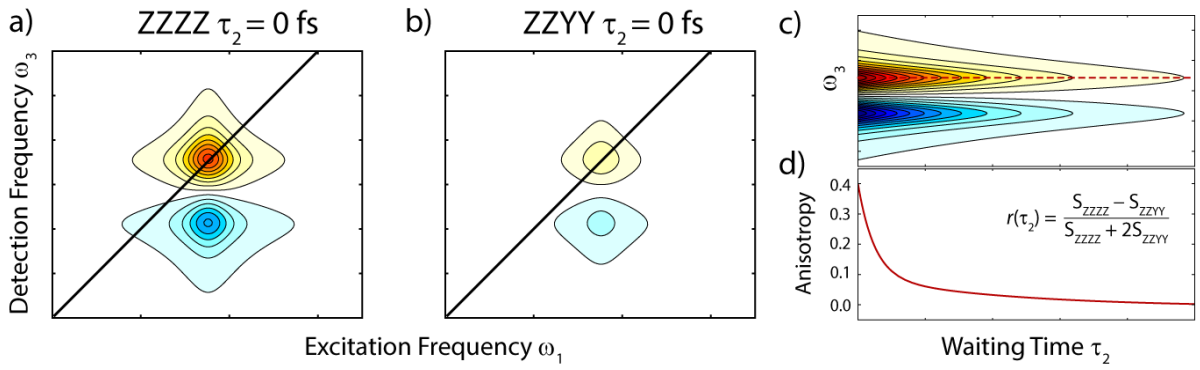

Figure 2.8: Polarization anisotropy effects on a diagonal peak in 2D IR and TA spectroscopy. The (a) ZZZZ and (b) ZZYY spectra, presented on the same scale to show the 3:1 amplitude ratio. (c) The isotropic TA trace for the 2D IR doublet. The dashed red line indicates the center frequency of the GSB, used for recording the TA anisotropy decay in (d). The initial anisotropy is 0.4 and decays to 0 with increased waiting time.

In general, the fluctuations of the molecular environment will cause the orientational diffusion of the dipole such that the initial anisotropy decays to zero over time (Fig. 2.8c-d). This anisotropy decay is commonly distinct from the isotropic population relaxation of the doublet. Assuming a spherical rotor diffusing by infinitesimally small angular changes, the angular diffusion equation can be written as

$$\frac{\partial W(\Omega,t)}{\partial t} = \mathrm{D}_{\mathrm{or}} \nabla^2 W(\Omega,t) \tag{2.38}$$

where $W(\Omega,t)$ is probability of being at an orientation at time t, and D_{or} is the orientational diffusion constant. A derivation of the solution is presented elsewhere,[7,21] but we present the final results here. The time-dependent expressions for Y_{ZZZZ}^{aaaa} and Y_{ZZYY}^{aaaa} are

$$Y_{ZZZZ}^{aaaa}(\tau_3,\tau_2,\tau_1) = \frac{1}{9} c_1(\tau_1) c_1(\tau_3) \left(1 + \frac{4}{5} c_2(\tau_2) \right) \tag{2.39}$$

$$Y_{ZZYY}^{aaaa}(\tau_3,\tau_2,\tau_1) = \frac{1}{9} c_1(\tau_1) c_1(\tau_3) \left(1 - \frac{2}{5} c_2(\tau_2) \right), \tag{2.40}$$

where

$$c_J(\tau_n) = \exp\left[-J(J+1)\tau_n / \tau_{\text{or}}\right]. \tag{2.41}$$

The waiting-time dependent anisotropy decay is contained in the $c_2(\tau_2)$ term, as seen by plugging Eqs. 2.39 and 2.40 into Eq. 2.36:

$$r(\tau_2) = \frac{2}{5} c_2(\tau_2). \tag{2.42}$$

The definition of anisotropy in Eq. 2.36 isolates the anisotropic kinetics from the total response, removing contributions from isotropic processes like energy relaxation. By contrast, the denominator in Eq. 2.36 cancels out contributions from $c_2(\tau_2)$, which reveals that the denominator recovers the isotropic signal. Thus, from just the ZZZZ and ZZYY signal, it is possible to extract the orientational diffusion of a molecular dipole and also characterize the spectrum free from orientational considerations. One can also isolate the isotropic signal in an experiment where the pump and probe are rotated by 54.7° with respect to each other, known as the "magic angle." As will be shown in Chapter 3, we collect both of these signals simultaneously when measuring experimental spectra.

The orientational diffusion results presented in Eqs. 2.39-2.41 are commonly cited, but interpretation of an anisotropy decay measurement needs to be done carefully. First, even in the case of small angle diffusion, the decay timescale of $c_2(\tau_2)$ is scaled by the orientational timescale τ_{or} by a value that depends on the order of the correlation function. More importantly, $c_2(\tau_2)$ does not directly report on a physical rotational timescale, but the decay of a specific orientational time correlation function, $\left\langle P_2\left[\hat{\mu}_a(\tau_2)\cdot\hat{\mu}_a(0)\right]\right\rangle$, where P_2 is the second Legendre polynomial, $(3\cos^2 x - 1)/2$. There are other spectroscopic techniques where the P_2 TCF is the observable,

such as fluorescence depolarization spectroscopy, polarization-sensitive Raman spectroscopy, and pump-probe spectroscopy, which all involve multiple light interactions.[22,23] By contrast, linear spectroscopies like linear IR spectroscopy, NMR spectroscopy, and dielectric relaxation spectroscopy measure P_1 decorrelation.[24,25] Because these spectroscopies measure different correlation functions, they can in principle contain complementary information about a molecular system.

There can also be different mechanisms for the spectroscopic anisotropy decay signal that need to be considered, depending on the nature of the system. Orientational diffusion may occur by large angular jumps instead of small angle diffusion.[26] This situation is common in aqueous systems, where the tetrahedral geometry of the H-bond network results in large angular hops from one H-bonding conformation to another.[27,28] If the diffusion angle is known, then the physical timescale is scaled by a simple prefactor, but proving that an anisotropy decay mechanism arises from large angle diffusion requires comparison of the exact same process by techniques that measure different correlation functions.[28] This is experimentally challenging in general because different techniques are sensitive to different facets of a physical process, which eludes straightforward comparison. Additionally, radiative energy transfer between quasi-degenerate dipoles can scramble the anisotropy, such that anisotropy decay does not report on an activated physical process. This is common in vibrations that are delocalized over multiple strongly coupled oscillators, such as the O–H stretch in neat liquid water.[19,29,30] In general, care must be taken when interpreting a new anisotropy signal, but it can be quite useful for uncovering previously hidden physical processes, as will be shown in the case of the excess proton in Chapter 8.

2.5.2 Anisotropy from Two Dipoles

Polarization anisotropy can also be used to measure the relative orientation between two coupled dipoles. For this discussion, we concern ourselves primarily with the initial anisotropy, where τ_2 = 0 fs. Consider two unit dipole vectors $\hat{\mu}$ and $\hat{\nu}$ in the same molecular frame presented in Section 2.5.1, where $\hat{\mu}$ lies along the *a* axis and $\hat{\nu}$ lies in the *a*-*b* plane at an angle Θ from $\hat{\mu}$. In a 2D IR experiment pumping $\hat{\mu}$ and probing $\hat{\nu}$, the first two fields interact with $\hat{\mu}$ and the second two fields interact with $\hat{\nu}$. The geometry of these interactions is used to construct the form of the orientational response. In the previous section, the orientational averaging tensor Y_{ZZZZ}^{aaaa} was evaluated to account for four interactions with a single dipole parallel to the *a* axis. For the orientational response between two coupled dipoles, the first two interactions with $\hat{\mu}$ are the same as before, and the second two interactions involve the component of $\hat{\nu}$ in the direction of the *a* axis. This requires a Y_{ZZZZ}^{aaaa} term weighted by $(\hat{\nu}\cdot\hat{a})^2 = \cos^2\Theta$ for the second two field interactions. Another possibility is that the last two fields can interact with the component of $\hat{\nu}$ along the *b* or *c* axes, but we chose $\hat{\nu}$ to have no component along *c* for ease of calculation. This requires a tensor element $Y_{ZZZZ}^{aabb} = 1/15$ derived similarly as in Eqs. 2.34 and 2.35, weighted by $(\hat{\nu}\cdot\hat{b})^2 = \sin^2\Theta$. In total,

$$\begin{aligned} S_{ZZZZ} &\propto Y_{ZZZZ}^{aaaa}\cos^2\Theta + Y_{ZZZZ}^{aabb}\sin^2\Theta \\ &= \frac{1}{15}(1+2\cos^2\Theta). \end{aligned} \tag{2.43}$$

The values for all of the relevant Y_{IJKL}^{abcd} tensor elements for third-order spectroscopy have been tabulated elsewhere,[7,21] but can be derived through the same procedure outlined above. Like before, this is the response expected for one pathway, and the orientational response for multiple

pathways in a cross peak must be added together. We can also derive an expression for the orientational response for a ZZYY pathway:

$$\begin{aligned} S_{ZZYY} &\propto Y_{ZZYY}^{aaaa}\cos^2\Theta + Y_{ZZYY}^{aabb}\sin^2\Theta \\ &= \frac{1}{15}(2-\cos^2\Theta). \end{aligned} \tag{2.44}$$

Plugging Eqs. 2.43 and 2.44 into Eq. 2.36 for the rotational anisotropy yields

$$\begin{aligned} r &= \frac{1}{5}\left(3\cos^2\Theta - 1\right) \\ &= \frac{2}{5}\left\langle P_2(\cos\Theta)\right\rangle, \end{aligned} \tag{2.45}$$

where $P_2(\cos\Theta)$ is the second Legendre polynomial, and angular brackets are included to indicate ensemble averaging. Eq. 2.43 demonstrates that the initial polarization anisotropy r in a third-order signal is directly related to the relative angle Θ between the two involved dipoles. For two parallel dipoles, $r = 0.4$, as was derived before for a single dipole. For two perpendicular dipoles, $r = -0.2$, which means that the cross peak will have a larger amplitude in the S_{ZZYY} signal than in S_{ZZZZ}.

In Fig. 2.9a, we show the polarization-sensitive cross peak doublet (assuming no coherences in τ_2) for two parallel dipoles, which is three times as intense in the ZZZZ polarization scheme as ZZYY, like the diagonal doublet in Fig. 2.8. Conversely, if the dipoles are perpendicular (Fig. 2.9b) then the ZZYY signal is twice as intense as in ZZZZ. While the polarization dependence is easily observable for this model system, it is generally challenging to obtain an exact angle from an experimental 2D IR cross peak because of interference within the doublet or with other peaks. This will be the case for the vibrations of the aqueous proton complex where lineshapes span hundreds of cm^{-1}, but the polarization anisotropy will still be able to reveal approximate orientational relationships that will be key to making assignments of these different modes.

As a final mention, the time-dependent anisotropy decay between two dipoles is determined by the time correlation function

$$c_2(\tau_2) = \left\langle P_2\left[\hat{\mu}(0)\cdot\hat{\nu}(\tau_2)\right]\right\rangle = \left\langle P_2\left[\cos\Theta(\tau_2)\right]\right\rangle, \tag{2.46}$$

which in general can have many contributions like the rotation of the molecular frame, time-dependent fluctuations in Θ in a flexible molecule, or energy transfer between the two dipoles. Disentangling these components individually requires careful analysis, but can be invaluable for determining the mechanisms of molecular interactions.

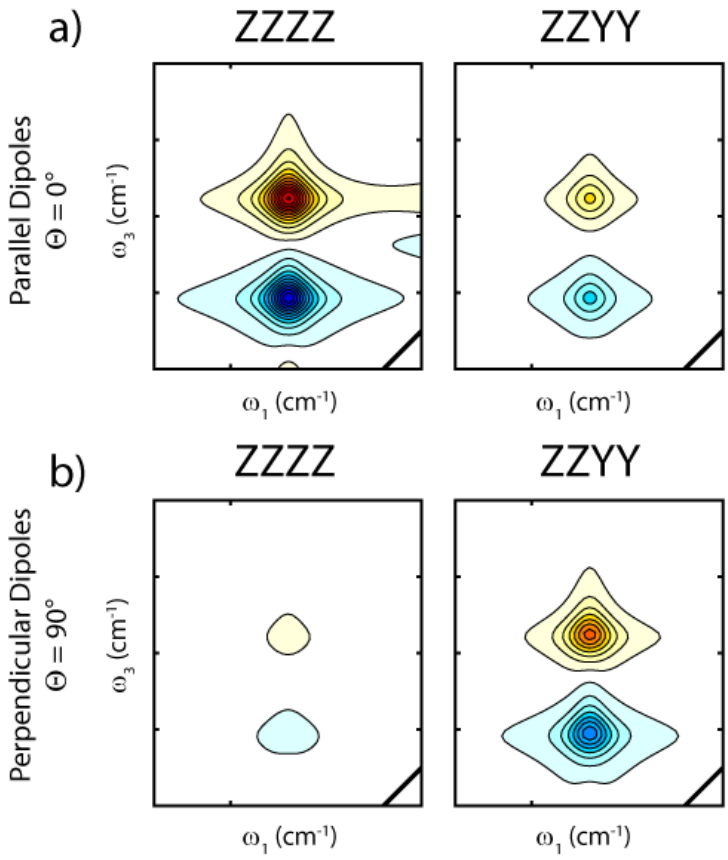

Figure 2.9: Polarization effects on a 2D IR cross peak. (a) ZZZZ and ZZYY spectra for two transitions with parallel dipoles, showing more intensity in the ZZZZ spectrum. (b) ZZZZ and ZZYY spectra for two perpendicular dipoles, where intensity is higher in the ZZYY spectrum. The diagonal of the 2D IR spectrum is indicated by the solid black line in the lower right-hand corner of each panel.

2.6 High-Level Vibrational Calculations on Hydrated Proton Clusters

We close the chapter with a discussion of the anharmonic calculations used to calculate IR spectral densities for the aqueous excess proton. The computational results in this thesis were calculated by Dr. Qi Yu using the vibrational self-consistent field/virtual configuration (VSCF/VCI) method developed in the Bowman group at Emory University. This method generates accurate spectral densities using a fully quantum-mechanical treatment of electronic and nuclear coordinates. This method has successfully calculated the IR spectrum of gas-phase clusters,[31–34] and has been extended to generate the IR spectrum of liquid H_2O and D_2O.[35,36] Its capability at handling calculations on highly anharmonic and multidimensional nuclear potential energy surfaces make it an appropriate technique for disentangling the complex vibrational spectrum of the aqueous proton.

A nonlinear molecule or molecular cluster with N atoms has 3N–6 degrees of freedom. In the harmonic limit, these vibrations are described as normal modes Q_i which diagonalize the Hessian matrix of the nuclear potential. The coordinates Q_i form the spatial basis for finding solutions to the nuclear Schrödinger equation with the harmonic Hamiltonian H_0:

$$\hat{H}_0 \Psi_K = \left[T + \frac{1}{2} \sum_i k_i Q_i^2 \right] \Psi_K = \varepsilon_K \Psi_K, \tag{2.47}$$

where $\varepsilon_K = \sum_i \hbar \omega_i (n_i + 1/2)$, and $\Psi_K = \prod_i \psi_{n_i}(Q_i)$. The harmonic spectral density of a molecule can be calculated with electronic structure software packages using various levels of theory, from density functional theory up to the highest levels such as coupled cluster theory. The spectral density results are typically presented as stick spectra representing the frequency positions and

intensities from the squared transition dipole, but do not include the lineshape information necessary to reproduce the IR absorption spectrum.

For an anharmonic molecular system with exact Hamiltonian H, the vibrational wavefunctions are not in general separable, but can be described as a linear combination of normal modes, which form a complete orthonormal basis. The goal of VSCF/VCI calculations is to find the coefficients $c_K^{(L)}$ to describe the wavefunctions Ψ_L which are solutions to the exact Hamiltonian such that

$$\Psi_L = \sum_K c_K^{(L)} \Psi_K, \tag{2.48}$$

where the squared coefficients sum to one. The coefficients $c_K^{(L)}$ arise because of the multidimensional nature of the nuclear potential, which couples the various normal modes. These coefficients are useful for characterizing the vibrational character of an anharmonic mode. When a particular coefficient is greater than 0.9, a mode can be fairly well represented in the harmonic limit, but frequently anharmonic modes are described as a mixture of multiple normal modes. Eq. 2.48 grows exponentially with the number of normal modes and accessible excited states, and in general solving the Schrödinger equation for the anharmonic Hamiltonian is intractable for systems as small as $N = 4$ atoms.

One way to approximate the exact solution is to iteratively solve the Schrödinger equation until convergence using the vibrational self-consistent field (VSCF) method, where the exact Hamiltonian is assumed to be separable with one-coordinate effective potentials that are dependent on the mean potential of the other coordinates. The VSCF method is similar to the Hartree-Fock method in electronic structure calculations and finds a set of one-coordinate vibrational wavefunctions whose corresponding eigenvalues converge. Typically the multidimensional

potential has been fit to a permutationally invariant, high-order polynomial.[18] In these calculations, nuclei are treated quantum mechanically, which is particularly important for light atoms like hydrogen. The resulting wave functions can be used as a new basis for determining virtual configuration interaction (VCI) states, which evaluate the interactions between various energy levels. For the results in this thesis, the VCI states include up to quadruple excitations of the vibrational modes, consisting of high harmonics and combination bands. Selecting this excitation space keeps the VCI matrix size to approximately $10^4 \times 10^4$.

It is necessary to make further approximations to make VSCF/VCI computationally accessible. One significantly useful approximation is the *n*-mode representation of the potential, where the full multidimensional potential is decomposed into sums of various orders:

$$\begin{aligned} V(Q_1,Q_2,...,Q_{3N-6}) = &\sum_i V_i^{(1)}(Q_i) + \sum_{i,j} V_{ij}^{(2)}(Q_i,Q_j) \\ &+ \sum_{i,j,k} V_{ijk}^{(3)}(Q_i,Q_j,Q_k) \\ &+ \sum_{i,j,k,l} V_{ijkl}^{(4)}(Q_i,Q_j,Q_k,Q_k) + ... \end{aligned} \tag{2.49}$$

$V_i^{(1)}(Q_i)$ represents the 1D slice of the potential along one coordinate, $V_{ij}^{(2)}(Q_i,Q_j)$ represents the two-dimensional potential energy surface over two coordinates, and so on. For the calculations in this thesis, the potential was evaluated in the 4-mode representation, and 10 grid points were used in each coordinate for evaluating the potential energy surfaces. Generating a multidimensional representation of the potential is the most expensive step, but it can reliably capture anharmonic mode coupling effects. The efficacy of the calculation relies on a highly accurate potential energy surface and dipole moment surface,[18] beyond what can be generated with DFT calculations.

The final major approximation is to break up a large molecular system into a collection of local monomers (LMs) such as individual molecules and discarding the coupling constants

between monomers, which significantly reduces the number of coupled vibrational modes. For instance, for a system of six water molecules, the full system would consist of $3N - 6 = 48$ normal modes, whereas the local monomer approach reduces the number of normal modes to $6(3 \cdot 3 - 6) = 18$, and anharmonic coupling would be accounted within sets of three modes rather than the throughout the entire system. Since the total wavefunction is the product of single-mode wavefunctions, this significantly reduces the complexity of the calculation. For instance, spectral density of liquid H_2O has been calculated with the LM method,[37] reproducing the position and intensity of the bend-libration combination band at 2200 cm^{-1}, which is typically challenging to reproduce due to its anharmonic character. The LM approximation works best with high-frequency anharmonic modes ($\omega > 700$ cm^{-1}), whereas low-frequency, delocalized modes are more challenging to model. For these intermolecular modes, one can simulate the IR spectrum using the dipole TCF, but this approach is unable to capture the coupling information that is produced from the VSCF/VCI calculation.[38]

Altogether, the VSCF/VCI method with the local monomer approximation enables the calculation of highly accurate vibrational spectral densities for anharmonic systems, such as the aqueous proton. As a demonstration, we present the vibrational calculations of a central Zundel $H_5O_2^+$ local monomer solvated by a shell of four H_2O monomers. Computational details beyond what was described in this section are provided in Chapter 6. A comparison of the double harmonic spectral density (Fig. 2.10a) and VSCF/VCI spectral density (Fig. 2.10b) shows that the VSCF/VCI calculation is in much better agreement with experiment (Fig. 2.10c).[39] Improvements in both frequency position and intensity are obtained, owing to a more appropriate treatment of anharmonic mode mixing and nuclear quantum effects. However, the calculation omits lineshape

considerations, and as such misses the broad lineshapes arising from coupling to low-frequency modes.[40]

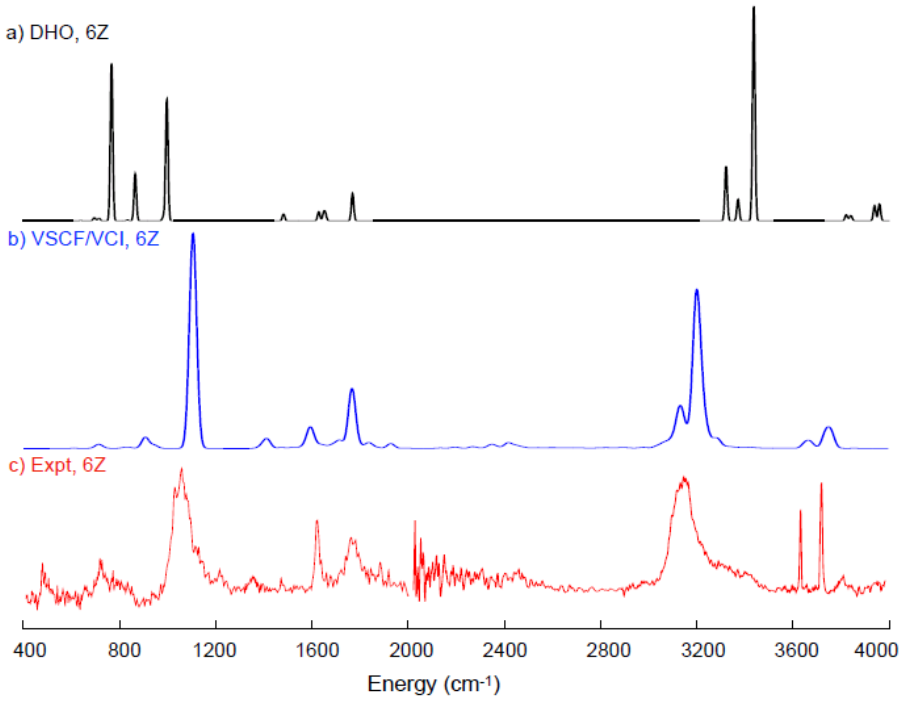

Figure 2.10: Calculated spectral densities of the 6-Zundel $H^+(H_2O)_6$ gas-phase hexamer. (a) Double harmonic spectral density calculated with the B3LYP functional. (b) VSCF/VCI calculated spectral density with a $H_5O_2^+$ central local monomer and four solvating water local monomers. Features are broadened with 20 cm^{-1} Gaussians. (c) Experimental spectrum measured with IR-IR double resonance predissociation spectroscopy (Ref. 39).

In addition to the linear spectrum, the VSCF/VCI calculation generates other useful quantities. First, the calculation provides excited states up to 6500 cm^{-1} which can be directly compared to ESAs in 2D IR spectra. Additionally, transition dipole amplitudes and angles for fundamental and excited-state transitions are recorded, leading to calculated spectral densities and anisotropy surfaces to compare to experiment. Recording the VCI coefficients $c_K^{(L)}$ is also useful for describing the vibrational character of an arbitrary mode. Finally, the monitoring of interacting energy levels can be used to generate a type of two-dimensional spectral density, which can be

compared to 2D IR spectra. All of these qualities make VSCF/VCI calculations useful for making vibrational assignments for the linear and nonlinear excess proton spectra, which we will show in Chapters 6 and 7.

2.7 Summary and Conclusion

The theory behind linear and nonlinear IR spectroscopy is well-developed and enables the intuitive interpretation of spectra for well-behaved systems. In linear spectroscopy, the interaction of the molecular dipoles with an incident oscillating electromagnetic field produces a polarization characterized by the linear response function $R^{(1)}(\tau)$. Nonlinear response is described in terms of multiple interactions of ultrashort pulses with the system's density matrix, which create a macroscopic, coherent polarization that can be detected experimentally. In third-order spectroscopy, this enables experiments such as 2D IR and transient absorption spectroscopies. 2D IR spectroscopy is capable of interrogating the anharmonicity and coupling of different vibrational modes in the form of cross peaks. By controlling the polarizations of the incident fields, it is possible to observe the orientational diffusion of a dipole and the relative orientation between two dipoles. These analyses are useful for making vibrational assignments for different motions, but computational assistance is necessary for connecting the spectroscopy to vibrational assignments. VSCF/VCI calculations can handle anharmonic and multidimensional systems such as the aqueous proton, and will be invaluable for interpreting the experimental results. The subject of the next chapter will describe the necessary tools and methods needed to measure these spectra.

2.8 References

(1) Mukamel, S. *Principles of Nonlinear Optical Spectroscopy*; Oxford University Press: New

York, 1995.

(2) Cho, M. Coherent Two-Dimensional Optical Spectroscopy *Chem. Rev.* **2008**, *108*, 1331.

(3) Hamm, P.; Zanni, M. T. *Concepts and Methods of 2D Infrared Spectroscopy*; Cambridge UP: Cambridge, 2011.

(4) Khalil, M.; Demirdöven, N.; Tokmakoff, A. Coherent 2D IR Spectroscopy: Molecular Structure and Dynamics in Solution. *J. Phys. Chem. A* **2003**, *107*, 5258.

(5) Nitzan, A. *Chemical Dynamics in Condensed Phases*; Oxford University Press: New York, 2006.

(6) Kubo, R. In *Fluctuation, Relaxation and Resonance in Magnetic Systems*; Ter Haar, D., Ed.; Oliver & Boyd: Edinburgh, 1962; pp 23–68.

(7) De Marco, L. The Molecular Dynamics of Hydrogen-Bonding Explored with Broadband Two Dimensional Infrared Spectroscopy, Massachusetts Institute of Technology, 2016.

(8) Sung, J.; Silbey, R. J. Four wave mixing spectroscopy for a multilevel system *J. Chem. Phys.* **2001**, *115*, 9266.

(9) Svelto, O. *Principles of Lasers*, 5th ed.; Hanna, D. C., Ed.; Springer: New York, NY, 2010.

(10) Butcher, P. N.; Cotter, D. *The Elements of Nonlinear Optics*; Cambridge UP: Cambridge, 1990.

(11) Franken, P. A.; Hill, A. E.; Peters, C. W.; Weinreich, G. Generation of optical harmonics *Phys. Rev. Lett.* **1961**, *7*, 118.

(12) Shen, Y. R. *The Principles of Nonlinear Optics*; John Wiley \& Sons: Hoboken, 2003.

(13) Ni, Y.; Skinner, J. L. Communication: Vibrational sum-frequency spectrum of the air-water interface, revisited *J. Chem. Phys.* **2016**, *145*, 031103.

(14) Schmidt, J. R.; Corcelli, S. A.; Skinner, J. L. Pronounced non-Condon effects in the ultrafast infrared spectroscopy of water. *J. Chem. Phys.* **2005**, *123*, 044513.

(15) Stenger, J.; Madsen, D.; Hamm, P.; Nibbering, E. T. J.; Elsaesser, T. A Photon Echo Peak Shift Study of Liquid Water † *J. Phys. Chem. A* **2002**, *106*, 2341.

(16) Fecko, C. J.; Eaves, J. D.; Loparo, J. J.; Tokmakoff, A.; Geissler, P. L. Ultrafast Hydrogen-Bond Dynamics in the Infrared Spectroscopy of Water. *Science* **2003**, *301*, 1698.

(17) Guasco, T. L.; Johnson, M. A.; McCoy, A. B. Unraveling anharmonic effects in the vibrational predissociation spectra of $H_5O_2^+$ and its deuterated analogues *J. Phys. Chem. A* **2011**, *115*, 5847.

(18) Qu, C.; Yu, Q.; Bowman, J. M. Permutationally Invariant Potential Energy Surfaces *Annu. Rev. Phys. Chem.* **2018**, *69*, 151.

(19) Ramasesha, K.; De Marco, L.; Mandal, A.; Tokmakoff, A. Water vibrations have strongly mixed intra- and intermolecular character *Nat. Chem.* **2013**, *5*, 935.

(20) Khalil, M.; Tokmakoff, A. Signatures of Vibrational Interactions in Coherent Two-Dimensional Infrared Spectroscopy *Chem. Phys.* **2001**, *266*, 213.

(21) Golonzka, O.; Tokmakoff, A. Polarization-selective third-order spectroscopy of coupled vibronic states *J. Chem. Phys.* **2001**, *115*, 297.

(22) Gordon, R. G. Molecular Collisions and the Depolarization of Fluorescence in Gases *J. Chem. Phys.* **1966**, *45*, 1643.

(23) Eaves, J. D.; Fecko, C. J.; Stevens, A. L.; Peng, P.; Tokmakoff, A. Polarization-selective femtosecond Raman spectroscopy of low-frequency motions in hydrated protein films *Chem. Phys. Lett.* **2003**, *376*, 20.

(24) Endom, L.; Hertz, H. G.; Thül, B.; Zeidler, M. D. A Microdynamic Model of Electrolyte Solutions as Derived from Nuclear Magnetic Relaxation and Self-Diffusion Data *Berichte Der Bunsengesellschaft Fur Phys. Chemie* **1967**, *71*, 1008.

(25) Nicodemus, R. A.; Corcelli, S. A.; Skinner, J. L.; Tokmakoff, A. Collective Hydrogen Bond Reorganization in Water Studied with Temperature-Dependent Ultrafast Infrared Spectroscopy *J. Phys. Chem. B* **2011**, *115*, 5604.

(26) Ivanov, E. N. Theory of Rotational Brownian Motion *Sov. Phys. JETP* **1964**, *18*, 1041.

(27) Laage, D.; Hynes, J. T. A molecular jump mechanism of water reorientation *Science* **2006**, *311*, 832.

(28) Ji, M.; Odelius, M.; Gaffney, K. J. Large angular jump mechanism observed for hydrogen bond exchange in aqueous perchlorate solution. *Science* **2010**, *328*, 1003.

(29) De Marco, L.; Fournier, J. A.; Thämer, M.; Carpenter, W.; Tokmakoff, A. Anharmonic exciton dynamics and energy dissipation in liquid water from two-dimensional infrared spectroscopy *J. Chem. Phys.* **2016**, *145*, 094501.

(30) Paarmann, A.; Hayashi, T.; Mukamel, S.; Miller, R. J. D. Probing intermolecular couplings in liquid water with two-dimensional infrared photon echo spectroscopy *J. Chem. Phys.* **2008**, *128*, 191103.

(31) Yu, Q.; Bowman, J. M. Communication: VSCF/VCI vibrational spectroscopy of $H_7O_3^+$ and $H_9O_4^+$ using high-level, many-body potential energy surface and dipole moment surfaces *J. Chem. Phys.* **2017**, *146*, 121102.

(32) Kaledin, M.; Kaledin, A. L.; Bowman, J. M. Vibrational Analysis of the $H_5O_2^+$ Infrared Spectrum Using Molecular and Driven Molecular Dynamics **2005**, *110*, 2933.

(33) Chen, Q.; Bowman, J. M. Quantum approaches to vibrational dynamics and spectroscopy: Is ease of interpretation sacrificed as rigor increases? *Phys. Chem. Chem. Phys.* **2018**.

(34) Yu, Q.; Bowman, J. M. High-Level Quantum Calculations of the IR Spectra of the Eigen, Zundel, and Ring Isomers of $H^+(H_2O)_4$ Find a Single Match to Experiment *J. Am. Chem. Soc.* **2017**, *139*, 10984.

(35) De Marco, L.; Carpenter, W.; Liu, H.; Biswas, R.; Bowman, J. M.; Tokmakoff, A. Differences in the Vibrational Dynamics of H_2O and D_2O: Observation of Symmetric and Antisymmetric Stretching Vibrations in Heavy Water *J. Phys. Chem. Lett.* **2016**, *7*, 1769.

(36) Liu, H.; Wang, Y.; Bowman, J. M. Quantum Local Monomer IR Spectrum of Liquid D_2O at 300 K from 0 to 4000 cm^{-1} Is in Near-Quantitative Agreement with Experiment *J. Phys. Chem. B* **2016**, *120*, 2824.

(37) Liu, H.; Wang, Y.; Bowman, J. M. Quantum calculations of the IR spectrum of liquid water using ab initio and model potential and dipole moment surfaces and comparison with experiment *J. Chem. Phys.* **2015**, *142*, 194502.

(38) Esser, T. K.; Knorke, H.; Asmis, K. R.; Schöllkopf, W.; Yu, Q.; Qu, C.; Bowman, J. M.; Kaledin, M. Deconstructing Prominent Bands in the Terahertz Spectra of $H_7O_3^+$ and $H_9O_4^+$: Intermolecular Modes in Eigen Clusters *J. Phys. Chem. Lett.* **2018**, *9*, 798.

(39) Heine, N.; Fagiani, M. R.; Rossi, M.; Wende, T.; Berden, G.; Blum, V.; Asmis, K. R. Isomer-Selective Detection of Hydrogen-Bond Vibrations in the Protonated Water Hexamer *J. Am. Chem. Soc.* **2013**, *135*, 8266.

(40) Leavitt, C. M.; Deblase, A. F.; Johnson, C. J.; Van Stipdonk, M.; McCoy, A. B.; Johnson, M. A. Hiding in plain sight: Unmasking the diffuse spectral signatures of the protonated N-terminus in isolated dipeptides cooled in a cryogenic ion trap *J. Phys. Chem. Lett.* **2013**, *4*, 3450.

Chapter 3

Experimental Implementation of Nonlinear IR Spectroscopy

3.1 Overview of the Spectrometer

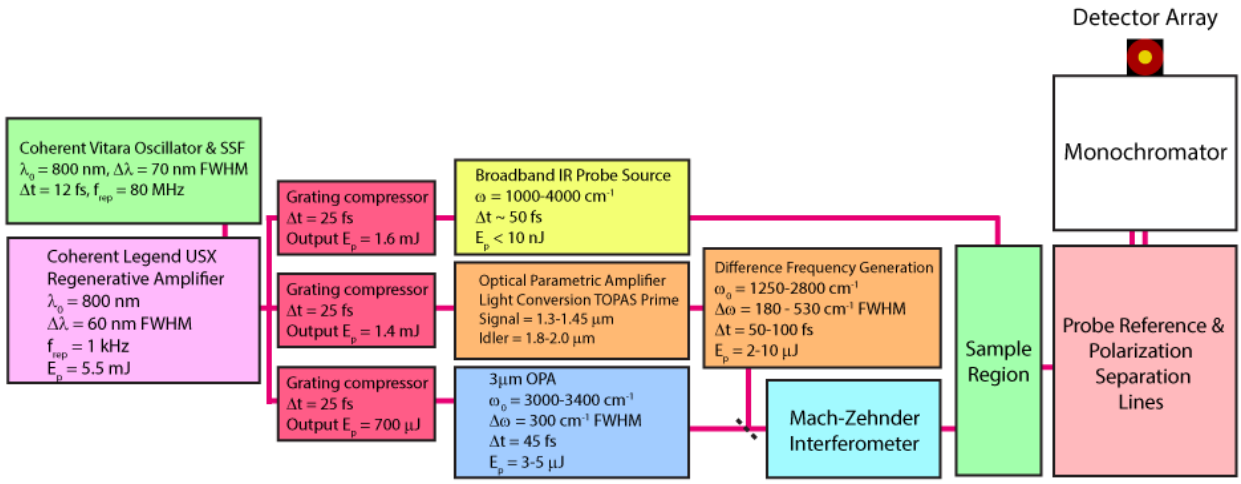

Figure 3.1: A schematic of the main components of the TA and 2D IR spectrometer.

To directly monitor aqueous vibrational dynamics with ultrafast IR spectroscopy, we need to generate temporally short, spectrally broad, and intense mid-IR pulses. While the fundamental principles of ultrashort light generation are well established, it is only in the last decade or so that their application in the mid-IR has advanced enough for reliable experiments on the aqueous proton. The implementation of transient absorption (TA) and two-dimensional infrared (2D IR) spectroscopy in practice involves a remarkable coordination of many highly sensitive components

that generate, modify, and detect ultrafast pulses of infrared light. If any one of these components fails, the entire experiment cannot function. As a result, the operating research assistant gains an intimate knowledge of each component over the years through iterative rounds of troubleshooting, optimization, and development. This chapter begins with a top-level overview of the various pieces of the 2D IR spectrometer (Fig. 3.1) before delving into each piece of the experiment in more detail.

The foundation of the experiment lies in the generation of intense, ultrashort 800 nm pulses. Broad-bandwidth 800 nm pulses are first generated in a mode-locked oscillator at nJ pulse energies. They are then stretched in time and amplified to multiple mJ per pulse at a repetition rate of 1 kHz. These intense 800 nm pulses are split into three independently controlled compressors, bringing the pulse widths down to 25 fs each, and are used to pump three infrared light generation sources.

IR pump pulses come from one of two separate light generation sources. Tunable excitation pulses centered between 3 μm and 3.3 μm are generated in a home-built two-stage optical parametric amplifier (OPA) that yields pulses with 3-4 μJ pulse energy, 45 fs pulse width, and S-polarization.[1] Another 800 nm arm pumps a commercial OPA to generate a pair of collinear near-IR pulses, which are then mixed in a nonlinear crystal to produce tunable mid-IR light via difference frequency generation (DFG). This process generates pump pulses with center wavelength between 4-8 μm, pulse energy between 7-10 μJ, and pulse width between 50-100 fs. With either of these two arms, we can vibrationally excite anywhere in the 1000-3000 cm^{-1} proton continuum of absorption.

The pump pulse is then guided through a Mach-Zehnder interferometer (MZI) to generate a pulse pair for the 2D IR experiment while simultaneously recording the pump spectrum. The

interferometer splits the pump into two arms, one static and chopped at 500 Hz and the other on a motorized stage controlling the pump time delay τ_1. These arms are re-overlapped to generate two output arms. One outgoing arm is guided to the sample region, and the second arm is sent to a single-channel detector, which records the pump interferogram as a function of τ_1. This interferogram is processed to measure the pump's spectrum and phase errors from slight misalignments, both of which are needed for 2D IR measurements.

To detect the vibrational response of the sample, we use a broadband IR probe pulse based on plasma filamentation in nitrogen gas.[2] To generate these pulses, the third 800 nm arm is used to produce 400 nm and 267 nm light via second harmonic generation (SHG) and sum-frequency generation (SFG), respectively, in beta-barium borate (β-Ba_2BO_4, BBO). These three beams are focused into a stream of N_2, generating a plasma filament that produces light spanning THz, IR, and visible frequencies. The mid-IR light of interest is isolated by transmission through a thin wafer of silicon set to transmit 45°-polarized light and passed through a spatial filter before being guided to the sample area.

At the sample region, the pump and probe pulses cross at a common focal point in the sample. The pulses are also overlapped in time via a motorized translation stage in the probe line, which determines the waiting time delay τ_2. After propagating through the sample, the pump is blocked but can be guided to a single channel detector to measure its temporal profile. As a consequence of the pump-probe geometry, the generated nonlinear signal is phase matched collinearly with the probe such that they propagate together.

Before detection, the probe and signal are split into two arms with S and P polarization to simultaneously measure polarization-resolved TA and 2D IR spectra. Each arm is guided into a monochromator and then dispersed onto a 2×64 photodetector array where each 64-element stripe

detects the response from the two polarization schemes as a function of a detection frequency ω_3. The data are recorded as change of absorption after excitation by the pump, referenced by the power fluctuations of the probe so as to mitigate shot-to-shot variations in laser intensity. Frequency-dispersed and polarization-resolved TA spectra are collected by stepping the τ_2 delay, which records vibrational relaxation kinetics and polarization anisotropy decay. Polarization-resolved 2D IR spectra are collected as a series of TA spectra which oscillate over τ_1 for a fixed τ_2. This time-frequency representation of the data is then Fourier transformed across τ_1 to generate an IR spectrum in terms of excitation frequency ω_1 and detection frequency ω_3. Polarization-resolved 2D IR can be used to disperse polarization anisotropy over ω_1 and ω_3, and 2D IR τ_2 series can be collected to measure frequency correlation kinetics.

In this chapter, I will describe the components of the spectrometer, motivate their importance for the experiment, and demonstrate how data are collected and processed. While not described in exhaustive detail, the descriptions of the various pieces should be a useful introduction for new graduate students and postdocs in the lab. This chapter will also serve as a record of experimental conditions such as IR pulse widths and energies. Where appropriate, thoughts on potential future improvements will be included so that future group members can continue to develop the experiment.

3.2 Generation and Amplification of Ultrafast 800 nm Pulses

Every pulse in the 2D IR experiment originates from an 800 nm seed pulse generated in a Titanium:sapphire (Ti:Sapphire) oscillator. The oscillator (Coherent *Vitara-T*) consists of a laser cavity where the gain medium is a sapphire crystal (Al_2O_3) with ~1% of the Al^{3+} sites substituted for Ti^{3+}.[3] The cavity is pumped by a continuous-wave, optically-pumped semiconductor laser

(Coherent *Verdi-G*) at 532 nm and emits around 800 nm. Due to the Jahn-Teller splitting of the Ti^{3+} crystal field environment and vibronic coupling with Ti:Sapphire phonons, the bandwidth of the 800 nm laser field can span up to 100 nm,[4] broad enough for supporting ultrashort pulses. Pulses with 12 fs pulse width are generated by mode-locking the cavity, which induces a well-defined phase relationship between all of the frequencies in the band. These pulses fire at 80 MHz with average power of approximately 400-450 mW, corresponding to about 5 nJ per pulse.

To increase the bandwidth and reduce the pulse width of the amplified 800 nm pulses, the seed beam is guided through a spectral shaper (Coherent *SSF*), which is a band-rejection filter spanning 780-820 nm. The resulting spectrum is bimodal, peaked at 770 and 830 nm with some remaining intensity in between. Without spectral shaping, the amplified 800 nm pulse would be comparatively narrower in frequency and longer in time due to the variation in amplifier gain across the bandwidth of the pulse.[3] The spectral shaper pre-compensates for this loss in bandwidth. A $\lambda/2$ waveplate before the SSF modulates the band-rejection depth, which can be tuned within a couple degrees to minimize 800 nm pulse width and optimize mid-IR power down the line.

After spectral shaping, the 800 nm seed pulse undergoes chirped pulse amplification in a regenerative amplifier (Coherent *Legend* USX), whereby the pulse is temporally stretched, amplified in a second Ti:Sapphire cavity, and then temporally recompressed. This procedure allows for attaining high peak powers ($> 1\times10^{12}$ W) without risking damage to cavity optics or the gain medium. A seed pulse is stretched when diffraction off a grating disperses its frequencies in pathlength, spreading out the frequencies in time. A single stretched pulse from the 80 MHz pulse train is then switched into the amplifier cavity via a Pockels cell, which applies a high-voltage electrical pulse to an electro-optic component to act as a polarization gate for the selected seed pulse. The Pockels cell (and all other electronic devices on the table) are synced to the amplifier's

pump laser (Coherent *Evolution*), which fires at a 1 kHz repetition rate. The pump is a Q-switched, frequency-doubled Nd:YLF laser ($\lambda = 527$ nm) generating nanosecond pulses with average power of approximately 20 W. Once the Ti:sapphire crystal has been pumped, the seed pulse bounces within the cavity 14 times, each time stimulating emission at 800 nm. A second Pockels cell controls the exit of the 800 nm, now amplified to an average power of 5.5 W. The pulse is split between three arms whose intensities are determined by nested polarizing beamsplitters and $\lambda/2$ waveplates. Each arm has an independent grating compressor,[5] which uses a pair of parallel gratings to re-equalize the pathlengths of all frequencies in the pulse and bring the pulse width down to 25 fs. The amount of power in each line can be manipulated to guide energy into one of the pump lines and the probe line for a particular experiment. We have characterized the pulse temporal properties with a single-shot frequency-resolved optical gating (FROG) autocorrelator (Swamp Optics *GRENOUILLE 8-20-USB*), which retrieved a pulse width of 32 fs. This value serves as an upper bound because the SHG crystal is not able to simultaneously phase match across the entire bandwidth of the pulse.

3.3 Generation and Characterization of Mid-IR Pump Pulses

3.3.1 Introduction to OPA

It is necessary to convert the intense 800 nm beams to pulses in the mid-IR, which is achieved by utilizing nonlinear optics. In standard linear optics, the polarization of a material typically depends linearly on the amplitude of an incident electric field, whereas nonlinear optics deals in the regime where the material's polarization depends on higher orders of the electric field. This regime is typically reached with intense, ultrashort pulses where the field amplitude is compressed into the femtosecond regime. With a nonlinear optical material, typically a birefringent crystal, it is possible to convert the frequencies of an incoming beam to new

frequencies of output light. Some common examples of these are second harmonic generation (SHG), sum and difference frequency generation (SFG/DFG), and optical parametric amplification (OPA). Useful introductions to nonlinear optics and OPA is provided in the textbook by Butcher and Cotter[6] and a pedagogical review by Manzoni and Cerullo,[7] but here I will provide a brief introduction of the concepts behind IR light generation from 800 nm pulses.

For frequency conversion techniques like OPA and DFG, we care primarily about the second-order terms in the nonlinear polarization P_{NL}, which for collinear beams propagating in time t along the z-axis, can be expressed as

$$P_{\mathrm{NL}}(z,t) = 2\epsilon_0 d_{\mathrm{eff}} E^2(z,t), \tag{3.1}$$

where ϵ_0 is the vacuum permittivity and d_{eff} is an effective nonlinearity coefficient. This coefficient is a positive scalar which depends on the nonlinear process and the identity of the nonlinear medium. Because the incident electric fields are oscillatory, P_{NL} oscillates as well, which becomes a source of electromagnetic radiation.

In second-order processes, we generally consider three-wave mixing between a high-frequency electric field with angular frequency ω_3 and two fields at lower frequencies ω_1 and ω_2. For this discussion, ω_1 and ω_3 do not refer to the excitation and detection frequencies from 2D IR spectra, introduced above. Because P_{NL} depends on the square of the total incoming field, the outgoing electric field will contain cross terms at the sum and difference frequencies of ω_1, ω_2, and ω_3. As the three fields propagate through the material, they can exchange energy amongst each other facilitated by the nonlinear medium. In SFG, for example, when the amplitudes of ω_1 and ω_2 are large and the initial amplitude of ω_3 is zero, the ω_1 and ω_2 fields interact to generate an electric field with angular frequency $\omega_3 = \omega_1 + \omega_2$. In DFG, the amplitudes of ω_1 and ω_3 are large while the initial amplitude of ω_2 is zero, and combination in the nonlinear medium generates an electric

field at the difference frequency $\omega_2 = \omega_3 - \omega_1$. Energy conservation is obeyed both in terms of frequency and intensity. When treating intensity as photon flux, three-wave mixing can be interpreted as creation and annihilation of photons at different frequencies. In contrast to lasing, the medium does not absorb energy. Rather, it serves as a coupling mechanism between the photons.

In OPA, the amplitude of the incoming ω_3 field (known as the *pump*) is many orders of magnitude larger than the ω_1 field (known as the *seed*), and the amplitude of the ω_2 field is zero. The higher-frequency field amongst ω_1 and ω_2 is known as the *signal* and the lower-frequency field is known as the *idler*. The energy from the pump is channeled into the signal and idler fields to amplify them both by many orders of magnitude. Qualitatively, this process can be described like a positive feedback sequence of DFG steps: when the material is excited by a photon of energy $\hbar\omega_3$, a photon of $\hbar\omega_1$ seeds a stimulation process which generates a photon at $\hbar\omega_1$ and a second photon at $\hbar\omega_2$, where $\hbar\omega_1 + \hbar\omega_2 = \hbar\omega_3$. The new $\hbar\omega_2$ then stimulates the emission of another pair of $\hbar\omega_1$ and $\hbar\omega_2$ photons. Assuming perfect phase matching and a sufficiently long pathlength through the medium, the amplitudes of the ω_1 and ω_2 fields can grow exponentially. There are additional details to consider which limit amplification efficiency, such as temporal walk-off between ultrafast pulses. However, this simple model can be generalized to other amplification schemes, such as amplification of broadband pulses by noncollinear wave mixing.

The efficiency of any three-wave mixing process depends on the term $\Delta k = k_3 - k_1 - k_2$, known as the wavevector mismatch, where k_i is the wavevector of the electric field of frequency ω_i. When $\Delta k = 0$, phase matching is achieved and nonlinear wave mixing is maximized. This condition ensures that the three beams stay in phase with each other while propagating through the medium. One of the experimental handles for ensuring phase matching is to exploit the

birefringence of the nonlinear medium. This is because the phase matching condition can be rewritten by relating k to the angular frequency ω, the medium's index of refraction n, and the speed of light in a vacuum c_0 as $k = \omega n/c_0$. Plugging into the phase matching condition above yields:

$$n_3\omega_3 - n_1\omega_1 - n_2\omega_2 = 0. \tag{3.2}$$

In a birefringent crystal, the index of refraction at a particular frequency depends on the orientation of the light's polarization and propagation direction with respect to the optical axis. When propagating normal to the optical axis, a beam can experience the same index as that along the optical axis, known as the ordinary refractive index n_o, or a different index known as the extraordinary refractive index n_e. Depending on the details of the type of nonlinear crystal and the three-wave mixing process, phase matching can be achieved when the beams propagate at a particular angle θ with respect to the optical axis of the crystal. This angle satisfies the phase matching condition because n_1, n_2, and n_3 are θ-dependent mixtures of n_o and n_e. A useful visualization of how refractive indices change with θ is shown in Fig. 6 of the review by Manzoni and Cerullo.[7] In practice, phase matching is found by tuning the crystal angle on output power and center frequency of the desired pulse. The dependence of phase matching on polarization results in two main phase matching schemes: type I phase matching where the polarizations of the k_1 and k_2 fields are parallel to each other but orthogonal to k_3, and type II phase matching, where the polarization of k_3 is parallel to k_1 and perpendicular to k_2.

3.3.2 Generation of 3 μm Light

3 μm pulses are generated in a home-built two-stage OPA, which is described in detail elsewhere.[1] Briefly, approximately 500 μJ of P-polarized 800 nm light is split into three paths with

intensity ratios 1:34:65. These paths are used for white light generation, pumping the first OPA stage, and pumping the second OPA stage, respectively. The white light continuum is generated by focusing 800 nm into a 1 mm thick piece of sapphire, and is used as the seed for the first OPA step. The white light seed is collinear with the first 800 nm pump in a 1 mm BBO crystal cut at $\theta = 29°$ and set to $\theta = 21.5°$, the angle for collinear type I phase-matching with a 1100 nm signal. The 1100 nm component of the white light is amplified to 500 nJ for seeding in the second OPA step. In the second OPA stage, the 1100 nm pulse is mixed collinearly with the second 800 nm pump to generate an S-polarized 3 μm idler via type I phase matching in 1 mm of potassium niobite (KNB) cut at $\theta = 41°$. Tilting the KNB crystal adjusts the phase-matching angle θ, providing frequency tunability of the output light. For center frequencies around 3000 cm^{-1}, pulse energies are typically greater than 5 μJ, but drop to below 3 μJ for center frequencies above 3400 cm^{-1}. The power stability is typically 2%, but can improve to 1.5% at higher pulse energy. The pulsewidth is 45 fs as measured by SHG FROG in $AgGaS_2$.[1] The output energy may be improved by exchanging sapphire for yttrium aluminum garnet (YAG) for white light generation, which has been shown to increase the seed intensity by up to 2.5 times.[8] We have not seen indications that we have saturated either of the OPA processes, so increasing the seed intensity should help amplify 3 μm output.

3.3.3 Generation of Tunable Mid-IR Pump Pulses Spanning 1250-2800 cm^{-1}

To excite vibrational frequencies in other regions of the mid-IR, we first employ OPA to generate near-IR signal and idler beams.[7] 1.4 W of compressed 800 nm light is sent into a commercial OPA (Light Conversion *TOPAS Prime*) to generate tunable near-IR pulses centered between 1.3-1.45 μm (signal) and 1.8-2.0 μm (idler). The OPA occurs in two stages. The incoming P-polarized 800 nm pump is separated into three lines with relative intensities of approximately

1:10:200. The first beam passes through a λ/2 waveplate and is focused into a sapphire plate for generating an S-polarized white light continuum, serving as the seed for an 800 nm-pumped, noncollinear OPA step in BBO with type I phase matching. Because of the noncollinear geometry, the amplified signal is spatially separated from the pump and idler and can be tuned between 1.3-1.45 μm by adjusting the BBO angle and the pump-white light timing. The signal is spatially overlapped with the third 800 nm arm for a collinear second OPA step in BBO. The process is type II phase matched to generate P-polarized idler centered between 1.8-2.0 μm, which can also be tuned by rotating the angle of the BBO with respect to the beam path. The collinear signal and idler beams transmit through an 800 nm high-reflector to separate residual pump. The signal and idler beams contain about 300 μJ and 200 μJ of pulse energy, respectively.

The generation of mid-IR light is accomplished by DFG between the near-IR signal and idler in a homebuilt assembly (Fig. 3.2). The collinear beams are first separated into two arms then recombined on a dichroic mirror, where timing and spatial overlap between the two beams are optimized for DFG in a nonlinear crystal ($AgGaS_2$ or GaSe). The DFG is separated from the signal and idler by transmitting through a long-pass filter (Spectrogon), which was chosen to ensure approximately constant broadband transmission (80 ± 5%) from 3-12 μm. A HeNe tracer beam is reflected off this optic for overlap with the mid-IR. The beam is collimated and expanded to a $1/e^2$ diameter of 8 mm with a folded reflective telescope. At the output, the mid-IR power is approximately 7-10 μJ, depending on center frequency.

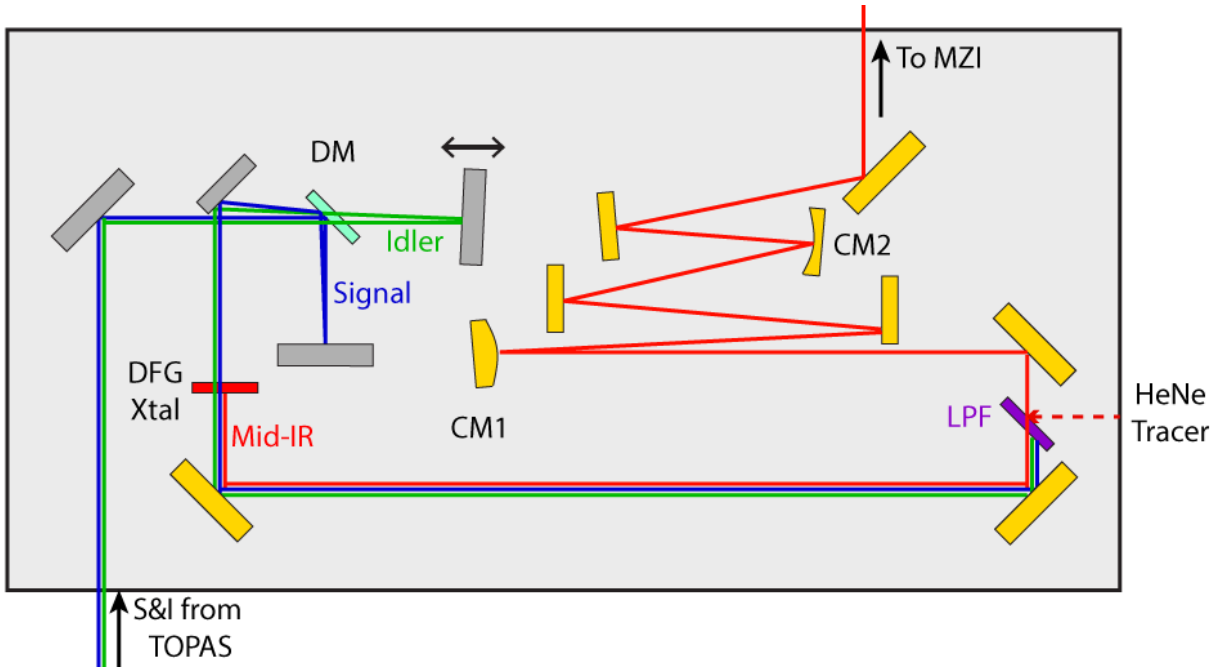

Figure 3.2: Diagram of the DFG source. Protected silver mirrors are shown in gray, and bare gold mirrors are shown in yellow. DM: dichroic mirror. LPF: long-pass filter, transmitting 2.5-10 μm. CM1: curved mirror 1, f = -2000 mm. CM2: curved mirror 2, f = 2500 mm.

We use a few different DFG crystals for tuning across the mid-IR. To generate 4 μm light, we employ a 1 mm thick, anti-reflection coated (for 1.1-2.4 μm on the front face and 2.4-11 μm on the back face) $AgGaS_2$ (AGS) crystal cut at $\theta = 47.2°$ (Eksma Optics). The S-polarized mid-IR is generated by type II phase matching between the S-polarized near-IR signal and P-polarized idler. These pulses are typically 300 cm^{-1} in bandwidth at full-width half maximum (FWHM), 9 μJ in pulse energy, and 55 fs in pulse width (see Figs. 3.5 and 3.7 below). For 6-7 μm pulses, we employ a 0.5 mm thick AGS crystal cut at $\theta = 42.0°$ to generate light that is also S-polarized from type II phase matching. The reduced pathlength diminishes pulse energy (7 μJ), but relaxes the phase matching condition $\Delta k = 0$, enabling broader DFG bandwidth (530 cm^{-1}) and shorter pulse width (50 fs). For both of these pulses, we can typically achieve stability of 0.7-1%.

We have used two different methods for generating pulses at 8 μm. The first involves tilting a 1 mm AGS crystal cut at θ = 42.0° until a center frequency of 1250 cm^{-1} was reached. This produced pulses with relatively small bandwidth (180 cm^{-1} FWHM) due to crystal thickness and low pulse energy (2 μJ) due to the low effective nonlinearity of this process in AGS (d_{eff} = 1.5 pm/V).[9] We had more success with DFG in 0.5 mm of Z-cut GaSe. For this process, we found type I phase matching produced the steepest phase matching curve, dramatically increasing bandwidth (280 cm^{-1} FWHM). Additionally, the pulse energy increased to 10 μJ because of the much higher effective nonlinearity in GaSe (57.1 pm/V).[9] This high power sharply reduces with redder pump frequencies, however, so we keep the pump centered at 1250 cm^{-1}. We found that a type II process was also phase matched but with narrower bandwidth and orthogonal polarization. We therefore optimized power on the P-polarized type I process, which was isolated with a ZnSe polarizer at the exit of the DFG assembly. One downside with using GaSe, however, is that it cannot be AR coated and produces ghost pulses at 8 ps, setting an upper bound on accessible delay times.

We have found that in developing pumping capabilities at 8 μm, many standard IR materials absorb in this region, which required us to update most of our optics. Primarily, all protected gold mirrors were swapped for bare gold since Si-O stretches on the silica protective coating absorbed between 8-10 μm. Dispersion becomes more of a problem in this region as well. Non-negligible third-order dispersion arises from transmission through the germanium long-pass filter. We found that other transmissive optics designed for application between 4-6 μm were dispersive and/or absorptive in the 8-10 μm regime. CaF_2 polarizers and beamsplitters are the biggest offender, with clear absorption starting at 8 μm. ZnSe optics are an improvement, but they

impart significant negative second-order dispersion between 8-10 μm. We have found that KBr beamsplitters in the pump line significantly reduced dispersion in 8 μm pulses.

3.3.4 Spectral Characterization of Mid-IR Pump Pulses with a Mach-Zehnder Interferometer

We characterize mid-IR pump pulses in a Mach-Zehnder interferometer, which splits the beam into two arms and recombines them as two output arms. A diagram of the interferometer is shown in Fig. 3.3. The introduced beam is split on a 50:50 beamsplitter (BS1, 5 mm KBr substrate) into transmitted and reflected arms, E_T and E_R, respectively. The reflected arm E_R is retroreflected in a static arm chopped at a 500 Hz repetition rate by an optical chopper (Newport *3501*) that is phase-locked and synchronized to the 1 kHz repetition rate from the Q-switch such that every other E_R shot is blocked. E_R is then subsequently split on a second 50:50 beamsplitter (BS2) into reflected and transmitted arms E_{RR} and E_{RT}, respectively. The transmitted arm E_T is retroreflected in an arm with a computer-controlled stage (Aerotech *ANT-25L*), which controls the time delay τ_1 between the two arms. E_T is also split on BS2 to generate E_{TT} and E_{TR}, which are collinear with E_{RR} and E_{RT}, respectively.

The two output arms of the interferometer are used to record the spectral content of the pump pulses in the time domain. The $E_{RT} + E_{TR}$ output arm is sent to the sample area after transmission through a ZnSe wire grid polarizer (Thorlabs). In this arm, each field has transmitted through a beamsplitter exactly once, so that the temporal dispersion is matched. This arm is sometimes called the "bright" arm because at $\tau_1 = 0$ fs, the two arms constructively interfere. In the other arm, the $E_{RR} + E_{TT}$ output is focused onto a HgCdTe photodetector, which can either be a room-temperature detector or an element cooled by liquid nitrogen (IR Associates, *MCT-13-0.5*) if higher sensitivity is necessary. This arm records an interferogram of the pump pulse, which

measures how the beam interference changes as a function of τ_1. This second arm is known as the "dark arm" because at $\tau_1 = 0$ fs delay, the E_{TT} and E_{RR} beams destructively interfere to approximately zero intensity. This arises because the first reflection in the E_{RR} line is at an interface where the beam travels from low to high refractive index and induces a π phase shift, unlike the second reflection. In the other arm, E_{RT} and E_{TR} carry the same π phase factor from one reflection each. Despite the phase difference in the two arms, they both record the same spectral information.

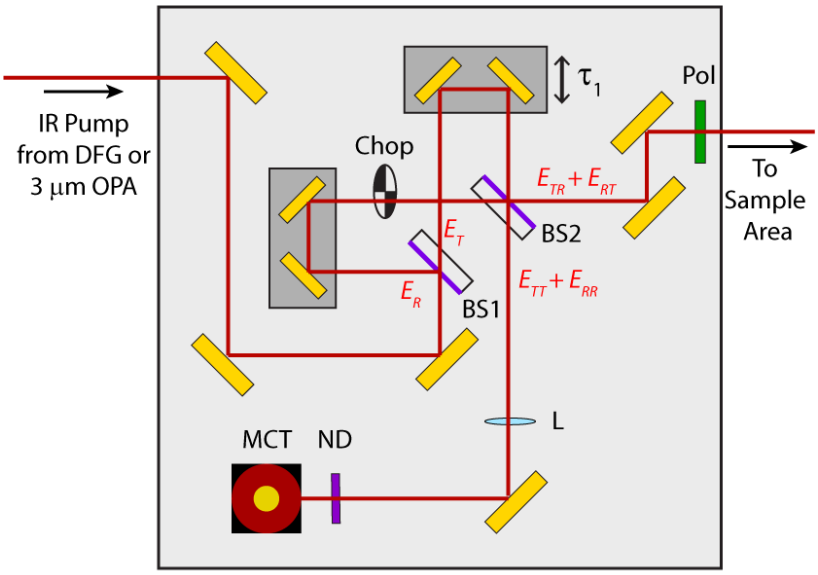

Figure 3.3: Schematic of the Mach-Zehnder interferometer. BS1 and BS2: beamsplitters 1 and 2. Chop: optical chopper. L: f = 150 mm KBr focusing lens. ND: neutral density filters. MCT: liquid-N_2 cooled or room temperature HgCdTe single-channel photodetector. Pol: wire grid polarizer. E_R/ E_T: electric fields of reflected/transmitted beams after BS1. E_{TR}/ E_{RT}/ E_{TT}/ E_{RR}: electric fields of recombined beams labeled by transmission through or reflection off of BS1 followed by transmission through or reflection off of BS2, respectively.

An interferogram of a typical 6 μm pulse is shown in Fig. 3.4a. The interferogram displays oscillating intensity as a function of pump delay τ_1 at an optical period of the center frequency (~20 fs here) and an envelope with a width that is inversely related to the bandwidth of the spectrum. At $\tau_1 = 0$ fs, the interference is at its extreme because all frequency components interfere together constructively. As τ_1 increases, the various frequencies oscillate with their own periods

and their interferences cancel each other out. For times far from $\tau_1 = 0$ fs, the intensity offset reflects the total intensity of two non-interfering beams. We collect asymmetric interferograms where the absolute values of the first and last waiting times differ (here, τ_1 = -300 to 500 fs), which allows us to capture the spectral information in the oscillating regions of the interferogram and reduce time collecting data in regions with low information content.

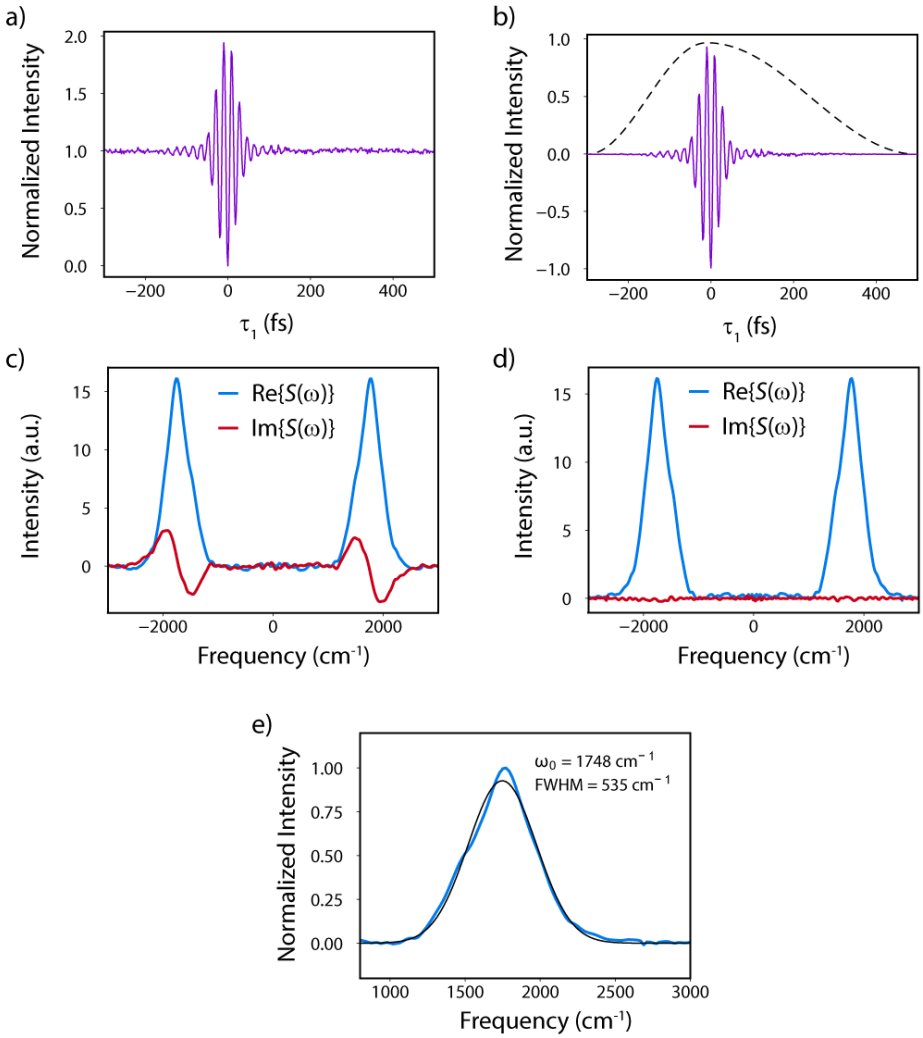

Figure 3.4: Procedure for processing an interferogram to generate a pump spectrum. (a) Raw interferogram from the MZI dark arm. (b) Windowed interferogram (purple) and the accompanying window function (dashed black). (c) The Fourier transform of the windowed interferogram with real (blue) and imaginary (red) frequency components. (d) Fourier transform of the pump spectrum after the Mertz correction, leaving only noise in the imaginary spectrum. (e) The resulting spectrum (blue) and Gaussian fit (black).

To process this interferogram, multiple steps are performed before Fourier transformation to accurately retrieve the pump spectrum. First, the constant background is subtracted and a window is applied to the interferogram (Fig. 3.4b). Multiplication by a window function reduces noise at the wings and prevents a sudden jump between the first and last points during Fourier transformation, which can introduce artificial oscillations in the spectrum. Because we sample the interferogram asymmetrically across τ_1, we use a modified asymmetric Hanning window, which takes the form:

$$\begin{cases} \frac{1}{2}\left[\cos\left(\frac{\pi\tau_1}{\tau_{max}}\right)+1\right] & \text{if } \tau_1 \geq 0 \\ \frac{1}{2}\left[\cos\left(\frac{\pi\tau_1}{|\tau_{\min}|}\right)+1\right] & \text{if } \tau_1 < 0 \end{cases} \tag{3.3}$$

As can be seen in Fig. 3.4b, the wings of the interferogram smoothly go to zero without noticeable distortion of the envelope. The Hanning window can be further modified by applying an exponent α if necessary, where $\alpha < 1$ generates a less aggressive window, whereas $\alpha > 1$ is more aggressive. An overly aggressive window function will compress the envelope of the interferogram and artificially broaden the spectrum, so care must be taken when choosing a window.

The interferogram is then Fourier transformed, which can produce a complex-valued spectrum (Fig. 3.4c). An ideal interferogram is an even function of τ_1, which means that the Fourier transform should be entirely real. Inspection of Fig. 3.4a-b reveals that the sample interferogram is not symmetric about $\tau_1 = 0$ fs, leading to an imaginary component to the spectrum. This arises from slight misalignments in the interferometer, asymmetry in the arms, or drifts in τ_1, but can be accounted for using the Mertz correction.[10] The phase error ϕ can be computed numerically as:

$$\varphi(\omega_1) = \tan^{-1}\left(\frac{\mathrm{Im}\{S(\omega_1)\}}{\mathrm{Re}\{S(\omega_1)\}}\right), \tag{3.4}$$

where $S(\omega_1)$ is the pump spectrum. This phase is then corrected for by multiplication of the complex spectrum by $\exp[-\varphi(\omega_1)]$, which can be viewed as a rotation of $S(\omega_1)$ onto the real axis. Fig 3.4d shows the spectrum after the Mertz correction, which no longer contains imaginary signal. In practice, we compute the phase over the reduced interval $-|\tau_{min}| \leq \tau_1 \leq |\tau_{min}|$, which is lower resolution than sampling evenly out to $\pm\tau_{max}$ on both sides of the interferogram. However, assuming continuity of the phase over the bandwidth of the spectrum, we interpolate the low-resolution phase onto the full frequency axis. The low-resolution approach begins to fail if τ_1 is not sampled far enough in negative time, and imaginary components persist in the spectrum even after applying the Mertz correction. We have found that for our purposes, sampling out to τ_{min} = -300 fs is sufficient, but artifacts emerge when $\tau_{min} \geq$ -200 fs.

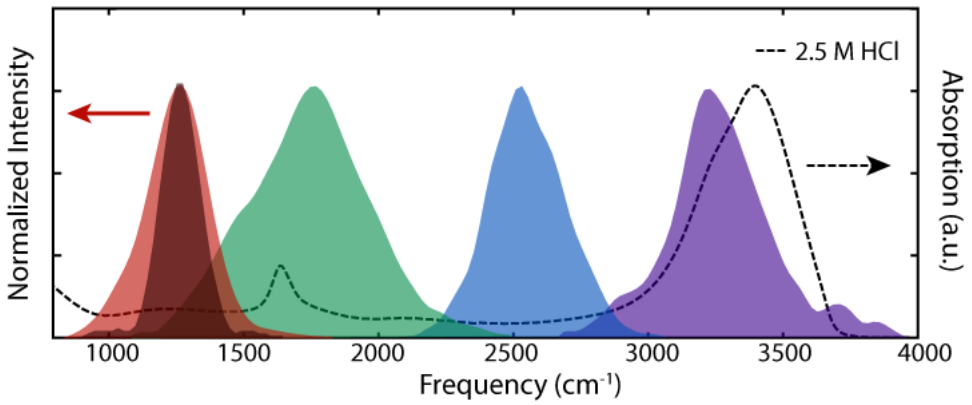

Figure 3.5: Spectra of the OPA/DFG pump pulses. The absorption spectrum of 2.5 M HCl (dotted black line) is included for comparison.

The spectra of the pulses used in our experiments are shown in Fig. 3.5, each centered at features of interest for the aqueous proton. Typical bandwidths and pulse energies in the different regions are included in Table 3.1. Even though spectra at four center frequencies are shown, we

can tune to any center frequency between 1250 and 3400 cm^{-1}. The lowest-frequency region shows the two spectra arising from DFG in AGS (narrower) and GaSe (broader) because data using both pulses will be shown in Chapter 5. For the other three pulses, the bandwidths exceed 300 cm^{-1} FWHM, the broadest being 530 cm^{-1} FWHM. According to the Fourier transform limit for Gaussian pulses, a spectrum with 300 cm^{-1} FWHM bandwidth can support pulses as short as τ_p = 49 fs, which decreases further with increasing bandwidth. However, the Fourier limit is insufficient for knowing the pulse width and only provides a lower bound. To characterize the temporal profile of our pulses, we turn to interferometric autocorrelation.

Table 3.1: Summary of Spectral and Temporal Characteristics of Mid-IR Pump Pulses

Center Freq. (cm^{-1})	**FWHM (cm^{-1})**	**Pulse Energy (μJ)**	**Pulsewidth w/o Window (fs)**	**Sample Window**	**Additional Material**
3260	400	4	45	1mm CaF_2	3mm CaF_2*
2550	340	9	57	1mm CaF_2	6mm CaF_2
1750	530	7	50	0.2mm CaF_2	-
1250 ($AgGaS_2$)	180	2	100	0.2mm CaF_2/ 0.4mm Diamond	-
1260 (GaSe)	280	10	67	0.2mm CaF_2/ 0.4mm Diamond	1mm Ge

* taken with 3 mm CaF_2 beamsplitters and CaF_2 polarizer in MZI

3.3.5 Temporal Characterization of mid-IR Pump Pulses with Interferometric Autocorrelation

For the best temporal resolution and maximum amplitude of nonlinear signal in our experiments, it is important to attain the shortest possible pulses. We measure their temporal pulse

widths with interferometric autocorrelation. This technique is used to extract the intensity autocorrelation profile of a pulse using a collinear geometry.[11] A great presentation of various temporal characterization techniques is provided in Ref. 11, but an introduction to interferometric autocorrelation is presented here. In this measurement, two collinear copies of a pulse of interest are focused in a nonlinear medium to generate SHG, and the SHG intensity is scanned as a function of pulse pair delay τ_1. The fundamental is filtered out with a polarizer and/or an IR-absorbing material serving as a short-pass filter. For 6-8 μm pulses, 1-2 mm of silica are sufficient, but 5-6 mm of silica is needed to effectively filter 4 μm beams. For detection, we focus the SHG on a single-channel liquid nitrogen cooled HgCdTe photodetector (IR Associates *MCT-13-0.5*). In the measurement, τ_1 is stepped evenly between -500 fs and 500 fs below the Nyquist frequency of the second harmonic, typically in steps of 2 fs. The result is an oscillating SHG signal peaked at $\tau_1 = 0$ fs (Fig. 3.6a). In contrast to a pulse's interferogram envelope (Fig. 2.4a), the envelope of the interferometric autocorrelation is not symmetric across the baseline. Instead, at $\tau_1 = 0$ fs, the interferometric autocorrelation is eight times as intense as the baseline. This 8:1 ratio is a signature of the nonlinear process, and ratios less than 8:1 may indicate sub-optimal phase matching or residual transmission of the fundamental.

The asymmetric interferometric pattern arises from the superposition of SHG signals that oscillate with the optical period of the fundamental (20 fs here) and the second harmonic (10 fs) frequencies. Fourier transformation (Fig. 3.6b) separates these from the zero-frequency component. For a Gaussian pulse with linear chirp, the fundamental and second harmonic features can be distorted. However, the zero-frequency component is the Fourier transform of the intensity autocorrelation, which accurately reports on the temporal width of a Gaussian pulse. Applying a low-pass filter and inverse Fourier transforming, the intensity autocorrelation is recovered

(Fig. 3.6c). The intensity autocorrelation reports on the convolution between the two copies of the pulse. For an intensity autocorrelation with FWHM width τ_{auto} and a Gaussian pulse with FWHM width τ_p, $\tau_{auto} = \sqrt{2}\tau_p$.

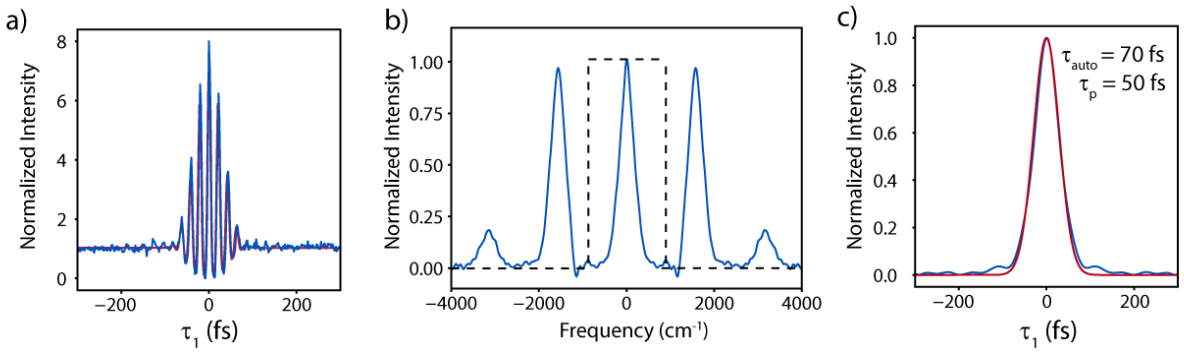

Figure 3.6: An example interferometric autocorrelation of a 6 μm pulse. (a) Raw measured interferometric autocorrelation (blue) and fit (red) for a Gaussian pulse with linear chirp. (b) Fourier transformation of the raw data (blue) and low-frequency spectral window (dashed black) for isolating the zero-frequency component. (c) Inverse Fourier Transform of the zero-frequency component produces the intensity autocorrelation (blue) with Gaussian (red).

Typical interferometric autocorrelations and extracted intensity autocorrelations for pulses generated by OPA/DFG are presented in Fig. 3.7. Both of the 8 μm pulses are somewhat longer than those at higher frequencies, but the 8 μm pulse generated in GaSe (Fig. 3.7b,f) is the shorter of the two. With an optical period of 27 fs at 8 μm, a pulse width of 67 fs corresponds to a 2.5-cycle pulse. Similarly, at 6 μm we can produce 50 fs, 2.5-cycle pulses. Some of these pulses require material to compensate for dispersion from certain transmissive optics, which are included in Table 3.1. The autocorrelations presented here are without transmission through the sample window. The most appropriate window materials are shown in Table 3.1, each of which increase the pulse widths by no more than 10%. For pulse frequencies below 2000 cm^{-1}, we found that using 0.2 mm thick CaF_2 windows (Crystran) was a sufficient trade-off between ease of use and reduction of dispersion. For 8 μm pulses, polycrystalline CVD-deposited diamond windows

(Diamond Materials) are not dispersive, but suffer from high reflective losses and some scatter due to microscopic graphite granules, adding new challenges to data collection. At these low frequencies, it may be feasible to compensate for the dispersion from 0.2 mm CaF_2 sample windows with Ge or Si, but previous attempts were not effective, likely due to effects from third-order dispersion.

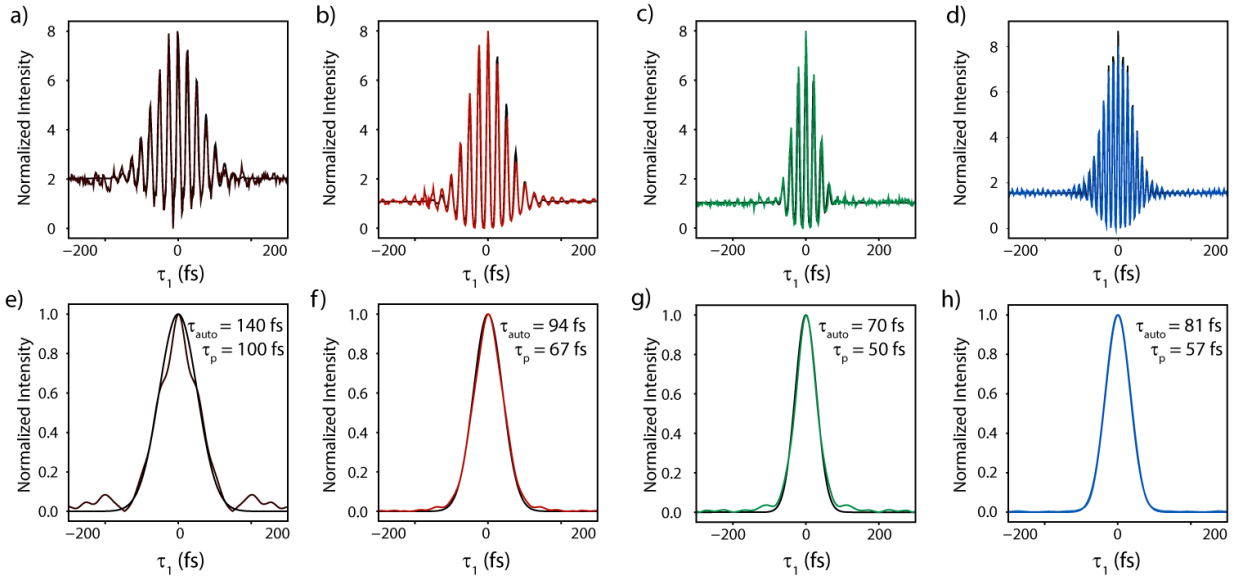

Figure 3.7: Interferometric autocorrelations of the (a) 8 μm pulses generated by DFG in $AgGaS_2$ and (b) 8 μm pulses generated by DFG in GaSe, (c) 6 μm pulses, and (d) 4 μm pulses. (e)-(h) Extracted intensity autocorrelations and measured pulse widths for the respective pulses.

3.4 Generation and Characterization of Broadband Mid-IR Probe Pulses

The success of our 2D IR measurements depends on the ability to generate a coherent, ultrafast broadband IR (BBIR) probe pulse (Fig. 3.8). Because the details have been presented elsewhere,[2] I will summarize the main aspects here and include updated experimental details. After compression, 1.7 W of P-polarized 800 nm light is guided into the setup and retroreflected on a computer-controlled motorized stage (Aerotech *ANT-95L*) to control the pump-probe waiting time τ_2. The beam transmits through 0.2 mm of BBO cut at $\theta = 29.2°$ for collinear SHG generation of

S-polarized 400 nm. The collinear 800 nm and 400 nm beams are then transmitted through a 2 mm thick BBO crystal cut at 66° to adjust the timing between the two pulses at the nitrogen filament. Next, a λ/2 waveplate for 800 nm rotates the fundamental to S-polarization for type I SFG in 0.1 mm BBO cut at 44.6°, which generates S-polarized 267 nm light.

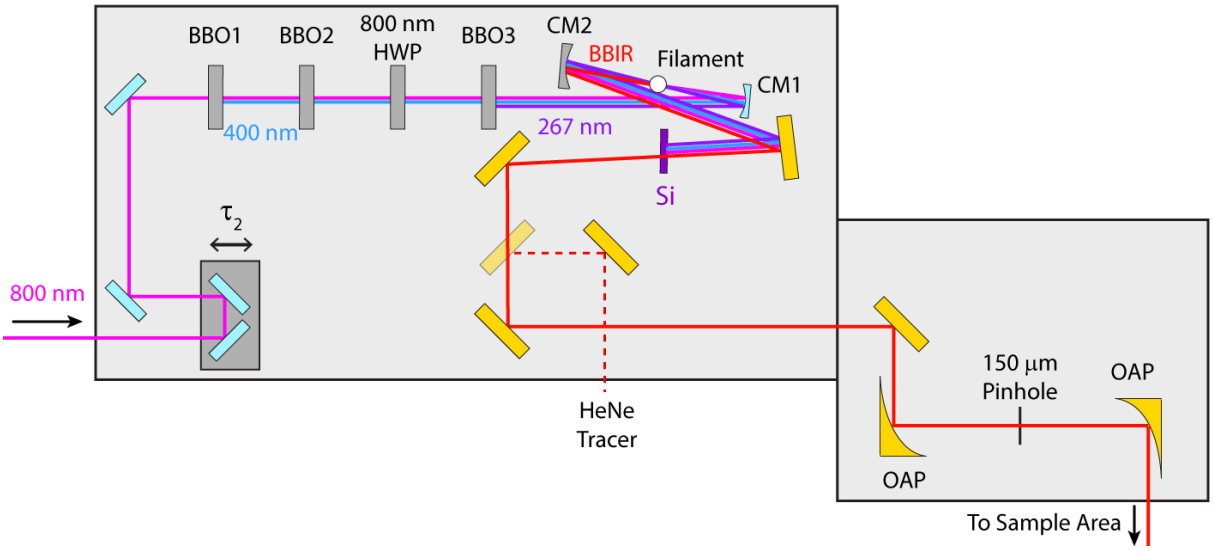

Figure 3.8: Diagram of the broadband IR generation source. BBO1: First BBO crystal (0.2 mm, $\theta = 29.2°$) for doubling 800 nm. BBO2: Second BBO crystal (2 mm, $\theta = 66°$) for delay compensation. HWP: λ/2 waveplate for rotating 800 nm polarization. BBO3: Third BBO crystal (0.1 mm, $\theta = 44.6°$) for 267 nm generation. CM1: f = 10 mm focusing curved mirror with high-reflective coating for 800, 400, and 267 nm (Layertec). CM2: f = 10 mm bare silver collimating mirror. Si: 0.4 mm silicon wafer. OAP: 90° off-axis parabolic mirror with 101.6 mm effective focal length.

The 800 nm and its two harmonics are then focused into a gentle stream of nitrogen, which generates a plasma that radiates P-polarized light with frequencies spanning from the THz to the visible. The IR beam is collimated on a silver curved mirror and isolated by transmitting through a 0.4 mm wafer of silicon. We select for a component that is polarized at 45° from vertical by mounting the silicon at 45° and then rotating to Brewster's angle (78° in the mid-IR). In practice, the beam is about 55° from vertical with an approximately 20:1 polarization purity in intensity. The mid-IR is too weak to measure on a thermal power head, but we estimate with a liquid N_2

cooled MCT detector (IR Associates, *MCT-13-0.5*) that the pulse energy is about 10 nJ with approximately 3-5% stability and a slow power drift that oscillates on the order of one minute. The slow drift is Fourier filtered out of 2D experiments, but contributes to noise in TA experiments particularly when signal is less than 1 mOD. The spatial mode of the beam is non-Gaussian, so we filter the spatial mode with a 150 μm pinhole at the focus of a bare gold off-axis parabolic mirror with effective focal length of 101.6 mm. The beam is recollimated on a matching off-axis parabolic mirror to a $1/e^2$ diameter of approximately 9 mm. To guide the BBIR beam, we spatially overlap it with a red diode laser. To limit transmission through material and therefore dispersion of the BBIR, we have placed a flipper mirror in the BBIR beam path for the diode laser to trace the BBIR beam path. While not ideal, it has proved to be sufficient for our alignment procedures.

The spectrum of the BBIR light source is shown in Fig. 3.9, measured with a Mach-Zehnder interferometer in the probe line. The spectrum is peaked at approximately 1800 cm^{-1} with a long tail to high frequencies. In practice, adjustment of the BBO crystals and the location of the spatial filter can be used to maximize throughput in a desired frequency region. Adjustment of the spectral shaper after the oscillator can optimize the power uniformly across the frequency range. In the region between 1000-1200 cm^{-1}, many IR materials absorb, and this is seen in the intensity drop-off from using a CaF_2 lens to focus onto the detector. We have found that lenses made with ZnSe, KBr, and BaF_2 are more appropriate for these low frequencies, revealing that there is substantial broadband light generated below 1000 cm^{-1}. We avoid this problem before the detection array by focusing with a bare gold off-axis parabolic mirror. Like in the pump lines, we replaced all other mirrors with bare gold to reduce absorption by the silica protective coating. Near the BBIR generation plasma, this results in corrosion over time, so the closest two bare metal mirrors are replaced once or twice a year.

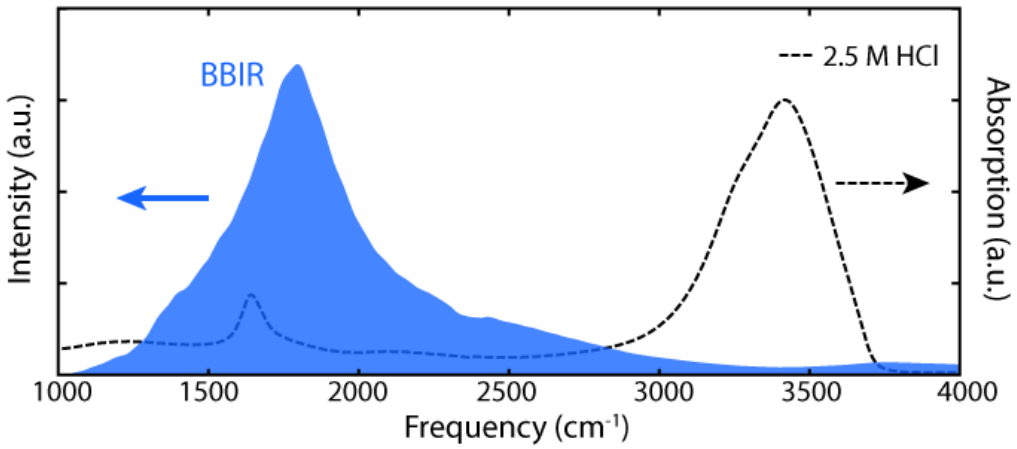

Figure 3.9: Spectrum of the broadband IR source. The IR absorption spectrum of 2.5 M HCl is shown for comparison.

To characterize the temporal properties of the BBIR, we measure a FROG cross-correlation in a 0.4 mm wafer of Si at the sample area, with the mid-IR pump as a reference pulse. To prevent multi-photon absorption, we attenuate the pump until the transient response only occurs during pulse overlap. The non-resonant response in Si with the GaSe-generated 8 μm pump is presented in Fig. 3.10 with different amounts of material in the pump and probe beams. With no material, the response looks essentially vertical, indicating that all frequencies arrive at the sample within the same 100 fs interval. Introduction of 0.2 mm CaF_2 introduces some dispersion between 1000-1200 cm^{-1}, making the nonresonant response somewhat U-shaped. This is exacerbated further with 1 mm CaF_2 windows, and pulse arrivals vary over 500 fs. Thin CaF_2 windows ensure sufficiently narrow instrument response for our 2D IR measurements. When data is presented, τ_2 = 100 fs or 150 fs will represent the earliest measurable waiting time.

There are many challenges associated with the BBIR beam due to its nonstandard generation mechanism and broad spectrum. Continuum THz and mid-IR generation has been attributed to optical rectification in the plasma medium,[12,13] which is consistent with its high

sensitivity on 800 nm bandwidth and pulse width. Spatial chirp is observed, which may arise from the distribution of wavevector combinations introduced with focusing. As a result, the various frequencies in the BBIR would be phase matched at different angles, resulting in spatial chirp. Interestingly, the BBIR generated with gentle focusing displays a ring-like spatial mode,[13–15] but is less apparent in our experiment perhaps due to the tighter focusing. We have also found that residual visible pulse energy induces transient absorption in silicon, which enables intraband IR absorption in the conduction band and introduces a hole in the IR spatial mode. A broadband reflective alternative to the Si wafer such as indium tin oxide (ITO) would improve the throughput of the broadband, assuming high reflective efficiency across the whole spectrum. Finally, it is worth stating that an exciting development is underway for amplifying the BBIR probe with OPA in GaSe to generate a broadband IR pump for nonlinear experiments. We have achieved greater than 10 μJ pulse energy, corresponding to 1000× amplification, but further optimization, characterization, and resolution of spatial chirp issues are necessary for it to be incorporated into experiments.

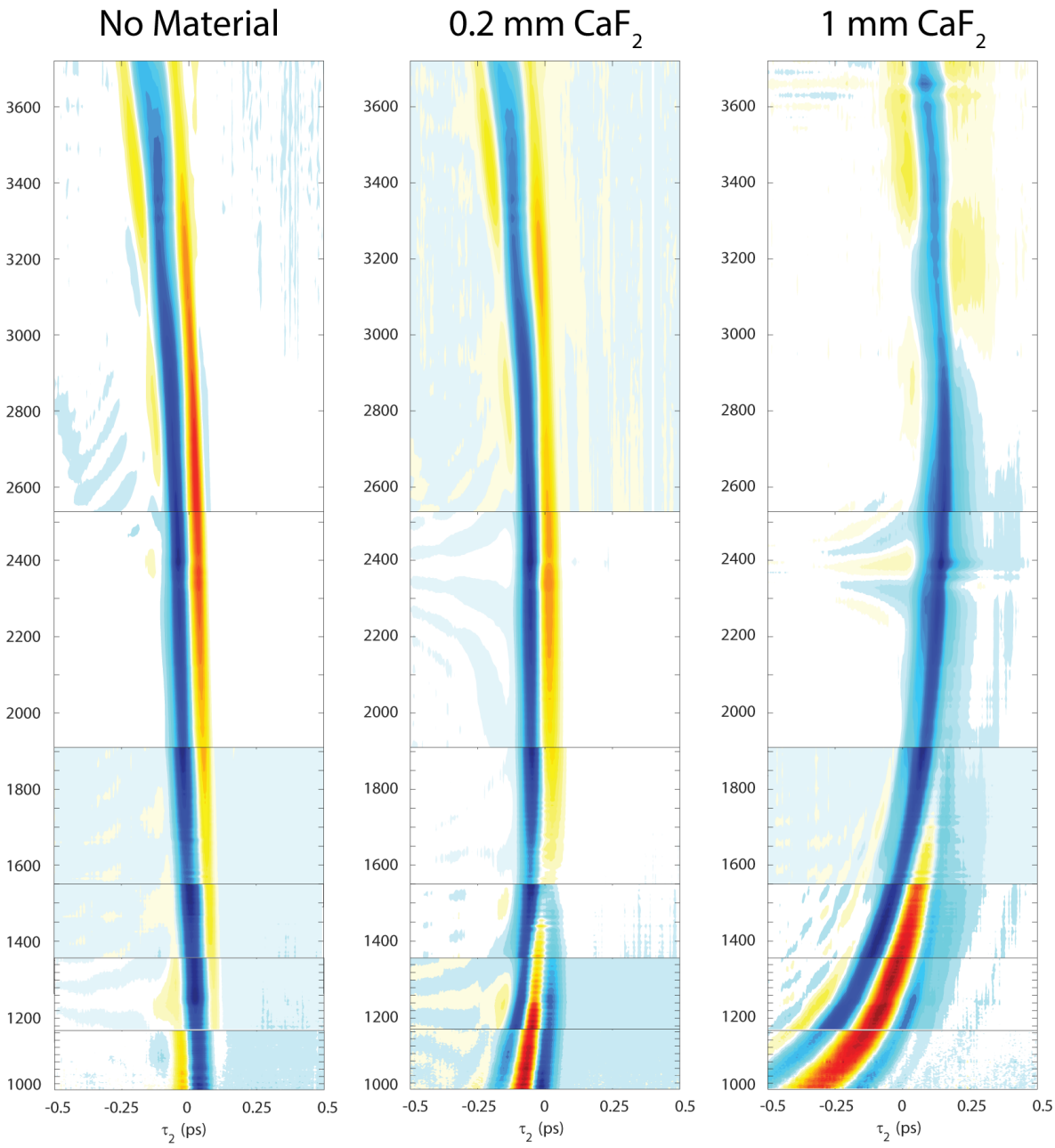

Figure 3.10: Silicon FROG cross-correlation traces with 8 μm pump pulses (a) with no material (b) 200 μm thick CaF_2 sample windows, and (c) 1 mm CaF_2 windows.

3.5 Spatial and Temporal Arrangement of Pulses for Nonlinear Spectroscopy

We conduct TA and 2D IR experiments in the pump-probe geometry, which comes with certain benefits and drawbacks. The biggest benefit is the simplicity of alignment: only the pump and probe beams need to cross at the sample. Additionally, both of the rephasing and nonrephasing nonlinear signals are phase matched collinear to the probe and are collected together. As a result, the nonlinear signal is always collected as transient absorption surfaces without the "phase twists" inherent to rephasing and nonrephasing surfaces. Additionally, the signal is self-heterodyned with the probe, removing the need to align and time up an external local oscillator. Heterodyning with the probe is convenient, but for us the 3-5% stability of the BBIR probe background contributes to noise in the transient signal.

At the sample area, the pump and probe beams are parallel and displaced 25 mm apart before focusing at the sample with a bare gold 90° off-axis parabolic mirror (effective focal length of 101.6 mm). About 30% of the pump power from the DFG (Table 3.1) makes it to the sample at $\tau_1 = 0$ with the chopper open. The spatial profile of the pump at the focus has not been rigorously imaged, but approximately 30% of the intensity transmits through a 100 μm pinhole at the focus, suggesting a $1/e^2$ beam waist diameter of 230 μm. The pump and probe beams are then recollimated on a matched parabolic mirror. The pump beam is blocked after the parabolic mirror, whereas the probe is guided to the detection area. We also have placed an iris centered and closed down on the probe beam to block any pump scatter off of the sample.

The setting $\tau_2 = 0$ fs between the pump and probe beams slightly differs depending on the pump source. When the pump comes from the 3 μm OPA, the pathlengths of the pump and probe beams are approximately 2 m from the regenerative amplifier to the sample, and the two beams are phase stable with respect to each other. As a result, it is straightforward to time them up with

the interference between the probe and the pump scattered off of a 100 μm pinhole at the sample position. However, when the pump is from the OPA/DFG line, the pathlengths increase by another 3 m in both lines, and the pump and probe are no longer phase stable. As a result, scanning τ_2 on pinhole scatter generates a flat line when shots are averaged (typically over 250 shots per time point). Instead, we collect the minimum and maximum scatter intensities summed over elements on the detector array for each τ_2, which recovers a temporal envelope reflecting the bandwidth of frequencies on the array. The maximum of the envelope is set to $\tau_2 = 0$ fs with approximately 5 fs resolution.

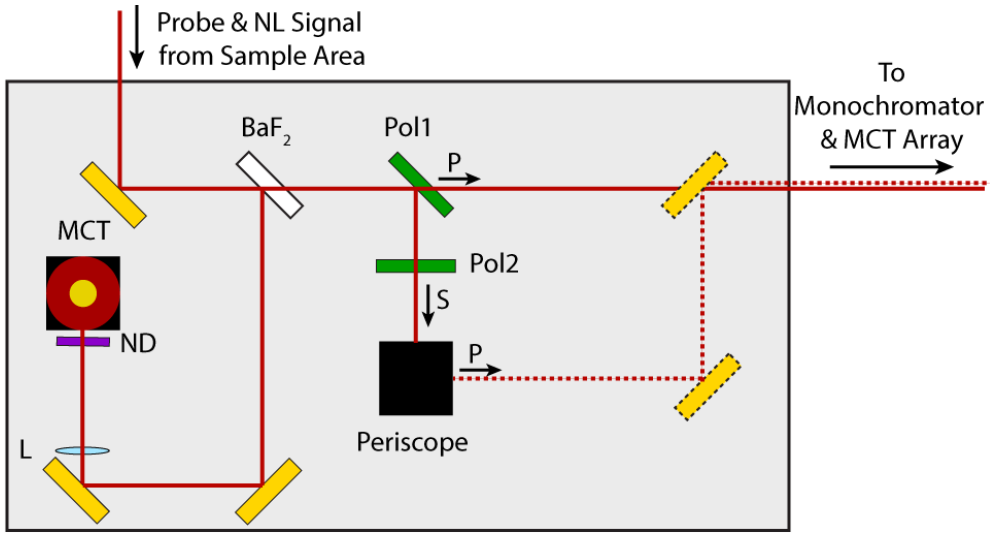

Figure 3.11: Diagram of the probe reference beam path and polarization-resolved detection lines. MCT: HgCdTe single-channel probe reference detector. ND: neutral density filter. L: 100 mm KBr lens. Pol1: CaF_2 wire grid polarizer set to transmit P polarization. Pol2: CaF_2 or ZnSe wire grid analyzing polarizer set to transmit S-polarized light. Dotted beam and mirrors are vertically displaced 25 mm from the original line.

After leaving the sample area, the probe beam is guided to a detection line designed to reference for shot-to-shot probe beam intensity fluctuations (Fig. 3.11). A reflection off of a BaF_2 window is guided to a single-channel, liquid nitrogen cooled MCT photodetector (IR Associates, *MCT-13-0.5*), which is used as a reference of the probe intensity fluctuations (described below in

Section 3.6). Ideally, the probe intensity fluctuations would be measured as a function of frequency without transmitting through the sample, but the vast majority of the fluctuations are frequency-independent and the change in transmission in our samples is less than .1%, which is a negligible contribution to the magnitude of the frequency-integrated intensity fluctuations.

The probe is then split into S- and P-polarization components with a CaF_2 wire grid polarizer (Specac) set to transmit P and reflect S polarization. This is used to simultaneously collect the ZZZZ and ZZYY response for TA and 2D anisotropy measurements, which reduces artifacts from carrying out two separate experiments. A wire grid analyzing polarizer set to transmit vertical polarization is placed in the reflected arm, and the polarization of the vertical arm is rotated to horizontal with a 90° off-axis periscope to assure matched grating diffraction efficiency for both arms in the monochromator. The two beams propagate parallel to each other, displaced vertically by 25 mm, and sent to a 45° off-axis parabolic mirror with 150 mm effective focal length, focused on a slit at the entrance of the monochromator.

3.6 Detection of Nonlinear Signal

The two probe beams are dispersed in a monochromator for detection in the frequency domain (ω_3) by a dual-stripe 2×64 element MCT array (IR Associates *MCT-9-128*). The monochromator disperses frequencies with one of three diffraction gratings blazed for 6000 nm light with 75-300 grooves/mm. If the ω_3 region of interest is less than 2000 cm^{-1}, a long-pass filter is placed in front of the entrance slit to prevent spatial overlap of second order diffraction of probe frequencies between 2000 and 4000 cm^{-1}. We typically use the least dispersive grating because of the broad lineshapes of aqueous features. With this grating, the ω_3 resolution is 1-2 cm^{-1} near 1000 cm^{-1}, 3-4 cm^{-1} around 1600 cm^{-1}, 13-14 cm^{-1} at 2500 cm^{-1}, up to 38 cm^{-1} at 3400 cm^{-1}, which

varies so dramatically since diffraction angle is linear with wavelength instead of frequency. To calibrate the frequency positions of each element on the array, we scatter pump light off of a 100 μm pinhole to put pump light on the probe line, scan between τ_1 = -2 ps to 2 ps and Fourier transform the interferogram on each element.

The optical signals are recorded and processed electronically with a multi-channel boxcar integrator (IR Systems *FPAS 0144*), which collects 0-5 V analog signals from the MCT array and 16 external channels. The duty cycle for detection is approximately 0.001 from the ~1 μs excited state lifetime of the MCT in the photodetector and 1 ms spacing between pulses. The boxcar integrator collects analog voltage from an approximately 0.8 μs time window on each element, synced to the Q-switch trigger. This optimizes the signal-to-noise ratio by integrating over signal and excluding detector electrical noise during the other 99.9% of the cycle. This voltage is converted to digital signal with a 16-bit analog-to-digital converter for on-the-fly processing in LabVIEW and data storage on the lab PC. For instance, referenced transient absorption is calculated for each shot according to the following expression:

$$\Delta A(\omega_3) = -\log\left[\frac{S_i(\omega_3)}{R_i}\cdot\frac{R_{i+1}}{S_{i+1}(\omega_3)}\right]. \tag{3.5}$$

S_i and R_i refer to the intensities of the transmitted probe and reference pulses for a given shot i (i+1), where each even (odd) shot was measured with the pump chopper open (closed). For a given time point, ΔA is averaged over 250-1000 shots, depending on the amplitude of the TA signal.

On the detector array, the top and bottom rows of pixels measure signal from the P- and S-polarized probe lines, respectively (Fig. 3.12). For an S-polarized pump, this corresponds to the perpendicular (ZZYY) and parallel (ZZZZ) third-order responses, respectively, and is reversed when the pump is P-polarized. Fig 3.12a demonstrates that the P-polarized arm is much more

intense than the S-arm at low frequencies, probably due to incomplete filtering of the BBIR polarization to 45° from horizontal, losses due to poor reflection off of the CaF_2 beamsplitting polarizer, and transmissive losses through the analyzer. Transient absorption values are not impacted by this difference since absorption by definition is referenced to the amount of transmitted light, but the low light of the S-polarized arm results in poorer signal-to-noise. The low amount of transmitted light is exacerbated by the continuous linear absorption of aqueous strong acid solutions, attenuating transmission by almost an order of magnitude (Fig. 3.12b). For ~1 mOD transient absorption features, we have found that at least 1000 counts of linear transmission are necessary for high-quality data. Below this, the few counts of electrical noise from the detector pushes the signal-to-noise ratio to < 1. Broadband IR transmission could be further improved in the S-polarized arm by substituting the beamsplitting polarizers to ones on BaF_2 substrate, since CaF_2 absorbs below 1200 cm^{-1}, and ZnSe suffers from high reflective losses.

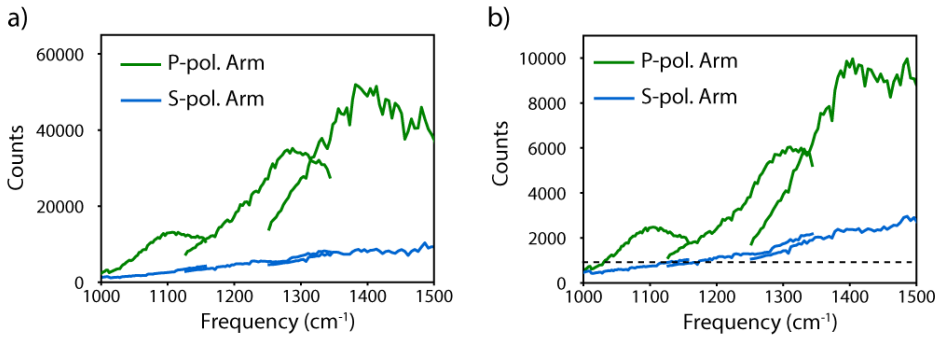

Figure 3.12: Polarization-resolved detection of BBIR probe at low frequencies. (a) Detection of the S and P-polarized arms without sample. (b) Linear transmission of BBIR through 3.6μm of 2M HCl. The horizontal dashed line at 1000 counts represents the minimum amount of transmitted light needed for signal-to-noise > 1. Note the different scales between panels.

3.7 Processing TA and 2D IR Data

In a TA spectrum, transient absorption dispersed in ω_3 is stepped over waiting time τ_2, typically out to $\tau_2 \geq 5$ ps. For the low-amplitude transient absorptions in this thesis ($\Delta A \approx 1$-

6 mOD), 50,000 shots per τ_2 point are averaged, requiring about 2 hours for a TA surface collected at a single grating position. For weaker features such the transient absorption spectrum of the proton stretch vibration ($\Delta A < 0.5$ mOD at $\tau_2 = 150$ fs), more than 2×10^5 shots are averaged per time point. The polarization-separated detection lines enable simultaneous measurement of ZZZZ and ZZYY TA surfaces. To ensure the rows are properly balanced, we compare a known isotropic transient signal (such as the H_2O hot ground state at $\tau_2 = 20$ ps) on the ZZZZ and ZZYY stripes to ensure that they are equal in amplitude and frequency alignment. From these two stripes, we calculate the isotropic (ZZZZ + 2×ZZYY) and anisotropic (ZZZZ – ZZYY) TA surfaces, as well as the TA anisotropy r = (ZZZZ – ZZYY)/(ZZZZ + 2×ZZYY).

Figure 3.13 shows sample TA spectra of the O-D stretch for 2% HOD in H_2O using the 2500 cm^{-1} pump. The sample was held between two 1 mm thick CaF_2 windows with a 50 μm Teflon spacer. For these surfaces, 11,000 shots were average per τ_2 point, which took at total of 25 minutes. Figs. 3.13a and 3.13b show the TA spectra in the ZZZZ and ZZYY polarization geometries, respectively. The positive ground state bleach (GSB) is centered at 2500 cm^{-1}, while the excited state absorption (ESA) feature is negative and anharmonically shifted to approximately 2350 cm^{-1}. Figure 3.13c plots the TA traces at $\omega_3 = 2500$ cm^{-1} for both polarization geometries. At negative waiting times, the signal amplitude is close to zero, with weak oscillations due to a coherent effect known as perturbed free induction decay.[16] At $\tau_2 = 0$ fs, there is a rapid increase in signal followed by a ps-timescale decay. Within the 100 fs pulse overlap, there is a sharp dip in signal due to interfering nonresonant response from the CaF_2 windows. At $\tau_2 = 150$ fs, the ZZZZ trace is approximately three times more intense than the ZZYY trace, but they become approximately equal in amplitude at approximately $\tau_2 = 5$ ps. The orientational relaxation is plotted in Fig. 13d as polarization anisotropy r. At $\tau_2 = 150$ fs, $r = 0.28$ and decays towards zero on a

3.5 ps timescale, which is in agreement with the 3.0 ps timescale measured previously,[17] within this dataset's uncertainty. The early-time value is less than the theoretical maximum of 0.4, which arises from a 50-fs librational orientational relaxation component. Finally, as the population of the excited state decays, the signal-to-noise of the anisotropy measurement decreases, which limits the time window for the measurement.

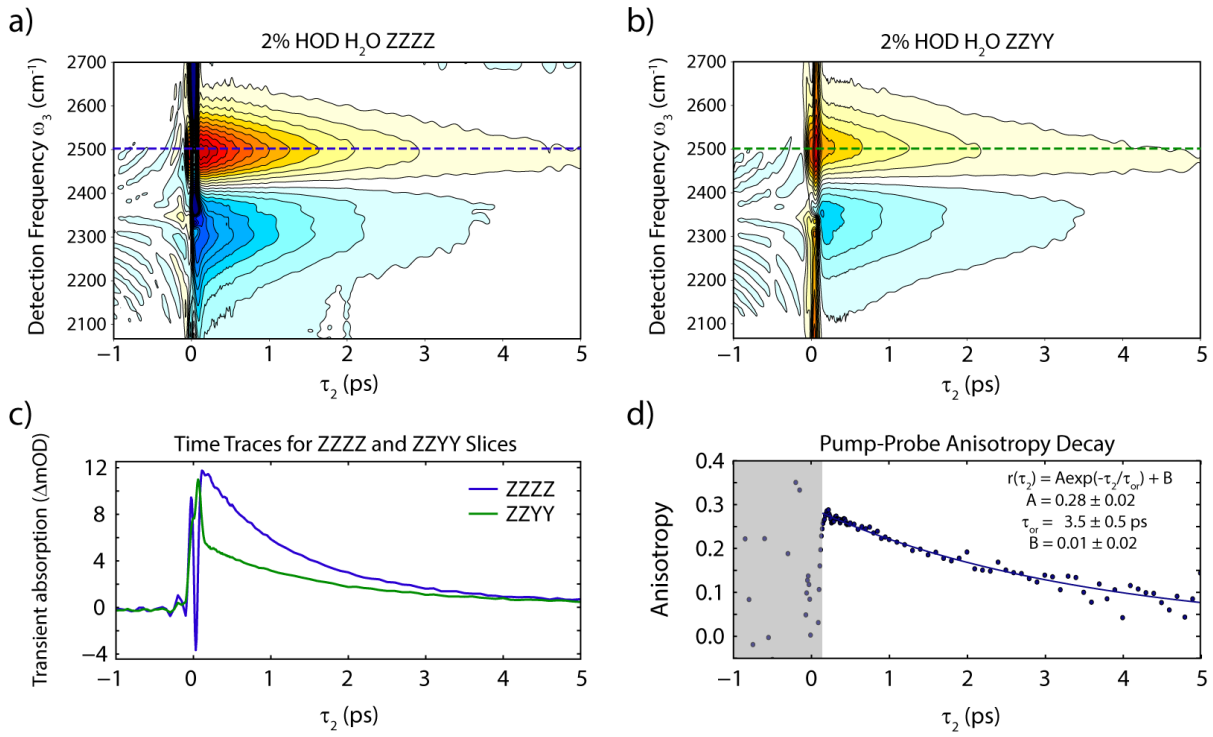

Figure 3.13: Sample experimental TA spectra of the O–D stretch of 2% HOD in H_2O with simultaneous polarization collection in the (a) ZZZZ and (b) ZZYY polarization geometries. (c) The TA time traces from both polarization geometries at ω_3 = 2500 cm^{-1}, corresponding to the dotted lines in (a) and (b). (d) The polarization anisotropy decay of the O–D stretch at 2500 cm^{-1}, fit to an exponential decay.

Acquiring reliable TA anisotropy decays requires much more attention to detail than collecting the TA surfaces alone. First, residual nonresonant response from sample windows contribute to the measured anisotropy at early waiting times out to 200 fs. If the windows are thick or if the molecular response is weak, the effect will be more noticeable. For the sample data shown

above, the response from 1 mm thick CaF_2 influences the data out to τ_2 = 150 fs, which is slightly beyond the 100 fs pulse overlap measured in silicon. For weaker signals ($\Delta A \approx 1$ mOD), anisotropy is only reliable beyond 200 fs. Using 0.2 mm CaF_2 sample windows is helpful for minimizing the window contribution. At late time, we have also seen artifacts due to misalignments between the two arms. This includes long-time non-zero anisotropy offsets, which can be as large as ± 0.1. We have found that careful frequency alignment of the two arms is necessary to remove this artifact.

To collect a 2D IR surface, ω_3-dispersed transient absorption is measured as a function of stepping the pump coherence delay τ_1 (Fig. 3.14a) at a fixed value of τ_2. The interference between the collinear pump pulses introduces an oscillating signal in the macroscopic polarization of the sample, known as the free induction decay (FID). The FID oscillates with the optical period of the central pump frequency, but its decay as a function of τ_1 reflects the lineshape of the molecular response, including contributions from dephasing, spectral diffusion, and population relaxation of the vibrational feature. To generate the 2D IR spectrum, we Fourier transform across τ_1 to generate the ω_1 frequency axis. The procedure for this Fourier transformation is closely related to the procedure for processing the pump spectrum (Section 3.3.4). First, the baseline from TA signal between the static arm and the probe is subtracted. We then apply an asymmetric Hanning window to the FID, which helps remove signal at negative τ_1 times from unwanted phase matching pathways. We Fourier transform and calculate the phase error from the pump interferogram, which is collected simultaneously with the 2D IR measurement. The pump Mertz correction is then applied to the 2D IR spectrum, and the real component of the 2D IR spectrum is kept for analysis. The 2D IR data are windowed in ω_1 by the pump spectrum, so spectral information at the wings of the spectrum are lost. Because the 2D IR signal is not strictly a convolution of pulses and the response function, it is not recommended to correct for the lineshape without full response

calculations. This technical limitation underscores the importance of developing a broadband pump pulse for measuring accurate 2D lineshapes.

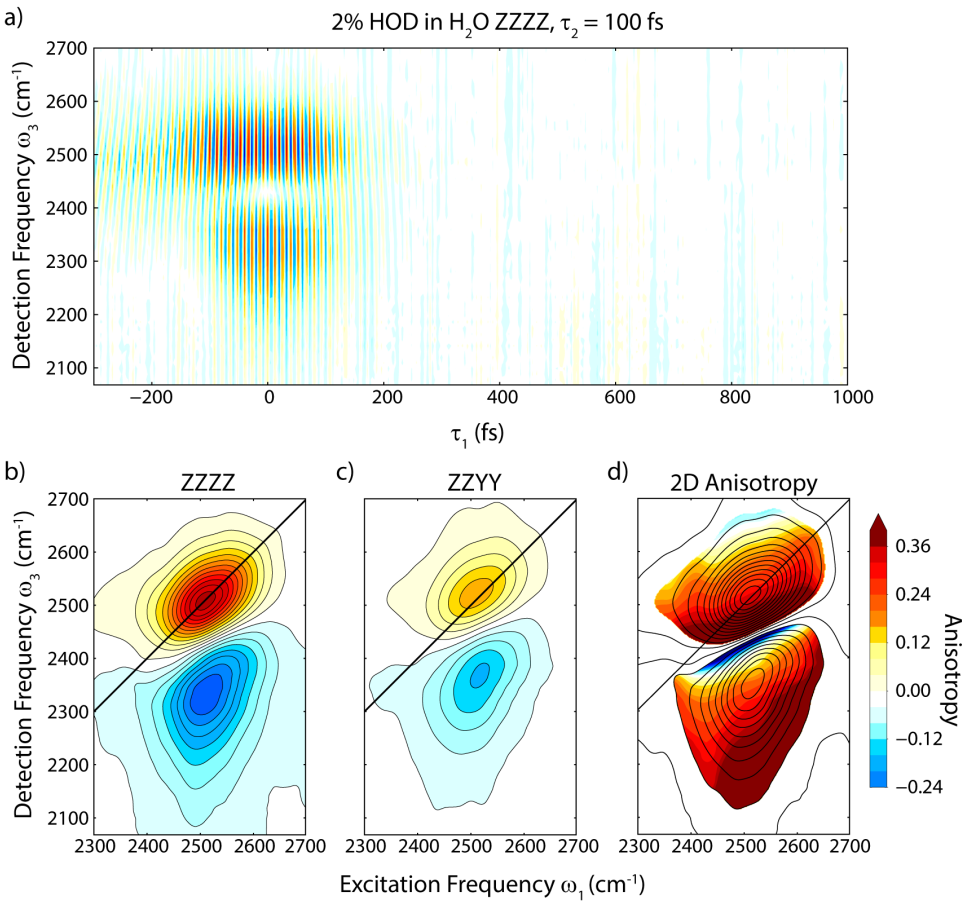

Figure 3.14: (a) A sample experimental 2D IR spectrum of the O-D stretch of 2% HOD in H_2O in the time-frequency domain. The (b) ZZZZ and (c) ZZYY 2D IR spectrum after processing. These surfaces are not corrected for the pump spectrum. (c) The 2D anisotropy surface generated from the ZZZZ and ZZYY spectra. Black contours in (c) are from the measured isotropic 2D IR surface, and anisotropy values are only shown in regions with at least 5% the absolute magnitude of the GSB peak value.

The ZZZZ and ZZYY 2D IR spectra of 2% HOD in H_2O are shown in Figs. 3.14b and 3.14c, respectively. For these spectra, τ_1 was scanned from -300 to 1000 fs in steps of 4 fs with 8000 shots averaged per time point, taking 25 minutes to collect. The GSB is on the diagonal at 2500 cm^{-1}, while the ESA is directly below it at (ω_1, ω_3) = (2500 cm^{-1}, 2350 cm^{-1}), which matches the peak frequency positions of the TA spectrum. By the projection slice theorem for

multidimensional spectroscopy, the projection of the 2D IR surface onto the ω_3 axis is equivalent to the TA spectrum at τ_2 = 100 fs. Like in the TA spectra, the ZZZZ 2D IR surface is approximately three times more intense than the ZZYY spectrum. The lineshape of the GSB is diagonally elongated, indicative of inhomogeneous broadening from a distribution of local environments, which can be quantified by various metrics such as center-line slope, nodal line slope, or phase line slope.[17,18]

Simultaneous polarization detection enables the straightforward collection of 2D anisotropy surfaces. The 2D polarization anisotropy $r(\omega_1, \omega_3)$ adds frequency correlation information to the orientational relaxation response. This can be used to measure the change in anisotropy values or kinetics with reduced spectral congestion. For HOD in H_2O, the 2D anisotropy surface (Fig. 3.14d) shows anisotropy values of around 0.3 near the peaks of the GSB and ESA, and the anisotropy surface is also diagonally elongated due to frequency correlations at early waiting time. Around the node, where there is interference between positive and negative signals, the anisotropy value becomes less reliable.

Collecting 2D IR spectra for broad, weak features ($\Delta A \approx 1$ mOD) requires time for stepping both τ_1 and τ_2, and collection on up to four grating settings. For one waiting time and one grating position, it takes approximately 2 hours to collect a 2D IR spectrum at 3×10^4 shots per τ_1 point. The collection time for weaker samples can be reduced by sampling up to the pump Nyquist frequency or employing an undersampling scheme. Additionally, for the broad features in water, the 16 fs ω_1 resolution by sampling out to τ_1 = 1000 fs is not necessary, and can be cut in half to reduce the collection time per average. For thin aqueous samples to last more than a couple hours before drying out, we have found that wrapping the window edges with parafilm and warming to 40°C provides a good seal, and samples can last reliably up to 48 hours.

3.8 Conclusion

This chapter demonstrates that many highly sophisticated instruments are necessary for the successful operation of a TA or 2D IR experiment. Not only must light be generated, but it must be appropriately characterized and carefully handled as it travels throughout the setup, eventually reaching the various detectors. The reward is the ability to directly measure excited state features, multidimensional lineshapes, and ultrafast population and orientational relaxation kinetics. All of these observables will be necessary for characterizing the spectroscopy of the aqueous proton and the kinetics associated with irreversible proton transfer. With the experimental details in place, I will first present a nonlinear spectroscopic study of the bending vibrations of H_2O. This background will more concretely provide context for the spectra collected for the aqueous proton.

3.9 References

(1) Fecko, C. J.; Loparo, J. J.; Tokmakoff, A. Generation of 45 Femtosecond Pulses at 3 μm with a $KNbO_3$ Optical Parametric Amplifier. *Opt. Commun.* **2004**, *241*, 521.

(2) Petersen, P. B.; Tokmakoff, A. Source for ultrafast continuum infrared and terahertz radiation. *Opt. Lett.* **2010**, *35*, 1962.

(3) Svelto, O. *Principles of Lasers*, 5th ed.; Hanna, D. C., Ed.; Springer: New York, NY, 2010.

(4) Moulton, P. F. Spectroscopic and Laser Characteristics of Ti:Al_2O_3 *J. Opt. Soc. Am. B* **1986**, *3*, 125.

(5) Treacy, E. B. Optical Pulse Compression with Diffraction Gratings *IEEE J. Quantum Electron.* **1969**, *5*, 454.

(6) Butcher, P. N.; Cotter, D. *The Elements of Nonlinear Optics*; Cambridge UP: Cambridge, 1990.

(7) Manzoni, C.; Cerullo, G. Design criteria for ultrafast optical parametric amplifiers *J. Opt.* **2016**, *18*, 103501.

(8) Bradler, M.; Baum, P.; Riedle, E. Femtosecond continuum generation in bulk laser host materials with sub-μJ pump pulses *Appl. Phys. B* **2009**, *97*, 561.

(9) SNLO nonlinear optics code available from A. V. Smith, AS-Photonics, Albuquerque, NM.

(10) Mertz, L. Auxiliary computation for Fourier spectrometry *Infrared Phys.* **1967**, *7*, 17.

(11) Diels, J.; Rudolph, W. *Ultrashort Laser Pulse Phenomena*; Academic Press: San Diego, 1996.

(12) Cook, D. J.; Hochstrasser, R. M. Intense Terahertz Pulses by Four-Wave Rectification in Air. *Opt. Lett.* **2000**, *25*, 1210.

(13) Fuji, T.; Nomura, Y. Generation of Phase-Stable Sub-Cycle Mid-Infrared Pulses from Filamentation in Nitrogen *Appl. Sci.* **2013**, *3*, 122.

(14) Nomura, Y.; Shirai, H.; Ishii, K.; Tsurumachi, N.; Voronin, A. a.; Zheltikov, A. M.; Fuji, T. Phase-stable Sub-Cycle Mid-Infrared Conical Emission from Filamentation in Gases *Opt. Express* **2012**, *20*, 24741.

(15) Mizushima, S.-I.; Simanouti, T.; Nagakura, S.; Kuratani, K.; Tsuboi, M.; Baba, H.; Fujioka, O. The Structure of N-Methylacetamide *J. Am. Chem. Soc.* **1950**, *72*, 3490.

(16) Hamm, P. Coherent effects in femtosecond infrared spectroscopy *Chem. Phys.* **1995**, *200*, 415.

(17) Nicodemus, R. A.; Corcelli, S. A.; Skinner, J. L.; Tokmakoff, A. Collective Hydrogen Bond Reorganization in Water Studied with Temperature-Dependent Ultrafast Infrared Spectroscopy *J. Phys. Chem. B* **2011**, *115*, 5604.

(18) Roberts, S. T.; Loparo, J. J.; Tokmakoff, A. Characterization of spectral diffusion from two-dimensional line shapes. *J. Chem. Phys.* **2006**, *125*, 084502.

Chapter 4

Delocalization and Stretch-Bend Mixing of the HOH Bend in Liquid Water

The work presented in this chapter has been published and is reprinted with permission from:
Carpenter, W.B.; Fournier, J.A.; Biswas, R.; Voth, G.A. Tokmakoff, A. Delocalization and stretch-bend mixing of the HOH bend in liquid water. *Journal of Chemical Physics* **2017**, *147* (8), 084503.

4.1 Abstract

Liquid water's rich sub-picosecond vibrational dynamics arise from the interplay of different high- and low-frequency modes evolving in a strong, yet fluctuating hydrogen bond network. Recent studies of the O–H stretching excitations of H_2O indicate that they are delocalized over several molecules, raising questions about whether the bending vibrations are similarly delocalized. In this paper, we take advantage of an improved 50 fs time-resolution and broadband IR spectroscopy to interrogate the 2D IR line shape and spectral dynamics of the HOH bending vibration of liquid H_2O (δ_{HOH}). Indications of strong bend-stretch coupling are observed in early-time 2D IR spectra through a broad excited state absorption which extends from 1500 cm^{-1} to beyond 1900 cm^{-1}, which corresponds to transitions from the bend to the bend overtone and O–H stretching band between 3150 – 3550 cm^{-1}. Pump-probe measurements reveal a fast 180 fs

vibrational relaxation time, which results in a hot-ground state spectrum that is the same as observed for water IR excitation at any other frequency. The fastest dynamical time scale is 80 fs for the polarization anisotropy decay, providing evidence for the delocalized or excitonic character of the bend. Normal mode analysis conducted on water clusters extracted from molecular dynamics simulations corroborate significant stretch-bend mixing and indicate delocalization of δ_{HOH} on 2-7 water molecules.

4.2 Introduction

Water is a remarkable liquid whose unusual properties arise from the complex behavior of its ordered yet fluctuating hydrogen bond (H-bond) network. The vibrational modes of water molecules in the liquid include high-frequency modes such as stretching and bending motions and lower-frequency intermolecular degrees of freedom such as librations, H-bond stretching and distortions of the H-bond network. Additionally, the H-bond interactions between molecules are strong enough that stretching and bending frequencies are heavily dependent on intermolecular configurations. Whereas water's intermolecular modes have long been described as highly collective,[1] high-frequency motions have traditionally been thought of as localized intramolecular vibrations. However, recent experiments[2–7] and theory[8–16] have demonstrated that short-pulse infrared excitation of O–H stretching vibrations (ν_{OH}) in H_2O results in a vibrational exciton delocalized over multiple molecules. The strong intermolecular couplings between different ν_{OH} oscillators responsible for this delocalization also manifest themselves as rapid energy dissipation to low-frequency modes, orientational randomization, and decay of the frequency-frequency correlation function, all occurring on time scales faster than the structural relaxation of the liquid.

The bending vibration in water (δ_{HOH}) also has the potential to be delocalized as a result of intermolecular bend-bend interactions or coupling of the bend to the excitonic O–H stretch. Recent simulations have examined the ultrafast vibrational dynamics[10,17–19] and delocalization of δ_{HOH}.[9,10,20] They modeled the rapid 200 fs vibrational relaxation of δ_{HOH}[21–24] and fast decay of the frequency-frequency correlation function (120 fs)[9] and concluded that δ_{HOH} is actually more delocalized than ν_{OH} in liquid H_2O.[20] While ν_{OH} is expected to delocalize over ~5 water molecules,[8,20] δ_{HOH} was predicted to delocalize over ~20 molecules, extending to the second solvation shell around a central water. Other computational studies also reproduced the fast vibrational relaxation processes and provided a detailed description of efficient and ultrafast transfer of bending energy in one molecule to librational motion of its solvation shell.[17–19] These studies did not specifically account for intermolecular bend coupling needed to address delocalization.

Despite the wealth of experimental studies on ν_{OH} and recent theoretical predictions, experimental studies characterizing the ultrafast relaxation dynamics of δ_{HOH} in H_2O are sparse. Infrared pump-probe studies of the bend mode have observed the fast relaxation and strong coupling to ν_{OH},[21,25] and the 2D bend lineshape has been compared against the HOD bend in D_2O.[24] The O–H stretch and HOH bend vibrations have been demonstrated to mix significantly due to the anharmonicity of their nuclear potentials.[2,3] Ultrafast nonlinear infrared (IR) spectroscopies have been instrumental in characterizing stretch-bend coupling, owing to the short time scales accessible in these experiments and the ability to detect these anharmonic interactions as cross peaks.[2,3,21,22,25,26] Delocalization of the bend vibration in H_2O remains to be experimentally addressed. A detailed 2D IR and polarization anisotropy study should be able to elucidate bending

frequency correlations, the nature of the interaction with ν_{OH}, and the possible presence of delocalization.

In this paper, we take advantage of a 50 fs, 350 cm^{-1} bandwidth pump pulse and a broadband IR probe to accurately capture the fast dynamics of the bending vibration in liquid H_2O using two-dimensional infrared (2D IR) and polarization-dependent transient absorption (TA) spectroscopy. To highlight the strongly coupled environment of neat liquid H_2O, we contrast the bending modes of neat H_2O with the bending mode of H_2O monomers in acetonitrile. 2D IR and TA spectroscopy reveals an excited state absorption (ESA) of δ_{HOH} in neat H_2O that extends over the range of 1500-1900 cm^{-1}, which originates in the anharmonic nature of the coupled stretching and bending modes. We also observe an 80 fs anisotropy decay of δ_{HOH} in liquid H_2O, reminiscent of the anisotropy decay of the excitonic ν_{OH}. The fast decays and the strong mixing with the excitonic stretch suggest that the δ_{HOH} excitation is delocalized. DFT-based normal mode analysis of water clusters extracted from molecular dynamics simulations corroborate significant stretch-bend mixing and delocalization of δ_{HOH} on up to 7 water molecules.

4.3 Methods

4.3.1 Experimental Methods

2D IR spectroscopy was used to characterize the IR spectral dynamics and interactions of the water bending mode. The output of a Ti:Sapphire regenerative amplifier (Coherent, *Legend USX,* 800 nm, 5 mJ pulse energy, 1 kHz, 25 fs) is split into two paths with independent grating compressors. One path pumps a commercial two-stage optical parametric amplifier (Light Conversion, *TOPAS Prime*) to generate signal and idler pulses with wavelengths 1.4 μm and 1.8 μm, respectively. The collinear signal and idler pulses combine in a homebuilt difference frequency generation (DFG) setup in a 0.5 mm thick $AgGaS_2$ crystal cut at 42.7 degrees and tilted

to phase match at 1685 cm^{-1} (5 μJ pulse energy, FWHM 350 cm^{-1}, 50 fs). The autocorrelation interferogram, extracted pulse time profile, and power spectrum are shown in Figs. 3.5 and 3.7 in Chapter 3. The interferometric autocorrelation was fit to the autocorrelation expression for a Gaussian pulse with linear chirp,[27] yielding center frequency of 1682 cm^{-1} and a pulse width of 51 fs. The second path pumps a homebuilt broadband IR source, which has been described in detail elsewhere.[28] Briefly, 500 μJ of the 800 nm pulses generated the second and third harmonics collinear with the 800 nm beam, which were focused into a gentle stream of nitrogen gas. The resulting plasma radiates broadband IR light centered at 2000 cm^{-1}, with bandwidth that allows us to probe from 1000 cm^{-1} to 4000 cm^{-1}, pulsewidth of 50 fs, and pulse energy of < 10 nJ.

The 6 μm pulses were aligned into a Mach-Zehnder interferometer equipped with two KBr beamsplitters and high-accuracy translation stages (Aerotech *ANT-25L)* to generate two pulse pairs. The pulses in each pulse pair are separated by an experimentally controlled time delay τ_1 with resolution of 0.3 fs, and the fixed arm is chopped at 500 Hz. One pulse pair passes through a tunable zero-order CdSe waveplate (*Alphalas)* and a ZnSe wire-grid polarizer (*Specac*) before focusing at the sample. The CdSe waveplate was chosen to minimize dispersion in the 6 μm region, since the zero-dispersion point is at 6 μm. The second pulse pair is sent to a single-pixel room temperature MCT detector which is used for collecting the interferogram of the pulses and for applying an automatic phase correction for the 2D IR spectra.[29]

The 2D IR spectra were collected in the pump-probe geometry,[30] with the 6 μm pulse pair serving as the pump, and the broadband IR source acting as the probe, with a controllable waiting time delay τ_2. The time delay is generated by another high-accuracy translation stage (Aerotech *ANT-25L*) in the broadband IR path. A gold parabolic mirror focuses the three pulses at the sample with spot size of 130 μm and generates a third-order nonlinear polarization in the sample, which

radiates a signal field in the direction of the probe. After passing through an analyzing polarizer, the heterodyned signal is dispersed by a 50 groove/mm grating onto one stripe of a 2 × 64 pixel MCT array detector (Infrared Systems). Half of the probe field is sent directly to the other stripe of the detector to serve as a reference pulse to correct for power fluctuations in the probe.

To collect the 2D IR signal at a single waiting time τ_2, the heterodyned signal was measured as a function of detection frequency (ω_3) as the pulse pair delay (τ_1) was stepped in 4 fs increments. For each point in τ_1 the signal was collected as a change in absorption of the probe beam as $\Delta A_i = -\log[(S_i/R_i)(R_{i+1}/S_{i+1})]$ where i is measured with the chopped arm open, $i+1$ is measured with the chopped arm closed, S_i is the signal from the sample, and R_i is the reference arm used to correct for fluctuations in probe intensity. For a fixed detection frequency ω_3, the resulting signal is an oscillating free induction decay (FID) with a constant offset from the pump-probe signal arising between the static arm and the broadband probe. The constant offset is subtracted and the FID is phased with the Mertz correction[31] determined from one output of the Mach-Zehnder interferometer. A Hann window is applied to the FID, and the data is zero padded before Fourier transformation along the τ_1 axis for each point in ω_3. This produces the excitation frequency axis, ω_1.

The 2D IR spectra were collected with magic angle (MA) polarization, and transient absorption (TA) spectra were collected with MA, ZZZZ (parallel), and ZZYY (perpendicular) polarization schemes. Polarizations were controlled by rotating the polarization of the pump-pulses with the CdSe waveplate, and keeping the polarization of the probe beam fixed. For the ZZZZ and ZZYY polarizations, we made sure to match the pump pulse power. For a given frequency in detection frequency ω_3, the anisotropy was calculated as $r(\tau_2) = (\Delta A_{ZZZZ} - \Delta A_{ZZYY}) / (\Delta A_{ZZZZ} + 2\Delta A_{ZZYY})$.

To minimize chirp and the nonresonant signal from the sample windows, we held samples of neat H_2O between two 200 μm thin CaF_2 windows (Crystran). We characterized the nonresonant response of the thin windows by taking TA spectra of D_2O sandwiched between the thin windows (~1 μm sample pathlength). Because the absorption of D_2O is minimal in the 6 μm region, the positive signal we observe at early waiting times corresponds to the signal from the windows. Chirp is insignificant in the desired frequency range. In order to assure that minimal nonresonant response contributed to our dataset, we only analyzed data taken after τ_2 = 100 fs.[32]

The linear IR spectra were measured with an FTIR spectrometer equipped with an MCT detector (Bruker). For neat H_2O, 1 μL of sample was sandwiched between two 1 mm thick CaF_2 windows, such that the absorbance of ν_{OH} was approximately OD 1, corresponding to ~1 μm path length. Neat H_2O samples were purified by reverse osmosis and ion exchange to 18 MΩ·cm resistivity (Millipore, *Milli-Q*). Dilute H_2O in acetonitrile (Acn) samples were prepared by diluting H_2O to 5% (by mole) in HPLC grade Acn (Sigma Aldrich), resulting in solutions of 1.6M H_2O. The dilute H_2O/Acn samples were placed between two 1 mm thick CaF_2 windows with a 50 μm Teflon spacer, such that the optical density of δ_{HOH} was ~0.4.

4.3.2 Simulation Details

To investigate the extent of delocalization of the water bending vibration, we performed a DFT-based normal mode analysis of water clusters drawn from molecular dynamics (MD) simulations. This builds on our recent study of the vibrational spectroscopy of water and aqueous protons, where the description of the computational details is provided.[33] Briefly, 500 clusters consisting of water molecules within 5Å of a central hydrogen (typically 18 molecules total) were drawn from a simulation of 256 SPC/Fw waters. Normal modes of the clusters determined from the Hessian of the potential energy were used to calculate a density of states and spectral density

(IR transition dipole intensity weighted density of states) by averaging over all clusters. Adiabatic potential energy surfaces were calculated at the B3LYP 6-311++G(d,p) level and basis set using the Gaussian 09 package[34]. Normal modes of cluster vibrations were obtained from the eigenvectors e_i of the Hessian with frequency eigenvalues ω_i, and intensities of the normal modes were calculated as the square of the dipole moment (μ) derivative with respect to normal mode coordinate q_i,

$$I(\omega_i) = \left| \frac{d\mu}{dq_i} \right|^2 . \tag{4.1}$$

The normal mode analysis is shown as the spectral density, $\rho(\omega)$, averaged over the number of clusters, $N_{clusters}$,

$$\rho(\omega) = \frac{1}{N_{clusters}} \sum_{clusters} \sum_{\text{modes } i} I(\omega_i)\delta(\omega - \omega_i). \tag{4.2}$$

To analyze the delocalization of modes, the participation ratio PR_i of the i^{th} normal mode was calculated from the mode displacement vectors e_i as[35]

$$PR_i = \left[N \sum_{\alpha=1}^{3N} \left(e_i^{\alpha} \cdot e_i^{\alpha} \right)^2 \right]^{-1} , \tag{4.3}$$

where N is the total number of atoms in the cluster and α refers to the $3N$ Cartesian coordinates describing the atomic displacements for each normal mode. For reference, a local mode yields a $PR \approx N^{-1}$, whereas a fully delocalized mode will approach $PR=1$. As an alternative representation of delocalization, we also calculated the number of atoms, N_{atoms}, with $|e| \geq 0.1$ Å participating in each vibrational mode. To minimize the contribution of surface water molecules, we calculated the PR of only those normal modes which have non-zero contribution to the central water molecule for each water cluster. To analyze the vibrational character of each mode, we used HOH bond-

angle changes of $\delta\theta_{HOH} > 1°$ and O-H bond length changes of $\delta r_{OH} > 0.01$ Å as cutoffs for determining whether a mode had bend character, stretch character, or both.

4.4 Results

4.4.1 Early-time 2D IR Spectrum of H_2O

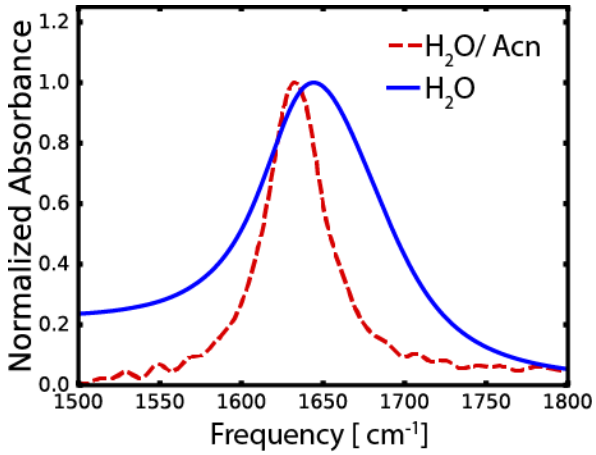

Figure 4.1: The linear absorption spectrum of neat H_2O (solid blue), and 1.6M H_2O in Acn (dashed red). The H_2O/Acn spectrum is shown with Acn solvent subtracted.

To highlight the effect of the H-bond network on the HOH bending vibration, we first contrast the FTIR spectrum of neat H_2O with the 2D IR spectrum of 1.6M H_2O in acetonitrile (Fig. 4.1). At this concentration in Acn, water is solvated primarily in the monomer form which forms relatively weak H-bonds to the CN moieties of the solvent.[36,37] In the FTIR spectrum, the frequency of the bend resonance red-shifts and narrows in linewidth (ω_{HOH} = 1630 cm^{-1}, 40 cm^{-1} FWHM) compared to the neat liquid (ω_{HOH} = 1650 cm^{-1}, 85 cm^{-1} FWHM).[37,38] Previous simulations of the bend in neat H_2O have demonstrated that the bend exhibits non-Gaussian frequency fluctuations, and the lineshape broadens due to intermolecular coupling.[39]

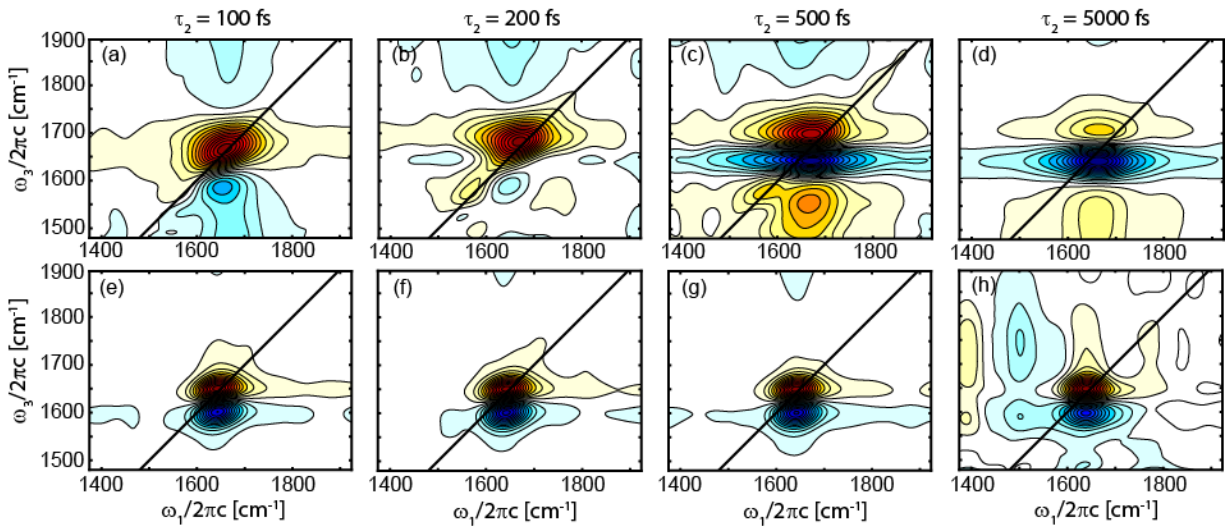

Figure 4.2: The 2D IR waiting time series of δ_{HOH} for (a) – (d) neat H_2O and (e) – (h) water monomers in acetonitrile. The bend feature at τ_2 = 100 fs in neat H_2O displays a broad ESA that flanks the GSB. Each spectrum has been individually normalized to the feature with the maximum absolute amplitude. The low signal to noise ratio in panel (h) is due to decreased amplitude from population relaxation. H_2O/Acn spectra are shown without Acn subtraction.

The 2D IR spectrum of H_2O at early waiting time (τ_2 = 100 fs) is presented in Fig. 4.2. The 2D IR spectra of δ_{HOH} in 1.6M H_2O/Acn display a doublet typical of a weakly anharmonic mode, with a positive ground state bleach (GSB) of the 0→1 transition at 1630 cm^{-1} on the diagonal, and a negative 1→2 excited state absorption (ESA) anharmonically red shifted to ω_3 = 1600 cm^{-1}. The peaks are roughly equal in intensity and linewidth and show no diagonal elongation, implying homogeneous broadening. The characteristics of these peaks exemplify what one would expect for a weakly anharmonic bend vibration,[40] with weak interactions between the H_2O monomer and the Acn solvent.

By contrast, the associative nature of neat water's H-bond network results in a dramatic change in the 2D IR spectrum of the HOH bend in neat H_2O (Fig. 4.2a). As expected for a stronger H-bond interaction, the GSB of δ_{HOH} at 1650 cm^{-1} is blue shifted compared to δ_{HOH} of the H_2O monomer in Acn. Although its linewidth is 100 cm^{-1}, the bleach spreads from ω_1 <1500 cm^{-1} to

>1800 cm^{-1}. The ESA presents as a negative feature red shifted with respect to the GSB, peaked at $\omega_3 = 1590\ cm^{-1}$, consistent with a $55\ cm^{-1}$ anharmonicity reported previously.[41] The ESA exhibits a long tail to the red in ω_3,[42] which is absent in the spectrum of monomeric H_2O. We also observe an additional ESA that arises from excitation of δ_{HOH} which is blue shifted in ω_3 from the GSB and spans $\omega_3 = 1750 - 1900\ cm^{-1}$. The 2D IR spectrum at higher detection frequencies reveals that the ESA continues up to $\omega_3 = 2800\ cm^{-1}$, beyond the bend-libration combination band around $2100\ cm^{-1}$. It is likely that the two ESAs we observe arise from one extremely broad induced absorption whose intensity interferes with the GSB. As a result, it is difficult to say whether the diagonal broadening of the GSB line shape reflects inhomogeneous broadening. As one feature, the ESA stretching from $\omega_3 = 1500\text{-}1900\ cm^{-1}$ would correspond to excitation from the δ_{HOH} singly excited state at $\omega = 1650\ cm^{-1}$ to excited states spanning the stretch and bend overtone region: $3150\text{-}3550\ cm^{-1}$. Our data on the GSB are similar to previously reported 2D IR spectra of δ_{HOH}.[24] However, the broader frequency pulses used in this dataset enable us to characterize the breadth of the bleach in ω_1 and the length of the ESA in ω_3.

We also observe a diagonal bleach at $1570\ cm^{-1}$, most clearly visible at $\tau_2 = 500$ fs but also present at $\tau_2 = 100$ fs and 200 fs. Although a narrow resonance is not clearly present in the linear absorption spectrum, the feature could be a weak resonance such as a hot band hidden within the broad background on the low frequency wing of the δ_{HOH} absorption.[43–45] Since it aligns in ω_3 with the bend ESA, one might expect this signal to arise from a fifth order nonlinear process that drives the system higher up the vibrational ladder.[46,47] If so, its amplitude is expected to grow quadratically with pump intensity. Given the weak signal and limited range of available pump energy at the sample, we were unable to conclusively determine if the intensity dependence of the feature is nonlinear.

4.4.2 Waiting Time Dependence of 2D IR Spectra of H_2O

We next focus on the waiting time series of the bending features of neat and monomeric H_2O in Fig. 4.2. In 1.6M H_2O/Acn, the GSB and ESA slowly decay to zero amplitude with the same rate and with negligible change in line shape, typical for traditional vibrational relaxation of a homogeneous lineshape. For neat H_2O, however, the intensity and lineshape rapidly evolve throughout the spectrum, which we quantify by tracking integrated intensities for several features in Fig. 4.3. The GSB decays as an exponential with a 180 fs time scale, which is within the literature range of 170 – 260 fs.[21,22,24] For the induced absorption features, the lower-frequency portion (ESA_2) decays in 150 fs, while the blue-shifted component (ESA_1) decays in 110 fs. This is consistent with the notion that these features are of similar origin, both tracking efficient dissipation into lower-frequency modes.

In addition to fast relaxation processes, all integration windows are influenced to varying extents by a common 840 fs exponential rise, due to a signal that rises to a constant plateau after ~3 ps. This signal represents the change in absorption of δ_{HOH} after the energy from the pump pulse dissipates into low-frequency modes and is referred to as the "hot ground state" (HGS).[22,32,48–50] The long-time spectral shape which results from the growth of the HGS signal is invariant in ω_1, which demonstrates that the energy dissipation has randomized the initial excitation. As such, each intensity decay was fit with a common second exponential with an 840 fs time scale, determined by the frequency window bounded in purple in Fig. 4.3, and is comparable to other measurements.[2,3,21,26,42,49] This window shows minimal amplitude from the δ_{HOH} GSB but substantial response from the HGS. While the decays of the GSB and ESA portions were normalized to the initial value in Fig. 4.3,the HGS is displayed as a rise to large positive signal (ω_3 = 1650 cm^{-1} in Fig. 4.2d) to highlight the rising nature of the HGS. Because the HGS signal varies in intensity across different integration regions, the amplitude of the HGS component varies

in each biexponential decay. This is evident in the traces of ESA_1 and ESA_2, where the relative HGS amplitudes are 36% and 16% respectively, giving the misleading appearance of a slower decay of ESA_1. Regardless, the fast decay time scales of the two ESA regions are distinct within error.

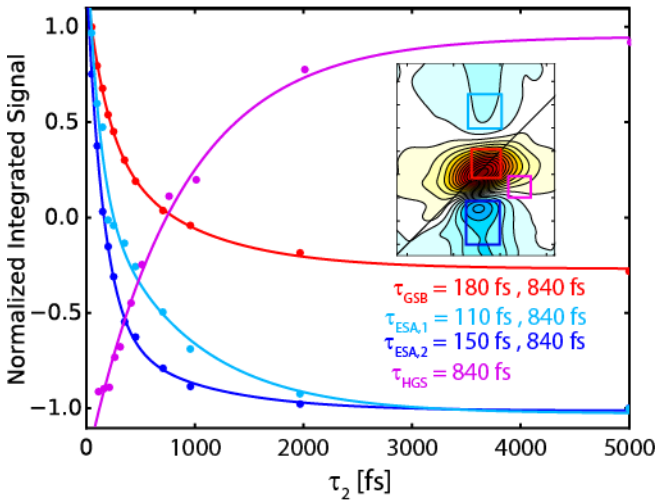

Figure 4.3: Time dependence of integrated intensity of the main features in the 2D IR spectrum of neat H_2O. Inset: 2D IR spectrum of H_2O with colored squares indicating integration intervals for the respective colored lines. The features were integrated with the following (ω_1,ω_3) spectral ranges: GSB = (1640-1710 cm^{-1}, 1650-1710 cm^{-1}), ESA_1 = (1620-1700 cm^{-1}, 1750-1825 cm^{-1}), ESA_2 = (1620-1700 cm^{-1}, 1500-1590 cm^{-1}), and HGS = (1750-1800 cm^{-1}, 1600-1650 cm^{-1}).

4.4.3 Transient Absorption Spectra and Anisotropy Decay of δ_{HOH}

In Fig. 4a and 4b, we present the magic angle TA spectra for H_2O in Acn and in neat H_2O, respectively. In 1.6M H_2O/Acn, the GSB (ω_3=1640 cm^{-1}) and ESA (ω_3=1590 cm^{-1}) decay exponentially with the same 2.4 ps time scale (Fig. 4.5). In neat H_2O, the early-time features such as the GSB centered at ω_3 = 1650 cm^{-1} and ESA stretching from ω_3 = 1500 – 1850 cm^{-1} decay rapidly in 170 fs and 140 fs, respectively, followed by an 840 fs rise of the HGS signal. To effectively contrast the fast decays in neat H_2O with the slower relaxation of monomers in Acn, we plot the TA decays in Fig. 4.5. Traces have been normalized to the initial time point $S(0)$ after subtracting the frequency-dependent value of the HGS spectrum at long times, $S(\infty,\omega_3)$:

$$\Delta S(\tau_2,\omega_3)=\frac{S(\tau_2,\omega_3)-S(\infty,\omega_3)}{S(0,\omega_3)-S(\infty,\omega_3)}. \tag{4.4}$$

At τ_2 = 5 ps, the TA spectrum closely resembles a temperature difference FTIR spectrum of H_2O, similar to observations of the HGS spectrum when other water resonances are excited and allowed to relax.[2,3,22,25] Both the temperature difference spectrum and the HGS spectrum result from an overall weakening of the H-bond network. There is a weak bleach feature centered at ω_3 = 1550 cm^{-1}, an induced absorption centered at ω_3 = 1620 cm^{-1}, with a weak bleach centered at ω_3 = 1690 cm^{-1}. This bleach/induced absorption/bleach pattern is consistent with the red-shifting and narrowing of δ_{HOH}. For the bending mode, then, this implies that weakening the HBs results in a slightly more homogeneous environment. The HGS spectrum and the temperature difference spectrum vary slightly on the low frequency side, which suggests subtle differences between thermal heating of the sample and sub-ps energy dissipation into low-frequency modes.

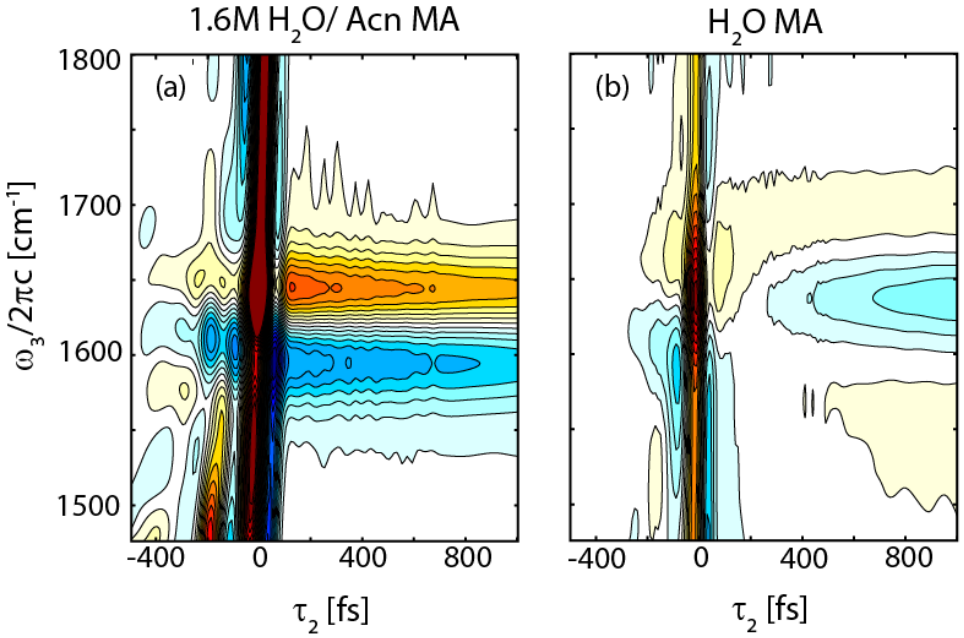

Figure 4.4: Transient absorption spectra of δ_{HOH} in (a) 1.6M H_2O/ Acn and (b) neat H_2O in the magic angle polarization scheme. Orange features correspond to negative absorption, and blue features correspond to positive absorption. At τ_2 = 0 in both spectra, there is a stripe of bleach along all ω_3, which corresponds to nonresonant response from the CaF_2 windows.

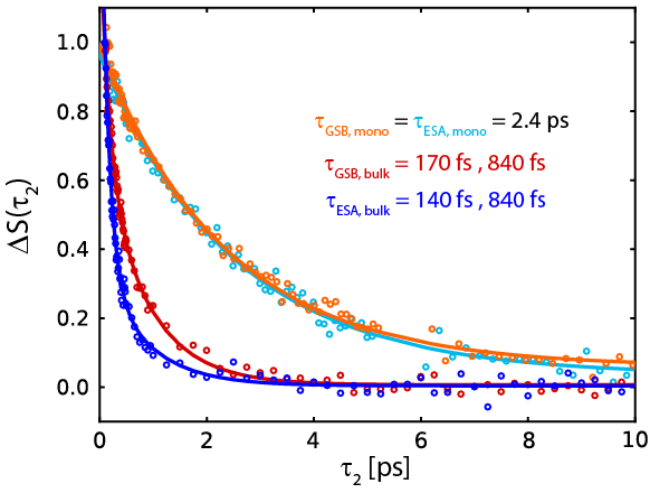

Figure 4.5: Time dependence of integrated intensity of the main features in the TA spectra of neat H_2O and H_2O monomers in acetonitrile. The features were integrated with the following ω_3 spectral ranges: GSB, bulk = 1650-1710 cm^{-1}; ESA, bulk = 1500-1590 cm^{-1}; GSB, mono = 1620-1670 cm^{-1}; ESA, mono = 1590-1610 cm^{-1}.

Pump-probe anisotropy decays were calculated from parallel and perpendicular polarization TA experiments after correcting for the growth of the HGS.[49,51,52] Since the HGS spectrum grows in uniformly for all ω_3, we generated a surface describing the HGS growth by scaling the long-time pump-probe trace with an exponential rise:

$$S_{HGS}(\tau_2,\omega_3) = [1-\exp(-\tau_2 / \tau_{HGS})]S(\infty,\omega_3), \tag{4.5}$$

where τ_{HGS} = 840 fs. The difference of S_{HGS} from the neat H_2O TA surface corrects for the isotropic HGS signal and removes a zero-crossing in the denominator of the anisotropy expression.

The resulting ZZZZ and ZZYY TA traces from ω_3 = 1645-1655 cm^{-1} (Fig. 4.6a) yield the pump-probe anisotropy in Fig. 4.6b. The anisotropy decay was fit to an exponential with a floating offset to qualitatively capture the decay dynamics, even though the data demonstrate that the anisotropy is not the best described with a single exponential. Regardless, the anisotropy decays rapidly and monotonically with a e^{-1} time scale of 80 fs. As a way to obtain a mean relaxation time,

the first moment of the relaxation curve was calculated to be 120 fs, which is similarly rapid. This fast decay is similar in time scale to the anisotropy decay of the O–H stretching vibration in H_2O.[3] Additionally, a shoulder and a beat arise at τ_2 = 65 fs in the ZZZZ and ZZYY traces, respectively, which corresponds roughly to a librational period. These features are not retained in the anisotropy, nor are they present in the magic angle decay, which only reports on population relaxation dynamics. To contrast, we also present the pump-probe anisotropy decay of δ_{HOH} in 1.6M H_2O/Acn, which decays on 240 fs and 2.2 ps time scales (Fig. 4.6d). The long time scale roughly agrees with the reorientation of neat Acn,[53] and the fast time scale agrees with the fast anisotropy decay component seen for the O–H stretches in the H_2O monomer, previously attributed to intramolecular energy transfer.[37] The 2.2 ps time scale has also been observed in the anisotropy decay of the O–H stretches of the H_2O monomer and has been attributed to the reorientation of H_2O in Acn.[37]

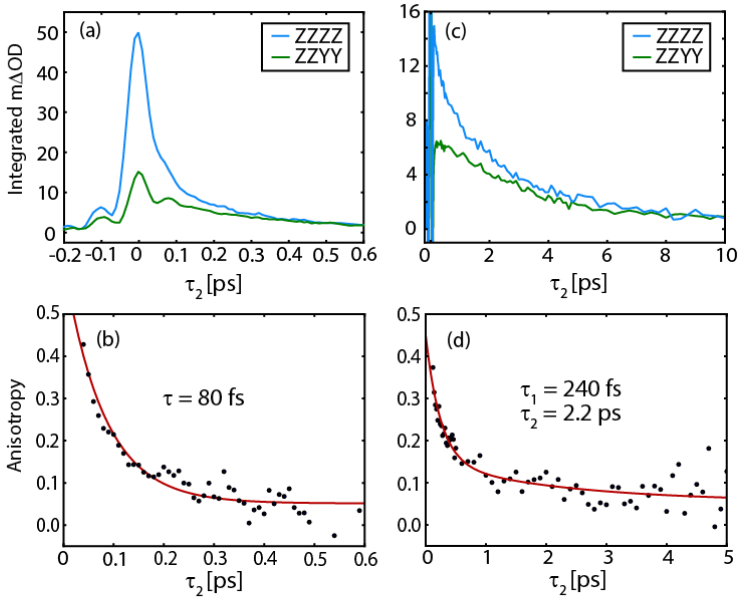

Figure 4.6: (a) TA traces for δ_{HOH} in ZZZZ polarization scheme (solid blue) and ZZYY scheme (dashed green) over the range ω_3 = 1645 cm^{-1}-1655 cm^{-1}. (b) Pump-probe anisotropy decay of δ_{HOH}. (c) ZZZZ and ZZYY traces of δ_{HOH} for monomers in Acn. (d) Pump-probe anisotropy decay of δ_{HOH} for monomers in Acn.

4.5 Discussion

4.5.1 The 2D IR Spectrum of δ_{HOH}

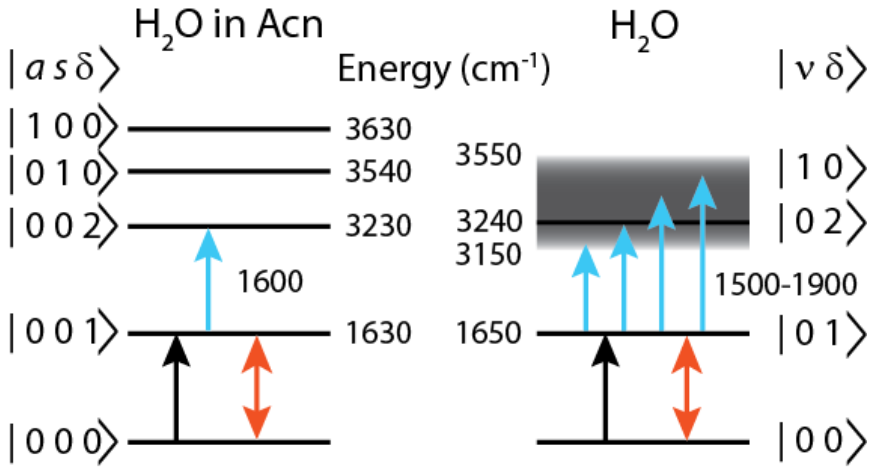

Figure 4.7: Energy level diagram for transitions observed in the 2D IR spectra. (Left) Energies of the asymmetric (*a*) and symmetric stretch (*s*) and bend (δ) vibrations of H_2O monomers in Acn. (Right) Bend (δ) and stretch (ν) exciton states in neat H_2O. Black arrows correspond to pump excitation of δ_{HOH}. Probing step is illustrated as double-headed orange arrows for the GSB, and blue arrows for the ESA. In H_2O monomers, we do not observe an ESA to stretches, but in neat H_2O ESA to the extremely broad ν_{OH} is indeed observed.

The 2D IR spectroscopy of the bending vibration of liquid H_2O is dramatically different from that of H_2O monomers in acetonitrile. The 2D lineshape of the GSB in neat H_2O broadens substantially along and against the diagonal, indicating both faster dephasing and a larger distribution of local H-bond environments. While the GSB and the ESA of the monomer bend are the same width, the ESA of the bend in neat H_2O is extensively broadened in ω_3. Previously, we also observed extreme broadening of the absorption induced by exciting the O–H stretching vibration of H_2O, with an ESA that spread from a peak near 3000 cm^{-1} to <1500 cm^{-1}.[2,3] For the case of ν_{OH}, the ESA reflected the large vibrational anharmonicity originating in the H-bond network in addition to stretch-bend coupling via Fermi resonance, which resulted in transitions from a stretch exciton band to doubly excited states with stretch and bend character.

The interpretation of the broad ESA for the H_2O bend observed here has origins in the same anharmonic interactions, but manifests itself somewhat differently in the 2D spectrum. The greatest ESA intensity is located at ω_3 = 1590 cm^{-1}, which indicates that the most facile transition is directly to the bend overtone. However, this is a small part of an induced absorption that spreads from <1500 cm^{-1} to >1900 cm^{-1}. After accounting for the ω_1 = 1650 cm^{-1} excitation frequency, the blue-shifted ESA extending from ω_3 = 1750-1900 cm^{-1} corresponds to a band of vibrational states with energy 3400-3550 cm^{-1}, the frequency of the ν_{OH} fundamental band in the linear IR spectrum. The ESA to the bend overtone (~3240 cm^{-1}) is also merged with the stretching band in the linear IR spectrum, as a result of the ~2:1 Fermi resonance between stretch and bend frequencies.[54,55] Therefore, it is reasonable to consider that the two ESAs that we observe are actually two regions of one broader ESA, with a breadth that reflects the stretching band of the linear IR spectrum, as shown in Fig. 4.7.

While the bend-to-stretch ESA is initially surprising, it is not completely unexpected in hindsight and is even observable in previous experiments and simulations. The feature is not expected for weakly anharmonic modes since transitions from one quantum of one normal mode to one quantum of another normal mode is forbidden in the harmonic limit, but the strong anharmonicity imbued upon the modes from the H-bond network relaxes this selection rule. Upon closer inspection of previous reports of δ_{HOH}, the extended ESA is visible in vibrational pump-probe spectra of δ_{HOH}[22] and non-equilibrium molecular dynamics simulations of the 2D IR spectrum of δ_{HOH} using the flexible and polarizable TTM3-F potential.[10]

Given the unusual nature of the initial excitation, the relaxation of the bend is not readily described by simple relaxation pathways. For H_2O monomers in acetonitrile, both the GSB and ESA of δ_{HOH} relax in 2.4 ps, which is typical for simple dissipation of a weakly anharmonic mode.

Similar behavior with longer lifetimes is observed for H_2O monomers in chloroform,[56] which indicate the important role that intermolecular interactions play in mediating vibrational relaxation.[57] By contrast, in neat H_2O the GSB of the bend decays in 180 fs, and the ESA decays slightly faster. The influence of the water H-bond network are also apparent when considering the δ_{HOH} relaxation time of ~400 fs for the δ_{HOH} vibration of quasi-monomeric H_2O in a 6M solution of H_2O in D_2O.[41] Non-equilibrium simulations of bend vibrational relaxation in H_2O attribute the fast relaxation to dissipation into high frequency librations primarily of the first solvation shell.[17,18] When the solvent is treated fully flexibly, this fast relaxation also includes transfer of bend excitation to δ_{HOH} modes on neighboring molecules, which is comparable to the rate of stretch-to-bend relaxation.[10] The mixing of the stretch and bend vibrations is clearly seen in the stretch-bend crosspeak of H_2O.[2,3] We also note the signature of more complex mixing of bend, stretching, and libration vibrations apparent from the uphill 2D cross-peak in which H_2O excitation between 1300-1500 cm^{-1} leads to immediate (τ_2 = 100 fs) crosspeaks to the stretch and bend overtone region at 3000-3700 cm^{-1}.[58] The combination of the experimental observables and relaxation simulations indicates that all inter- and intramolecular degrees of freedom in H_2O are intertwined, resulting in the observation of similarly fast relaxation processes regardless of excitation or detection frequency.

4.5.2 The Excitonic Nature of δ_{HOH}

Strong intermolecular couplings mean that excitation of the water bending transition with a short, broad bandwidth pump pulse enables coherent excitation of multiple interacting water molecules. In the neat liquid, all bend transitions are resonant, and thus, the bend excitation consists of a superposition of oscillations whose dipoles have a component along the polarization of the pump's electric field. The rapid δ_{HOH} anisotropy decay demonstrates that this coherence

quickly randomizes its orientation, much faster than both the 180 fs lifetime and the 1.5 ps time scale of molecular rotation. By contrast, experiments on the H_2O monomer in Acn result in a local mode excitation that reorients in 2.2 ps as a result of diffusive molecular rotation. This anisotropy also includes an additional faster component arising from excitation reorientation due to intramolecular mixing of the bend, symmetric stretch, and antisymmetric stretch, in close agreement with the O–H stretch anisotropy decay for H_2O in Acn previously measured.[37] In the case of neat H_2O, the extremely rapid anisotropy decay has been observed several times with the O–H stretch, and attributed to intermolecular interactions that scramble the direction of the initial excitation, either as a result of excitation hopping between molecules or excitonic interactions.[2–4,6,11,12,59,60] Given that the anisotropy of the bend occurs on a on the time scale of librations (the fastest intermolecular motions of the liquid),[61] and that the bend is strongly coupled with the other vibrations, our results point toward a collective excitonic excitation which evolves with liquid dynamics. Similar arguments have been used to explain the ultrafast anisotropy relaxation of the excitonic ν_{OH} as well.[2,3,12]

Because the bend couples strongly with the excitonic stretch, it may not be entirely surprising that the bend behaves excitonically as well. In both of these modes, the H-bond network is the common infrastructure that couples adjacent oscillators. Similarly, librational motion is the common mechanism that induces rapid randomization of the transition dipole, even without reorientation of individual molecules. This leads to the question of how delocalized the bend might be. Previous simulations suggest that δ_{HOH} delocalizes over more molecules than ν_{OH}.[20] Assuming that water vibrations lie in an intermediate coupling regime in which the strength of intermolecular interactions are of the same scale as the energetic disorder, we might expect that the vibrational delocalization scales with the distribution of vibrational frequencies. This was demonstrated in the

2D depolarization surface of ν_{OH}, which displayed a lower depolarization ratio for strongly hydrogen-bonded stretches, versus higher delocalization for stretches of intermediate frequency.[3] In comparison to the bend, the OH stretching frequency is particularly sensitive to the H-bond environment. Thus, for bends, it is possible that a narrower frequency distribution results in higher delocalization.

Compared to the bend of the H_2O monomer, however, the linear IR feature for δ_{HOH} in liquid water is broadened due to hydrogen bonding frequency shifts *and* intermolecular coupling. In a previous mixed quantum/classical analysis of the HOH bend, intermolecular couplings were necessary to accurately calculate the FTIR spectrum of δ_{HOH} in neat H_2O.[39] Setting the intermolecular coupling to zero also accurately reproduced the spectrum of the HOH bend for dilute H_2O in D_2O. While this analysis did not quantify the extent of delocalization of δ_{HOH}, it nonetheless demonstrated that bending motions on nearby molecules resonantly couple with each other, resulting in a dramatic change in the lineshape of the bend.

4.5.3 Simulation of the Mode-Mixing and Delocalization of δ_{HOH}

To further investigate the extent of delocalization of the water bending vibration, we performed a DFT-based normal mode analysis of water clusters drawn from molecular dynamics (MD) simulations. The results of these calculations are presented in Fig. 4.8. The spectral density (Fig. 4.8a) shows three main peaks centered at 1000 cm^{-1}, 1730 cm^{-1}, and 2900 cm^{-1}, which are assigned as librations, δ_{HOH}, and ν_{OH} resonances. These peaks differ from experimental frequencies primarily as a result of DFT overestimating H-bond strength.[62] The bending modes primarily have pure bend or mixed stretch-bend character, as expected. On the other hand, stretching modes are primarily pure stretch character; however, modes with bending and mixed stretch-bend character appear on the low frequency side of the band, where the overtone of δ_{HOH} is expected. Furthermore,

the librational band clearly has stretch and bend character associated with it, emphasizing the highly coupled nature of these vibrations.

The participation ratio (*PR)* is characterized as a function of vibrational frequency in Fig. 4.8b. The mean *PR* reaches a maximum at the center of each vibrational band and decreases with increasing mode frequency when comparing the stretch, bend, librational, and intermolecular (<500 cm^{-1}) peaks. The variance in the *PR* is large and also reaches a maximum coincident with the peaks in the spectral density. As a complement, the delocalization in terms of N_{atoms} participating in the normal mode is presented in Fig. 4.8c, which shows the same trends as the *PR*.

Focusing on the bending vibration (insets of Fig. 4.8c), these calculations reinforce that δ_{HOH} is delocalized over multiple water molecules. They indicate that the center of the band (1730 cm^{-1}) is more delocalized than the wings (1620 cm^{-1} and 1800 cm^{-1}), with a PR corresponding to 6-21 atoms. This value is about half the value predicted from a previous normal mode analysis of δ_{HOH},[20] but roughly corresponds to delocalization over a central molecule and its first solvation shell, consistent with *ab initio* MD simulations of spatially-resolved IR spectra of H_2O.[63] We also observe that δ_{HOH} is more delocalized than ν_{OH}, which involves on average ~6 atoms, a value that is low compared to literature.[8] Frozen cluster normal mode analysis will tend to underestimate the degree of delocalization due to a large fraction of molecules residing at the cluster surface. Taken together, however, these calculations, theoretical studies, and our experimental findings indicate that that the H_2O bending vibration delocalizes over multiple molecules.

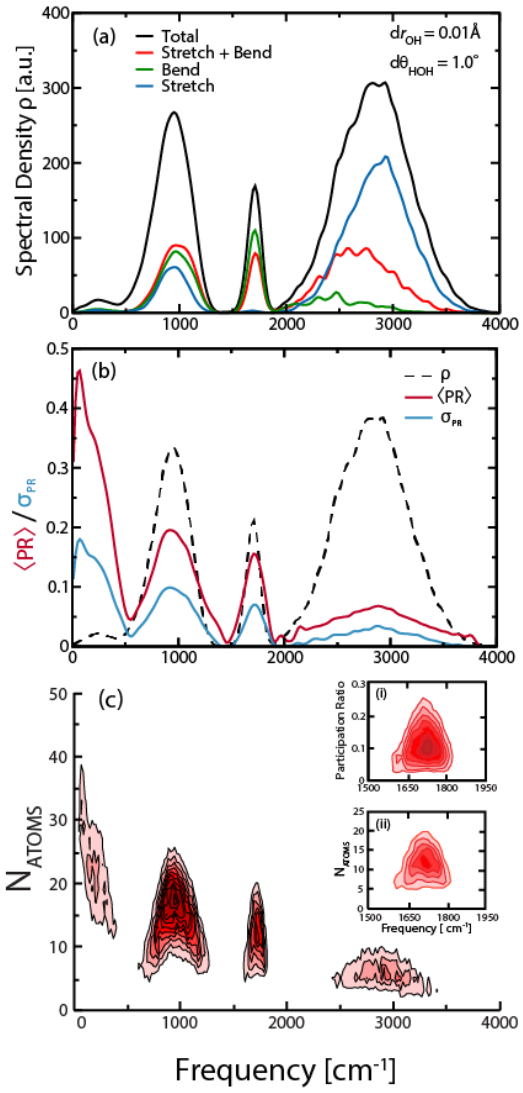

Figure 4.8: (a) Spectral density for 5Å-cutoff water clusters, decomposed by stretch/bend character. The total spectral density is shown in black, stretch-only modes ($\delta r_{OH} > 0.01$ Å and $\delta\theta_{HOH} < 1°$) are shown in blue, bend-only modes ($\delta r_{OH} < 0.01$ Å and $\delta\theta_{HOH} > 1°$) are shown in green, and stretch-bend mixed modes ($\delta r_{OH} > 0.01$ Å and $\delta\theta_{HOH} > 1°$) are shown in red. δ_{HOH} shows significant mixing of stretch and bend character, but very little pure stretch character. (b) Mean ⟨PR⟩ and standard deviation $\sigma_{PR} = [\langle PR^2\rangle - \langle PR\rangle^2]^{1/2}$ of the participation ratio as a function of vibrational frequency. (c) Number of atoms participating in the normal modes of H_2O. Inset i: The participation ratio of the δ_{HOH} normal mode, which is highest in the center of the band and lowest on the wings. Inset ii: Number of atoms participating in the δ_{HOH} normal mode, which follows the same trend as the participation ratio.

4.5.4 The Hot Ground State

The delocalization of δ_{HOH} goes hand-in-hand with the fast vibrational relaxation observed. After preparing the initial delocalized bend excitation, small amplitude changes of the extended hydrogen bond network allow the excitation to migrate and localize among bending motions of nearby molecules. Simultaneously, there is a likelihood on any given molecule that the energy can relax to librational motions, which further contributes to ultrafast energy dissipation. Because the excitation is delocalized over multiple molecules, relaxation involves many parallel channels that are together far more efficient than relaxation from a localized mode. The net result is that energy is dissipated into low frequency modes such as librations, hydrogen-bond stretches and distortions of the H-bond network, which is spectroscopically observed as the growth of the HGS.

The appearance of the HGS signal mimics a temperature difference spectrum since both spectra reflect overall H-bond weakening. When temperature is increased, HBs weaken on average due to the increase in randomized thermal motions, and the change in H-bond environment manifests as spectral shifts and changes in intensity. Remarkably, the HGS signal rises on an ultrafast, 840 fs time scale in liquid H_2O (Fig. 4.3), which suggests that the signal we observe is not a new equilibrium characterized by a Boltzmann distribution at an elevated temperature. Rather, the system is still in a highly nonequilibrium state characterized by a net excess of kinetic energy in the low-frequency intermolecular vibrations,[10,64,65] and the 2D IR measurement is sensitive to this weakened H-bond network.[3]

The time scale of HGS growth in H_2O has been measured to be ~800 fs, regardless of the measurement method or the initial mode excited.[3,21,23,24,42,49,66] This observation is inconsistent with a purely cascading relaxation mechanism between weakly coupled stretch and bend modes, which would predict a HGS growth time scale that is longer for stretch excitation than bend excitation. The 800 fs time scale lies between the vibrational lifetime (~200 fs) in neat liquid water

and collective molecular rotation (1.5 ps),[49] and has been modeled with frequency resolved transient kinetic energy analysis.[64,67] In that framework, librational excitations relaxed to low frequency intermolecular motions, such as the stretching and distortion of hydrogen bonds and collective reorganization of the H-bond network, predicted to occur in 790 fs. In our interpretation stretch, bend, and librations are intimately coupled, and that any IR vibrational excitation seamlessly drives intermolecular motions of the H-bond network.

4.6 Conclusion

We have used ultrafast 2D IR and pump-probe spectroscopy to explore the ultrafast dynamics of the bending vibration in liquid H_2O. Anharmonic interactions result in strong mixing of bend and stretch, as demonstrated by the ESA transition between these bands. The 80 fs pump-probe anisotropy decay is extremely rapid compared to the 180 fs bend lifetime and the 1.5 ps hydrogen bond reorganization time. The H-bond network induces anharmonic coupling between adjacent molecules with sufficient strength such that the initial excitation is delocalized over multiple molecules, and the orientation of the bend dipole is quickly scrambled by librational oscillation. Cascading relaxation from highest frequency to lowest frequency modes does not capture the full extent of the dynamics observed in H_2O. Strong couplings also allow bend excitation to drive stretching motions (up-pumping), in addition to efficient downhill relaxation from the bend to low-frequency modes.

Many questions remain regarding the delocalized nature of high frequency vibrations in water, which leaves challenges for experiment and theory. What experimental tests can be used to quantify the extent of delocalization of high frequency vibrational excitations and follow these in a time-resolved manner? Existing experiments provide evidence for vibrational excitons, but are difficult to translate into a microscopic picture. Theoretical studies are needed to provide a

molecular picture of the exciton dynamics, including the initially prepared state, spatial transport, localization, and dissipation. Previous non-equilibrium simulations of δ_{HOH} dissipation have excited only one water molecule; however, bend excitation by an infrared electromagnetic field should take delocalization into account,[5] perhaps using non-equilibrium simulations with an explicit pulsed external field.[68–70] Addressing delocalization effects may also help resolve differences in conclusions regarding how the excited bend energy is partitioned to other modes.[10,19,71] Additional relaxation channels are present and should also be considered, such as Fermi resonances (both intra- and intermolecular) and nonadiabatic dynamics involving vibrational conical intersections.[72] We hope that the present experiments will work to spur interest in modeling these topics. Unravelling these dynamics could potentially lead to a rich description of a class of vibrational dynamics of a very different nature than most solution phase problems.

4.7 References

(1) Cho, M.; Fleming, G. R.; Saito, S.; Ohmine, I.; Stratt, R. M. Instantaneous normal mode analysis of liquid water *J. Chem. Phys.* **1994**, *100*, 6672.

(2) Ramasesha, K.; De Marco, L.; Mandal, A.; Tokmakoff, A. Water vibrations have strongly mixed intra- and intermolecular character *Nat. Chem.* **2013**, *5*, 935.

(3) De Marco, L.; Fournier, J. A.; Thämer, M.; Carpenter, W.; Tokmakoff, A. Anharmonic exciton dynamics and energy dissipation in liquid water from two-dimensional infrared spectroscopy *J. Chem. Phys.* **2016**, *145*, 094501.

(4) Paarmann, A.; Hayashi, T.; Mukamel, S.; Miller, R. J. D. Nonlinear response of vibrational excitons: Simulating the two-dimensional infrared spectrum of liquid water *J. Chem. Phys.* **2009**, *130*, 204110.

(5) Nagata, Y.; Yoshimune, S.; Hsieh, C.-S.; Hunger, J.; Bonn, M. Ultrafast Vibrational Dynamics of Water Disentangled by Reverse Nonequilibrium Ab Initio Molecular Dynamics Simulations *Phys. Rev. X* **2015**, *5*, 021002.

(6) Kraemer, D.; Cowan, M. L.; Paarmann, A.; Huse, N.; Nibbering, E. T. J.; Elsaesser, T.; Miller, R. J. D. Temperature Dependence of the Two-Dimensional Infrared Spectrum of Liquid H_2O. *Proc. Natl. Acad. Sci. U.S.A.* **2008**, *105*, 437.

(7) van der Post, S. T.; Hsieh, C.-S.; Okuno, M.; Nagata, Y.; Bakker, H. J.; Bonn, M.; Hunger, J. Strong frequency dependence of vibrational relaxation in bulk and surface water reveals sub-picosecond structural heterogeneity *Nat. Commun.* **2015**, *6*, 8384.

(8) Auer, B. M.; Skinner, J. L. IR and Raman spectra of liquid water: theory and interpretation. *J. Chem. Phys.* **2008**, *128*, 224511.

(9) Imoto, S.; Xantheas, S. S.; Saito, S. Ultrafast dynamics of liquid water: Frequency fluctuations of the OH stretch and the HOH bend *J. Chem. Phys.* **2013**, *139*, 044503.

(10) Imoto, S.; Xantheas, S. S.; Saito, S. Ultrafast Dynamics of Liquid Water: Energy Relaxation and Transfer Processes of the OH Stretch and the HOH Bend *J. Phys. Chem. B* **2015**, *119*, 11068.

(11) Torii, H. Ultrafast anisotropy decay of coherent excitations and the non-coincidence effect for delocalized vibrational modes in liquids *Chem. Phys. Lett.* **2000**, *323*, 382.

(12) Jansen, T. l. C.; Auer, B. M.; Yang, M.; Skinner, J. L. Two-dimensional infrared spectroscopy and ultrafast anisotropy decay of water *J. Chem. Phys.* **2010**, *132*, 224503.

(13) Choi, J. H.; Cho, M. Computational IR spectroscopy of water: OH stretch frequencies, transition dipoles, and intermolecular vibrational coupling constants *J. Chem. Phys.* **2013**, *138*, 174108.

(14) Buch, V.; Tarbuck, T.; Richmond, G. L.; Groenzin, H.; Li, I.; Shultz, M. J. Sum frequency generation surface spectra of ice, water, and acid solution investigated by an exciton model *J. Chem. Phys.* **2007**, *127*, 204710.

(15) Falvo, C.; Palmieri, B.; Mukamel, S. Coherent infrared multidimensional spectra of the OH stretching band in liquid water simulated by direct nonlinear exciton propagation *J. Chem. Phys.* **2009**, *130*, 184501.

(16) Shi, L.; Skinner, J. L.; Jansen, T. la C. Two-dimensional infrared spectroscopy of neat ice Ih *Phys. Chem. Chem. Phys.* **2016**, *18*, 3772.

(17) Rey, R.; Ingrosso, F.; Elsaesser, T.; Hynes, J. T. Pathways for H_2O Bend Vibrational Relaxation in Liquid Water *J. Phys. Chem. A* **2009**, *113*, 8949.

(18) Ingrosso, F.; Rey, R.; Elsaesser, T.; Hynes, J. T. Ultrafast Energy Transfer from the Intramolecular Bending Vibration to Librations in Liquid Water *J. Phys. Chem. A* **2009**, *113*, 6657.

(19) Rey, R.; T. Hynes, J. Tracking energy transfer from excited to accepting modes: application to water bend vibrational relaxation *Phys. Chem. Chem. Phys.* **2012**, *14*, 6332.

(20) Imoto, S.; Xantheas, S. S.; Saito, S. Molecular origin of the difference in the HOH bend of the IR spectra between liquid water and ice *J. Chem. Phys.* **2013**, *138*, 054506.

(21) Ashihara, S.; Huse, N.; Espagne, A.; Nibbering, E. T. J.; Elsaesser, T. Vibrational couplings and ultrafast relaxation of the O–H bending mode in liquid H2O *Chem. Phys. Lett.* **2006**, *424*, 66.

(22) Lindner, J.; Vöhringer, P.; Pshenichnikov, M. S.; Cringus, D.; Wiersma, D. A.; Mostovoy, M. Vibrational relaxation of pure liquid water *Chem. Phys. Lett.* **2006**, *421*, 329.

(23) Ashihara, S.; Fujioka, S.; Shibuya, K. Temperature dependence of vibrational relaxation of the OH bending excitation in liquid H2O *Chem. Phys. Lett.* **2011**, *502*, 57.

(24) Chuntonov, L.; Kumar, R.; Kuroda, D. G. Non-linear infrared spectroscopy of the water bending mode: direct experimental evidence of hydration shell reorganization? *Phys. Chem. Chem. Phys.* **2014**, *16*, 13172.

(25) Lindner, J.; Cringus, D.; Pshenichnikov, M. S.; Vöhringer, P. Anharmonic bend–stretch coupling in neat liquid water *Chem. Phys.* **2007**, *341*, 326.

(26) Ashihara, S.; Huse, N.; Espagne, A.; Nibbering, E. T. J.; Elsaesser, T. Ultrafast structural dynamics of water induced by dissipation of vibrational energy. *J. Phys. Chem. A* **2007**, *111*, 743.

(27) Diels, J.; Rudolph, W. *Ultrashort Laser Pulse Phenomena*; Academic Press: San Diego, 1996.

(28) Petersen, P. B.; Tokmakoff, A. Source for ultrafast continuum infrared and terahertz radiation. *Opt. Lett.* **2010**, *35*, 1962.

(29) Helbing, J.; Hamm, P. Compact implementation of Fourier transform two-dimensional IR spectroscopy without phase ambiguity *J. Opt. Soc. Am. B* **2010**, *28*, 171.

(30) DeFlores, L. P.; Nicodemus, R. A.; Tokmakoff, A. Two-dimensional Fourier transform spectroscopy in the pump-probe geometry *Opt. Lett.* **2007**, *32*, 2966.

(31) Mertz, L. Auxiliary computation for Fourier spectrometry *Infrared Phys.* **1967**, *7*, 17.

(32) Fecko, C. J.; Loparo, J. J.; Roberts, S. T.; Tokmakoff, A. Local Hydrogen Bonding Dynamics and Collective Reorganization in Water: Ultrafast Infrared Spectroscopy of HOD/D$_2$O. *J. Chem. Phys.* **2005**, *122*, 54506.

(33) Biswas, R.; Carpenter, W.; Fournier, J. A.; Voth, G. A.; Tokmakoff, A. IR spectral assignments for the hydrated excess proton in liquid water *J. Chem. Phys.* **2017**, *146*, 154507.

(34) Frisch, M. J.; Trucks, G. W.; Schlegel, H. B.; Scuseria, G. E.; Robb, M. A.; Cheeseman, J. R.; Scalmani, G.; Barone, V.; Mennucci, B.; Petersson, G. A.; Nakatsuji, H.; Caricato, M.; Li, X.; Hratchian, H. P.; Izmaylov, A. F.; Bloino, J.; Zheng, G.; Sonnenberg, J. L.; Hada, M.; Ehara, M.; Toyota, K.; Fukuda, R.; Hasegawa, J.; Ishida, M.; Nakajima, T.; Honda, Y.; Kitao, O.; Nakai, H.; Vreven, T.; Montgomery Jr, J. A.; Peralta, J. E.; Ogliaro, F.;

Bearpark, M. J.; Heyd, J.; Brothers, E. N.; Kudin, K. N.; Staroverov, V. N.; Kobayashi, R.; Normand, J.; Raghavachari, K.; Rendell, A. P.; Burant, J. C.; Iyengar, S. S.; Tomasi, J.; Cossi, M.; Rega, N.; Millam, N. J.; Klene, M.; Knox, J. E.; Cross, J. B.; Bakken, V.; Adamo, C.; Jaramillo, J.; Gomperts, R.; Stratmann, R. E.; Yazyev, O.; Austin, A. J.; Cammi, R.; Pomelli, C.; Ochterski, J. W.; Martin, R. L.; Morokuma, K.; Zakrzewski, V. G.; Voth, G. A.; Salvador, P.; Dannenberg, J. J.; Dapprich, S.; Daniels, A. D.; Farkas, Ö.; Foresman, J. B.; Ortiz, J. V; Cioslowski, J.; Fox, D. J. Gaussian, Inc.: Wallingford, CT, USA 2009,.

(35) Sastry, S.; Deo, N.; Franz, S. Spectral statistics of instantaneous normal modes in liquids and random matrices. *Phys. Rev. E. Stat. Nonlin. Soft Matter Phys.* **2001**, *64*, 016305.

(36) Bakó, I.; Megyes, T.; Pálinkás, G. Structural investigation of water–acetonitrile mixtures: An ab initio, molecular dynamics and X-ray diffraction study *Chem. Phys.* **2005**, *316*, 235.

(37) Cringus, D.; Jansen, T. L. C.; Pshenichnikov, M. S.; Wiersma, D. A. Ultrafast anisotropy dynamics of water molecules dissolved in acetonitrile. *J. Chem. Phys.* **2007**, *127*, 084507.

(38) Dahms, F.; Costard, R.; Nibbering, E. T. J.; Elsaesser, T. Ultrafast vibrational energy flow in water monomers in acetonitrile *Chem. Phys. Lett.* **2016**, *652*, 50.

(39) Ni, Y.; Skinner, J. L. IR and SFG vibrational spectroscopy of the water bend in the bulk liquid and at the liquid-vapor interface, respectively *J. Chem. Phys.* **2015**, *143*, 014502.

(40) Khalil, M.; Demirdöven, N.; Tokmakoff, A. Coherent 2D IR Spectroscopy: Molecular Structure and Dynamics in Solution. *J. Phys. Chem. A* **2003**, *107*, 5258.

(41) Larsen, O. F. A.; Woutersen, S. Vibrational relaxation of the H[sub 2]O bending mode in liquid water *J. Chem. Phys.* **2004**, *121*, 12143.

(42) Huse, N.; Ashihara, S.; Nibbering, E. T. J.; Elsaesser, T. Ultrafast vibrational relaxation of O–H bending and librational excitations in liquid H2O *Chem. Phys. Lett.* **2005**, *404*, 389.

(43) Walrafen, G. E.; Blatz, L. A. Weak Raman bands from water *J. Chem. Phys.* **1973**, *59*, 2646.

(44) Moskovits, M.; Michaelian, K. H. A reinvestigation of the Raman spectrum of water *J. Chem. Phys.* **1978**, *69*, 2306.

(45) Zelent, B.; Nucci, N. V.; Vanderkooi, J. M. Liquid and ice water and glycerol/water glasses compared by infrared spectroscopy from 295 to 12 K *J. Phys. Chem. A* **2004**, *108*, 11141.

(46) Kemlin, V.; Bonvalet, A.; Daniault, L.; Joffre, M. Transient Two-Dimensional Infrared Spectroscopy in a Vibrational Ladder *J. Phys. Chem. Lett.* **2016**, *7*, 3377.

(47) Thielges, M. C.; Fayer, M. D. Time-Dependent Fifth-Order Bands in Nominally Third-Order 2D IR Vibrational Echo Spectra *J. Phys. Chem. A* **2011**, *115*, 9714.

(48) Lock, A. J.; Woutersen, S.; Bakker, H. J. Ultrafast Energy Equilibration in Hydrogen-Bonded Liquids *J. Phys. Chem. A* **2001**, *105*, 1238.

(49) Steinel, T.; Asbury, J. B.; Zheng, J.; Fayer, M. D. Watching Hydrogen Bonds Break: A Transient Absorption Study of Water. *J. Phys. Chem. A* **2004**, *108*, 10957.

(50) Wang, Z.; Pang, Y.; Dlott, D. D. Hydrogen-bond disruption by vibrational excitations in water *J. Phys. Chem. A* **2007**, *111*, 3196.

(51) Bakker, H. J.; Rezus, Y. L. A.; Timmer, R. L. A. Molecular Reorientation of Liquid Water Studied with Femtosecond Midinfrared Spectroscopy *J. Phys. Chem. A* **2008**, *112*, 11523.

(52) Rezus, Y. L. A.; Bakker, H. J. Orientational dynamics of isotopically diluted H_2O and D_2O *J. Chem. Phys.* **2006**, *125*, 144512.

(53) Foggi, P.; Bartolini, P.; Bellini, M.; Giorgini, M. G.; Morresi, A.; Sassi, P.; Cataliotti, R. S. Intermolecular and diffusive dynamics of pure acetonitrile isotopomers studied by depolarized Rayleigh scattering and femtosecond optical kerr effect *Eur. Phys. J. D* **2002**, *21*, 143.

(54) Sceats, M. G.; Stavola, M.; Rice, S. A. On the role of Fermi resonance in the spectrum of water in its condensed phases *J. Chem. Phys.* **1979**, *71*, 983.

(55) Wang, Z.; Pakoulev, A.; Pang, Y.; Dlott, D. D. Vibrational substructure in the OH stretching transition of water and HOD *J. Phys. Chem. A* **2004**, *108*, 9054.

(56) Seifert, G.; Patzlaff, T.; Graener, H. Pure intermolecular vibrational relaxation of the OH bending mode of water molecules. *J. Chem. Phys.* **2004**, *120*, 8866.

(57) Lin, Y. S.; Ramesh, S. G.; Shorb, J. M.; Sibert, E. L.; Skinner, J. L. Vibrational energy relaxation of the bend fundamental of dilute water in liquid chloroform and d-chloroform *J. Phys. Chem. B* **2008**, *112*, 390.

(58) Fournier, J. A.; Carpenter, W.; De Marco, L.; Tokmakoff, A. Interplay of Ion–Water and Water–Water Interactions within the Hydration Shells of Nitrate and Carbonate Directly Probed with 2D IR Spectroscopy *J. Am. Chem. Soc.* **2016**, *138*, 9634.

(59) Woutersen, S.; Bakker, H. J. Resonant intermolecular transfer of vibrational energy in liquid water *Nature* **1999**, *402*, 507.

(60) Torii, H. Time-domain calculations of the polarized Raman spectra, the transient infrared absorption anisotropy, and the extent of delocalization of the OH stretching mode of liquid water. *J. Phys. Chem. A* **2006**, *110*, 9469.

(61) Yagasaki, T.; Ono, J.; Saito, S. Ultrafast energy relaxation and anisotropy decay of the librational motion in liquid water: A molecular dynamics study *J. Chem. Phys.* **2009**, *131*, 164511.

(62) Gillan, M. J.; Alfe, D.; Michaelides, A. Perspective: How good is DFT for water? *J. Chem. Phys.* **2016**, *144*, 130901.

(63) Heyden, M.; Sun, J.; Funkner, S.; Mathias, G.; Forbert, H.; Havenith, M.; Marx, D. Dissecting the THz spectrum of liquid water from first principles via correlations in time and space. *Proc. Natl. Acad. Sci. U. S. A.* **2010**, *107*, 12068.

(64) Yagasaki, T.; Saito, S. A novel method for analyzing energy relaxation in condensed phases using nonequilibrium molecular dynamics simulations: Application to the energy relaxation of intermolecular motions in liquid water *J. Chem. Phys.* **2011**, *134*, 184503.

(65) Yagasaki, T.; Saito, S. Ultrafast intermolecular dynamics of liquid water: a theoretical study on two-dimensional infrared spectroscopy. *J. Chem. Phys.* **2008**, *128*, 154521.

(66) Ramasesha, K.; Roberts, S. T.; Nicodemus, R. A.; Mandal, A.; Tokmakoff, A. Ultrafast 2D IR Anisotropy of Water Reveals Reorientation During Hydrogen-Bond Switching. *J. Chem. Phys.* **2011**, *135*, 54509.

(67) Yagasaki, T.; Saito, S. Fluctuations and relaxation dynamics of liquid water revealed by linear and nonlinear spectroscopy. *Annu. Rev. Phys. Chem.* **2013**, *64*, 55.

(68) Yagasaki, T.; Saito, S. Molecular Dynamics Simulation of Nonlinear Spectroscopies of Intermolecular Motions in Liquid Water *Acc. Chem. Res.* **2009**, *42*, 1250.

(69) Jansen, T. I. C.; Snijders, J. G.; Duppen, K. Third- and fifth-order nonlinear Raman response of liquid CS2 calculated using a finite field nonequilibrium molecular dynamics method *J. Chem. Phys.* **2000**, *113*, 307.

(70) Hasegawa, T.; Tanimura, Y. Calculating fifth-order Raman signals for various molecular liquids by equilibrium and nonequilibrium hybrid molecular dynamics simulation algorithms *J. Chem. Phys.* **2006**, *125*, 074512.

(71) Miguel, B.; Zúñiga, J.; Requena, A.; Bastida, A. Theoretical Study of the Temperature Dependence of the Vibrational Relaxation of the H_2O Bend Fundamental in Liquid Water and the Subsequent Distortion of the Hydrogen Bond Network *J. Phys. Chem. B* **2014**, *118*, 9427.

(72) Hamm, P.; Stock, G. Vibrational Conical Intersections as a Mechanism of Ultrafast Vibrational Relaxation *Phys. Rev. Lett.* **2012**, *109*, 173201.

Chapter 5

Linear and Nonlinear IR Spectra of Aqueous Acid Solutions

5.1 Introduction: The Linear IR Spectrum

To open this chapter, the linear IR spectra of 0-2M HCl solutions are shown in Fig 5.1a, revealing continuous 1000-3200 cm^{-1} absorption that increases in amplitude with concentration. The IR absorption component due to HCl addition (Fig. 5.1b) can be isolated through a singular value decomposition (SVD) analysis followed by a maximum entropy method (MEM) for the extraction of physically relevant constituents (see Appendix 5A).[1] In the HCl spectral component, there is a broad feature at 1200 cm^{-1}, a feature at 1750 cm^{-1} which appears like a shoulder of the water bend, a continuum spanning the 2000-3000 cm^{-1} region, and a local maximum around 3000 cm^{-1}. For comparison, the bulk water IR spectral component matches the neat water absorption spectrum with two peaks at 1650 cm^{-1} for the water HOH bend (δ_{H_2O}) and 3400 cm^{-1} for the water O–H stretch (ν_{OH}). To account for the effect of Cl^- on the HCl acid component, SVD/MEM results are also shown for a concentration series of NaCl solutions, which reveal peaks barely shifted from the bulk water bend and stretch due to slightly weakened H-bonds donated to the anions.

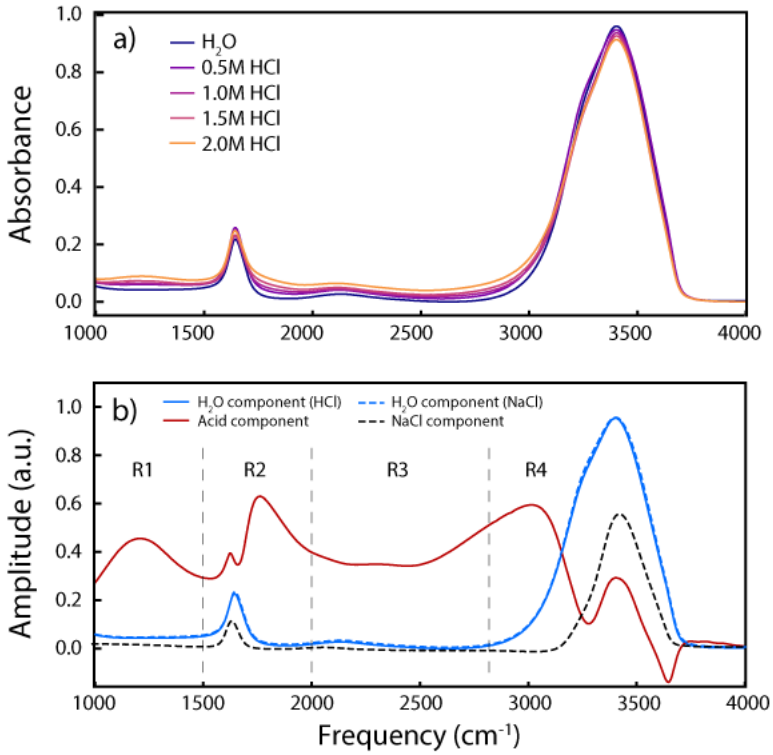

Figure 5.1: (a) Concentration series of aqueous HCl FTIR spectra. (b) Maximum entropy SVD components of the concentration series for HCl and NaCl solutions.

As discussed in Chapter 1, there is a fierce debate over the assignments of the aqueous proton IR spectrum, which in turn influence the debate on the speciation of the excess proton in terms of Eigen-like and Zundel-like complexes. The present uncertainty arises not only from the expected broad distribution of configurations, but also that the vibrational modes of the aqueous proton complex are strongly anharmonically mixed amongst themselves and with the vibrational modes of the surrounding waters. For simplicity, the IR spectrum can be decomposed into four regions whose boundaries are not strict. Region 1 spans 1000-1500 cm^{-1} and is thought to result from either asymmetric proton stretches of Zundel-like complexes[2–4] or umbrella vibrations of the H_3O^+ core of Eigen-like geometries.[5,6] Region 2 is represented by the feature at 1750 cm^{-1} and is generally considered to arise from bending modes of waters adjacent to the aqueous proton.[2,5,7–11]

However, it is unclear how Zundel-like or Eigen-like geometries contribute to this region since they are both expected to have bending vibrations in this region. Region 3 consists of the continuous absorption from 2000-2800 cm^{-1} considered to be either O-H stretches of the H_3O^+ core of Eigen-like geometries,[2,12] fluctuations of delocalized electronic charge over the Eigen complex,[13] or flanking O-H stretches of strongly hydrogen-bonded (H-bonded) waters in Zundel-like geometries.[3] Finally, Region 4 spans 2800-3200 cm^{-1} and is considered to be flanking O-H stretches of Zundel-like geometries.[3,10] Continuous absorption is also observed for isotopically dilute H^+ in DCl/D_2O solutions (Appendix 5B). The spectral shape of HX strong acid solutions is also conserved across anion exchange (Fig. 5C.1).

To characterize the aqueous proton's nuclear potential in detail, early-time (τ_2 = 100-150 fs) 2D IR spectra have been collected over the past six years, spanning Regions 1-4 in both excitation frequency ω_1 and detection frequency ω_3. These spectra reveal excited state transitions and correlations between different vibrational regions. Polarization-resolved 2D IR spectra of off-diagonal cross peaks reveal orientational correlations between vibrational modes in the form of cross peak anisotropy, which provides clues about relative transition dipole orientations of coupled vibrational modes. Obtained from TA spectra and 2D IR waiting time series, vibrational lifetimes and polarization anisotropy decays quantify the ultrafast energy and orientational relaxation kinetics of each vibrational feature. All of these features in the nonlinear spectra are useful for understanding the physical dynamics of the aqueous proton.

Collecting 2D IR spectra across the entire mid-IR came with substantial challenges to overcome. Getting broader bandwidth pulses was feasible with using thinner nonlinear crystals in DFG (Section 3.3.3), which came at a trade-off with pulse power and therefore non-linear signal amplitude. In particular, there were multiple iterations for generating reliable pulses at 1200 cm^{-1}

and collecting 2D IR spectra in along the Region 1 diagonal. The earliest and latest attempts are discussed in Section 5.3.1. In all regions, the vibrational features are broader than the bandwidth of our excitation pulses, resulting in a bandwidth in ω_1 that arises from the excitation pulse spectrum rather than the vibrational features themselves. On top of pump pulse challenges, mitigating dispersion and absorption of the broadband IR probe, particularly below 1400 cm^{-1}, required replacement of each optic in the probe beam path (see Section 3.4). To mitigate dispersion in both the pump and probe beams below 2000 cm^{-1}, we iterated through different types of sample windows, from 1mm thick CaF_2 windows to 0.2mm thick CaF_2 windows to 0.4 mm diamond windows, which is free from dispersion between 1000-1500 cm^{-1}. For all of the above reasons, the spectra are highly sensitive to experimental conditions, with further variations between replications with the same conditions. Because of this variability, any characterizations of the data presented here and subsequent conclusions are those which are supported by multiple rounds of replication.

Because there are 4 regions of interest in the linear IR spectrum, there are potentially 16 regions to study in the 2D spectrum. Not all of these regions have been studied, and the presentation of regions varies slightly to highlight the most important features. Because these data have been collected with the 2D spectrometer in different forms over the years, experimental details are provided at the end of each section, though some forms of data (e.g. polarization resolution) are missing in certain regions. The chapter is organized by first presenting an overview of the HCl 2D IR spectrum (Section 5.2), followed by the 2D IR and TA spectra of each diagonal region, with particular attention paid to Regions 1 and 2 (Section 5.3). The cross peaks between these features are presented in Section 5.4, with particular attention to both excitation and detection

in Regions 1-3. Counterion and concentration dependences, when feasible, have been included in Appendices 5C and 5D respectively.

5.2 Overview of the 2D IR Spectrum

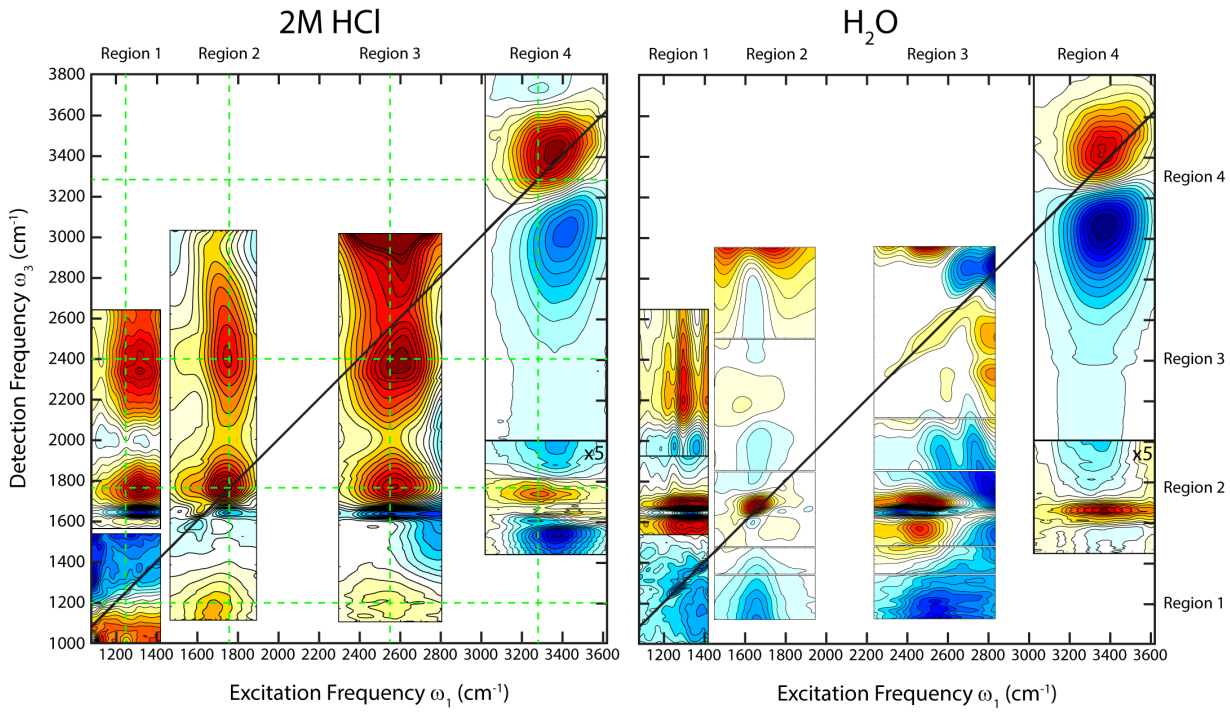

Figure 5.2: The isotropic 2D IR spectra of 2M HCl and H_2O. For excitation in Region 1, τ_2 = 150 fs. For all other excitation frequencies, τ_2 = 100 fs. Dashed green lines highlight the cross peak pattern between all features.

The 2D IR spectrum of the aqueous proton complex at early waiting time is shown in Fig. 5.2, revealing the spectroscopic features due to introduction of the proton to the solution. While typical 2D IR spectra are over a range of about 300 cm^{-1} in each direction, we have collected 2D IR data spanning approximately 2000 cm^{-1} along each dimension to produce a more complete picture of the aqueous proton vibrational spectroscopy. Along the diagonal, there are four broad ground state bleach (GSB) features, presented in orange. Excited state absorption (ESA) features

of opposite sign (blue) are difficult to discern or are not present, likely because they are broad and significantly overlap with the bleaches. The only diagonal ESAs that are clearly present are in Regions 1 and 4, centered at $(\omega_1, \omega_3) = (1200\ cm^{-1},\ 1360\ cm^{-1})$ and $(\omega_1, \omega_3) = (3200\ cm^{-1},\ 2950\ cm^{-1})$, respectively.

Between every pair of diagonal features is a cross peak, which indicates strong anharmonic coupling among all vibrational modes. This would suggest that there is a single species in solution instead of two distinct molecular ensembles. However, vibrational spectral overlap between two distinct species (like the Zundel asymmetric proton stretch and Eigen umbrella bend at 1200 cm^{-1}) could also allow for cross peaks to appear between their vibrations. Each spectral region will first be presented in detail, and the above scenarios will be discussed in Chapter 7 with the aid of spectral calculations.

5.3 2D IR Spectra Along the Diagonal

5.3.1 Region 1: Asymmetric Proton Stretch of Zundel-like Configurations

On the diagonal in Region 1 (Fig 5.3a), excitation at $\omega_1 = 1200\ cm^{-1}$ produces a 2D IR doublet: a GSB at $(\omega_1, \omega_3) = (1200\ cm^{-1},\ 1150\ cm^{-1})$ and an intense ESA centered near $(\omega_1, \omega_3) = (1200\ cm^{-1}, 1360\ cm^{-1})$, which is conserved across various concentrations (Fig. 5D.1). This arrangement indicates that the excited state transition frequency ω_{21} (1360 cm^{-1}) lies higher in energy than ω_{10} (1200 cm^{-1}), in contrast to typical anharmonic vibrational potentials where ω_{21} is lower in energy. This indicates that the shape of the vibrational potential is steeper than a quadratic form (Fig. 5.3b), as expected for the strongly H-bonded $O\text{-}H^{+}\text{-}O$ potential often associated with a Zundel-like arrangement. This pattern is also consistent, however, with the similar double-well potential shape associated with the umbrella inversion of H_3O^{+} configurations.[6] The oscillator strength of the gas-phase Zundel proton stretch is significantly

stronger than the hydronium umbrella mode in the gas phase,[11] so it is expected that this feature primarily arises from Zundel-like proton stretching motion. This 2D IR spectrum is consistent with the results of Dahms *et al*.,[4] but with our broader bandwidth pulses we reveal a stretched line shape in both dimensions.

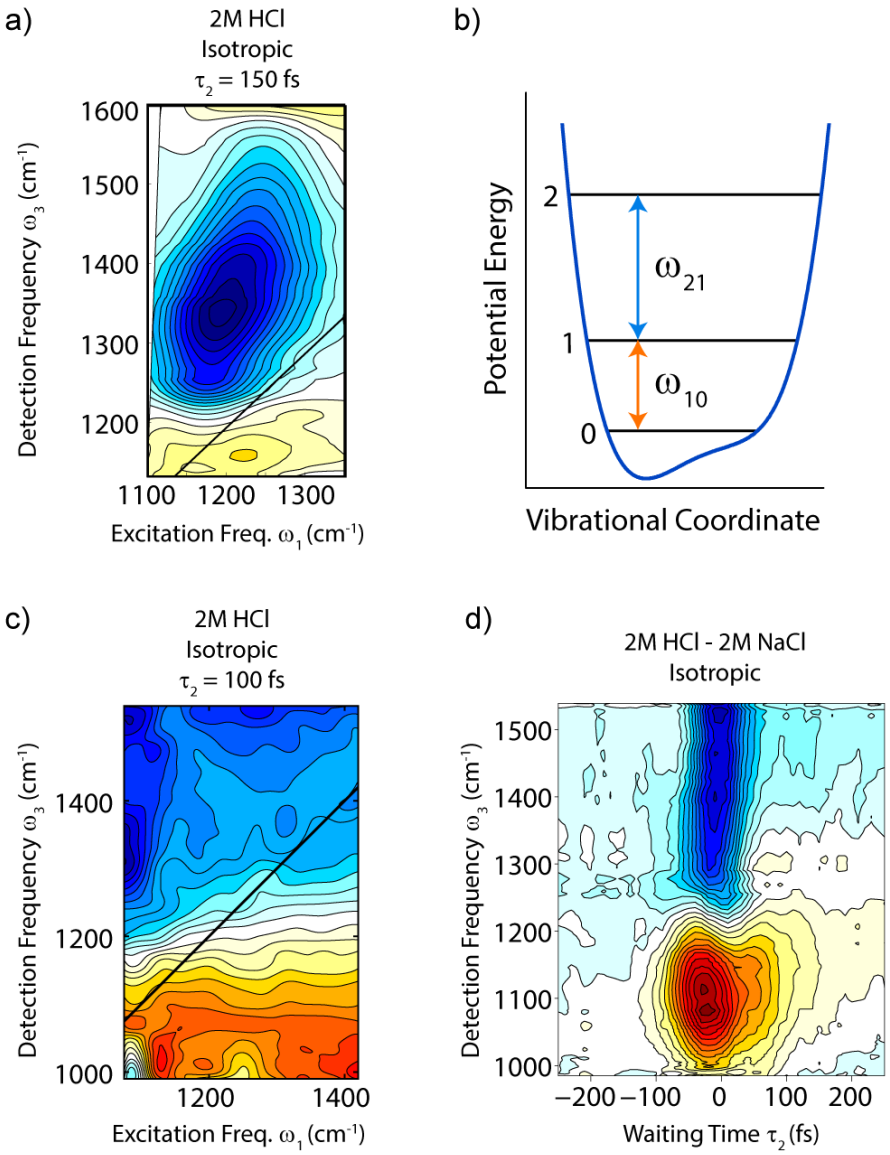

Figure 5.3: 2D IR and TA Spectra of the Region 1 diagonal. (a) The isotropic 2D IR spectrum of 2M HCl at τ_2 = 150 fs. b) A cartoon of the potential energy shape, highlighting that $\omega_{21} > \omega_{10}$. (c) The Region 1 diagonal 2D IR spectrum of 2M HCl taken with temporally shorter and spectrally broader pump pulses. (d) The isotropic TA spectrum of 2M HCl, subtracting off the background response represented by 2M NaCl.

Fig 5.3c shows the 2D IR spectrum in this region taken with updated experimental conditions to reduce artifacts from dispersion. The spectrum in Fig. 5.3a was taken with relatively long pulses (τ_p = 100 fs) with bandwidth of 180 cm^{-1} at full-width half maximum (FWHM) transmitting through 1 mm thick CaF_2 sample windows, which were later found to have dispersion issues (Fig. 3.10c). The spectra of 2M HCl taken in Fig. 5.3c was measured with spectrally broader and temporally shorter pulses ($\Delta\omega$ = 280 cm^{-1} FWHM, τ_p = 70 fs) using diamond sample windows which are not dispersive in this region. The TA spectral evolution with shorter pump pulses in this region (Fig. 5.3d) shows little noticeable dispersion revealing that the excited state absorption significantly decays by 100 fs. As a result, the signal-to-noise ratio of the 2D IR spectrum at τ_2 = 100 fs is particularly low.

The updated data collection conditions have revealed some differences between the two datasets. First, the signal-to-noise in Fig. 5.3a is significantly higher than in Fig. 5.3c. This likely arises from two effects. First, there are approximately 30% reflective losses off of the diamond sample windows due to its high refractive index, reducing the amount of light at the detector. Second, the dispersion introduced by the 1 mm thick CaF_2 windows used in Fig. 5.3a implies that there is still significant nonresonant response at τ_2 = 150 fs. As a result, there are likely artifacts due to unwanted signals and temporal dispersion across the ω_1 dimension. While the spectrum in Fig. 5.3c is noisier, the experimental conditions are more reliable. To someday improve signal-to-noise with reliable conditions, we have taken steps to increase the amount of probe light at the detector (discussed in Chapter 3). Combined with sampling schemes that reduce sample collection time and therefore increase averaging, it should be feasible to collect cleaner data in this region.

Even with knowledge of the transition frequencies and shape of the potential, it is not straightforward to draw definitive *structural* conclusions. Recent theoretical analysis of Daly *et*

al.[3] demonstrated that Zundel-like proton stretching potentials can arise from a continuum of configurations between traditionally defined Eigen and Zundel geometric criteria, and predicted nearly identical IR spectra for Eigen and Zundel configurations in solution. Therefore, connecting the vibrational spectrum to cluster geometry requires an understanding of additional coordinates within the vibrational spectrum, and will be the subject of analysis in Chapter 7.

Experimental Details

The 2D IR spectrum in Fig. 5.3a was taken of 2M HCl in H_2O, with a 6 μm Mylar spacer between two 1 mm thick CaF_2 windows. The 2 μJ pump pulses centered at 1250 cm^{-1} were generated via OPA/DFG in $AgGaS_2$ as described in Chapter 3. The polarization of the pump was rotated from S-polarized to the "magic angle" for collecting isotropic response (54.7° from the P-polarized probe) with a CdSe λ/2 waveplate (Alfalas). The probe was split with a 50:50 KBr beamsplitter, where one arm was sent to the sample and the second arm used as a reference arm traveling straight to the detector. The top stripe on the 2×64 MCT array collected transient absorption data from the sample, whereas the bottom stripe was used to reference the intensity fluctuations of the probe.

The 2D IR and TA spectra shown in Figs. 5.3c-d were taken of 2M HCl with a 3.6 μm Mylar spacer sandwiched between one 0.4 mm thick diamond window in front of the sample and one 0.2 mm CaF_2 behind. The 10 μJ, P-polarized pump pulses centered at 1250 cm^{-1} were generated by OPA/DFG in GaSe, characterized in detail in Chapter 3. A 45°-polarized component of the probe transmitted through the sample then split into S and P polarization components for simultaneous detection of the ZZZZ and ZZYY spectra, discussed in more detail in Chapter 3.

5.3.2 Region 2: Bending Vibrations

5.3.2.1 Isotropic 2D IR Surfaces

The $\tau_2 = 100$ fs isotropic 2D IR spectrum of 2M HCl in the 1500-2000 cm^{-1} region (Fig. 5.4) consists of two doublets along the diagonal centered at $\omega_1 = 1680$ cm^{-1} and $\omega_1 = 1750$ cm^{-1} (see Chapter 4 for the water 2D IR spectrum). These features arise from the water bend δ_{H_2O} and the bending vibrations of the hydrated proton complex δ_{H^+}. While this feature likely encompasses Zundel-like and hydronium bending motions, it is expected that the asymmetric, concerted bending vibration in Zundel-like complexes is more intense because of strong anharmonic mixing with the proton stretch in the gas-phase ion.[14] The two doublets are conserved across HCl concentration below 3M (Fig. 5D.2) and in 2M HI solution (Fig. 5C.2). The presence of two maxima along the diagonal, revealed by the quartic transition dipole scaling in 2D IR spectra, indicates that the δ_{H^+} feature is a separate resonance from δ_{H_2O} rather than a tail of the water peak. Both GSBs are accompanied by ESAs extending from $\omega_3 \approx 1600$ cm^{-1} to below 1500 cm^{-1}. Off the diagonal, there is a broad bleach cross peak feature that extends across (ω_1, ω_3) = (1500-1700 cm^{-1}, 1750 cm^{-1}). Because the feature is intense at the earliest measurable waiting time and extends in ω_1 beyond the linewidth of the δ_{H_2O} feature, we assign it as a cross peak arising from strong anharmonic coupling between the high-frequency edge of Region 1 to δ_{H^+}. There is also likely anharmonic coupling to δ_{H_2O}, but that cross peak would be limited to the region around (ω_1, ω_3) = (1650 cm^{-1}, 1750 cm^{-1}). The ω_1 center frequency of the δ_{H_2O} doublet (1670 cm^{-1}) is slightly blueshifted compared to the FTIR center frequency (1650 cm^{-1}) likely due to destructive interference with the δ_{H_2O} ESA.

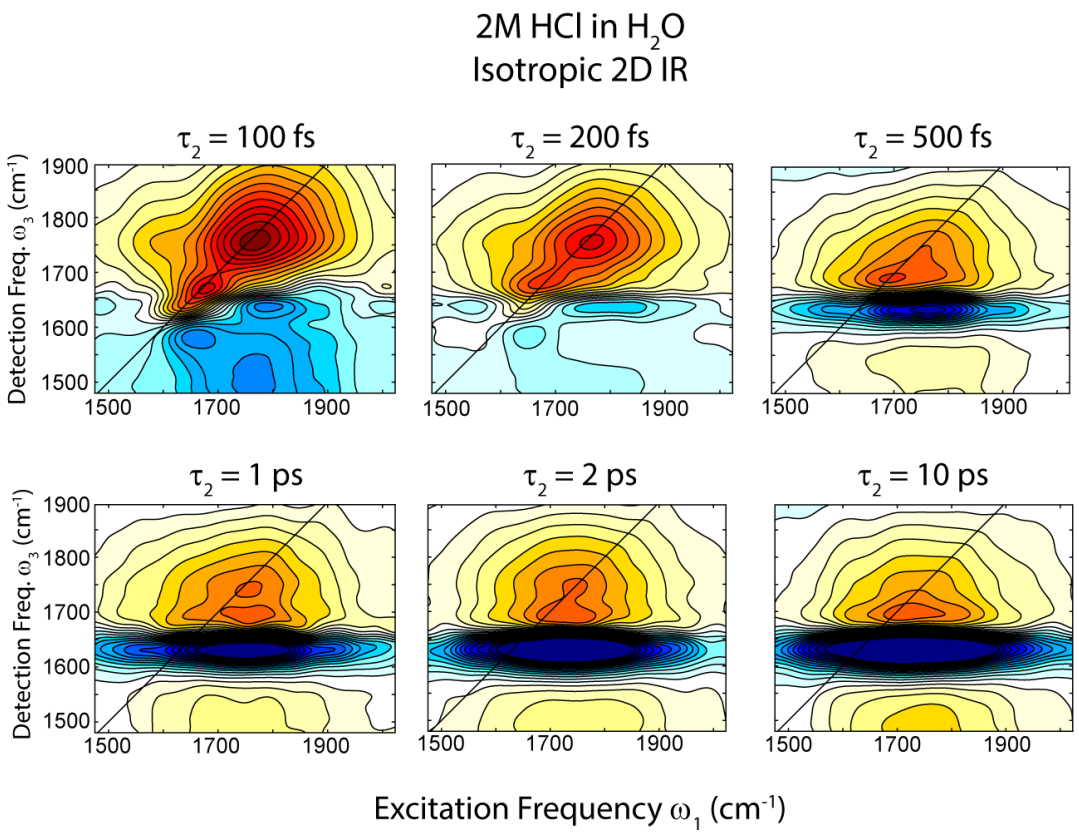

Figure 5.4: The isotropic 2D IR waiting time series of 2M HCl along the Region 2 diagonal. Spectra are all normalized to the absolute maximum value in the τ_2 = 100 fs spectrum.

As waiting time increases, the early-time signal decays by τ_2 = 500 fs and the hot ground state (HGS) signal grows in. As discussed in Chapter 4, the HGS arises from changes in absorption due to the dissipation of pump energy into low-frequency motions of the solution's H-bond network. In detection frequency, the HGS spectrum appears as induced absorption at ω_3 = 1620 cm^{-1} with flanking absorption losses. This is consistent with a temperature difference IR spectrum, where δ_{H_2O} narrows and gains intensity with increasing temperature. Since pump excitation energy is distributed throughout the sample, pump-frequency correlation is lost and the HGS lineshape along ω_1 reflects the overlap of the pump spectrum and linear absorption spectrum. While the spectrum appears like a temperature-difference spectrum, the origin for the signal is

non-equilibrium due to its rise on the ultrafast timescale. However, in both the HGS and temperature-difference spectra, the signals arise from deposition of energy into low-frequency modes that weaken the H-bond network around δ_{H_2O} and δ_{H^+} oscillators.

5.3.2.2 Anisotropic 2D IR Surfaces

The 2D anisotropy spectra (Fig. 5.5) present the polarization anisotropies of δ_{H_2O} and δ_{H^+} as functions of both ω_1 and ω_3. All spectra show positive anisotropy over δ_{H^+}, which vanishes by τ_2 = 10 ps. The 2D anisotropy surface at τ_2 = 100 fs displays anisotropy lower than the expected 0.4 value at this early waiting time, likely due to interference with residual CaF_2 nonresonant signal, and will not be analyzed here.

At τ_2 = 200 fs, the anisotropy across the δ_{H^+} bleach diagonal at 1750 cm^{-1} takes on values of roughly 0.3, and high anisotropy (≥0.4) is also seen in the ESA around (ω_1, ω_3) = (1750 cm^{-1}, 1500-1650 cm^{-1}). The anisotropy of the uphill cross peak for ω_1 < 1600 cm^{-1} is about as high as the δ_{H^+} diagonal and does not demonstrate any particular trend with ω_1 or ω_3. The anisotropy of δ_{H_2O} along ω_1 = 1650 cm^{-1} is strikingly different, displaying low anisotropy values of ~0.1. The δ_{H_2O} anisotropy extends to ω_3 > 1650 cm^{-1} since the δ_{H_2O} ESA incorporates a transition directly from one quantum of δ_{H_2O} to one quantum of ν_{OH}, which is at higher frequency and coupled to the bend overtone via Fermi resonance (see Chapter 4). The fast anisotropy decay of δ_{H_2O} is due to the delocalized nature of the water bend, which allows fast excitation transfer and orientational scrambling.[15] The frequency resolution of the 2D anisotropy measurement clearly separates the anisotropy components with respect to different excited vibrations, which are projected together in a TA measurement.

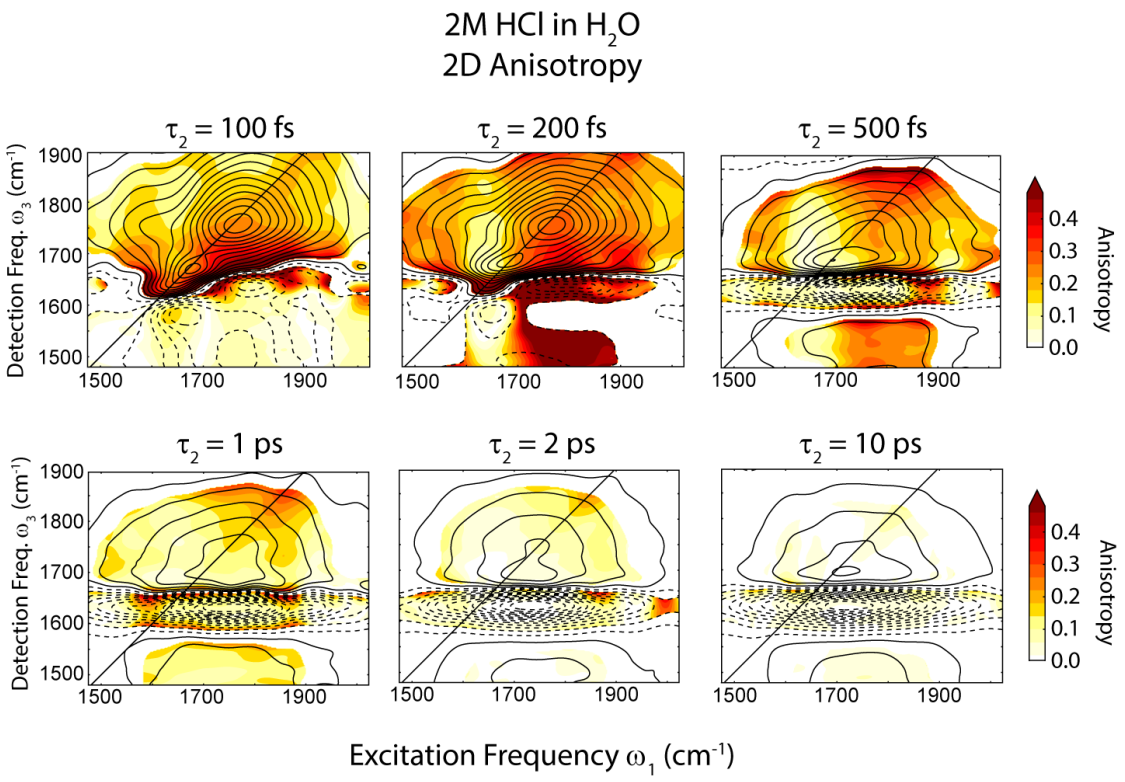

Figure 5.5: The 2D anisotropy waiting time series of 2M HCl along the Region 2 diagonal. Black contours are from the corresponding isotropic spectrum, where solid lines indicate positive features and dashed lines indicate negative features. 2D anisotropy is only shown in regions of the spectra whose absolute intensity is at least 10% of the maximum.

As waiting time increases, the anisotropy of δ_{H^+} decreases while the anisotropy of the δ_{H_2O} band remains low. At τ_2 = 500 fs, the anisotropy of δ_{H^+} in the bleach regions is around 0.2, but the anisotropy in the induced absorption region around ω_3 = 1620 cm^{-1} is even lower at approximately 0.1. Along the diagonal at 1900 cm^{-1}, the polarization anisotropy is higher which can be attributed to small residual scatter contributing preferentially in the ZZZZ polarization geometry. As the HGS grows in, the anisotropy value is relatively uniform across the HGS, particularly at τ_2 = 1 ps and beyond. By 10 ps, the anisotropy is essentially fully decayed. These 2D anisotropy measurements confirm that the HGS signal retains its own anisotropy.

5.3.2.3 Polarization-Resolved Transient Absorption Kinetics

The polarization-resolved TA spectral evolution of δ_{H^+} have been measured in Region 2. By comparing the 2M NaCl and 2M HCl spectra (Fig. 5.6), it is apparent that H_2O relaxation processes dominate the dynamics for detection frequencies $\omega_3 < 1700$ cm^{-1}. In H_2O, the bleach ($\omega_3 = 1660$ cm^{-1}) rapidly decays with a 170 fs time constant followed by an HGS signal rise on a 840 fs timescale.[15]

In addition to the H_2O features, the TA spectra for 2M HCl show a prominent bleach centered at $\omega_3 = 1750$ cm^{-1} from δ_{H^+} in the frequency range not influenced by bulk H_2O. Unlike in 2M NaCl, these spectra show a striking polarization dependence, as seen in Figs. 5.6c-d. After the instrument-response limited spike around $\tau_2 = 0$, the parallel spectrum rises to a maximum at $\tau_2 = 170$ fs for all detection frequencies between 1730-1900 cm^{-1}, before a slower decay toward the offset resulting from the HGS. The perpendicular trace does not show such a strong recurrence, but grows slowly toward the same offset over several ps.

The vibrational relaxation decay of the 1750 cm^{-1} bleach is presented in Fig. 5.7a as the isotropic TA trace, normalized at $\tau_2 = 100$ fs. The vibrational relaxation follows an exponential decay with a 280 fs timescale and a significant offset due to the HGS. The fast timescale of these processes indicates rapid vibrational energy dissipation. However, the anisotropic trace decays on a much slower timescale, on the order of 3 ps, which is unusual because it is an order of magnitude longer than the population of the vibrational excitation and it is still distinguishable at long waiting times.

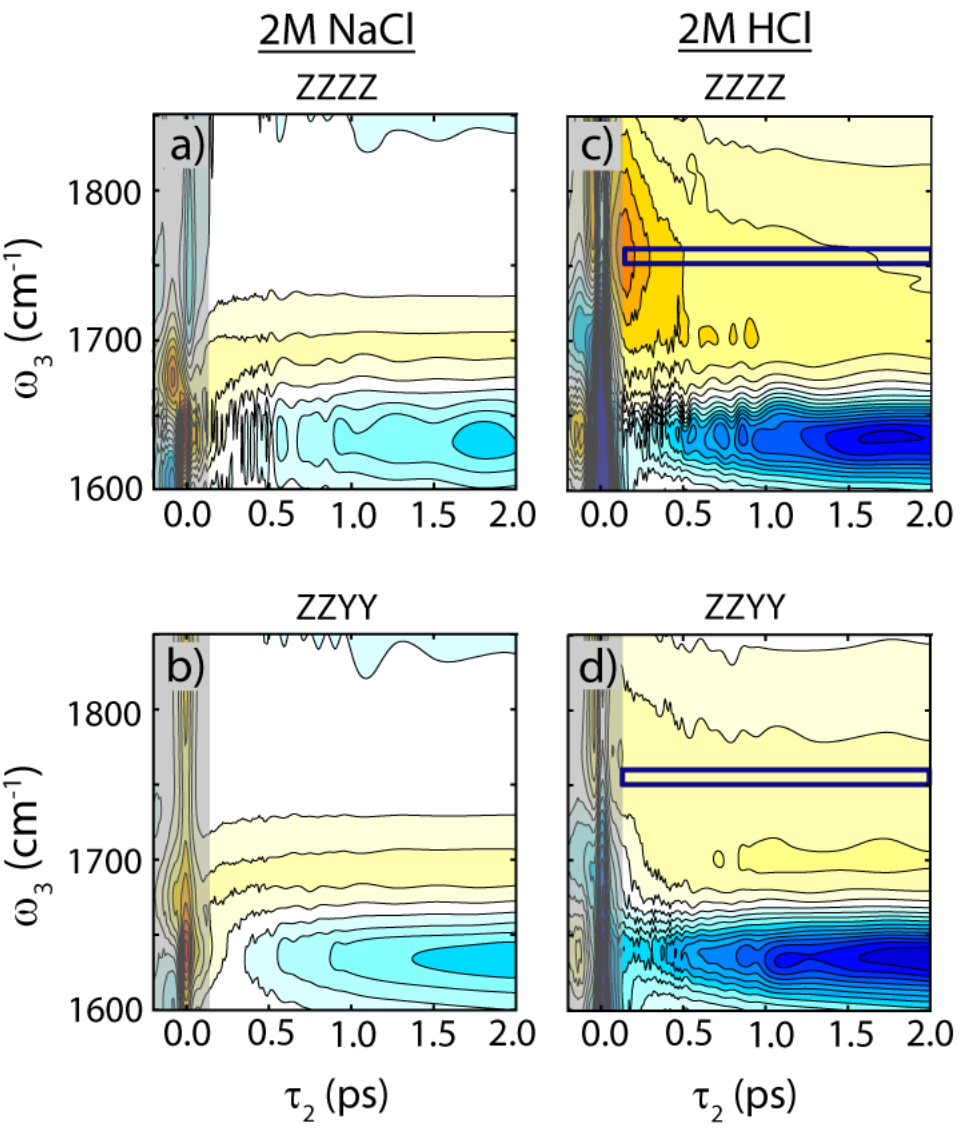

Figure 5.6: TA spectra of the Region 2 diagonal of (a)-(b) 2M NaCl and (c)-(d) 2M HCl in the ZZZZ and ZZYY pump-probe polarization schemes, respectively. Surfaces are on a common normalization equal to the maximum amplitude of the isotropic 2M HCl spectrum at τ_2 = 10 ps. In all spectra, the signal around τ_2 = 0 fs at all ω_3 is due to the instantaneous polarization response from the solution and the CaF_2 windows. Grayed out regions indicate waiting times before τ_2 = 200 fs, which are omitted from analysis. The colored boxes in (c) and (d) represent the frequency range ω_3 = 1750–1760 cm^{-1} plotted in Fig. 5.7.

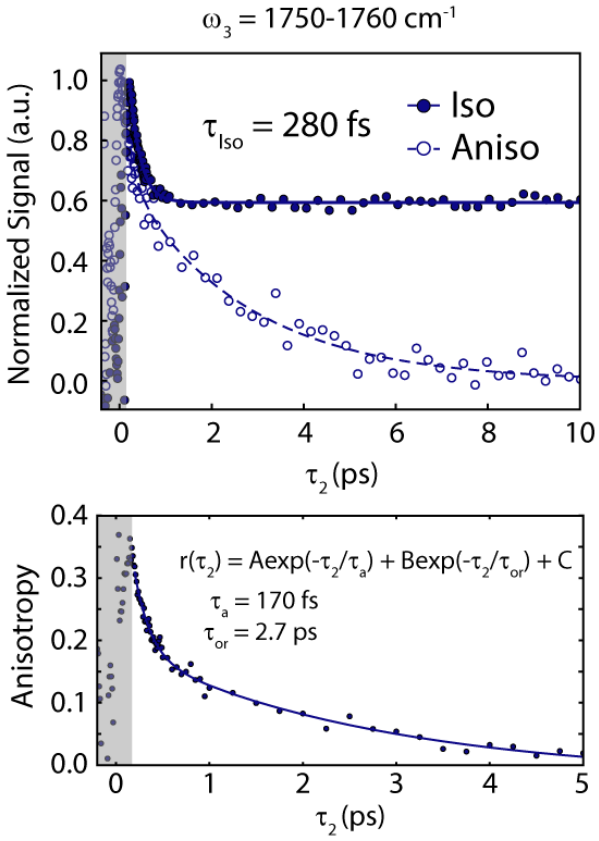

Figure 5.7: TA isotropic and anisotropic traces and TA anisotropy of δ_{H^+} in 2M HCl at ω_3 = 1750–1760 cm^{-1}. (a) Isotropic and anisotropic TA traces from τ_2 = 200 fs to 10 ps, the latest measured waiting time, normalized to early-time values at τ_2 = 100 and 200 fs, respectively. (b) TA anisotropy decay after τ_2 = 200 fs, fit to a biexponential decay (solid line). Grayed regions denote waiting times excluded from analysis due to the instrument response and interference from window nonresonant signal. Together, these graphs demonstrate that the anisotropic signal persists longer than the isotropic signal but decays to zero by 10 ps.

To isolate the orientational relaxation component of the TA spectrum, the TA anisotropy decay as a function of waiting time is shown in Fig. 5.7b. At τ_2 = 200 fs, the TA anisotropy starts at 0.35 and decays biexponentially to zero with 170 fs and 2.7 ps time constants. The fast component likely arises from vibrational energy transfer within the aqueous proton complex. However, the anisotropy persists over an order of magnitude longer than the 280 fs lifetime of δ_{H^+} and the 80 fs anisotropy decay of the H_2O bend in neat water (see Chapter 4).[15] With the 2D

anisotropy measurements (Fig. 5.5), the anisotropy appears preserved in the HGS signal, which is peculiar because it suggests that this energy dissipation signal retains some orientational information. The slow relaxation of the anisotropy is not strongly influenced by the identity of the counterion (Fig. 5C.3), but the relaxation timescale increases modestly with acid concentration (Fig. 5D.3).

The orientational relaxation of δ_{H^+} indicates that the transition dipole moment orientation is diffusing on a ps timescale, but the physical origin of this reorientation is not immediately clear. The process is not likely vibrational energy transfer between δ_{H^+} chromophores because the relaxation timescale increases with concentration. The timescale is similar to ca. 3 ps H-bonding reorganization in neutral H_2O,[16,17] suggesting that the origin is due to collective H-bond network rearrangement. However, it is expected that the H-bonds in the immediate vicinity of the excess charge would be relatively stronger than in pure H_2O by a few kcal/mol, suggesting that these proximal H-bonds would remain relatively intact at room temperature. Additionally, the reorientation of an intact Zundel-like or Eigen-like arrangement would involve the rupture of many H-bonds, which is energetically costly compared to thermal fluctuations. Another possibility is that the anisotropy decay occurs as a result of Grotthuss proton transfer through a bent H-bond network, but this hypothesis needs to be assessed carefully and will be the subject of Chapter 8.

Experimental Details

The 2D IR and TA spectra shown in this section were taken with 2M HCl in a 3.6 μm Mylar spacer sandwiched between two 0.2 mm thick CaF_2 windows, which produced OD 1 linear absorption at 1650 cm^{-1}. The 7 μJ, S-polarized pump pulses were centered at 1750 cm^{-1} with 530 cm^{-1} bandwidth FWHM. A 45°-polarized component of the probe was sent to the sample, then

split into S and P polarization components for simultaneous detection of the ZZZZ and ZZYY spectra as presented in Chapter 3.

5.3.3 Region 3: Continuous IR Absorption of O-H Stretches Adjacent to the Excess Proton

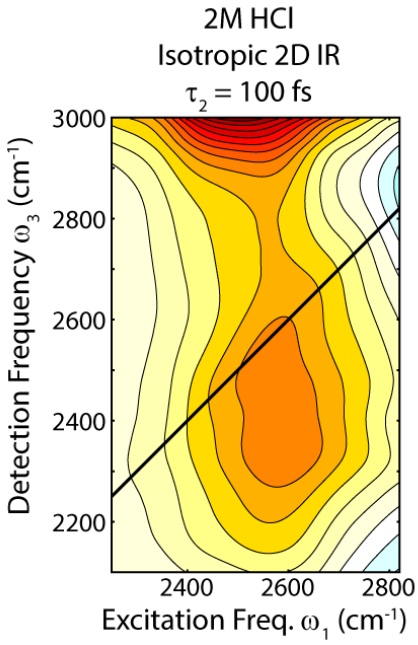

Figure 5.8: The early-time isotropic 2D IR spectrum of the Region 3 diagonal in 2M HCl.

Region 3 spans ~2,000-2,800 cm^{-1}, giving rise to a broad 2D bleach (Fig. 5.8). In contrast to the low absorption in the FTIR spectrum in this region (see Fig. 5.1), the 2D feature shows a broad maximum centered at ω_3 = 2400 cm^{-1}. This difference between the FTIR and 2D IR spectra likely derives from the quartic intensity scaling of the 2D measurement. These observations indicate that Region 3 has a distinct molecular origin, rather than being a featureless continuum. This region is attributed to O-H stretches adjacent to the excess proton, either as hydronium O-H stretching motions[2] or as strongly H-bonded flanking O-H stretches in Zundel-like arrangements.[3] The bleach appears roughly homogeneously broadened, which implies O-H stretch frequency

fluctuations faster than the time resolution of the experiment. With the limited pump pulse bandwidth, we cannot draw conclusions about the spectral dynamics of the Region 3 bleach, but a broadband excitation source will provide the necessary bandwidth to reliably measure the 2D lineshape of this feature. There is no visible ESA counterpart to the bleach, likely because both are broad and highly overlapping. For $\omega_3 > 2800$ cm^{-1}, there is a bleach wing associated with the cross peak to Region 4, but no visible induced absorption. Overlap between the ESA of the cross peak to Region 4 may explain why the maximum of the Region 3 bleach lies below the diagonal.

The TA spectrum of Region 3 (Fig. 5.9) shows fast relaxation of the broad bleach, followed by a ps-timescale rise of the hot ground state. Above $\omega_3 = 2800$ cm^{-1}, the tail of the cross peak to Region 4 is present. Comparing the ZZZZ and ZZYY spectra in Figs 5.9a and 5.9b, there is a difference in amplitude around $\tau_2 = 0$ fs, but otherwise the spectra look similar. Fig. 5.9c shows the evolution of the isotropic response integrated over $\omega_3 = 2300$-2600 cm^{-1}. The bleach decays on a 100 fs timescale, followed by a 1.6 ps rise of the HGS to a nonzero offset. The polarization anisotropy in this region (Fig. 5.9d) decays on a 125 fs timescale to zero offset. The fast vibrational relaxation and anisotropy decay are indicative a delocalized vibration that efficiently relaxes through many relaxation channels in solution. This is perhaps not too surprising given the frequency overlap between Region 3 and the H_2O bend-libration combination bend at 2100 cm^{-1}, which is highly delocalized and strongly coupled to low-frequency modes of the solvent. Despite the presence of HGS signal in this region, we do not observe anisotropy out to multiple ps like in Region 2, which means this anisotropy is not useful for reporting on physical reorientation. Interestingly, recent TA studies in 7M HCl solution have measured anisotropy decay in this region on a 1.6 ps timescale,[18] which may imply that the nature of the vibrational excitation changes at significantly higher concentrations.

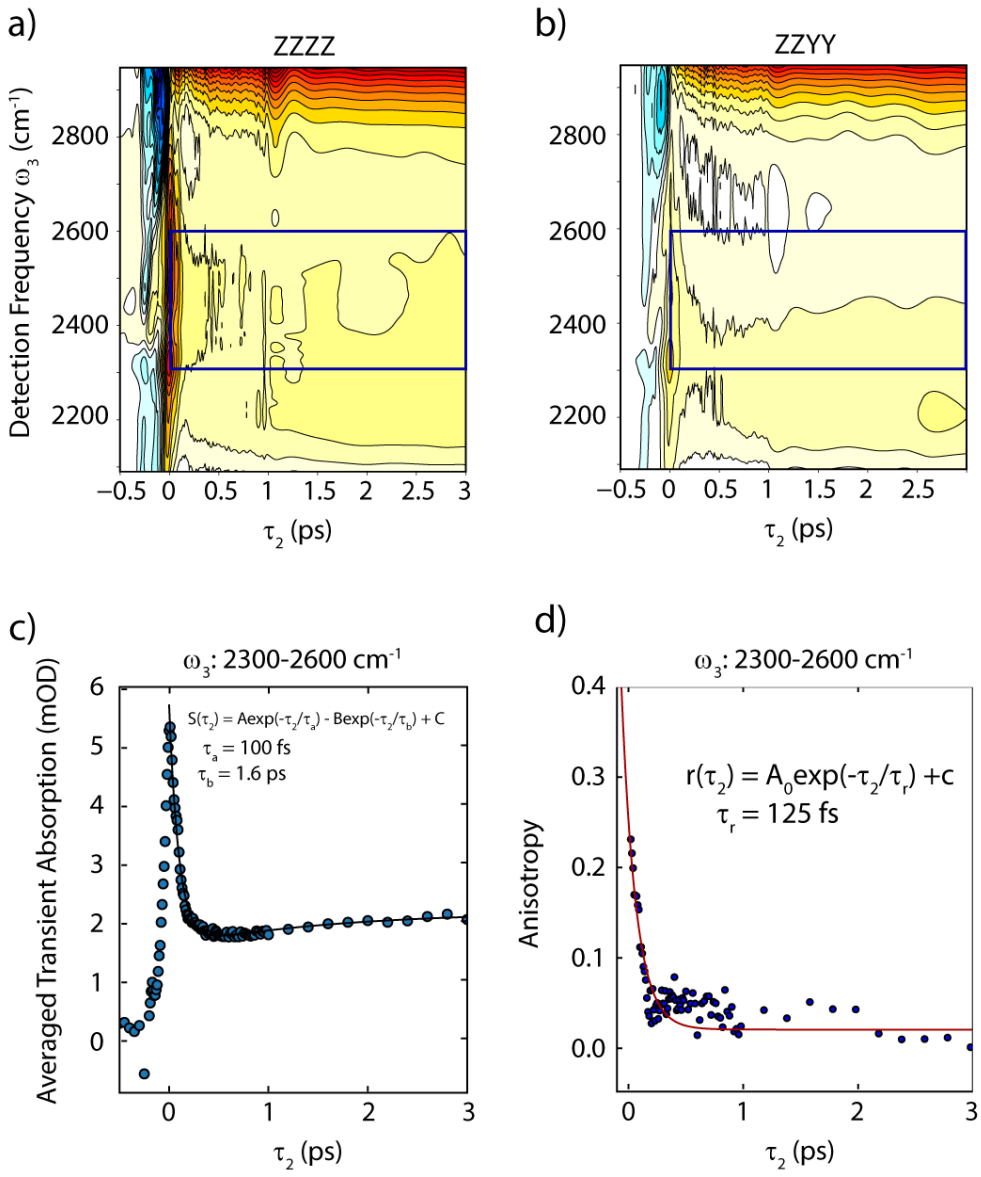

Figure 5.9: TA spectra of the Region 3 diagonal with the (a) ZZZZ and (b) ZZYY polarization schemes. The two spectra are plotted on the same scale. (c) Isotropic and (d) anisotropy TA traces in this region, averaged over ω_3 = 2300-2600 cm^{-1}. The colored boxes in (a) and (b) represent the frequency range ω_3 = 2300–2600 cm^{-1} plotted in (c) and (d).

Experimental Details

This dataset was taken for 2M HCl in H_2O, with a 6 μm Mylar spacer between two 1 mm thick CaF_2 windows. The pump pulses were centered at 2550 cm^{-1} with 300 cm^{-1} bandwidth FWHM. The polarization of the pump was rotated between S, P, and magic angle (54.7° from the

P-polarized probe) with a CdSe λ/2 waveplate (Alfalas), such that spectra were not collected simultaneously. The probe was split with a 50:50 KBr beamsplitter, where one portion was sent to the sample and the second half was used as a reference traveling straight to the detector. The top stripe on the 2×64 MCT array collected transient absorption data from the sample, whereas the bottom stripe was used to reference the intensity fluctuations of the probe.

5.3.4 Region 4: Flanking O–H Stretches of Zundel-like Complexes

A 2D IR waiting times series of 4M HCl in Region 4 is shown in Fig. 5.10a. From earlier analysis of this 2D IR spectral region by Thämer *et al.*, this region is expected to report on the flanking O-H stretches in Zundel-like configurations.[10] However, it is unclear if these flanking stretches behave as local modes due to different local H-bonding environments, or have more normal mode character over the complex. At $\tau_2 = 100$ fs, the bleach is centered at (ω_1, ω_3) = (3250 cm^{-1}, 3300 cm^{-1}) and the ESA is anharmonically downshifted in ω_3 to a peak position of (ω_1, ω_3) = (3250 cm^{-1}, 2950 cm^{-1}). The response by this region is dominated by bulk water, as seen by the 4M NaCl 2D IR series (Fig. 5.10b), where the broad ESA arises from strong anharmonic coupling between water molecules in the liquid.[19,20] Comparing the acid and salt solution spectra at $\tau_2 = 100$ fs, the Region 4 bleach of the acid species is slightly broader in both ω_1 and ω_3 and the ESA intensity is slightly lower in the acid spectrum. Both of these details point to increased bleach intensity from the acid continuum. Additionally, there is a weak induced absorption feature peaked at $\omega_3 = 3600$ cm^{-1}. All of these characteristics are preserved when the counterion is exchanged (Fig. 5C.4).

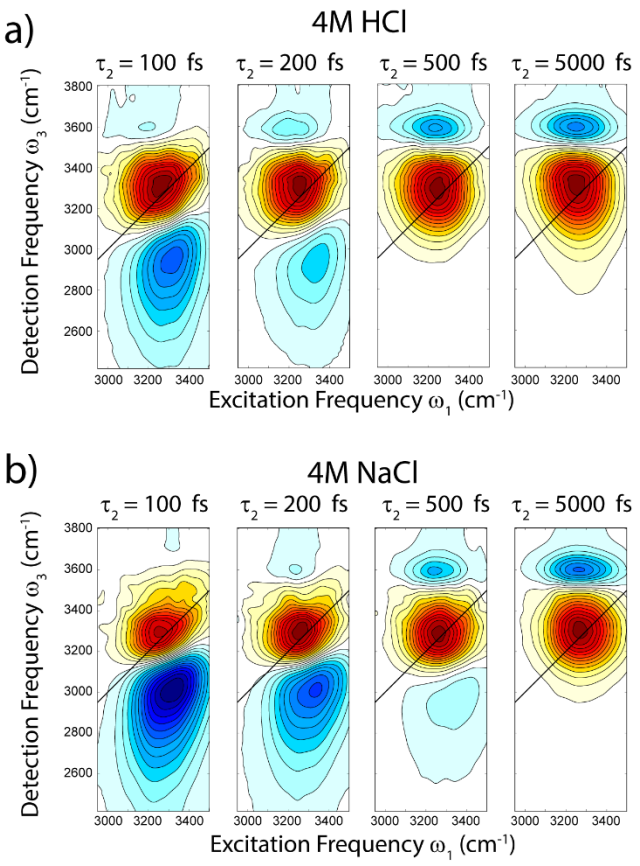

Figure 5.10: Isotropic 2D IR waiting times series of (a) 4M HCl and (b) 4M NaCl solutions. Spectra are each normalized to their respective absolute maximum values.

Inspection of the rest of the waiting time series shows that the early-time response decays by τ_2 = 500 fs, giving way to the growing HGS signal. The HGS for the water O-H stretch consists of an intense bleach centered at $\omega_3 = 3300$ cm^{-1}, accompanied by a small, narrow induced absorption at $\omega_3 = 3600$ cm^{-1}. This pattern reflects the bleaching of strongly H-bonded O-H oscillators and the induced absorption of weakly H-bonded O-H oscillators upon ultrafast energy deposition. The small induced absorption at $\omega_3 = 3600$ cm^{-1} in the $\tau_2 = 100$ fs surface reveals that the spectral signatures of this energy deposition are present at the earliest measurable waiting times in the acid solution. This indicates that the most redshifted, strongly H-bonded O-H stretches are

more intimately coupled to nonadiabatic relaxation pathways in solution.[20] This is reinforced by the faster relaxation of the ν_{OH} ESA in HCl compared to in NaCl.

In Fig. 5.11, the center-line slope decay (CLS) of the O-H stretch bleach is compared between acid and salt solutions. The initial values of the center-line slope indicate the degree of inhomogeneous broadening in each solution, while the timescale of the decay reports on the frequency-frequency correlation loss for the O-H stretch. The CLS in NaCl solution starts at an initial value of 0.2 and decays to zero on a 270 fs timescale, which is slightly longer than the 170 fs value measured for bulk water.[20] This reveals that the O-H stretch oscillators in salt solution fluctuate on a slightly slower timescale than in bulk water due to the obstructions imposed by the solute. For context, 4M concentration corresponds to approximately 6 water molecules per ion, indicating there is little bulk water in solution. In 4M HCl, the initial center line slope is above 0.3, indicating more inhomogeneous broadening than in NaCl in the presence of the excess proton, and longer decay timescale of 360 fs. The larger initial value indicates that acid solutions create a broader distribution of water H-bonding geometries in solution, which could arise from flanking waters in Zundel-like complexes or waters in second solvation shells of the excess proton.

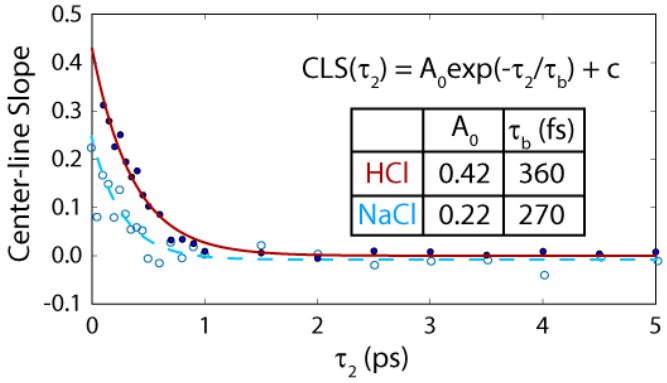

Figure 5.11: Center-line slope decays of the O–H stretch in 4M HCl and 4M NaCl, fit to exponential decays.

The strong response from bulk O-H oscillators makes it challenging to isolate the response in Region 4 due to the acid. Additionally, because these samples are assembled sandwiched between two windows without spacers, we cannot currently control the pathlength. However, it may be feasible to isolate this signal with an HCl concentration series of 2D IR spectra and an SVD analysis (see Appendix 5A) to find the component of the 2D IR spectrum due to increasing HCl concentration. This may help determine if the peak at 3100 cm^{-1} is a separate peak from the O-H stretch or reflects the broadening of the tail of O-H stretch absorption.

Experimental Details

This dataset was taken with 4M HCl or 4M NaCl in H_2O sandwiched between two 1 mm thick CaF_2 windows without spacer. The pump pulses centered at 3250 cm^{-1} were generated via OPA as described in Chapter 3. The polarization of the pump was rotated to magic angle (54.7° from the P-polarized probe) with a MgF_2 λ/2 waveplate (Alfalas). The probe was split with a 50:50 KBr beamsplitter, where one arm was sent to the sample and the second arm used as a reference arm traveling straight to the detector. The top stripe on the 2×64 MCT array collected transient absorption data from the sample, whereas the bottom stripe was used to reference the intensity fluctuations of the probe.

5.3.5 Summary of 2D IR Spectra Along the Diagonal

The 2D IR and TA spectra of Regions 1-4 along the diagonal provide new spectral information regarding the vibrational modes of aqueous proton complexes. In Region 1, the ESA appears at higher ω_3 than the GSB, which is consistent with the confined anharmonic potential shape for a shared proton oscillating between two waters in Zundel-like arrangements. This potential shape is also expected for umbrella inversion, but the Zundel proton stretch is expected

to be more intense. The feature in Region 2 is due to bending motions of the aqueous proton complex, once again likely to be over-represented by Zundel-like configurations due to intensity borrowing from the asymmetric proton stretch. In particular, this feature displays anisotropy decay kinetics with a 2.7 ps timescale which is consistent with physical reorientation perhaps associated with proton transfer. Region 3 represents a broad feature peaked at $\omega_3 = 2400$ cm^{-1} due to strongly redshifted O-H stretches, either in hydronium or strongly H-bonded flanking stretches in Zundel-like complexes. Region 4 is likely represented by the flanking O-H stretches of Zundel-like complexes and demonstrates slower frequency fluctuation dynamics than in bulk water.

5.4 Cross Peaks

The 2D IR spectra along the diagonal are useful for characterizing the vibrations in detail, but these assignments can be further scrutinized by examining the cross peaks between each of these features. In particular, polarization dependence of the cross peaks is invaluable for determining orientational relationships between these vibrations, which provide a stringent test for the assignments that cannot be accomplished with linear spectroscopy alone. "Uphill" cross peaks refer to the regions were $\omega_3 > \omega_1$, whereas "downhill" refer to the opposite case $\omega_3 < \omega_1$. Analogous uphill and downhill cross peaks between the same two vibrations can be collected to ensure a self-consistent description of the coupling between those modes.

5.4.1 Uphill Cross Peak Between Regions 1 and 2

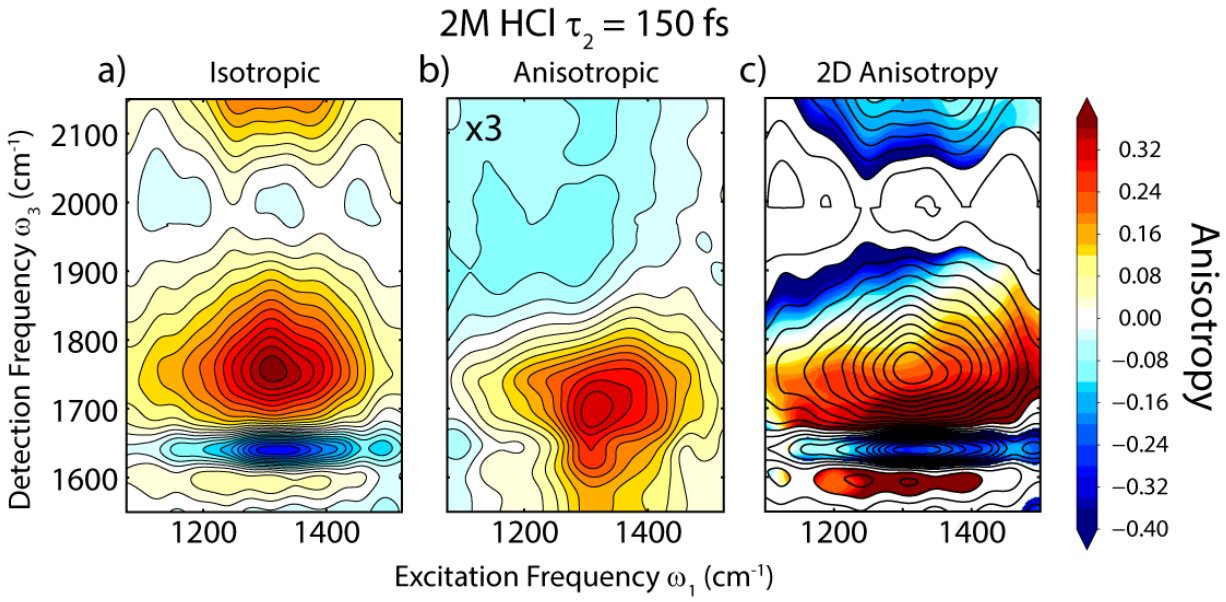

Figure 5.12: Polarization-resolved 2D IR cross peak spectra at τ_2 = 150 fs between Regions 1 and 2 in 2M HCl. (a) Isotropic, (b) Anisotropic, and (c) 2D anisotropy representations of the 2D IR spectrum. The anisotropic spectra is scaled by a factor of three compared to the isotropic spectum. Black contours in (c) are from the isotropic spectrum. 2D anisotropy is only shown in regions of the spectra whose absolute intensity is at least 10% of the maximum.

An intense cross peak bleach at ω_3 = 1750 cm^{-1} is immediately apparent after excitation at ω_1 = 1200 cm^{-1} in the 2D IR spectrum of 2M HCl (Fig. 5.12a), indicating anharmonic coupling between the vibrations in Regions 1 and 2. For this cross peak, the 2D IR spectrum is presented in the isotropic ($S_{\parallel}+2S_{\perp}$) and anisotropic ($S_{\parallel}-S_{\perp}$) representations to highlight the doublet in the anisotropic spectrum (Fig. 5.12b) In the anisotropic spectrum, the GSB at ω_3 = 1750 cm^{-1} appears with an ESA at ω_3 = 1900 cm^{-1} arising from excitation into the combination band between the Zundel-like stretch and bend vibrations. The induced absorption feature is hidden in the isotropic spectrum, likely because of overlap with the broad bleach in Region 3. This cross peak doublet displays the same inverted anharmonicity pattern as in Region 1, and is retained over various HCl concentrations (Fig 5D.4).

The 150 cm^{-1} splitting of the cross peak doublet demonstrates a massive coupling between these two vibrations, compared to typical couplings in weakly anharmonic systems of <30 cm^{-1}.[21] Strong anharmonic mode-mixing between proton stretch and bend modes in Zundel complexes has been predicted theoretically[2,14] and demonstrated experimentally in mixed-isotope gas-phase Zundel ions.[22] Invoking a simple mode-mixing model with two oscillators, the ~150 cm^{-1} coupling implies that local mode frequencies occur near ~1245 cm^{-1} and ~1705 cm^{-1}, respectively. However, we find that all transitions observed in our experiment cannot be satisfactorily described with only two strongly coupled modes, but requires a higher dimensional treatment of the nuclear potential.

The 2D anisotropy of this cross peak (Fig. 5.12c) offers important new clues into the assignment of the vibrational modes. The bleach displays an anisotropy greater than 0.25 at ω_3 = 1750 cm^{-1}, indicating roughly parallel preference between the two vibrations. The anisotropy decreases to negative values as ω_3 increases above 1750 cm^{-1}, likely due to interference with the continuum cross peak above (see Section 5.4.2). High initial 2D anisotropy is retained with varying HCl concentration (Fig. 5D.4). This cross peak polarization preference is consistent with strong mode-mixing of aligned proton stretching and flanking H-O-H bending coordinates along a common O-O axis in Zundel-like complexes.[2,14,23] The high positive anisotropy also rules out observable interaction between hydronium in-plane bending and umbrella modes because those transition dipoles are expected to point along and perpendicular to the molecular plane, respectively.

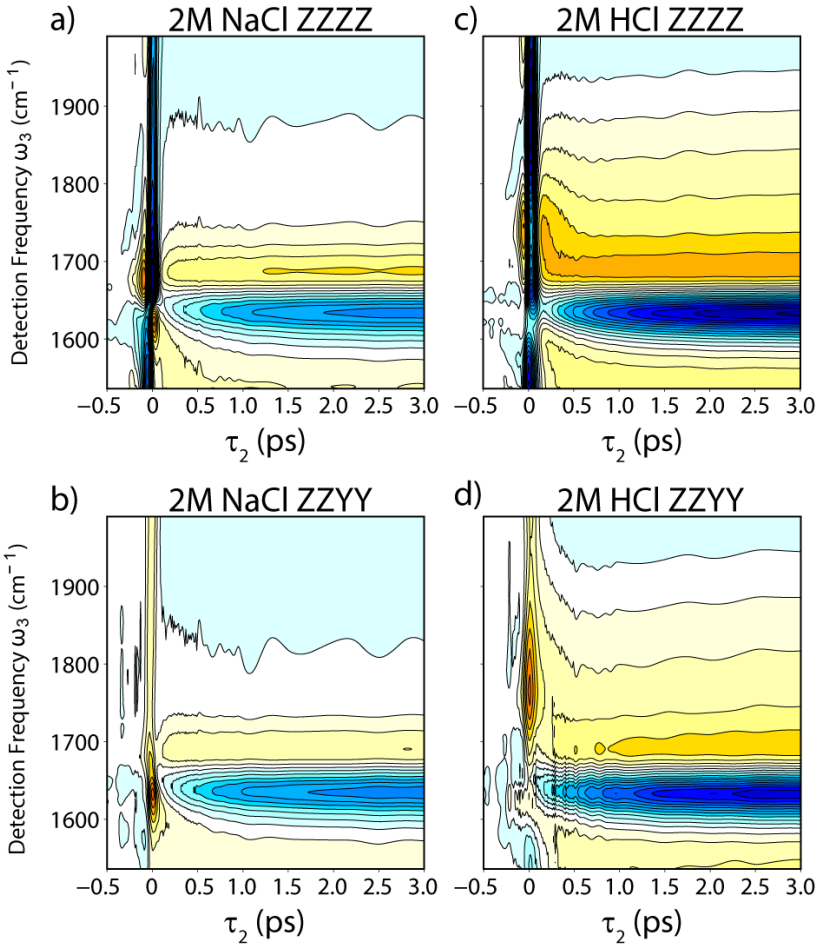

Figure 5.13: TA spectra of cross peak between Regions 1 and 2 for (a) and (b) 2M NaCl and (c) and (d) 2M HCl in the ZZZZ and ZZYY pump-probe polarization schemes. Surfaces are on a common normalization equal to the maximum amplitude of the isotropic 2M HCl spectrum at τ_2 = 10 ps. In all spectra, the signal at τ_2 = 0 fs and all ω_3 is instantaneous polarization response from the solution and the CaF_2 windows.

The polarization-resolved TA spectra of this cross peak region (Fig. 5.13) appear remarkably similar to the TA spectra of the δ_{H^+} diagonal (Fig. 5.6). Importantly, the δ_{H^+} bleach at ω_3 = 1750 cm^{-1} is present at early times in 2M HCl, followed by the rise of the HGS. The isotropic TA trace at this frequency (Fig. 5.14a) reveals an initial decay on a 260 fs timescale, followed by a 2.9 ps rise of the HGS. The anisotropy (Fig. 5.14b) of this signal decays biexponentially with 120 fs and 1.9 ps components, remarkably similar to the anisotropy decay of δ_{H^+} along the

diagonal (Fig. 5.7b). This ps anisotropy component is not visible on the Region 1 diagonal because the lifetime is on the order of the pulse overlap, and there is no HGS to retain the anisotropy like in Region 2. It is fascinating, therefore, that the ps anisotropy decay is present in the cross peak TA spectrum. Fig. 5.14b records the cross anisotropy decay between the Zundel-like stretching and bending vibrations, which is bounded above by the orientational anisotropy decays of each of the individual modes. For the ps component to be present in the cross anisotropy, it means that both δ_{H^+} and the proton stretch of Zundel-like complexes must retain orientational correlation on a ps timescale, even if the orientation correlation persists beyond both of their lifetimes. This suggests that there is some sort of persistence in the geometry of the aqueous proton complex for a few ps, even if its IR spectral signatures decay on a much faster timescale.

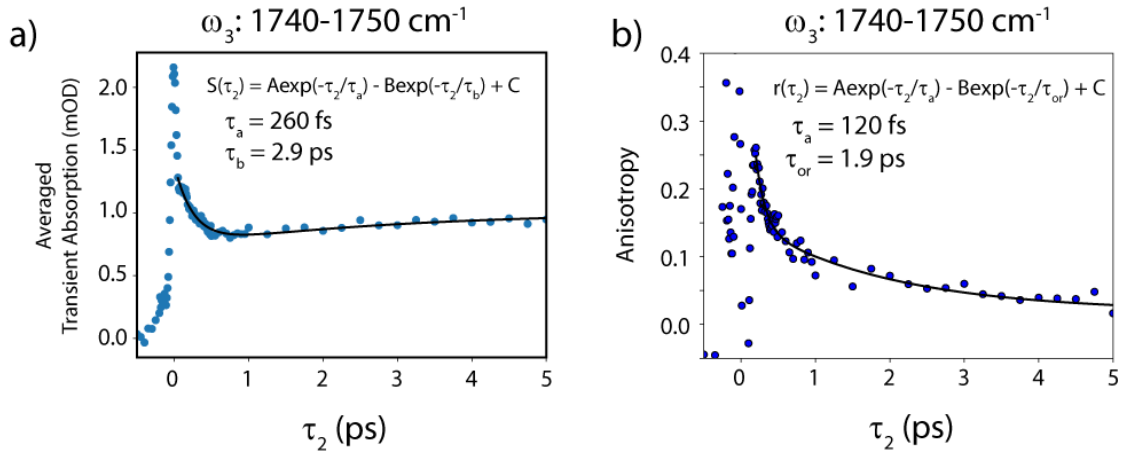

Figure 5.14: TA (a) isotropic and (b) polarization anisotropy traces of the proton stretch-δ_{H^+} cross peak in 2M HCl at ω_3 = 1750 cm^{-1}. Both traces are fit to a biexponential decay (solid line) starting at τ_2 = 200 fs.

Experimental Details

The 2D IR and TA spectra of this region were taken with 2M HCl in a 3.6 μm Mylar spacer sandwiched between two 0.2 mm CaF_2 windows, which produced OD 1 linear absorption at

1650 cm^{-1}. The 10 μJ, P-polarized pump pulses centered at 1250 cm^{-1} were generated by OPA/DFG in GaSe, characterized in detail in Chapter 3. A 45°-polarized component of the probe was sent to the sample, and later split into S and P polarization components for simultaneous detection of the ZZZZ and ZZYY spectra.

5.4.2 Uphill Cross Peak Between Regions 1 and 3

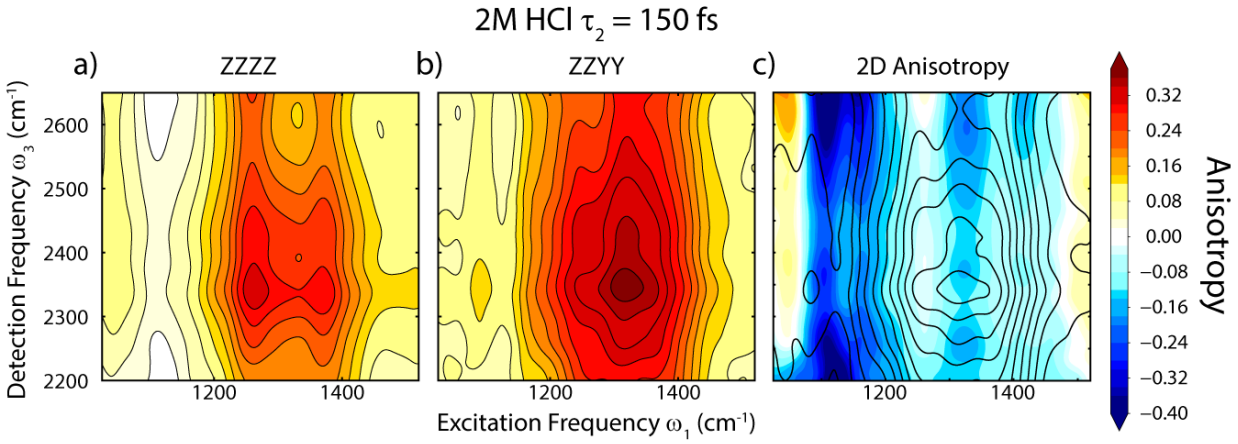

Figure 5.15: Polarization-resolved 2D IR cross peak spectra at τ_2 = 150 fs between Regions 1 and 3 in 2M HCl. (a) ZZZZ, (b) ZZYY, and (c) 2D anisotropy representations of the 2D IR spectrum. The ZZZZ and ZZYY spectra are scaled to the same normalization factor. Black contours in the 2D anisotropy are from the corresponding isotropic spectrum. 2D anisotropy is only shown in regions of the spectra whose absolute intensity is at least 10% of the maximum.

The early-time 2D IR spectrum of the cross peak between Regions 1 and 3 is shown in Fig. 5.15. The cross peak appears as a broad bleach centered at ω_3 = 2350 cm^{-1} in detection frequency with no noticeable ESA feature, much like the diagonal 2D IR spectrum of Region 3 (Fig. 5.8). The ZZYY (Fig. 5.15b) spectrum is more intense than the ZZZZ (Fig. 5.15a) spectrum, and the resulting 2D anisotropy (Fig. 5.15c) is negative across the feature. This polarization preference indicates that Region 1 and Region 3 correspond to vibrations with roughly perpendicular orientation. This would be consistent with Zundel-like stretches coupled to strongly H-bonded

flanking O-H stretches with either local mode character or asymmetric normal mode character pointing away from the O-O axis. However, this would also be consistent with the orthogonal polarization relationship between the hydronium umbrella and in-plane hydronium O-H stretches. Disentangling these two contributions will be aided with anharmonic vibrational calculations, which will be shown in Chapter 7. The perpendicular polarization preference rules out the possibility that Region 3 arises predominantly from Region 1 0→2 overtone transition expected at $\omega_{21} + \omega_{10} \approx 2550$ cm^{-1} or combination bands involving low-frequency O-O modes since these would display a parallel polarization preference.[9]

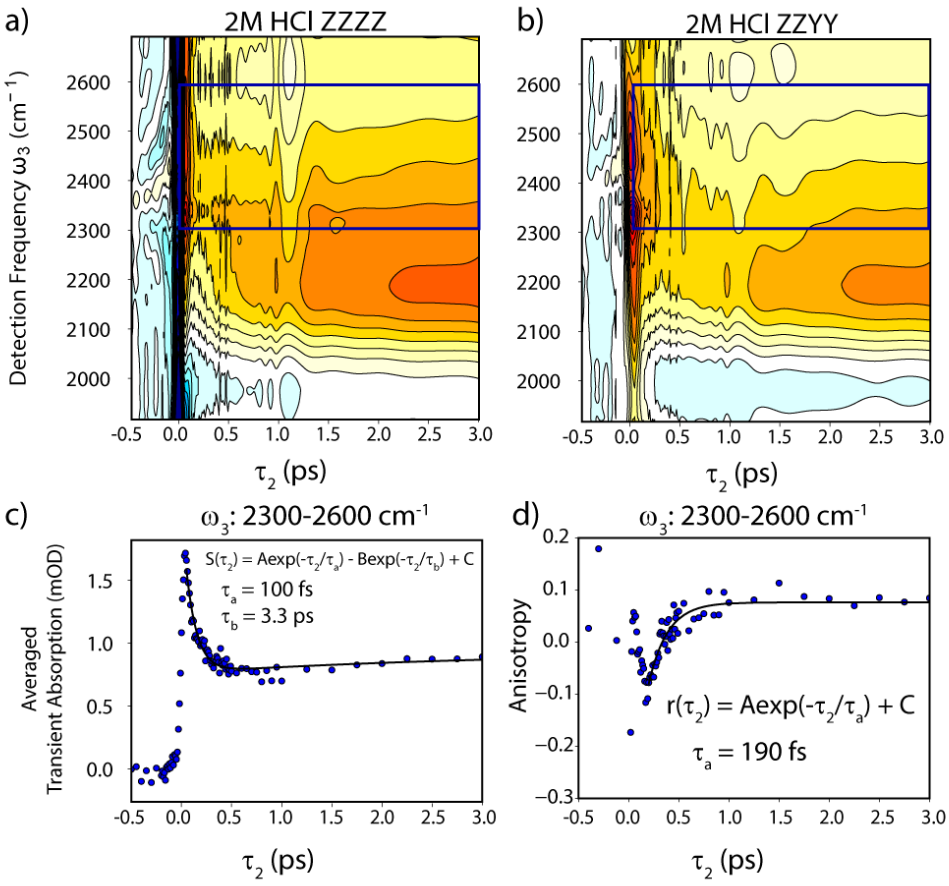

Figure 5.16: TA spectra of the cross peak between Regions 1 and 3 with the (a) ZZZZ and (b) ZZYY polarization schemes. The two spectra are plotted on the same scale. (c) Isotropic and (d) anisotropy TA traces in this region, averaged over ω_3 = 2300-2600 cm^{-1} as indicated by the colored boxes in (a) and (b).

The time dependence of this cross peak is plotted as the TA spectrum in Fig. 5.16. Similar to the diagonal of Region 3 (Fig. 5.9), there is a rapid decay of the vibrational population, followed by a slow rise of the hot ground state. The early time signal in the ZZYY spectrum (Fig. 5.16b) is more intense than the ZZZZ signal (Fig. 5.16a), which is consistent with the 2D IR results. The integrated TA trace of the isotropic signal (Fig. 5.16c) shows a 100 fs fast decay of the cross peak intensity, followed by a 3.3 ps-timescale rise of the HGS. The TA anisotropy (Fig. 5.16d) starts around -0.1 at $\tau_2 = 200$ fs, and rises to a constant baseline on a 190 fs timescale. The baseline deviates from zero, likely due to slightly misaligned ZZZZ and ZZYY detector stripes rather than a long-lived non-zero anisotropy from the sample. The 190 fs timescale is consistent with the fast anisotropy decay of the Region 3 diagonal, and suggests that it results from anisotropy decay due to energy transfer over a delocalized vibration, rather than by physical reorientation.

At this point, the uphill cross peak between Regions 1 and 4 have not been collected, but could provide interesting information to learn about the spectral relationships between these features. Polarization dependence of the cross peak would help determine the orientational relationships between the shared proton stretch and the flanking O-H stretches for Zundel-like species. Additionally, spectral dynamics of this cross peak could reveal chemical exchange between these modes due to proposed processes like proton rattling or special pair dancing. This experiment is complicated by the difference in absorbance between Region 1 and 4, which may result in low light at the detector. Vibrational energy transfer within the continuum could complicate the interpretation of any extracted timescale, which perhaps could be remedied by using isotopically dilute H^+ in DCl solution. Appendix 5B demonstrates, however, that extracting this signal is challenging and requires analysis of double-difference spectra.

Experimental Details

The 2D IR and TA spectra of the cross peak between Regions 1 and 3 were taken with 2M HCl in a 3.6 μm Mylar spacer sandwiched between two 0.2 mm CaF_2 windows. The 10 μJ, P-polarized pump pulses centered at 1250 cm^{-1} were generated by OPA/DFG in GaSe, characterized in detail in Chapter 3. A 45°-polarized component of the probe was sent to the sample, and later split into S and P polarization components for simultaneous detection of the ZZZZ and ZZYY spectra, which is discussed in more detail in Chapter 3.

5.4.3 Downhill Cross Peak Between Regions 2 and 1

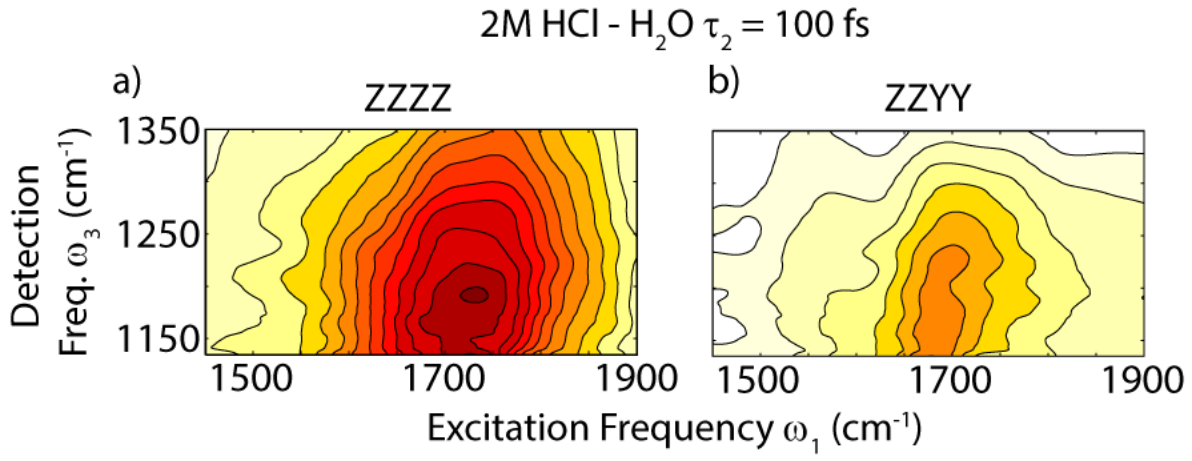

Figure 5.17: 2D IR spectra of 2M HCl – H_2O between Regions 2 and 1 at τ_2 = 100 fs in the a) ZZZZ and (b) ZZYY polarization schemes. Spectra are presented as differences due to the large amplitude of the water background in this region (Fig. 5.2).

The 2D IR cross peak measured upon exciting Region 2 and detecting in Region 1 (Fig. 5.17). In the downhill cross peak in 2M HCl (Fig. 5.17a), there is a strong contribution from the water background (Fig. 5.2) in both polarization schemes. Subtraction of the background reveals the polarization response associated with the excess proton, but is not completely rigorous because the fraction of water that is considered "bulk-like" water in 2M acid solution is not well

defined. Regardless, the difference spectrum displays an intense bleach centered at (ω_1, ω_3) = (1750 cm^{-1}, 1200 cm^{-1}) due to the coupling between asymmetric proton stretches and flanking bends in Zundel-like complexes. Like the uphill cross peak between Regions 1 and 2, this cross peak also displays a strong parallel preference and corroborates the assignment made from that region. Reliable TA spectra have not been collected in this region due to dispersion issues, but would likely decay rapidly like the Region 1 diagonal spectrum, and may not include more useful information than is already attainable from the corresponding uphill cross peak.

Experimental Details

This dataset was taken with 2M HCl in H_2O, with a 6 μm Mylar spacer between two 1 mm thick CaF_2 windows. The pump pulses were centered at 1750 cm^{-1} with 530 cm^{-1} bandwidth FWHM. The polarization of the pump was rotated between S and P with a CdSe λ/2 waveplate (Alfalas), such that ZZZZ and ZZYY spectra were not collected simultaneously. The probe was split with a 50:50 KBr beamsplitter, where one arm was sent to the sample and the second arm used as a reference arm traveling straight to the detector. The top stripe on the 2×64 MCT array collected transient absorption data from the sample, whereas the bottom stripe was used to reference the intensity fluctuations of the probe.

5.4.4 Downhill Cross Peak Between Regions 3 and 1

The downhill cross peak between Regions 3 and 1 is shown in Fig. 5.19. The 2D IR spectra in 2M HCl (Fig. 5.18) demonstrate a bleach in Region 1, with larger bleach amplitude in the ZZYY spectrum. Like in the case with the other downhill cross peaks, there is substantial water background (Fig. 5.2), but subtraction reveals a more intense ZZYY spectrum compared to ZZZZ.

The perpendicular polarization preference corroborates the polarization relationship found in the uphill cross peak between the features in Regions 1 and 3.

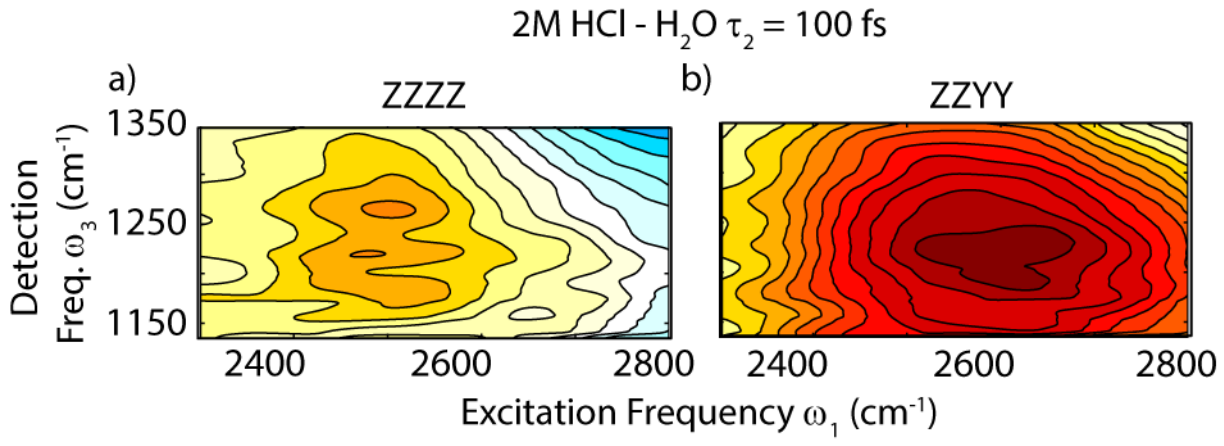

Figure 5.18: 2D IR spectra of 2M HCl – H_2O between Regions 3 and 1 at τ_2 = 100 fs in the a) ZZZZ and (b) ZZYY polarization schemes. Spectra are presented as differences due to the large amplitude of the water background in this region (Fig. 5.2).

Experimental Details

This dataset was taken with 2M HCl in H_2O, with 6 μm Mylar spacers between two 1 mm thick CaF_2 windows. The pump pulses were centered at 2550 cm^{-1} with 300 cm^{-1} FWHM. The polarization of the pump was rotated between S and P with a CdSe λ/2 waveplate (Alfalas), such that ZZZZ and ZZYY spectra were not collected simultaneously. The probe was split with a 50:50 KBr beamsplitter, where one arm was sent to the sample and the second arm used as a reference arm traveling straight to the detector. The top stripe on the 2×64 MCT array collected transient absorption data from the sample, whereas the bottom stripe was used to reference the intensity fluctuations of the probe.

5.4.5 Downhill Cross Peak Between Regions 3 and 2

Fig. 5.19 shows the cross peaks between Region 3 and Region 2. Within the bandwidth limits of the tuned excitation pulses, the cross peak appears as a continuous transition spanning ω_1 = 2300 cm^{-1} to 2700 cm^{-1}. In 2M HCl (Fig. 5.19), the ZZYY spectrum is much more intense than the ZZZZ spectrum, indicating a perpendicular polarization preference. This polarization preference is consistent with the earlier orientational assignments, where the bending modes of Region 2 are parallel to the O-O axis in Zundel-like complexes, but the O-H stretches in Region 3 are orthogonal to this direction. However, it is also possible that there are contributions from Eigen-like configurations, where hydronium bending and stretching normal modes are orthogonal to each other but lie in the molecular plane. At this time, the TA kinetics are missing for the cross peak region, but may be an interesting region to measure. Given that the bend hot ground state retains orientational anisotropy, it would be interesting to see if there is a ps component to the cross anisotropy between the stretches in Region 3 and the bends in Region 2.

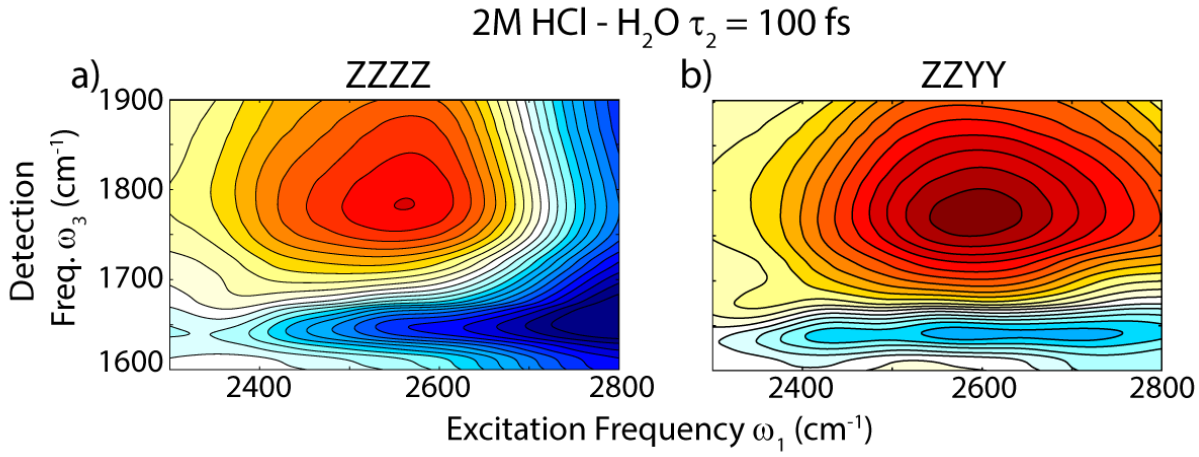

Figure 5.19: Polarization-resolved 2D IR spectra of the downhill cross peak between Regions 3 and 2 at τ_2 = 100 fs in 2M HCl – H_2O. The spectra are all scaled to the same normalization constant.

Experimental Details

This dataset was taken with 2M HCl in H_2O, with a 6 μm Mylar spacer between two 1 mm thick CaF_2 windows. The pump pulses were centered at 2550 cm^{-1} with 300 cm^{-1} FWHM. The polarization of the pump was rotated between S and P with a CdSe λ/2 waveplate (Alfalas), such that ZZZZ and ZZYY spectra were not collected simultaneously. The probe was split with a 50:50 KBr beamsplitter, where one arm was sent to the sample and the second arm used as a reference arm traveling straight to the detector. The top stripe on the 2×64 MCT array collected transient absorption data from the sample, whereas the bottom stripe was used to reference the intensity fluctuations of the probe.

5.4.6 Center Frequency Dynamics in the Cross Peak Between Region 4 and Region 2

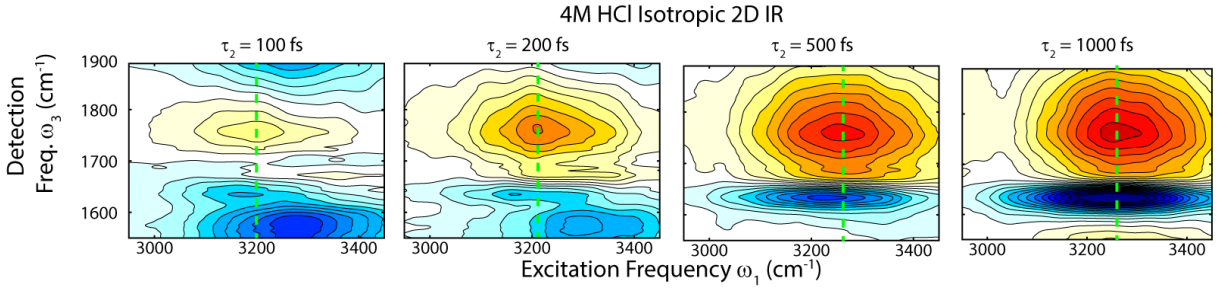

Figure 5.20: Waiting time series of 2D IR spectra of 4M HCl, taken at the magic angle polarization scheme to produce the isotropic 2D spectra. The maximum of the cross peak in ω_1 (dashed green) appears to blue shift with waiting time.

The last cross peak region in this chapter relates Regions 4 and 2, a cross peak region which was the subject of study by Thämer *et al.* previously.[10] On top of the broad ESA from the Region 4 diagonal, a cross peak appears at (ω_1, ω_3) = (3200 cm^{-1}, 1750 cm^{-1}) due to coupling between flanking O-H stretches and bends in Zundel-like arrangements (Fig. 5.20). Fig. 5C.4 demonstrates that this cross peak is present regardless of the counterion in solution. The early-time spectrum vanishes by τ_2 = 500 fs, giving way to the hot ground state. As these spectral patterns interchange,

it appears that the maximum of the bleach shifts to higher frequencies in ω_1. Reliable polarization-dependent spectra are missing in this region, but would be useful to assess the assignment of Region 4 as flanking O-H stretches. Additionally, it would be interesting to see if there are ps-timescale anisotropy kinetics in this cross peak, like in the cross peak between Regions 1 and 2.

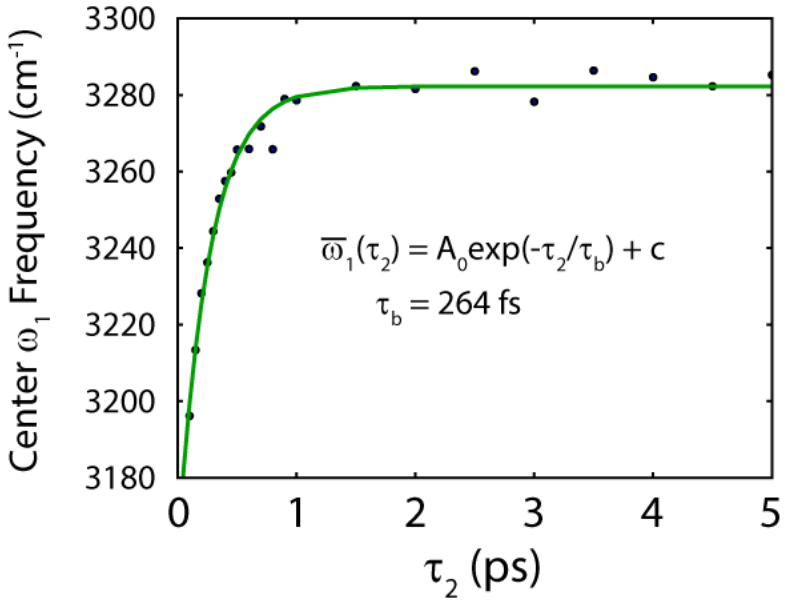

Figure 5.21: Center ω_1 frequency position of the cross peak bleach between Regions 4 and 2.

Analysis of this region by Thämer *et al.*[10] found that the cross peak appeared to shift to higher excitation frequency with increasing waiting time, which is corroborated by this measurement (Fig. 5.21). The blue shift indicates a growing correlation of the δ_{H^+} cross peak with bulk water O-H stretches with increasing waiting time. A frequency shift in ω_1 with waiting time is likely attributed to the decay of the early-time peak and a rise of a new peak at higher ω_1. This can arise from either chemical exchange or energy transfer involving bulk water, and the 260 fs timescale shown here serves as a lower bound on both of these timescales. This timescale is faster than the previous attained timescale of 480 fs.[10] Fig. 5C.5 demonstrates that this timescale was

consistent regardless of counterion identity, which suggests that the timescale difference between this analysis and the work by Thämer *et al.* arises from a difference in data processing or analysis.

5.5 Conclusion

The 2D IR and TA spectra presented in this chapter represent the vast majority of data collected in the last six years to extract new information about the vibrational response of the aqueous proton complex. By examining each of the diagonal features and cross peaks, we can assemble a holistic picture of aqueous proton spectroscopy. Each of the four regions shows significant anharmonic coupling with any other with clear polarization preferences. Based on the data alone, we can make some preliminary assignments (Fig. 5.22). Region 1 is primarily dominated by the stretching motions of the shared proton in Zundel-like complexes, likely with some small contribution from hydronium umbrella modes. Region 2 is consistent with the flanking bending modes of Zundel-like species as well, but the contribution from Eigen-like geometries is also possible. Region 3 is consistent with either flanking O-H stretches in Zundel-like complexes or the hydronium O-H stretches in Eigen-like configurations. Region 4 appears consistent with the flanking O-H stretches of Zundel-like complexes, but orientational information is missing. In Chapters 6 and 7, these results will be analyzed in more detail using high-level vibrational calculations to decompose the vibrational response by cluster geometry.

The vibrational kinetics in this system are fast, with most vibrational lifetimes within 100-200 fs. These ultrafast timescales reflect strong coupling to many relaxation channels within the aqueous proton complex, enabling efficient relaxation and a substantial hot ground state in some regions. The polarization anisotropies of these vibrations also include 200-300 fs decay timescales, which is typical for collective vibrational modes, indicating that these vibrations are not localized

on just one or two molecules immediately adjacent to the excess proton. Despite this, there is an interesting 2-3 ps anisotropy decay timescale associated with the δ_{H^+} feature at 1750 cm^{-1}, which persists for over an order of magnitude longer than the vibrational lifetime. This timescale is consistent with H-bond reorganization inducing reorientation of the aqueous proton complex and is consistent with proton transfer via the Grotthuss mechanism. Chapter 8 will examine this anisotropy decay in more detail and analyze what it implies mechanistically about the proton transfer process.

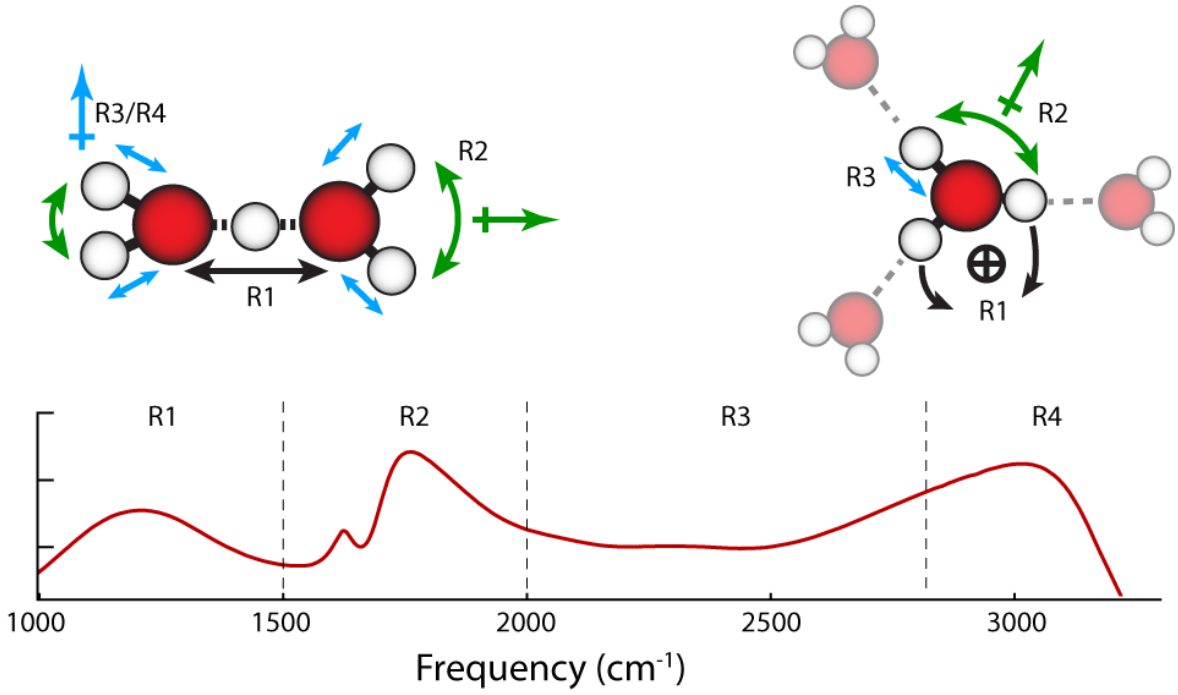

Figure 5.22: Schematic of aqueous proton vibrational assignments from nonlinear IR spectra. Double arrows represent vibrational displacement, while crossed arrows represent transition dipole orientations.

5.6 References

(1) Widjaja, E.; Garland, M. Pure component spectral reconstruction from mixture data using SVD, global entropy minimization, and simulated annealing. Numerical investigations of admissible objective functions using a synthetic 7-species data set *J. Comput. Chem.* **2002**, *23*, 911.

(2) Biswas, R.; Carpenter, W.; Fournier, J. A.; Voth, G. A.; Tokmakoff, A. IR spectral assignments for the hydrated excess proton in liquid water *J. Chem. Phys.* **2017**, *146*, 154507.

(3) Daly, C. A.; Streacker, L. M.; Sun, Y.; Pattenaude, S. R.; Hassanali, A. A.; Petersen, P. B.; Corcelli, S. A.; Ben-Amotz, D. Decomposition of the Experimental Raman and Infrared Spectra of Acidic Water into Proton, Special Pair, and Counterion Contributions *J. Phys. Chem. Lett.* **2017**, *8*, 5246.

(4) Dahms, F.; Fingerhut, B. P.; Nibbering, E. T. J.; Pines, E.; Elsaesser, T. Large-amplitude transfer motion of hydrated excess protons mapped by ultrafast 2D IR spectroscopy *Science* **2017**, *357*, 491.

(5) Fournier, J. A.; Wolke, C. T.; Johnson, M. A.; Odbadrakh, T. T.; Jordan, K. D.; Kathmann, S. M.; Xantheas, S. S. Snapshots of Proton Accommodation at a Microscopic Water Surface: Understanding the Vibrational Spectral Signatures of the Charge Defect in Cryogenically Cooled $H^+(H_2O)_{n=2–28}$ Clusters *J. Phys. Chem. A* **2015**, *119*, 9425.

(6) Hassanali, A. A.; Giberti, F.; Sosso, G. C.; Parrinello, M. The role of the umbrella inversion mode in proton diffusion *Chem. Phys. Lett.* **2014**, *599*, 133.

(7) Kalish, N. B.-M.; Shandalov, E.; Kharlanov, V.; Pines, D.; Pines, E. Apparent Stoichiometry of Water in Proton Hydration and Proton Dehydration Reactions in CH_3CN/H_2O Solutions *J. Phys. Chem. A* **2011**, *115*, 4063.

(8) Dahms, F.; Costard, R.; Pines, E.; Fingerhut, B. P.; Nibbering, E. T. J.; Elsaesser, T. The Hydrated Excess Proton in the Zundel Cation $H_5O_2^+$: The Role of Ultrafast Solvent Fluctuations *Angew. Chemie - Int. Ed.* **2016**, *55*, 10600.

(9) Kundu, A.; Dahms, F.; Fingerhut, B. P.; Nibbering, E. T. J.; Pines, E.; Elsaesser, T. Ultrafast vibrational relaxation and energy dissipation of hydrated excess protons in polar solvents *Chem. Phys. Lett.* **2018**, *713*, 111.

(10) Thämer, M.; De Marco, L.; Ramasesha, K.; Mandal, A.; Tokmakoff, A. Ultrafast 2D IR spectroscopy of the excess proton in liquid water *Science* **2015**, *350*, 78.

(11) Headrick, J. M.; Diken, E. G.; Walters, R. S.; Hammer, N. I.; Christie, R. A.; Cui, J.; Myshakin, E. M.; Duncan, M. A.; Johnson, M. A.; Jordan, K. D. Spectral Signatures of Hydrated Proton Vibrations in Water Clusters *Science* **2005**, *308*, 1765.

(12) Kim, J.; Schmitt, U. W.; Gruetzmacher, J. A.; Voth, G. A.; Scherer, N. E. The vibrational spectrum of the hydrated proton: Comparison of experiment, simulation, and normal mode analysis *J. Chem. Phys.* **2002**, *116*, 737.

(13) Xu, J.; Zhang, Y.; Voth, G. A. Infrared spectrum of the hydrated proton in water *J. Phys. Chem. Lett.* **2011**, *2*, 81.

(14) Vendrell, O.; Gatti, F.; Meyer, H.-D. Full dimensional (15-dimensional) quantum-dynamical simulation of the protonated water dimer. II. Infrared spectrum and vibrational dynamics *J. Chem. Phys.* **2007**, *127*, 184303.

(15) Carpenter, W. B.; Fournier, J. A.; Biswas, R.; Voth, G. A.; Tokmakoff, A. Delocalization and stretch-bend mixing of the HOH bend in liquid water *J. Chem. Phys.* **2017**, *147*, 084503.

(16) Loparo, J.; Fecko, C.; Eaves, J.; Roberts, S.; Tokmakoff, A. Reorientational and Configurational Fluctuations in Water Observed on Molecular Length Scales. *Phys. Rev. B* **2004**, *70*, 180201.

(17) Ramasesha, K.; Roberts, S. T.; Nicodemus, R. A.; Mandal, A.; Tokmakoff, A. Ultrafast 2D IR Anisotropy of Water Reveals Reorientation During Hydrogen-Bond Switching. *J. Chem. Phys.* **2011**, *135*, 54509.

(18) Sofronov, O. O.; Bakker, H. J. Slow Proton Transfer in Nanoconfined Water *ACS Cent. Sci.* **2020**, acscentsci.0c00340.

(19) Ramasesha, K.; De Marco, L.; Mandal, A.; Tokmakoff, A. Water vibrations have strongly mixed intra- and intermolecular character *Nat. Chem.* **2013**, *5*, 935.

(20) De Marco, L.; Fournier, J. A.; Thämer, M.; Carpenter, W.; Tokmakoff, A. Anharmonic exciton dynamics and energy dissipation in liquid water from two-dimensional infrared spectroscopy *J. Chem. Phys.* **2016**, *145*, 094501.

(21) Khalil, M.; Demirdöven, N.; Tokmakoff, A. Coherent 2D IR Spectroscopy: Molecular Structure and Dynamics in Solution. *J. Phys. Chem. A* **2003**, *107*, 5258.

(22) Guasco, T. L.; Johnson, M. A.; McCoy, A. B. Unraveling anharmonic effects in the vibrational predissociation spectra of $H_5O_2^+$ and its deuterated analogues *J. Phys. Chem. A* **2011**, *115*, 5847.

(23) Asmis, K. R.; Pivonka, N. L.; Santambrogio, G.; Brümmer, M.; Kaposta, C.; Neumark, D. M.; Wöste, L. Gas-phase infrared spectrum of the protonated water dimer. *Science* **2003**, *299*, 1375.

Appendix 5A: Acid Spectral Components from the Concentration Dependence of the HCl Linear IR spectrum

The work presented in this appendix is published and has been adapted with permission from:
Yu, Q.; Carpenter, W.B.; Lewis, N.H.C.; Bowman, J.M.; Tokmakoff, A., High-Level VSCF/VCI Calculations Decode the Vibrational Spectrum of the Aqueous Proton. *J. Phys.Chem. B.* **2019**, *123* (33), 7214-7224.

A concentration series of HCl FTIR and ATR spectra are presented in Fig. 5A.1. For both techniques, spectra were recorded of 0-2M HCl solutions (Figs. 5A.1a and 5A.1d). Because of the uncontrolled pathlengths of the FTIR spectra, the absorption at 3400 cm^{-1} in an FTIR spectrum was normalized to the value in the corresponding ATR-IR spectrum. To decompose the IR spectra into components associated with water and dissolved HCl, we implemented a singular value

decomposition (SVD) analysis followed by a maximum entropy method[1] (MEM) to attain physically relevant spectral components (see details below). The SVD/MEM analyses produced two positive absorption spectra, one corresponding to water absorption, and one corresponding to new absorption upon introduction of HCl (Figs. 5A.1b and 5A.1e). The ATR spectral components are both all positive, but there is some residual negative signal in the FTIR acid component around 3700 cm^{-1}, possibly due to over-correction by the dissimilarity term in the objection function or an effect from the variable pathlengths between FTIR signals. The ATR acid component includes some noise around 2100 cm^{-1}, likely because of the absorption by phonons in the diamond ATR prism.

We additionally include the two components resulting from the same analysis in NaCl solutions, which reveal a water component and water IR absorption perturbed by the Cl^- anions. In the ATR acid component spectrum, there is an absorption around 3450 cm^{-1} which seems to correspond to the O-H stretches perturbed by Cl^- but the correspondence is less clear in the FTIR component spectra. In Figs. 5A.1c and 5A.1f, we show how the two components change in amplitude with increasing acid concentration. In both ATR and FTIR spectra, the amplitude of the acid spectrum grows linearly with acid concentration, whereas the amplitude of the water component slightly decreases as it is "diluted" with solute. The spectral components and amplitudes in the FTIR and ATR spectral series show consistent trends with each other, reinforcing the validity of the decomposition. Importantly, the FTIR spectra contain only the absorption components of the complex refractive index, and thus are a more accurate measurement of the absorption spectra of the aqueous excess proton.

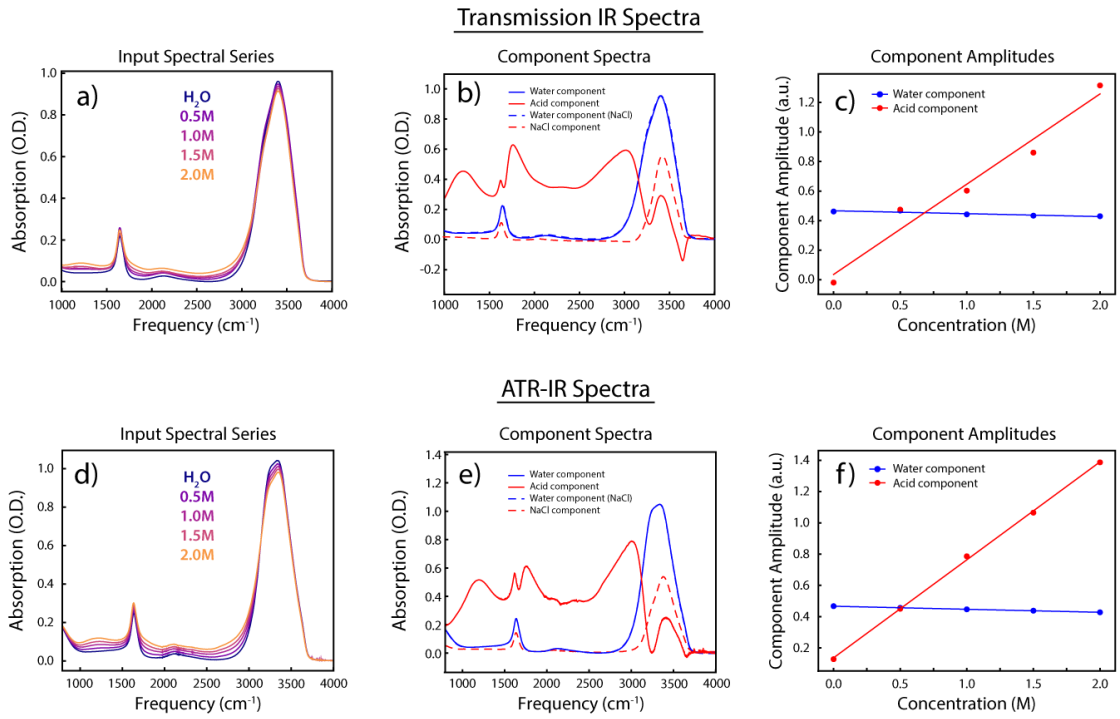

Figure 5A.1: SVD/MEM analysis of the IR spectra of HCl in H_2O at various concentrations, measured with both FTIR and ATR-IR spectroscopy. (a) The input transmission FTIR spectra of 0-2M HCl solutions, (b) the component spectra extracted from the SVD/MEM analysis, and (c) the amplitudes of the two components as a function of acid concentration. (d)-(f) show the analogous results for ATR-IR spectra.

Experimental Details

Infrared absorption spectra (Bruker *Tensor 27*) were measured for a series of HCl and NaCl solutions from 0-2M in steps of 0.5M. The spectra were collected between two 1 mm-thick CaF_2 windows without a spacer, such that the intensity of the O-H stretch was approximately 1 OD. HCl solutions were prepared by serial dilution of concentrated solution (37% by mass, Sigma Aldrich), and NaCl solutions were prepared by a serial dilution of 2M NaCl stock solution generated from the solid salt (Fisher). Contributions to the solution spectra from window absorption (particularly between 1000-1200 cm^{-1}) were subtracted.

We applied singular value decomposition (SVD) analysis to decompose the IR spectra of the acid concentration series into components relating to water and the hydrated excess proton. We applied the same maximum entropy analysis on the NaCl solutions to determine which spectral features in the HCl spectrum could arise from waters associated with chloride solvation instead of the proton hydration complex. In SVD analysis, the raw spectra, dependent on a variable (in this case concentration) are represented as a linear combination of n independent spectral components whose weights grow or decay as a function of the variable. A spectral series matrix A represented in terms of frequency ω and concentration c can be decomposed into three matrices:

$$A_{\omega \times c} = U_{\omega \times n} S_{n \times n} V^{T}_{c \times n} + E_{\omega \times c} \tag{5.1}$$

where $U_{\omega \times n}$ is a matrix of the two component spectra, $S_{n \times n}$ is a diagonal matrix of the singular values representing weighting of the spectral components, $V_{c \times n}$ is a matrix representing the concentration-dependent amplitude changes of each spectral component, and $E_{\omega \times c}$ is residual noise not captured by the n components. Two components were needed to describe 99% of the spectral information, determined by the values of the first two weights in $S_{n \times n}$. The first component, representing the water absorption spectrum, contains approximately 90% of the spectral information content, while a second component associated with the acid contains another 9% of spectral information and the remaining components comprising noise. The components from SVD analysis are mathematical quantities which may not represent physical absorption contributions. For instance, SVD analysis can produce negative absorption amplitudes in certain regions of the absorption spectrum.

To determine the physically relevant components, we applied a maximum entropy method to reweight the SVD components in a minimally biased way. To implement this, we introduce a mixing matrix $T_{n \times n}$, such that

$$A_{\omega \times c} = U_{\omega \times n} S_{n \times n} T^{-1}_{n \times n} T_{n \times n} V^{T}_{c \times n} \tag{5.2}$$

The reconstructed spectra are given by

$$C_{\omega \times c} = U_{\omega \times n} S_{n \times n} T^{-1}_{n \times n} \tag{5.3}$$

and the reconstructed concentration weights are determined as

$$a_{n \times c} = T_{n \times n} V^{T}_{c \times n} \tag{5.4}$$

The elements of the mixing matrix *T* are chosen such that the objective function

$$F = H + \gamma P + \lambda D \tag{5.5}$$

is minimized. *H* is a term that is minimized when information entropy across the spectral components is maximized, *P* is a term that penalizes negative amplitudes in the spectral and concentration domains, and *D* is a dissimilarity term that penalizes spectral overlap between components. H is calculated as

$$H = -\sum_{\omega} \sum_{c} h_{\omega c} \ln(h_{\omega c}) \tag{5.6}$$

where $h_{\omega c}$ is a normalized absolute value of the first derivative of the spectrum with respect to frequency

$$h_{\omega c} = \frac{|C'_{\omega c}|}{\sum_{\omega} |C'_{\omega c}|} \tag{5.7}$$

The positivity function *P* was calculated as

$$P = \sum_{n} \sum_{c} W(a_{nc}) a^2_{nc} + \sum_{\omega} \sum_{c} W(C_{\omega c}) C^2_{\omega c} \tag{5.8}$$

where *W(x)* is a weighting function for negative values

$$\begin{cases} 0 & \text{if } x \geq 0 \\ 1 & \text{if } x < 0. \end{cases} \tag{5.9}$$

The dissimilarity term D was calculated as the dot product of the two spectral components normalized by their respective maximum absolute amplitudes, which was included to ensure that the second component represented the new spectral features that grew in with HCl concentration, rather than recovering the spectrum of 2M HCl solution. The weights of the different penalty terms can be balanced by the positive scalars γ, λ, and α. We found that the most optimal results for the HCl spectral series were obtained with $\gamma = 500$, and $\lambda = 0.005$. The global minimum of the objective function was determined with a simulated annealing algorithm.

Appendix 5B: The Linear IR Absorption Spectrum of an Isotopically Dilute H^+ in DCl/D_2O

The work presented in this appendix is published and has been adapted with permission from:
Biswas, R.; Carpenter, W.B.; Voth, G.A.; Tokmakoff, A., Molecular Modeling and Assignment of IR Spectra of the Hydrated Excess Proton in Isotopically Dilute Water. *J. Chem, Phys.* **2016**, *145* (15), 154504.

To isolate the FTIR spectrum of a bare proton, we acquired FTIR spectra of isotopically dilute protons in otherwise deuterated hydrochloric acid solutions between 1000 and 4000 cm^{-1}. After proton exchange, the experimentally measured absorption spectrum of the solution obtained by mixing a small amount of H_2O into DCl contains contributions from multiple isotopologues of varying concentration. The experimental IR proton continuum spectrum for the dilute isotope in an otherwise D_2O environment (H^+/D_2O), here denoted as S_{H^+}, is superimposed on a strong background from the major isotope species (D_2O and D^+/D_2O) and weaker contributions from bulk water in the form of HOD. In our analysis of experimental spectra, we approximate the experimental spectrum S^{expt} as a sum of contributions from four different species:

$$S^{expt}_{H^+/D_2O}(\omega) = S_{H^+}(\omega) + S_{D_2O}(\omega) + S_{D^+}(\omega) + S_{HOD}(\omega) \tag{5.10}$$

where S_{D_2O}, S_{D^+}, and S_{HOD} represent the IR absorption arising from bulk D_2O, the aqueous excess deuteron in D_2O, and HOD in bulk D_2O. To isolate S_{H^+}, we performed difference spectroscopy using three additional experimental spectra for pure D_2O, isotopically pure D^+/DCl, and isotopically dilute HOD/D_2O. These spectra also include multiple additive contributions:

$$S^{expt}_{D_2O}(\omega) = S_{D_2O}(\omega), \tag{5.11}$$

$$S^{expt}_{D^+/D_2O}(\omega) = S_{D_2O}(\omega) + S_{D^+}(\omega), \tag{5.12}$$

$$S^{expt}_{HOD/D_2O}(\omega) = S_{D_2O}(\omega) + S_{HOD}(\omega). \tag{5.13}$$

S_{H^+} was obtained from the double-difference spectrum,

$$S_{H^+}(\omega) = \left[S^{expt}_{H^+/D_2O}(\omega) - S^{expt}_{HOD/D_2O}(\omega) \right] - \left[S^{expt}_{D^+/D_2O}(\omega) - S^{expt}_{D_2O}(\omega) \right]. \tag{5.14}$$

To perform this double-difference measurement with high accuracy, we used a singular value decomposition (SVD) analysis of a concentration series to minimize the error originating from irreproducibility of the sample path length. We first measured the FTIR spectra of DCl in D_2O with and without 10% HOD (Figs. 5.B1a and 5.B1b) as a function of DCl concentration. We then applied SVD analysis with two spectral components to extract the spectrum associated with the addition of acid, whose amplitudes are shown in Figs. 5.B1c and 5.B1d. With increasing acid concentration, the second component weight grows approximately linearly, and the first component drops slightly as a result of the decreasing concentration of pure water. The second component in isotopically pure series represents changes due to the growth of deuterated acid species, whereas the second component in the 10% HOD series represents the growth of acid species that are both deuterated and singly H labeled.

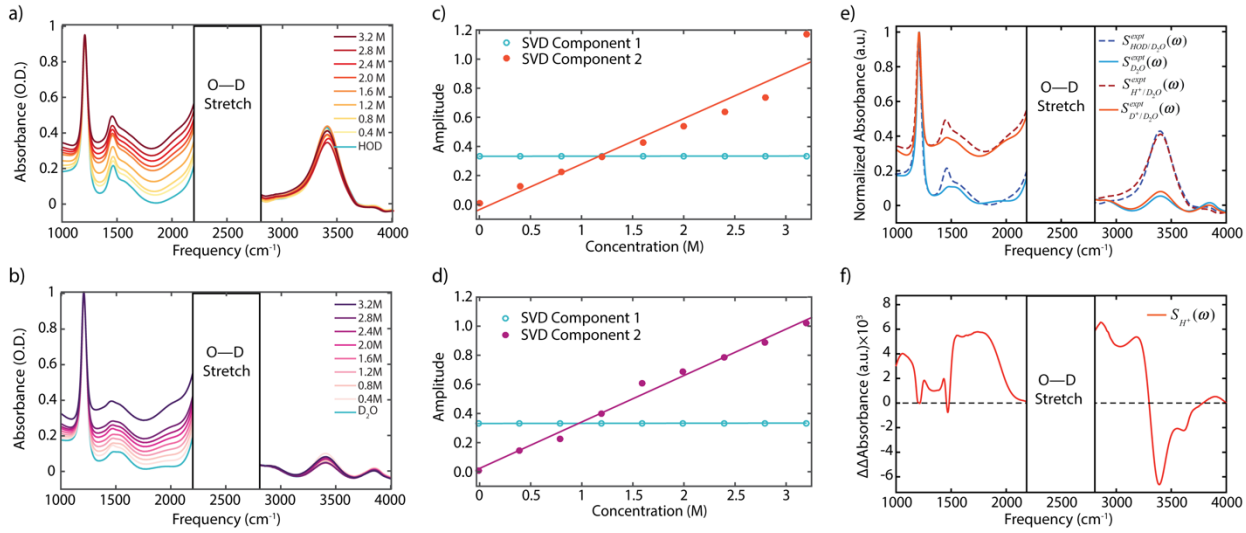

Figure 5B.1: Experimental isolation of the bare H^+ absorption spectrum. (a)-(b) 0-3.2M DCl concentration series with 10% HOD and isotopically pure DCl, respectively. (c)-(d) The concentration-dependent SVD weights of acid (filled circles) and water (cyan open circles) components of the concentration series. (e) The experimental FTIR spectra for D_2O (blue) and 3.2 M DCl solution (red) with (dashed line) and without (solid line) 10% HOD. (f) The double difference spectrum. Double difference spectrum was obtained by taking the difference of SVD reconstructed difference spectra of isotopically dilute and fully deuterated 3.2 M acid solutions. The difference spectra are first obtained by subtracting the pure water response from the corresponding acid solutions. The 2200–2800 cm^{-1} range is not shown, since the high optical density in the O–D stretching vibration range precludes a satisfactory analysis.

Finally, we reconstructed the 3.2M acid spectra using linear fits to the concentration-dependent weights of the first and second components, which serve as a method to correct for random error in sample concentration. We took the (10% HOD) D_2O reconstructed spectrum to be $S^{expt}_{HOD/D_2O}(\omega)$ and $S^{expt}_{D_2O}(\omega)$, and we took the (10% HOD) 3.2 M DCl reconstructed spectrum to be $S^{expt}_{H^+/D_2O}(\omega)$ and $S^{expt}_{D^+/D_2O}(\omega)$ (Fig. 5.B1e). We could then carry out the double difference subtraction as outlined in the procedure above to obtain the FTIR signal from the isolated H^+ in D_2O, $S_{H^+}(\omega)$ (Fig. 5.B1f).

Figures 5.B1e and 5.B1f shows the results of our analysis. Fig. 5.B1e shows the FTIR spectra for D_2O and 3.2 M DCl solutions with and without the isotopically dilute proton. The FTIR

spectrum of pure D_2O exhibits a sharp D-O-D bend at 1208 cm^{-1}, a broad bend-libration combination band around 1500 cm^{-1}, and an intense O-D stretch centered at ~2500 cm^{-1}. The O-D stretch peak in all of our spectra has a high enough optical density over the 2200 cm^{-1}-2800 cm^{-1} range that we cannot perform satisfactory difference spectra, and thus, we exclude this range from analysis. Due to imperfect isotope purity arising from sample contact with atmospheric H_2O, there remains a small amount of O-H stretch at 3400 cm^{-1} in the isotopically pure D_2O spectrum. Upon inclusion of HOD in D_2O, the weak HOD bend at 1460 cm^{-1} and the O-H stretch at 3400 cm^{-1} become visible on top of the D_2O features. The isotopically pure and dilute 3.2 M DCl spectra show an intense, broad continuum due to D^+ species from 1000 cm^{-1} to 2500 cm^{-1}. In the case of dilute HOD in 3.2 M DCl, extra intensity is seen along the continuum up to 3300 cm^{-1} due to the dilute excess proton. We isolate this signal by taking the double difference spectrum of the SVD reconstructed FTIR spectra.

Fig 5.B1f shows the double difference spectrum between isotopically pure and dilute 3.2 M DCl and D_2O, which represents the response of excess proton H^+/D_2O. Upon addition of acid, the reduction of bulk water O-H stretch response is manifested by the large dip around 3400 cm^{-1}, due to the population decrease of bulk HOD oscillators. The sharp rise around 3190 cm^{-1} arises from the O-H stretch of different proton-water complexes. The peak around 2860 cm^{-1} most likely arises from the Fermi resonance of H^+-O-D bend overtone and O-H stretch in proton-water complexes. The large positive broad band between 1550 and 1800 cm^{-1} also arises from the isotopically dilute H^+ species.

Experimental Details

We acquired the FTIR of aqueous hydrochloric acid solutions in a concentration series for samples of isotopically pure DCl/D_2O and DCl/D_2O with isotopically dilute HOD. Concentration series were acquired from 0 to 3.2 M DCl in steps of 0.4 M. For each series, solutions were prepared as a serial dilution of 4 M DCl prepared from 35% (by mass) DCl/D2O (99.5% D, Cambridge Isotope Laboratories) and D_2O (99.96% D, Cambridge Isotope Laboratories). Isotopically dilute solutions of 10% HOD in DCl/D_2O were prepared by including 5% H_2O (mole fraction) purified by reverse osmosis (to a resistivity of 18.2 MΩ·cm, Millipore *Milli-Q*). Transmission FTIR spectra are measured by holding 20 μL of sample between two 1 mm-thick CaF_2 windows separated by a 6 μm-thick Mylar spacer. This results in samples with optical density of ~3.0 in the O-D stretch and ~0.3 in the O-H stretch for the 10% HOD series.

In the SVD framework, the overall concentration dependent spectral responses are linearly decomposed into a set of independent spectral components and their concentration-dependent weights. For each concentration series, we found that two spectral components accurately model the FTIR spectra, capturing over 90% of the spectral information. We constrained the first component to the spectrum of bulk water (either D_2O or 10% HOD in D_2O), so that the second component corresponded to the change in the FTIR spectra upon adding acid. Because introducing 10% HOD reduces the concentration of D_2O, we normalize the 10% HOD series with about 95% the intensity of the isotopically pure series. This ratio was determined by the relative intensities of the D_2O bend seen in the attenuated total reflection (ATR) spectra of D_2O and 10% HOD in D_2O. We exclude the O-D stretch region (2200 cm^{-1} – 2800 cm^{-1}) since the O-D stretch saturates absorption over a 6 μm path length.

Appendix 5C: Anion Dependence of Selected Spectra

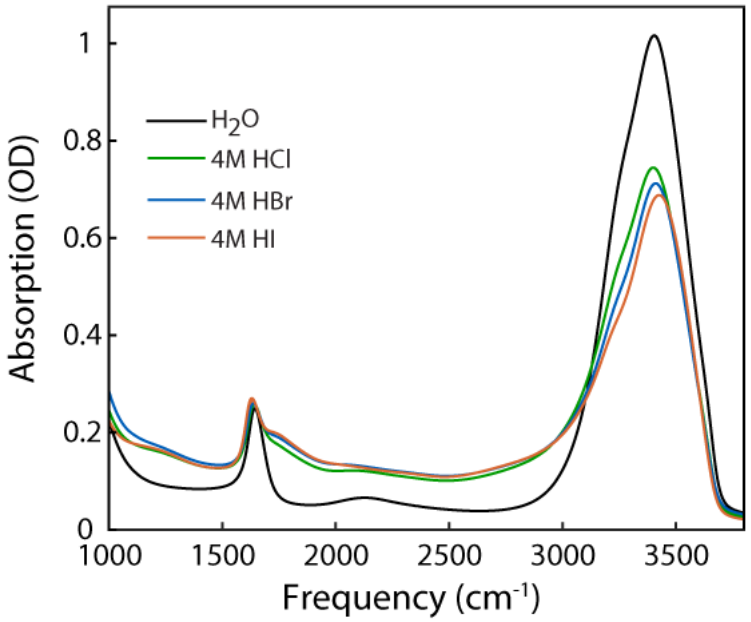

Figure 5C.1: Linear IR spectra of 4M HCl, HBr, and HI solutions, demonstrating that the continuum is a feature of the aqueous proton complex. Samples were prepared by sandwiching 1 μL of solution between two 1 mm thick CaF_2 windows.

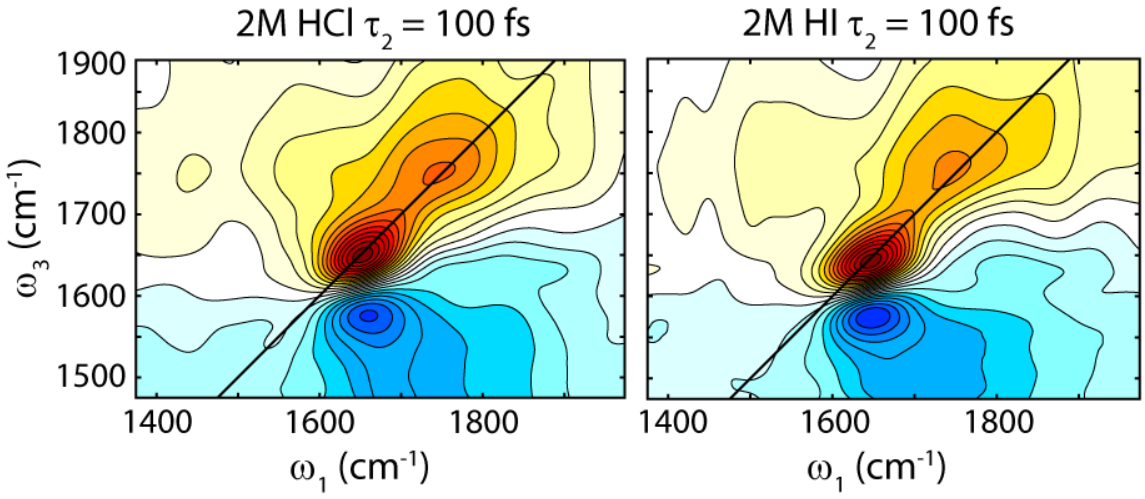

Figure 5C.2: Isotropic IR spectra of 2M HCl and 2M HI solutions at the Region 2 diagonal.

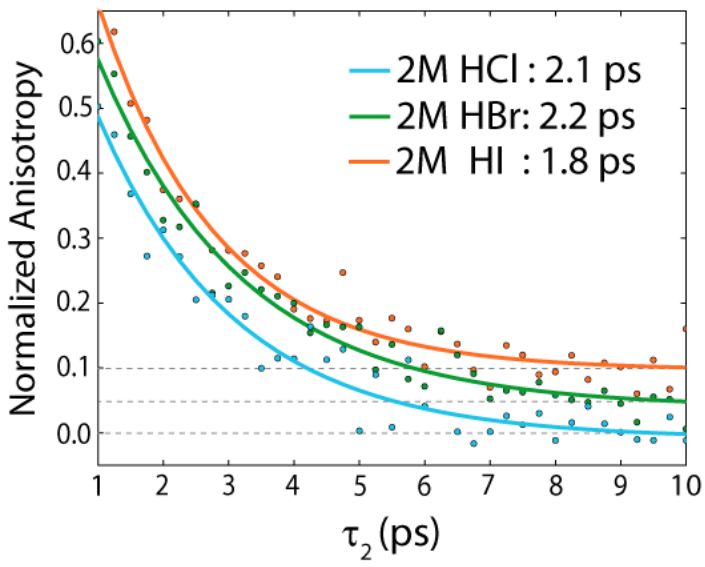

Figure 5C.3: Normalized long-time TA anisotropy decays between τ_2 = 1-10 ps for 2M HCl, 2M HBr, and 2M HI solutions at Region 2 diagonal spectral region. Anisotropy traces are offset for clarity (offsets shown as grey dashed lines).

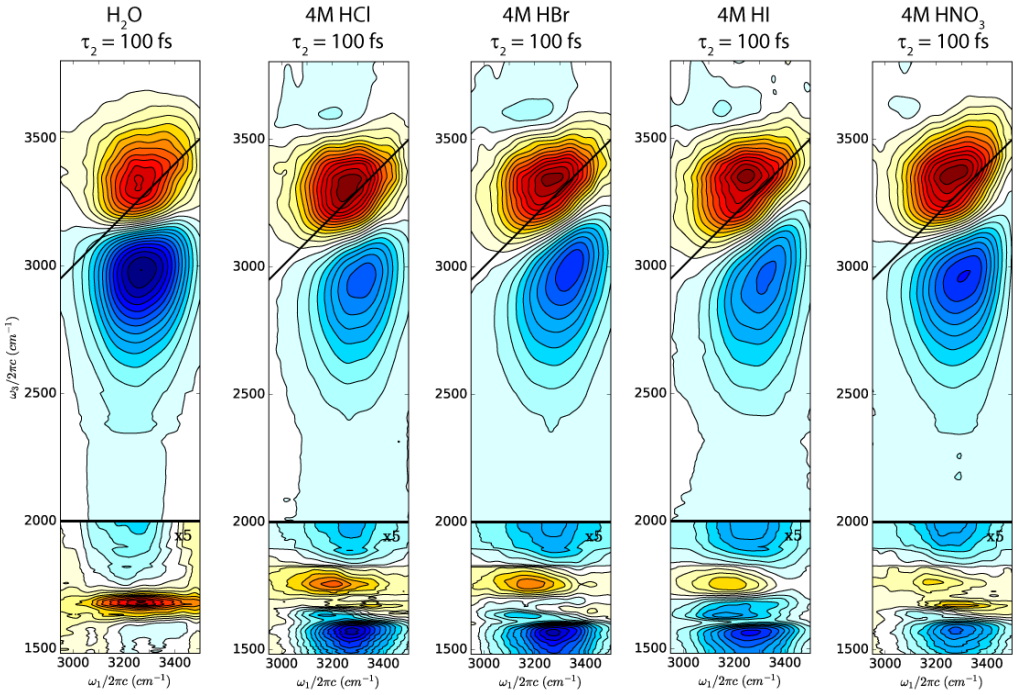

Figure 5.C4: Isotropic 2D IR spectra of 4M acid solutions in Region 4 at τ_2 = 100 fs. Spectra are each normalized to their respective absolute maximum values.

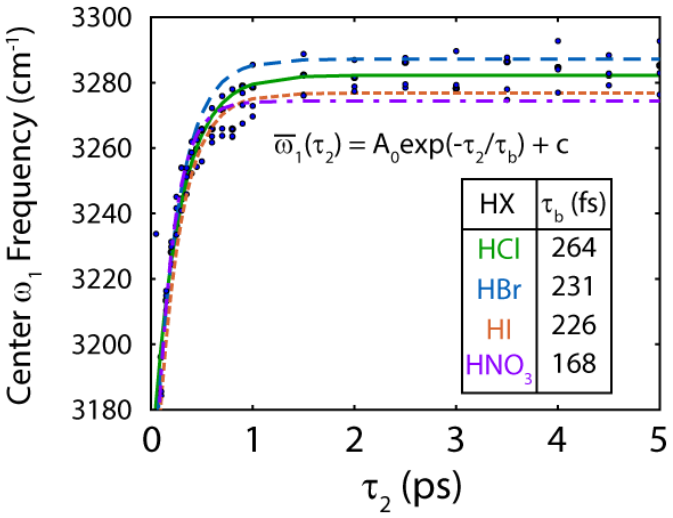

Figure 5C.5: Center ω_1 frequency position of the cross peak bleach between Regions 4 and 2, repeated with different acidic solutions: 4M HCl (solid green), HBr (dashed blue), HI (short dashed brown), and HNO_3 (dot-dashed purple).

Appendix 5D: Concentration Dependence of Selected Spectra

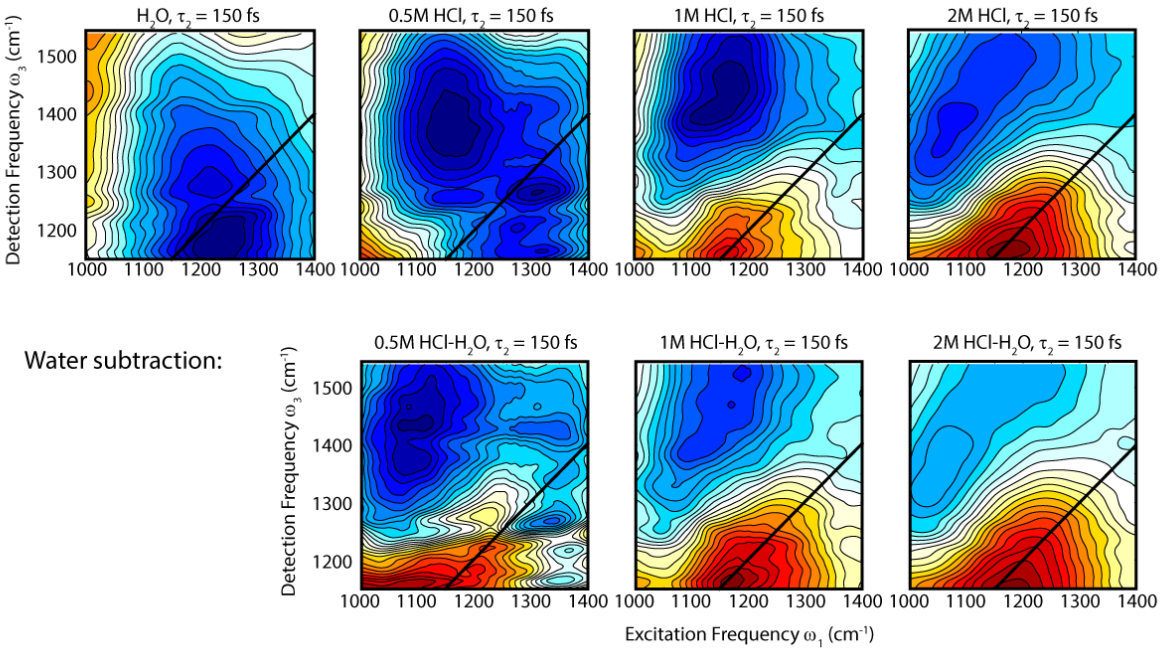

Figure 5D.1: 2D IR spectra of 0.5M, 1M, and 2M HCl along the Region 1 diagonal, and subtraction of the water background. These spectra were taken with 1mm CaF_2 windows with 100 fs pump pulses polarized at magic angle, and are normalized to their own maxima.

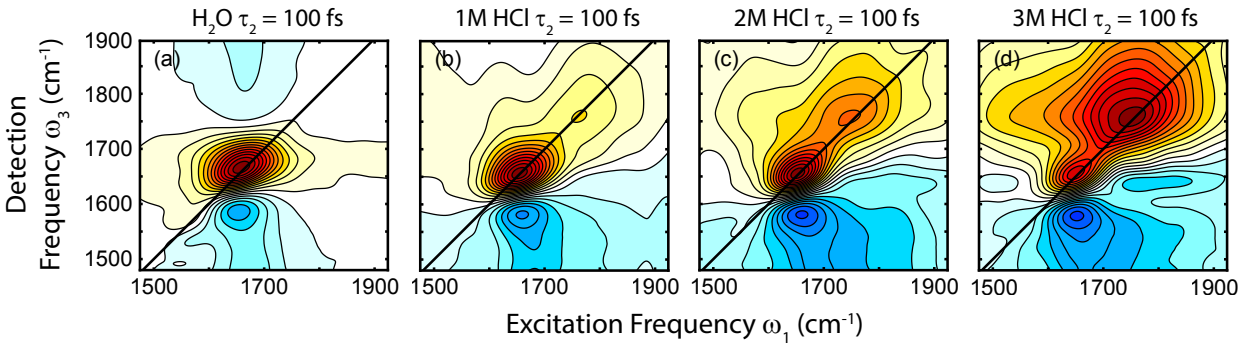

Figure 5D.2: Isotropic 2D IR spectra of H_2O, 1-3M HCl along the Region 2 diagonal.

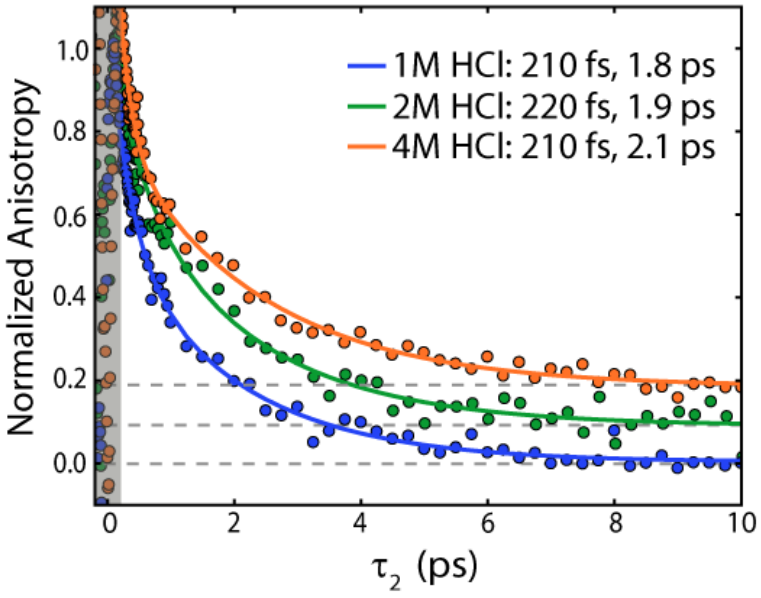

Figure 5D.3: Normalized TA anisotropy decays for 1M, 2M, and 4M HCl solutions at the Region 2 diagonal spectral region. Anisotropy traces are offset for clarity (offsets shown as grey dashed lines).

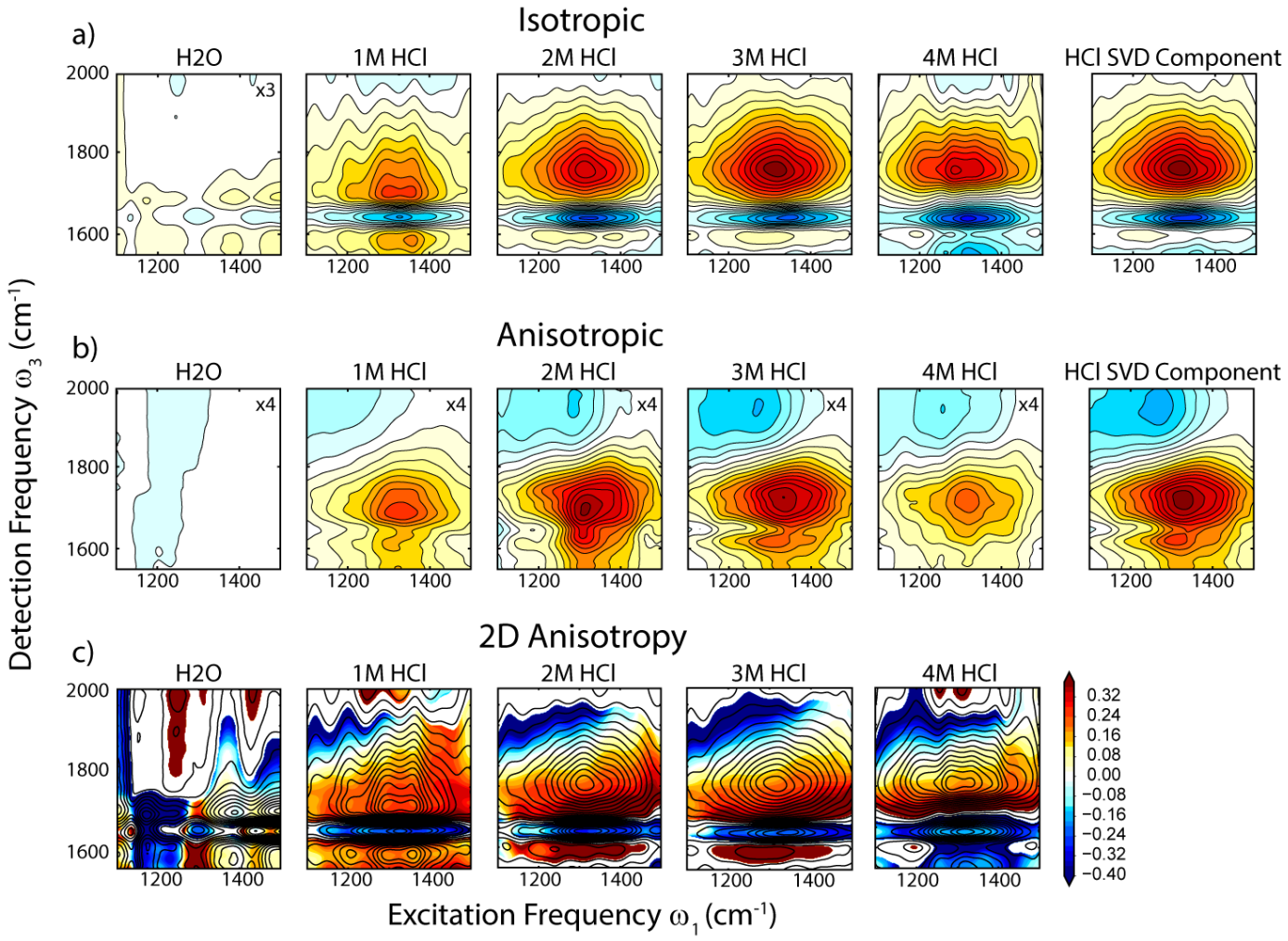

Figure 5D.4: (a) Isotropic, (b) anisotropic, and (c) 2D anisotropy surfaces at τ_2 = 150 fs for a concentration series of HCl in H_2O. All surfaces are shown with the same scaling or magnified by the factor in the given panel. The acid-associated component from an SVD/MEM analysis on the 2D IR surfaces is shown to the right of each concentration series for the isotropic and anisotropic 2D IR spectrum.

Chapter 6

High-Level VSCF/VCI Calculations Decode the Vibrational Spectrum of the Aqueous Proton

The work presented in this chapter has been published and is reprinted with permission from:
Yu, Q.; Carpenter, W.B.; Lewis, N.H.C; Tokmakoff, A.; Bowman, J.M. High-Level VSCF/VCI Calculations Decode the Vibrational Spectrum of the Aqueous Proton. *Journal of Physical Chemistry B* **2019**, *123* (33), 7214-7224.

6.1 Abstract

The hydrated excess proton is a common species in aqueous chemistry which complexes with water in a variety of structures. The infrared spectrum of the aqueous proton is particularly sensitive to this array of structures, which manifests as continuous IR absorption from 1000-3000 cm^{-1} known as the "proton continuum." Because of the extreme breadth of the continuum and strong anharmonicity of the involved vibrational modes, this spectrum has eluded straightforward interpretation and simulation. Using protonated water hexamer clusters from reactive molecular dynamics trajectories, and focusing on their central $H^+(H_2O)_2$ structures' spectral contribution, we reproduce the linear IR spectrum of the aqueous proton with a high-level local-monomer quantum method and highly accurate many-body potential energy surface. The accuracy of this approach is first verified in the vibrational spectra of the two isomers of the

protonated water hexamer in the gas phase. We then apply this approach to 800 $H^+(H_2O)_6$ clusters, also written as $[H^+(H_2O)_2](H_2O)_4$, drawn from MS-EVB simulations of the bulk liquid to calculate the infrared spectrum of the aqueous proton complex. Incorporation of anharmonic effects to the vibrational potential and quantum mechanical treatment of the proton produce better agreement to the infrared spectrum compared to the double-harmonic approximation. We assess the correlation of the proton stretching mode with different atomistic coordinates, finding the best correlation with $\langle R_{OH} \rangle$, the expectation value of the proton-oxygen distance R_{OH}. We also decompose the IR spectrum based on normal mode vibrations and $\langle R_{OH} \rangle$ to provide insight on how different frequency regions in the continuum report on different configurations, vibrational modes, and mode couplings.

6.2 Introduction

The aqueous proton is a fundamental cationic species whose transport process is ubiquitous and plays an important role in biological and chemical systems.[1–4] Due to the strength and flexibility of the hydrogen bond (H-bond) network, the aqueous proton system exhibits unique properties such as ultrafast proton mobility. The Grotthuss mechanism is used to explain this ultrafast rearrangement process, whereby a series of sequential transfers of individual protons result in overall charge transport.[5–7] Both experimental and theoretical efforts have been made in investigating the structures and ultrafast dynamics of the hydrated proton complex, from gas phase protonated water clusters[8–16] to the hydrated proton in the condensed phase.[7,17–26] The vibrational spectra of acidic solutions provide essential information on the ultrafast dynamics and various structures of the excess proton.[18,22,23,25,27,28] In the linear infrared[25,27,29] and Raman[25,30] spectra of acidic solutions, the "proton continuum" presents as a broad continuous absorption spanning the mid-IR from below 1000 cm^{-1} up to 3000 cm^{-1}. Even though rich information about the structure,

H-bonding environment, and dynamics of aqueous species can be obtained from vibrational spectroscopy,[19] the broad featureless spectrum of the excess proton eludes straightforward interpretation.

To address this issue, gas-phase vibrational spectroscopy of small protonated water clusters has provided invaluable insight on the fundamental geometries and motions of the excess proton. By carefully analyzing IR spectra of clusters ranging from hydronium H_3O^+ to larger clusters $H^+(H_2O)_{n,\ n=2\text{-}28}$,[10–12,14,31] researchers have described the structure of the aqueous proton within the framework of two idealized structures. On one end, the excess proton localizes on one water to form a hydronium ion with a particularly tight first solvation shell, known as the Eigen species $H_9O_4^+$.[32,33] On the other extreme, the proton is equally shared between two flanking waters, behaving collectively as the Zundel complex $H_5O_2^+$.[30] In the gas phase, the spectra of these two species display distinguishable sets of resonances that reflect the complexes' inherent molecular symmetries, and thus have been used to broadly categorize clusters of differing sizes as corresponding to Eigen-like or Zundel-like geometries. In particular, the protonated water hexamer $H^+(H_2O)_6$ is the smallest cluster for which both two structural motifs coexist at low temperature. In the experiment conducted by Asmis and coworkers, the IR spectra of these two isomers were decomposed via double-resonance spectroscopy, revealing distinct Eigen and Zundel forms whose resonances were significantly broadened and coupled due to anharmonicity in their nuclear potentials, as revealed by *ab initio* molecular dynamics (AIMD) simulations.[31]

Within the last few years, multiple simulation studies have begun to provide insight into the broad features in the aqueous-phase proton spectrum. With the aid of molecular dynamics simulations using the Multi-State Empirical Valence Bond (MS-EVB) force field,[34,35] the spectrum of the aqueous proton was modelled at the harmonic level, revealing spectral trends with the

geometry of the hydrated proton complex, the extent of vibrational delocalization, and the mixture of stretching and bending character in the normal modes.[29] Even at the harmonic level, the study uncovered that the vibrations of the excess proton are highly mixed and delocalized, requiring a careful interpretation of the vibrational bands. Another landmark study combined linear IR and Raman spectroscopies with anharmonic local-mode spectral calculations on protonated clusters drawn from *ab initio* simulations.[36] This study treated the stretching motions of the excess proton one-dimensionally, applying a discrete variable representation (DVR) of the Schrödinger equation to the proton stretch with potential energy also calculated with DFT at the B3LYP level. This study predicted the presence of asymmetric "Zundel-like" species in solution, similar to Zundel's original conception and later supported by ultrafast IR experiments.[18,25,37] Despite the contributions these studies have played in illuminating the nature of the aqueous excess proton, the multidimensional anharmonic nature of the vibrational potential was not addressed, which have been investigated in small gas-phase protonated water clusters.[13,16,38]

Recently, the 2D IR spectrum of the aqueous excess proton was measured to investigate the vibrational potentials of the various modes and to directly observe the effects of anharmonic mode mixing.[18,25] Excitation of the proton stretch mode at 1200 cm^{-1} produces an excited state absorption between the first and second vibrational excited states at higher frequency than the ground state bleach.[25] This indicates that the vibrational potential of the excess proton is strongly confined by two waters with Zundel-like vibrational behavior, rather than associating with solely with one water as predicted for a hydronium species. A subsequent 2D IR study spanning the entire mid-IR found that cross peaks between every main feature imply that one predominant motif describes the aqueous proton complex.[18] The polarization-dependent cross peaks between all of the main features can be self-consistently explained by a persistent Zundel-like core around the aqueous

proton. However, the relationship between the molecular configurations of aqueous proton complexes and the vibrational potentials of their highly anharmonic modes has yet to be understood. Thus, to capture the essentials of the vibrational spectrum of the hydrated proton complex, more rigorous theoretical tools should be applied for analysis.

Calculating the vibrational anharmonicity and mode mixing has previously been more successful in small protonated water clusters. Vendrell, Meyer and coworkers applied multiconfiguration time-dependent Hartree (MCTDH) method to decipher the spectrum of $H^+(H_2O)_2$ successfully.[13] For larger gas-phase clusters, the vibrational self-consistent field/virtual state configuration interaction (VSCF/VCI) approach was successfully applied to reproduce the IR spectra of $H^+(H_2O)_3$ and $H^+(H_2O)_4$.[16,38,39] These high-level quantum calculations are based on highly accurate *ab initio* potential energy surfaces and dipole moment surfaces (PES/DMS) of protonated water clusters that some of us developed.[40–42] The vibrational spectra of hydrated proton system can also be simulated from classical MD or path integral based molecular dynamics with an appropriate potential. However, these methods cannot fully include anharmonic effects or mode coupling which are essential in the hydrated proton. The interested reader is referred to our recent paper, where detailed comparison and discussion are given.[43] The VSCF/VCI approach and accurate PES/DMS have enabled access to the anharmonic and multi-dimensional nuclear potentials to disentangle the complicated spectra of protonated water clusters. However, as the size of clusters gets larger, such as in the cases of $H^+(H_2O)_6$ or aqueous proton complexes, it becomes unfeasible to conduct full-dimensional vibrational analysis due to the high dimensionality and cost of potential calculation.

To overcome the dimensionality limitations, the local monomer approximation was developed to calculate the IR spectra of larger systems.[44] This approximation reduces

computational cost by breaking a large system into smaller local monomer subgroups and discarding the coupling constants between vibrational modes on different local monomers. The spectrum of the whole system is a sum of contributions of vibrations from each defined monomer. This approximation has proved to be useful and accurate for calculating the IR spectra of the liquid and ice forms of H_2O and D_2O, capturing broad, anharmonic features such as the bend-libration combination band at 2200 cm^{-1} in H_2O.[45–48] Thus, it becomes natural to apply the local monomer approximation on the structures of the aqueous proton and efficiently generate accurate anharmonic vibrational spectra for the multiple possible configurations in the liquid phase.

In this study, we extend the local monomer approximation to VSCF/VCI calculations of hydrated proton clusters as a technique to analyze and interpret the IR spectrum of the aqueous proton. Hydrated proton configurations were drawn from 800 $H^+(H_2O)_6$ geometries accessed from aqueous-phase MS-EVB trajectories. As mentioned above, protonated hexamers constitute the smallest cluster that incorporates Eigen-like and Zundel-like species, providing a workable trade-off between calculation cost and incorporation of many-body effects from the solvation environment. $H^+(H_2O)_6$ can be rewritten as $[H^+(H_2O)_2](H_2O)_4$ where we define the local monomers as the central $H^+(H_2O)_2$ and four remaining water monomers. The vibrational spectrum of the aqueous proton can be approximated as the spectral contribution from central $H^+(H_2O)_2$ in those $[H^+(H_2O)_2](H_2O)_4$ clusters. To benchmark the local monomer approximation, we first compare our calculations of the gas-phase Eigen and Zundel isomers of the protonated water hexamer to the experimental spectra mentioned above, finding excellent agreements with peak position and intensity, even for subtler features. We then present the IR spectrum obtained from the VSCF/VCI calculations on protonated hexamer geometries drawn from aqueous MS-EVB simulations.[29] We also find agreement with the experimental aqueous-phase linear spectrum, and

we decompose the spectrum based on vibrational character to assign the various regions across the mid-IR. The difference with the harmonic spectrum underscores the importance of accounting for the full anharmonicity in the vibrational potentials of the aqueous proton. We then correlate shared proton stretch frequency with various structural parameters and decompose the full spectrum by geometry to uncover spectral trends as proton configurations transition from behaving more Zundel-like to more Eigen-like. This information can aid the interpretation of the experimental infrared spectrum in each IR frequency range. The high-level treatment of the anharmonicity in these calculations also reveals substantial mode mixture of different proton-associated vibrations, in particular the proton stretching and bending modes of Zundel-like complexes.

6.3 Methods

Experimental conditions and analysis for collecting linear IR spectra are presented in Chapter 5, Appendix 5A.

6.3.1 Computational Details

To analyze the spectrum of the aqueous proton, we made use of 800 clusters extracted from the snapshots of MS-EVB simulations performed in Ref. 29. In brief, the 1 ns trajectory was obtained with the MS-EVB 3.2 model[35] of one excess proton and chloride dissolved in 256 SPC/Fw water molecules.[49] We used the same criteria in identifying the proton position as in Ref. 29: from instantaneous configurations of the MS-EVB trajectory, we extracted clusters of molecules centered on a H atom that participates in an $O_1\cdots H\cdots O_2$ hydrogen bond, selecting them on the basis of the proton sharing parameter $\delta \mathrm{R}_{\mathrm{OH}} = \left| r_{O_1H} - r_{O_2H} \right|$. Among the three protons of the hydronium moiety, the proton with the lowest δR_{OH} was chosen as the excess proton. We selected 800 clusters from the MS-EVB trajectory snapshots with all waters whose oxygen atoms were within 5Å to the defined proton, written as $H^+(H_2O)_n$, $n \approx 16$-18. From each $H^+(H_2O)_n$ cluster, we

further decreased the cluster size to $H^+(H_2O)_6$ which only included the proton and its closest six water molecules. We identified the central $H^+(H_2O)_2$ structure with the proton and two closest water monomers for all 800 $H^+(H_2O)_6$ clusters and 800 $H^+(H_2O)_n$, $n \approx$ 16-18 clusters. The $H^+(H_2O)_n$, $n \approx$ 16-18 clusters were used for harmonic analysis to compare with the previously calculated harmonic spectra.[29] The $H^+(H_2O)_6$ clusters were used for both harmonic analysis and VSCF/VCI calculation based on local monomer approximation. Examples of the two sizes of clusters, $H^+(H_2O)_n$ and $H^+(H_2O)_6$ are shown in the right panel of Fig. 6.1 along with their central $H^+(H_2O)_2$ structure encircled in red. This central $H^+(H_2O)_2$ can be identified as proton with two water monomers or the hydronium H_3O^+ with its closest water according to different proton positions. We classified all cluster structures according to the proton asymmetry δR_{OH}, with the criterium of $\delta R_{OH} = 0.2$Å to identify Zundel-like (< 0.2Å) and Eigen-like (> 0.2Å) species. Among those 800 $H^+(H_2O)_6$ clusters, we obtain 53% Zundel-like clusters and 46% Eigen-like clusters which agrees with previous results.[29,36] Further decomposition by δR_{OH} of the total trajectory and the 800 analyzed configurations indicates that the clusters are representative of the trajectory.

For each $H^+(H_2O)_6$ cluster, we located the central $H^+(H_2O)_2$ as describe above. This central $H^+(H_2O)_2$, denoted as the "special pair,"[50,51] is the smallest structure that includes both Zundel-like and hydronium-like geometries and is the largest local monomer that we can apply in VSCF/VCI calculations. Larger structures like $H^+(H_2O)_3$ require much more computational cost mainly because of the increasing number of normal modes. In the local $H^+(H_2O)_2$ monomer analysis, we conducted normal mode analysis on the central $H^+(H_2O)_2$ structure with all remaining water monomers fixed at their geometries. Anharmonic VSCF/VCI calculations were then conducted for all 800 $H^+(H_2O)_6$ clusters using code MULTIMODE[52] in the basis of the 12-15 normal modes of a central $H^+(H_2O)_2$ and 4-mode representation of the potential (4MR). The

excitation space consists of single, double, triple and quadruple excitations resulting in a size of the final Hamiltonian matrix around 10,000 for each cluster. We also conducted local monomer and VSCF/VCI calculations for the two isomers of the gas-phase $H^+(H_2O)_6$ cluster. The local monomers for these two isomers include (1) central $H^+(H_2O)_2$ which is a proton with two water monomers for the Zundel isomer and hydronium with the closest water monomer for the Eigen isomer (2) each of four remaining water monomers. The VSCF/VCI spectrum of each isomer is sum of contributions from all above local monomers.

Both harmonic analysis and VSCF/VCI calculations were done based on accurate *ab initio* many-body PES/DMS. This PES/DMS has already been verified to be highly accurate in describing the structures, energies, and vibrational properties of different sizes of protonated water clusters.[16,38,41–43,53]

6.4 Results and Discussion

6.4.1 Harmonic Spectra of Clusters from the Aqueous Phase

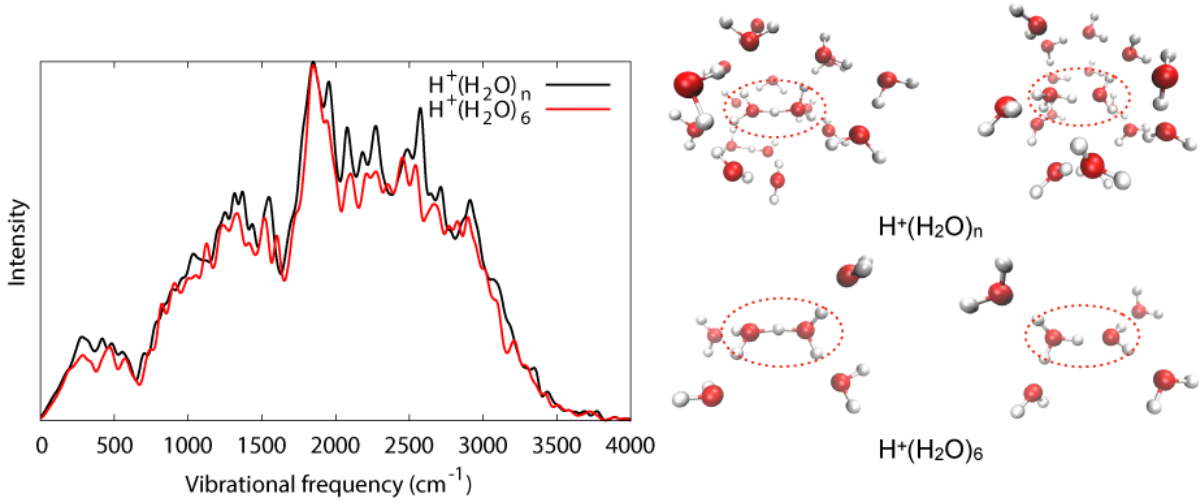

Figure 6.1: Double harmonic spectra of $H^+(H_2O)_2$ structures in 800 protonated water clusters with different sizes. $H^+(H_2O)_n$ has 16-18 water molecules and $H^+(H_2O)_6$ has proton with 6 water molecules. The harmonic frequencies are calculated from local $H^+(H_2O)_2$ monomer analysis where central $H^+(H_2O)_2$ structures are circled in the right panel for different clusters.

Before presenting the anharmonic spectrum of the aqueous proton, we briefly summarize the features of the harmonic spectra from local $H^+(H_2O)_2$ monomer analysis of two sizes of clusters, $H^+(H_2O)_n$, $n \approx$ 16-18 and $H^+(H_2O)_6$ (Fig. 6.1). For both sizes of clusters, the spectrum of their central $H^+(H_2O)_2$ consists of a broad continuum from below 1000 cm^{-1} to above 3000 cm^{-1}. This spectral shape agrees with the previously calculated difference spectral density for aqueous proton at the B3LYP level (Figures 3.e and 3.f in Ref. 29). Even though the spectrum in Fig. 6.1 is the spectral contribution from central $H^+(H_2O)_2$, the spectrum in the previous study was calculated from the difference spectral density between protonated water clusters and bulk water clusters.[29] The harmonic spectrum includes contributions from both Zundel-like $H^+(H_2O)_2$ cores and Eigen-like structures' central H_3O^+ and its closest water, which already produces the IR continuum of absorption. There are only small differences between the spectrum of the central $H^+(H_2O)_2$ moiety embedded in the $H^+(H_2O)_n$ and $H^+(H_2O)_6$ clusters, which implies that the central $H^+(H_2O)_2$ spectrum is more influenced by its first solvation shell and the excess proton than by the solvation water beyond the first four hydration molecules. These observations indicate that calculating the vibrational spectrum with a central $H^+(H_2O)_2$ in a $H^+(H_2O)_6$ cluster instead of in a $H^+(H_2O)_n$ cluster is a qualitatively reasonable approximation. Additionally, since the broad continuum is recovered using a local $H^+(H_2O)_2$ monomer, the VSCF/VCI calculation of these structures should also be able to recover the main features of the aqueous excess proton spectrum. To emphasize the local $H^+(H_2O)_2$ monomer strategy, we will denote the clusters as $[H^+(H_2O)_2](H_2O)_4$ rather than $H^+(H_2O)_6$ in the following text.

6.4.2 VSCF/VCI Spectra of Gas-Phase Protonated Water Hexamers

We next illustrate the accuracy of the local monomer VSCF/VCI calculations with two important isomers of the gas-phase protonated water hexamer $[H^+(H_2O)_2](H_2O)_4$, known as the

Zundel and Eigen isomers. The Zundel isomer consists of the symmetric "Zundel" core with four solvating water molecules, while the Eigen isomer has the standard "Eigen" core with additional two waters accepting H-bonds from the waters in hydronium's first solvation shell. Their calculated spectra and comparisons with experiment[31] are shown in Fig. 6.2. The double harmonic spectrum of the Zundel isomer is also plotted in Fig. 2.10. The harmonic spectra appear qualitatively different from the experimental spectra with peak position inaccuracies of several hundred wavenumbers for some features. However, upon including anharmonicity and mode coupling, the VSCF/VCI spectra achieve excellent agreement with experiment in terms of frequency positions and relative intensities, even with the local $H^+(H_2O)_2$ monomer and local water monomer approximation. Additionally, the agreement between the calculated and experimental spectra for the Eigen isomer demonstrate that the choice of a local $H^+(H_2O)_2$ monomer can also be applied for Eigen-like configurations.

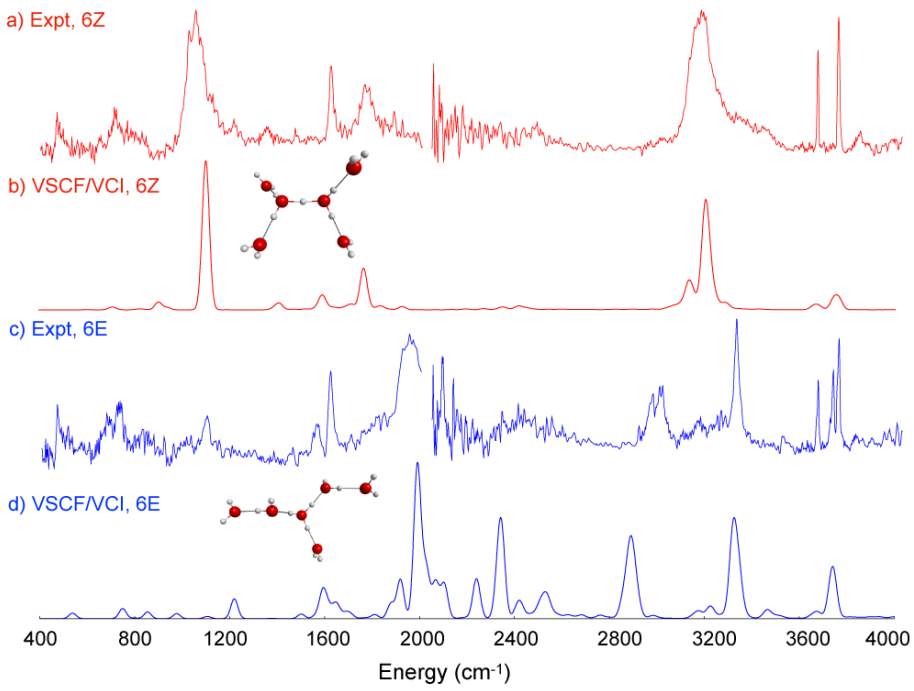

Figure 6.2: Vibrational spectra of (a)-(b) Zundel (6Z) and (c)-(d) Eigen (6E) isomers of protonated water hexamer from experiment[31] and VSCF/VCI calculations.

From the VSCF/VCI calculation, the Zundel isomer displays a strong proton stretch band at 1102 cm^{-1} which is more than 100 cm^{-1} blue-shifted from its harmonic frequency. Another signature band of the Zundel isomer is the bending mode of the proton's hydration waters at around 1760 cm^{-1}, which has relatively large intensity due to coupling with the proton stretch. The band at 3167 cm^{-1} from experiment is verified as the O–H stretch of the two flanking water monomers within the central $H^+(H_2O)_2$. The harmonic analysis predicts the frequency at around 3350 cm^{-1} which is almost 200 cm^{-1} higher than both experiment and VSCF/VCI calculations. The shift of important signature bands relative to their harmonic predictions is even larger in the Eigen isomer. Harmonic analysis produces three hydronium stretches at 3197, 2783 and 2728 cm^{-1}, but experiment demonstrates three strong and broad bands at 3007, 2425 and 1951 cm^{-1}. With the VSCF/VCI approach, we successfully reproduce these three important bands and verify their origins. The hydronium stretches are redshifted 200-700 cm^{-1} from their harmonic counterparts due to the anharmonicity of the system and extensive mode coupling within the local monomer. As introduced before, this phenomenon has been seen in vibrational analyses of other protonated water clusters, $H^+(H_2O)_3$ and $H^+(H_2O)_4$, where the VSCF/VCI approach works very well while harmonic and some post-harmonic approaches (like VPT2) cannot fully explain the experimental spectra.[16,38]

It should also be noted that there are still some small differences between the experimental and VSCF/VCI spectra, with respect to band position. This is likely due to the anharmonic coupling with low-frequency modes (notably the O···O stretches within and between local monomers) that are not included in our calculations and errors in the PES/DMS. Nevertheless, the efficacy of the VSCF/VCI method on these two configurations establishes confidence that the

technique can efficiently calculate the spectra of multiple $[H^+(H_2O)_2](H_2O)_4$ configurations drawn from the aqueous phase.

6.4.3 VSCF/VCI Spectrum of $H^+(H_2O)_2$ from Aqueous Configurations

To analyze the aqueous proton spectrum, we begin with an introduction to the experimental linear IR spectral features that grow in upon introduction of strong acid. The experimental spectrum associated with aqueous HCl solution is presented as the second spectral component derived from the maximum entropy analysis of the acid concentration series (Fig. 6.3a). We find that the component resembles an acid-water difference spectrum consisting of broad features centered around 1200 cm^{-1}, 1750 cm^{-1}, 3000 cm^{-1}, with continuous absorption between each of these maxima and also a small positive peak around 3500 cm^{-1}. Since the maximum entropy analysis cannot extract components due to solvation of the H^+ or the Cl^- individually, we also present the results of the same maximum entropy analysis on a NaCl concentration series, which shows features centered at 1640 cm^{-1} and 3470 cm^{-1}. As shown in Fig. 5A.1, the 3470 cm^{-1} peak in both the HCl and NaCl spectra are centered at the same frequency in the ATR spectrum, but it is nontrivial to directly interpret these spectral contributions in highly-congested spectral regions. Above 3500 cm^{-1}, we find issues with positivity in the absorption spectrum, but this artifact disappears in the ATR acid concentration series (Fig. 5A.1).

The calculated VSCF/VCI spectrum of the $H^+(H_2O)_2$ local monomers summed over 800 $[H^+(H_2O)_2](H_2O)_4$ configurations (Fig. 6.3b) consists of a continuum and three broad bands, consistent with experiment. The first signature band spans 1000-1500 cm^{-1} with center frequency at 1200 cm^{-1} in experiment but is blue-shifted to 1300 cm^{-1} in the VSCF/VCI calculations. According to previous analyses, the feature has been assigned to both asymmetric proton stretches in Zundel-like configurations[13,29] and umbrella modes in Eigen-like configurations.[54] The second

signature band is centered at 1750 cm^{-1} in both the harmonic and VSCF/VCI and harmonic calculations, but the bandwidths and relative intensities of the 1750 cm^{-1} and 1200 cm^{-1} features are better captured by the anharmonic calculations. The 1750 cm^{-1} band has been assigned to bending motions of the waters flanking the excess proton,[10,23,25,29] but other studies have demonstrated that highly redshifted hydronium O–H stretches in gas-phase $H^+(H_2O)_{21}$ clusters are also located at this frequency.[14]

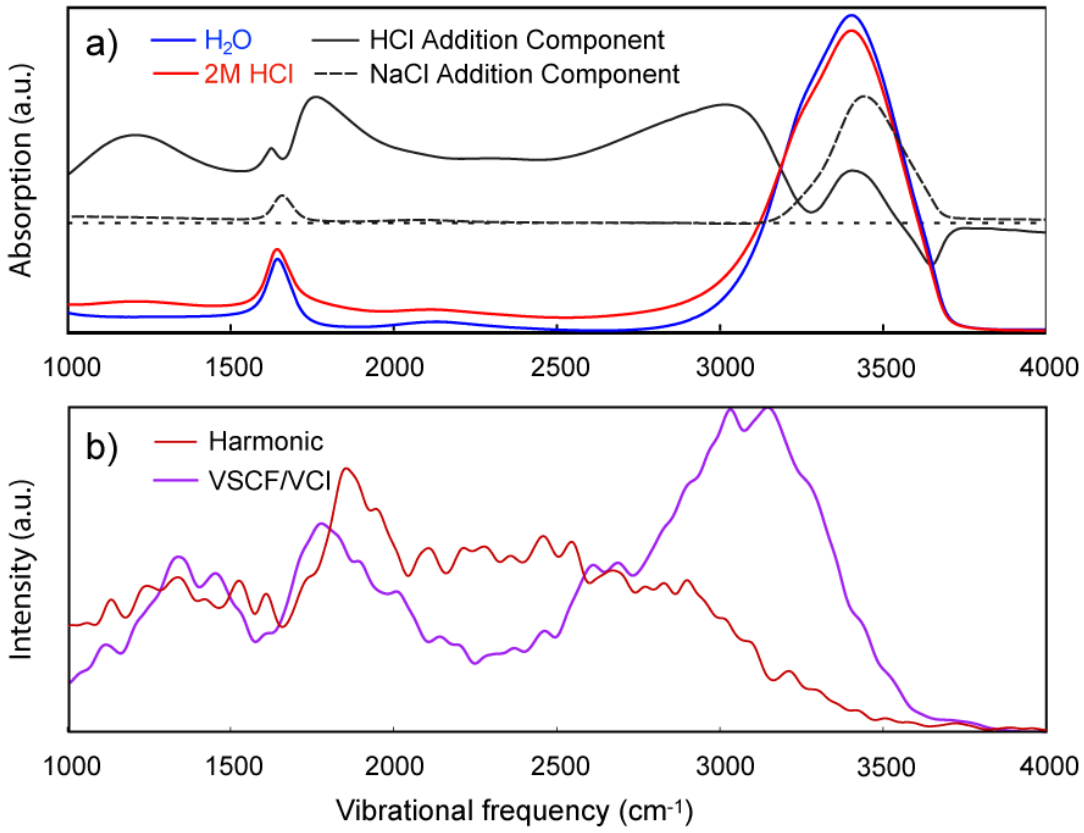

Figure 6.3: Infrared spectrum of the aqueous proton from experiment and VSCF/VCI calculations. (a) The experimental spectra include neat water (blue), 2M HCl (red) and the maximum entropy difference component (black). (b) The theoretical (VSCF/VCI) spectrum is spectra contributed from central $H^+(H_2O)_2$ part of 800 $[H^+(H_2O)_2](H_2O)_4$ clusters.

Between 1900 and 3000 cm^{-1} lies the proton continuum, which has been assigned to both hydronium stretches in Eigen-like configurations[55] and O–H stretches of the flanking waters in Zundel-like configurations.[18,36] The third signature band is around 3000 cm^{-1} both in experiment

and in our calculations. This band in the VSCF/VCI spectrum is more prominent than in the harmonic calculation. This feature has also been associated with Zundel-like configurations, arising from O–H stretches of the two flanking waters around the central excess proton.[10,13,23] To assess the various assignments across the mid-IR and to explore the influence of anharmonic mode-coupling, we will decompose this spectrum by geometric variables and vibrational character below.

The improved accuracy of the VSCF/VCI spectrum over the harmonic spectrum underscores the importance of anharmonic effects on the IR spectrum of the aqueous proton complex. The most apparent difference between the two methods is the intensity of the continuum across 1900-3000 cm^{-1}. According to harmonic analysis, this continuum is assigned as both hydronium-like O–H stretches in different distorted Eigen-like clusters and O–H stretches in flanking waters. However, the extremely large harmonic intensity and broad bandwidth of the hydronium-like stretches dominate over the flanking water stretches in this region. In the VSCF/VCI spectrum, strong anharmonicity and mode mixing make hydronium stretches undergo significant red-shifts and decreases in intensity, as in the cases of smaller gas-phase clusters.[43]

While the VSCF/VCI method is a great improvement over a harmonic treatment, the difference between the anharmonic calculation and the experimental spectrum indicates that the special pair local monomer spectrum does not fully represent the experimental aqueous proton spectrum. For instance, the experimental band at 1200 cm^{-1} is blueshifted to 1300 cm^{-1} in the VSCF/VCI spectrum. Besides the lack of mode coupling to other low-frequency modes (O···O stretches for example) within the local monomer, there may be some uncertainty associated with the MS-EVB model in providing correct statistics of aqueous protons structures. The MS-EVB model reproduces the experimental radial distribution functions better than other methods,[35] but

there is still some slight over-structuring that may influence the accessible configurations. We also expect the VSCF/VCI spectra can be further improved with more normal modes included in the calculation. Finally, the intensity of the 3000 cm^{-1} feature is larger than in experiment, but there is variability in the literature on the measured intensity of this feature,[29,36] subject to details of experimental collection. Even with the above caveats, this approach is cost-effective and reliable for calculating highly anharmonic IR spectra and analyzing the aqueous proton spectrum.

6.4.4 Decomposition of Spectrum by Vibrational Character

To assess the various assignments outlined above, we determined the spectral contributions from different vibrational components. For this analysis, the 800 clusters were binned into Zundel-like and Eigen-like configurations based on the proton asymmetry parameter δR_{OH}.[29,36] Due to the quantum delocalization of the proton in the VSCF/VCI calculations, the quantum expectation value, $\langle \delta R_{OH} \rangle$, with cutoff of 0.2Å was used. As seen in Fig. 6.4a, the spectrum of Zundel-like ($\langle \delta R_{OH} \rangle$ < 0.2Å) clusters display three intense and broad bands: 1300 cm^{-1}, 1750 cm^{-1} and 3000 cm^{-1}, whereas the spectrum due to Eigen-like configurations appears as a broad continuum from 1000-3500 cm^{-1} with maxima around 2000 cm^{-1} and 2600 cm^{-1}. We next used geometric cutoffs in normal mode displacements to identify the vibrational character. Normal modes with O–H stretching displacements greater than 0.01Å were counted as either proton stretching or flanking water stretching modes, depending on location of the H atom in the local monomer. Bending modes consisted of normal modes where both flanking waters changed angle by at least 1.0°, and umbrella modes consisted of normal modes where all three HOH angles of H_3O^+ changed by more than 0.8° with the same phase. Modes that consisted of both proton stretch and flanking bend character were also considered. After identifying the vibrational character of the normal mode basis in each cluster, for each VSCF/VCI state we multiplied the square of each of its normal

mode's VCI coefficients with their respective harmonic intensities. The results of this procedure summed over clusters are presented in Fig. 6.4b-d. Multiplying the square of VCI coefficient with normal mode's harmonic intensity is a good approximation to identify the spectrum contribution from different normal mode basis, which has been used to simulate the vibrational spectrum of the formic acid dimer.[56]

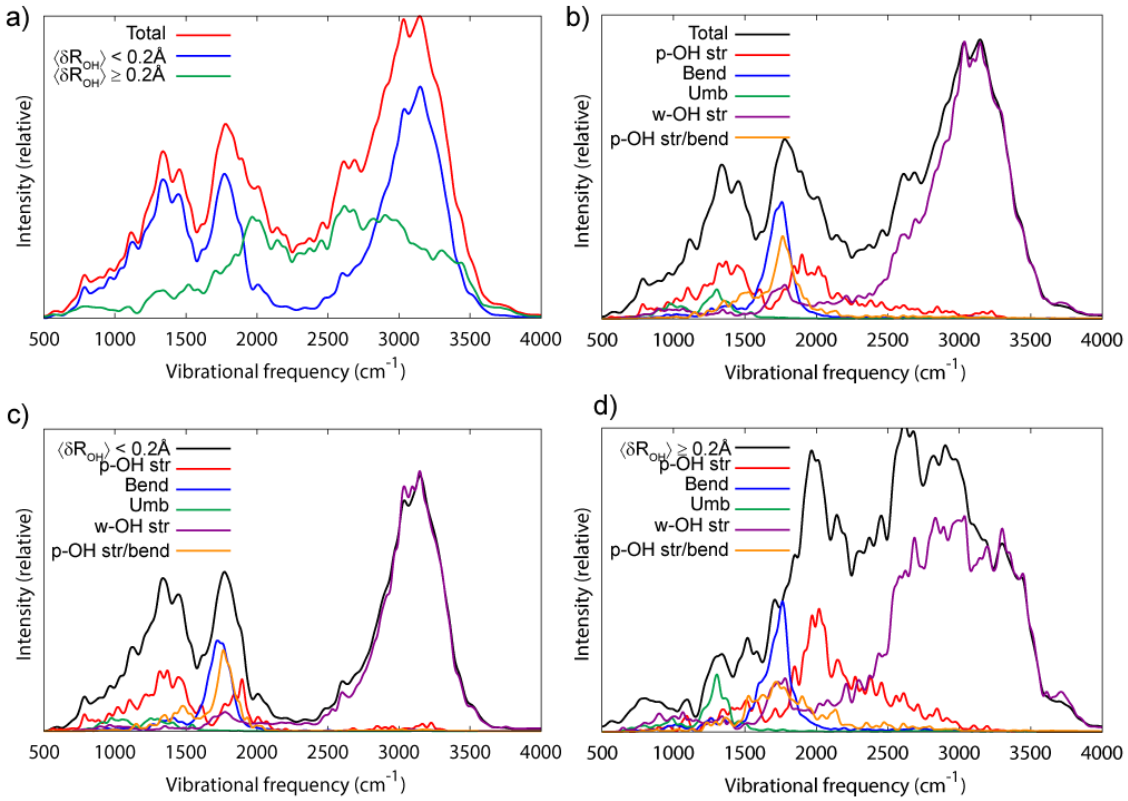

Figure 6.4: a) Calculated spectra of the aqueous proton from all 800 clusters, $\langle \delta R_{OH} \rangle < 0.2$Å (Zundel-like) clusters, and $\langle \delta R_{OH} \rangle \geq 0.2$Å (Eigen-like) clusters. b) Decomposition of the total spectra into different components, with p-OH str as proton stretch, bend as flanking water bend, Umb as hydronium umbrella motion, w-OH str as flanking water stretch, p-OH str/bend as motion which has both proton stretch and flanking water bend character. c)-d) Decomposition results for (c) Zundel-like and (d) Eigen-like configurations.

The vibrational character decomposition is shown for all configurations in Fig. 6.4b, with Zundel-like and Eigen-like decompositions in Figs. 6c and 6d, respectively. For Zundel-like configurations, the proton stretch has a significant contribution from 800-1600 cm^{-1} and 1700-

2000 cm^{-1} while the flanking water O–H stretch mainly contributes to the region in 2500-3500 cm^{-1}. Modes with primarily flanking water bend character and proton stretch-bend mixed character overlap strongly at 1750 cm^{-1}. Umbrella modes do not make significant contributions to the spectrum Zundel-like complexes. In Eigen-like configurations (Fig. 6d), the proton stretches span a broad region from 1500-2600 cm^{-1} with a maximum at 2000 cm^{-1}, whereas the flanking water stretches span 2500-3500 cm^{-1}. The spectral distribution of flanking waters in Eigen-like complexes is broader than those in Zundel-like configurations since the O–H stretches on the hydronium and nearest water differ.[36] There are bending modes of Eigen-like complexes at 1750 cm^{-1}, but they are weaker than those from Zundel-like complexes and there is less mixing with the proton stretch. Finally, there is weak umbrella mode character at 1200 cm^{-1}.

This decomposition assists in clarifying the various assignments presented above from the literature. At 1200 cm^{-1} in the total spectrum (Fig. 6b), the proton stretch of Zundel-like configurations dominates, with little contribution from umbrella modes of Eigen-like geometries. The intense and broad band from 1600-2000 cm^{-1} comes from multiple sources, listed in order of highest to lowest importance: flanking water bends and mixed stretch-bend modes in Zundel-like configurations, proton stretches in Zundel-like and Eigen-like clusters, and bending modes in Eigen-like configurations. This heterogeneity explains why there has been controversy in the assignment of this region, but all of these contributions should be considered when analyzing this region of the IR spectrum. The continuum from 2000-2700 cm^{-1} consists of contributions from Eigen-like proton stretches and flanking water stretches, while flanking water stretches in both Eigen-like and Zundel-like complexes are found at frequencies higher than 2700 cm^{-1}. In general, flanking water stretches do not show strong mixing with the other modes and therefore do not

donate their high intensity to those modes. As a result, the flanking water stretches become distinguishable on top of the continuum.

6.4.5 Influence of Structural Parameters on Proton Stretch Frequency

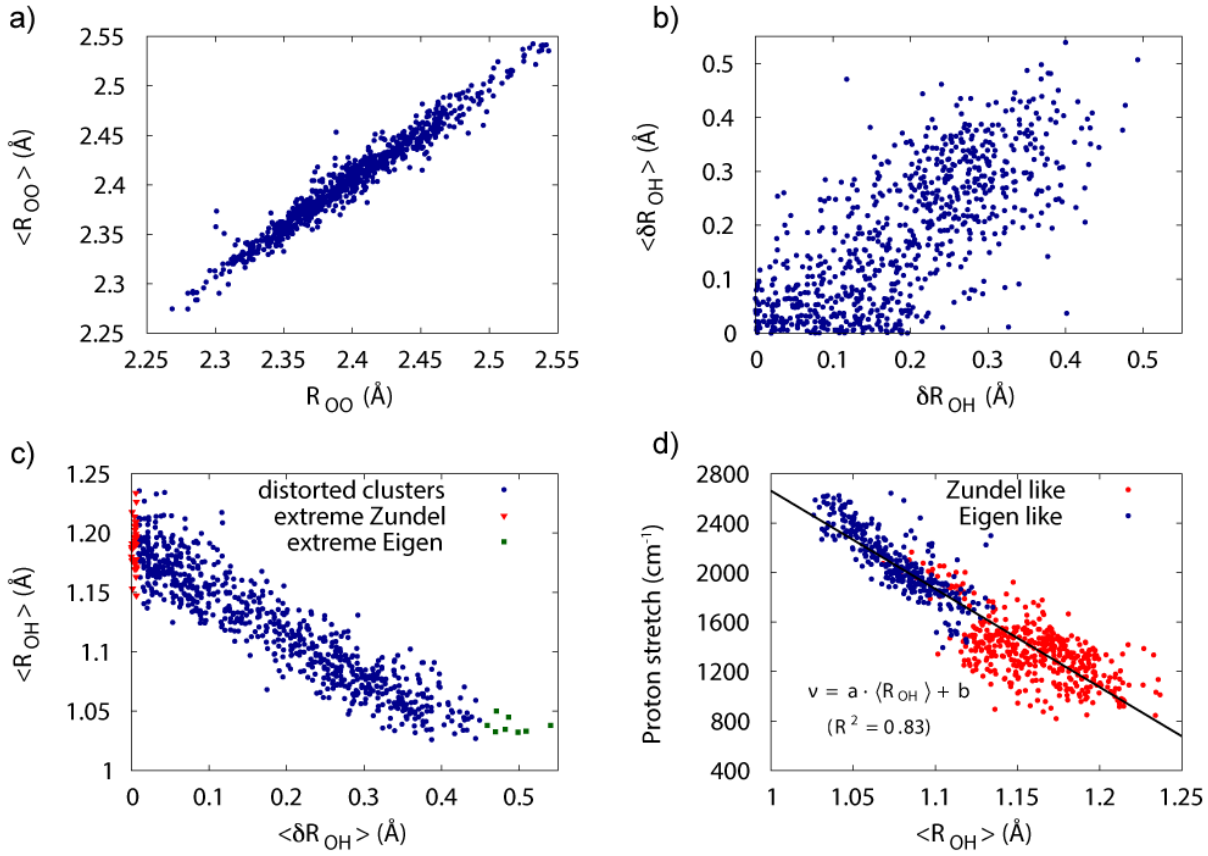

Figure 6.5: a) Distribution of R_{OO} and quantum expectation values $\langle R_{OO} \rangle$ from 800 clusters. b) Distribution of δR_{OH} and quantum expectation values, $\langle \delta R_{OH} \rangle$. c) Correlation between $\langle \delta R_{OH} \rangle$ and $\langle R_{OH} \rangle$. Extreme Zundel structures ($\langle \delta R_{OH} \rangle = 0.0$Å) are indicated in red triangles and extreme Eigen structures ($\langle \delta R_{OH} \rangle > 0.45$Å) are in green squares. d) Relationship between anharmonic proton stretch frequency and $\langle R_{OH} \rangle$ with linear least-squares fit (solid red line), $\nu = a \cdot \langle R_{OH} \rangle + b$ where $a = -7941.2$ cm^{-1}/Å, b=10603.0 cm^{-1}. Red points are from Zundel-like ($\langle \delta R_{OH} \rangle < 0.2$Å) structures and blue points are from Eigen-like ($\langle \delta R_{OH} \rangle \geq 0.2$Å) structures.

To disentangle structural information encoded in the calculated vibrational spectrum, we conduct a statistical analysis of several important proton-related structural parameters (R_{OO}, R_{OH}, δR_{OH}) and the associated proton stretch vibration in each chosen $[H^+(H_2O)_2](H_2O)_4$ cluster. In each local $H^+(H_2O)_2$ monomer, δR_{OH} is the previously defined proton asymmetry parameter, R_{OO} is the

distance between the oxygen atoms of the two flanking waters, and R_{OH} is the shortest distance between the excess proton and one of the oxygens. Previous studies have demonstrated that the proton stretch frequency is highly sensitive to its local environment,[25,57,58] and these local parameters may each be useful for characterizing the relationship between proton stretch frequency and local monomer configuration. Recently, some of us analyzed the distribution of hydronium R_{OH} in $H_7O_3^+$ and $H_9O_4^+$ from classical MD and thermostatted Ring Polymer MD (TRPMD) at 100 K.[43] It was found that the hydronium O–H distance significantly lengthens in TRPMD calculations, which reflects the strong nuclear quantum effects of the proton and is the main reason for large shifts in anharmonic vibrational spectra. To appropriately account for quantum delocalization of the proton, we also calculated the expectation value of each structural parameter using the VCI ground state wavefunction for every cluster.

Figs. 6.5a and 6.5b show the value of R_{OO} and δR_{OH} drawn from the classical simulation frames, and their expectation values from VSCF/VCI calculations. As seen in Fig. 6.5a, there exists high correlation between R_{OO} and its expectation value, $\langle R_{OO} \rangle$, which indicates that the nuclear quantum effects do not have significant impact on the central oxygen atoms. On the other hand, Fig. 6.5b shows that the quantum expectation value of δR_{OH} decorrelates substantially from the values in its associated cluster's initial structure, owing to a much larger nuclear quantum effect of the proton. A similar decorrelation is observed between R_{OH} and $\langle R_{OH} \rangle$. In the VSCF/VCI calculation, the proton delocalizes and explores a large region around the anharmonic potential energy surface, rather than remaining fixed at the initial structure. For flat, highly anharmonic potentials such as the proton stretch, the VSCF/VCI calculation therefore more accurately represents the delocalization of the proton in the vibrational ground state. In Table 6.1, we list the numbers of clusters in different δR_{OH} intervals based on initial structures and VSCF/VCI

expectation values. From the nuclear quantum effects of the proton, the distribution of expectation values of δR_{OH} is skewed more to the extremes of $\langle \delta R_{OH} \rangle$ (specially to low δR_{OH}) than the distribution of initial structures. Besides the nuclear quantum effects, it should be noted that the different potential models (MS-EVB for classical MD simulations and our *ab initio* PES for VSCF/VCI calculations) can be another source of differences in structural parameter distributions.

Table 6.1 Population Distribution of 800 Chosen Protonated Water Clusters from Initial Structures in MS-EVB MD Trajectory and VSCF/VCI Calculations

MS-EVB MD					
δR_{OH} (Å)	0.0–0.1	0.1–0.2	0.2–0.3	0.3–0.4	0.4–
number	184	240	248	112	16
VSCF/VCI					
$\langle \delta R_{OH} \rangle$ (Å)	0.0–0.1	0.1–0.2	0.2–0.3	0.3–0.4	0.4–
number	287	152	185	143	33

Considering the strong quantum effects on proton positions, we next explore the relationship between structural parameters and proton stretch frequency. Generally, the initial values of R_{OH} or δR_{OH} only weakly correlate with anharmonic proton stretch frequency, but the frequency correlations show significant improvement with $\langle R_{OH} \rangle$ and $\langle \delta R_{OH} \rangle$. As to the parameter R_{OO} or $\langle R_{OO} \rangle$, it can be seen that in Zundel-like structures, the anharmonic proton stretch decreases with longer $\langle R_{OO} \rangle$ while proton stretch frequencies in Eigen-like structures are less sensitive to changes in $\langle R_{OO} \rangle$. Finally, among the initial and quantum expectation values of all three parameters, we find the best correlation between proton stretch frequency and $\langle R_{OH} \rangle$ (Fig. 5d). Previous studies have raised issues with using δR_{OH} as a descriptive coordinate for the entire aqueous proton complex[36,58,59] due to the additional dependence of the proton potential on R_{OO} and the arbitrariness of δR_{OH} as a cutoff on a continuum of structures. Alternatively, R_{OH} has successfully been used to predict the red-shift of proton-related stretches in Zundel-like and Eigen-like protonated water clusters $H^+(H_2O)_n$, n=2-4.[42,43,57] Even more recently, vibrationally averaged R_{OH} values were

successfully analyzed to provide a unifying picture for predicting O–H stretch frequencies in bulk water, flanking waters in aqueous proton complexes, and waters in the first solvation shell of halide anions.[60] As shown in Fig. 6.5c, $\langle R_{OH} \rangle$ correlates well with $\langle \delta R_{OH} \rangle$ but correlates better with proton stretch frequency. Interestingly, the correlation is weaker between $\langle R_{OH} \rangle$ = 1.1Å and $\langle \delta R_{OH} \rangle$ = 1.2Å, which suggests that incorporating other coordinates is necessary to better describe the proton stretch frequency for Zundel-like configurations. This likely arises from anharmonic coupling to other degrees of freedom such as bending modes, which are known to strongly couple to the proton stretch in the gas phase.[10,13]

6.4.6 Decomposition of Spectrum by $\langle R_{OH} \rangle$

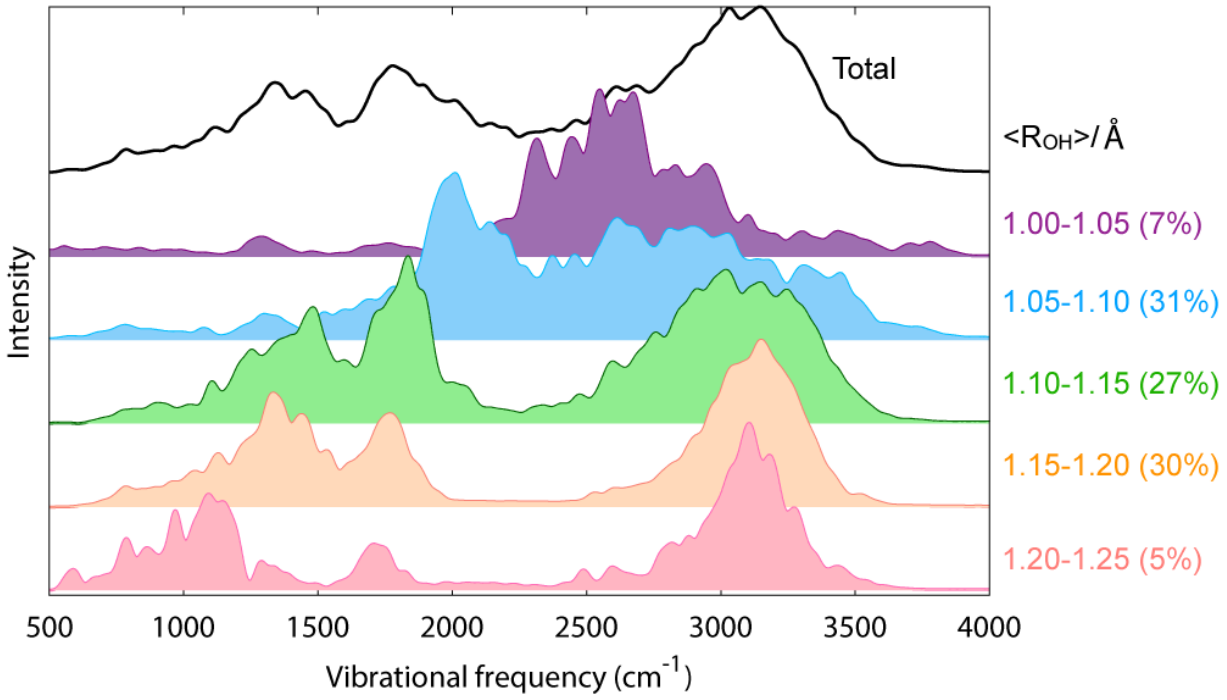

Figure 6.6: Decomposition of the calculated spectra of aqueous proton according to different $\langle R_{OH} \rangle$ values. The percentage of clusters in each group is included in parentheses.

To examine how the various vibrations shift with $\langle R_{OH} \rangle$, we present the full mid-IR spectrum decomposed by $\langle R_{OH} \rangle$ (Fig. 6.6). For $\langle R_{OH} \rangle$ between 1.00-1.05Å (extreme Eigen configurations),

the spectrum displays intense hydronium stretches at 2500-2700 cm^{-1} and a weak umbrella mode around 1250 cm^{-1}. When $\langle R_{OH} \rangle$ lengthens to 1.05-1.10Å, the continuum begins to bifurcate into two broad features centered around 2000 cm^{-1} and 2800 cm^{-1}. Comparing with Fig. 6.4d), the split reflects the symmetry breaking between the three hydronium protons, resulting in a "special pair" O–H stretch at 2000 cm^{-1} and flanking O–H stretches at higher frequencies. The extreme breadth of the higher-frequency feature may reflect that the flanking O–H stretches of the central hydronium and the O–H stretches in the adjacent water of the local monomer interact differently with the excess proton.[36]

As $\langle R_{OH} \rangle$ increases above 1.10Å ($\langle \delta R_{OH} \rangle < 0.2$Å), the spectral signatures of the aqueous proton complex appear more Zundel-like. As the proton stretch redshifts with $\langle \delta R_{OH} \rangle$, spectral overlap with the bending modes increases, resulting in stronger anharmonic mode mixing. At 1800 cm^{-1}, there is significant stretching and bending character, and the bending modes gain intensity as a result. The stretching modes of the shared proton are centered at 1400 cm^{-1}, while the flanking O–H stretch band blueshifts to 3000 cm^{-1} and narrows somewhat as the two flanking waters share the excess proton more equitably. For $\langle R_{OH} \rangle > 1.15$Å, the spectrum appears even more Zundel-like with three bands at 1400 cm^{-1}, 1750 cm^{-1}, and 3100 cm^{-1} and negligible intensity between 2000 and 2500 cm^{-1} (like the Zundel isomer of $H^+(H_2O)_6$ in Fig. 6.2).

These trends illustrate how the various frequency regions report on different instantaneous configurations. First, because the small populations of the extreme configurations $\langle R_{OH} \rangle < 1.05$Å and $\langle R_{OH} \rangle > 1.20$Å, the vast majority of spectra are best described as among a range of distorted Eigen-like to asymmetric Zundel-like vibrational spectra. The 1000-1500 cm^{-1} region primarily reports on proton stretches in Zundel-like configurations, whereas umbrella modes in Eigen-like configurations do not contribute significantly to the overall feature in the experimental spectrum.

The intensity of the bending feature at 1750 cm^{-1} is largest for 1.10Å < ⟨R_{OH}⟩ < 1.20Å, where the intensity is borrowed via anharmonic coupling with proton stretching motions. In distorted Eigen-like configurations, the stretch-bend coupling is reduced (Fig. 6.4d) and so bend features are less apparent on top of the continuum. For these distorted Eigen-like complexes, the bend also blueshifts to 1800 cm^{-1}, which has been observed in the gas phase[31] and more recently in contact ion pairs between $H^+(aq)$ and $NO^{3-}(aq)$.[61] The continuum is only seen in Eigen-like configurations, but a strongly blue-shifted O–H stretch involving the hydronium proton that donates a hydrogen bond to the closest water is present at 2000 cm^{-1}. There are multiple overlapping contributions between 1500 and 2000 cm^{-1}, where stretching and bending motions of both Zundel-like and Eigen-like complexes contribute. This ambiguity may be responsible for the counterintuitive polarization response in the 2D IR cross peak between the stretch and bend of the proton hydration complex.[18]

6.4.7 Challenges and Outlook

The results here have been useful for disentangling assignments for aqueous proton vibrations, but there are still some areas that require further study. As we mentioned above, the VSCF/VCI spectra presented here are calculated from static structures of local $H^+(H_2O)_2$ monomers drawn from MS-EVB frames, which altogether leave out various characteristics of the aqueous proton spectrum. In addition, recent 2D IR spectra of the aqueous proton demonstrated that all of the main features displayed cross peaks between each other, implying strong anharmonic mixing between every vibrational mode.[18] However, the spectral decomposition in Fig. 6.6 would imply that coupling between Eigen-like and Zundel-like complexes would be missing cross peaks. This might be reconciled with experiment by taking into account the spectral dynamics associated

with sub-100-fs proton rattling[20,51] that may blur the distinctions between Eigen-like and Zundel-like configurations.

Regardless, the anharmonic calculations here provide an exciting opportunity to interpret linear IR and also 2D IR spectrum of the aqueous excess proton. Excited state and combination band energies are calculated by the VSCF/VCI method, which can be directly compared to excited state absorptions and cross peaks in the 2D IR spectrum. Additionally, transition dipoles from various excitations are calculated, which can be related to measured 2D anisotropy measurements and could possibly bring clarity to the heterogeneity of vibrations in the 1500-2000 cm^{-1} region. The multi-dimensional nuclear potential for the anharmonic proton stretch can also be compared to its 2D lineshape to more accurately determine structure-frequency trends and to interpret low-dimensional projections of the potential. These tools may even be useful for benchmarking classical trajectories, which would help generate frequency and dipole trajectories needed for capturing spectral dynamics and reproducing the 2D spectrum of the excess proton.

6.5 Conclusion

We report the anharmonic spectrum of the aqueous proton calculated from the VSCF/VCI approach using 800 $H^+(H_2O)_6$ clusters. The accuracy of the theoretical scheme is verified in the Zundel and Eigen isomers of gas-phase $H^+(H_2O)_6$. The calculated vibrational spectrum of the aqueous proton improves in agreement to experiment compared to the harmonic spectrum, even though the spectrum consists of local $H^+(H_2O)_2$ monomers in hexamer clusters. By decomposing the spectrum into different normal mode components, we successfully verify and make assignments of proton stretch, flanking water stretch, and bending motions across the spectrum. The strong mixing between proton stretch and bending motion is also observed, particularly for Zundel-like snapshots. Further analysis finds strong nuclear quantum effects of the proton and also

strong correlation between excess proton-oxygen distance $\langle R_{OH} \rangle$ and associated anharmonic proton stretch. We finally decompose the anharmonic spectrum by $\langle R_{OH} \rangle$ to dissect the spread of IR response over a distribution of possible configurations. By comparing the trends based on $\langle R_{OH} \rangle$ and on normal mode decomposition, we discuss how one can interpret different frequency regions of the total spectrum in terms of geometry and vibrational character. We look forward to harnessing these anharmonic calculations for in-depth interpretation of the 2D IR spectrum of the aqueous proton and investigation of the strong anharmonic mixing between different vibrational modes.

6.6 References

(1) Heberle, J.; Riesle, J.; Thiedemann, G.; Oesterhelt, D.; Dencher, N. A. Proton migration along the membrane surface and retarded surface to bulk transfer *Nature* **1994**, *370*, 379.

(2) Stowell, M. H. B.; McPhillips, T. M.; Rees, D. C.; Soltis, S. M.; Abresch, E.; Feher, G. Light-induced structural changes in photosynthetic reaction center: Implications for mechanism of electron-proton transfer *Science* **1997**, *276*, 812.

(3) Luecke, H.; Richter, H. T.; Lanyi, J. K. Proton transfer pathways in bacteriorhodopsin at 2.3 angstrom resolution *Science* **1998**, *280*, 1934.

(4) Rini, M.; Magnes, B. Z.; Pines, E.; Nibbering, E. T. J. Real-time observation of bimodal proton transfer in acid-base pairs in water *Science* **2003**, *301*, 349.

(5) de Grotthuss, C. J. T. Sur la deć omposition de l'eau et des corps qu'elle tient en dissolution à l'aide de l'eĺectricité galvanique *Ann. Chim.* **1806**, *58*, 54.

(6) Agmon, N. The Grotthuss mechanism *Chem. Phys. Lett.* **1995**, *244*, 456.

(7) Marx, D.; Tuckerman, M. E.; Hutter, J.; Parrinello, M. The nature of the hydrated excess proton in water *Nature* **1999**, *397*, 601.

(8) Yeh, L. I.; Okumura, M.; Myers, J. D.; Price, J. M.; Lee, Y. T. Vibrational spectroscopy of the hydrated hydronium cluster ions $H_3O^+ \cdot (H2O)_n$ (n= 1, 2, 3) *J. Chem. Phys.* **1989**, *91*, 7319.

(9) Jiang, J. C.; Wang, Y. S.; Chang, H. C.; Lin, S. H.; Lee, Y. T.; Niedner-Schatteburg, G.; Chang, H. C. Infrared spectra of $H_+(H_2O)_{5-8}$ clusters: Evidence for symmetric proton hydration *J. Am. Chem. Soc.* **2000**, *122*, 1398.

(10) Asmis, K. R.; Pivonka, N. L.; Santambrogio, G.; Brümmer, M.; Kaposta, C.; Neumark, D. M.; Wöste, L. Gas-phase infrared spectrum of the protonated water dimer. *Science* **2003**, *299*, 1375.

(11) Shin, J. W.; Hammer, N. I.; Diken, E. G.; Johnson, M. A.; Walters, R. S.; Jaeger, T. D.; Duncan, M. A.; Christie, R. A.; Jordan, K. D. Infrared signature of structures associated with the H+(H 2O)n (n = 6 to 27) clusters *Science* **2004**, *304*, 1137.

(12) Headrick, J. M.; Diken, E. G.; Walters, R. S.; Hammer, N. I.; Christie, R. A.; Cui, J.; Myshakin, E. M.; Duncan, M. A.; Johnson, M. A.; Jordan, K. D. Spectral Signatures of Hydrated Proton Vibrations in Water Clusters *Science* **2005**, *308*, 1765.

(13) Vendrell, O.; Gatti, F.; Meyer, H. D. Dynamics and infrared spectroscopy of the protonated water dimer *Angew. Chemie - Int. Ed.* **2007**, *46*, 6918.

(14) Fournier, J. A.; Wolke, C. T.; Johnson, M. A.; Odbadrakh, T. T.; Jordan, K. D.; Kathmann, S. M.; Xantheas, S. S. Snapshots of Proton Accommodation at a Microscopic Water Surface: Understanding the Vibrational Spectral Signatures of the Charge Defect in Cryogenically Cooled $H^+(H_2O)_{n=2–28}$ Clusters *J. Phys. Chem. A* **2015**, *119*, 9425.

(15) Wolke, C. T.; Fournier, J. A.; Dzugan, L. C.; Fagiani, M. R.; Odbadrakh, T. T.; Knorke, H.; Jordan, K. D.; McCoy, A. B.; Asmis, K. R.; Johnson, M. A. Spectroscopic snapshots of the proton-transfer mechanism in water *Science* **2016**, *354*, 1131.

(16) Yu, Q.; Bowman, J. M. High-Level Quantum Calculations of the IR Spectra of the Eigen, Zundel, and Ring Isomers of $H^+(H_2O)_4$ Find a Single Match to Experiment *J. Am. Chem. Soc.* **2017**, *139*, 10984.

(17) Tuckerman, M. E.; Marx, D.; Parrinello, M. The nature and transport mechanism of hydrated hydroxide ions in aqueous solution *Nature* **2002**, *417*, 925.

(18) Fournier, J. A.; Carpenter, W. B.; Lewis, N. H. C.; Tokmakoff, A. Broadband 2D IR spectroscopy reveals dominant asymmetric $H_5O_2^+$ proton hydration structures in acid solutions *Nat. Chem.* **2018**, *10*, 932.

(19) Fecko, C. J.; Eaves, J. D.; Loparo, J. J.; Tokmakoff, A.; Geissler, P. L. Ultrafast Hydrogen-Bond Dynamics in the Infrared Spectroscopy of Water. *Science* **2003**, *301*, 1698.

(20) Berkelbach, T. C.; Lee, H. S.; Tuckerman, M. E. Concerted Hydrogen-Bond Dynamics in the Transport Mechanism of the Hydrated Proton: A First-Principles Molecular Dynamics Study *Phys. Rev. Lett.* **2009**, *103*, 238302.

(21) Day, T. J. F.; Schmitt, U. W.; Voth, G. A. The mechanism of hydrated proton transport in water *J. Am. Chem. Soc.* **2000**, *122*, 12027.

(22) Kulig, W.; Agmon, N. A "clusters-in-liquid" method for calculating infrared spectra identifies the proton-transfer mode in acidic aqueous solutions *Nat. Chem.* **2013**, *5*, 29.

(23) Thämer, M.; De Marco, L.; Ramasesha, K.; Mandal, A.; Tokmakoff, A. Ultrafast 2D IR spectroscopy of the excess proton in liquid water *Science* **2015**, *350*, 78.

(24) Agmon, N.; Bakker, H. J.; Campen, R. K.; Henchman, R. H.; Pohl, P.; Roke, S.; Thämer, M.; Hassanali, A. Protons and Hydroxide Ions in Aqueous Systems *Chem. Rev.* **2016**, *116*, 7642.

(25) Dahms, F.; Fingerhut, B. P.; Nibbering, E. T. J.; Pines, E.; Elsaesser, T. Large-amplitude transfer motion of hydrated excess protons mapped by ultrafast 2D IR spectroscopy *Science* **2017**, *357*, 491.

(26) Chen, M.; Zheng, L.; Santra, B.; Ko, H.-Y.; DiStasio Jr, R. A.; Klein, M. L.; Car, R.; Wu, X. Hydroxide diffuses slower than hydronium in water because its solvated structure inhibits correlated proton transfer *Nat. Chem.* **2018**, *10*, 413.

(27) Stoyanov, E. S.; Stoyanova, I. V.; Reed, C. A. The Structure of the Hydrogen Ion (H_{aq}^+) in Water *J. Am. Chem. Soc.* **2010**, *132*, 1484.

(28) Kundu, A.; Dahms, F.; Fingerhut, B. P.; Nibbering, E. T. J.; Pines, E.; Elsaesser, T. Hydrated Excess Protons in Acetonitrile/Water Mixtures: Solvation Species and Ultrafast Proton Motions *J. Phys. Chem. Lett.* **2019**, *10*, 2287.

(29) Biswas, R.; Carpenter, W.; Fournier, J. A.; Voth, G. A.; Tokmakoff, A. IR spectral assignments for the hydrated excess proton in liquid water *J. Chem. Phys.* **2017**, *146*, 154507.

(30) Zundel, G.; Metzger, H. Energiebänder der tunnelnden Überschuß-Protonen in flüssigen Säuren. Eine IR-spektroskopische Untersuchung der Natur der Gruppierungen $H_5O_2^+$ *Z. Phys. Chem.* **1968**, *58*, 225.

(31) Heine, N.; Fagiani, M. R.; Rossi, M.; Wende, T.; Berden, G.; Blum, V.; Asmis, K. R. Isomer-Selective Detection of Hydrogen-Bond Vibrations in the Protonated Water Hexamer *J. Am. Chem. Soc.* **2013**, *135*, 8266.

(32) Wicke, E.; Eigen, M.; Ackermann, T. Über den Zustand des Protons (Hydroniumions) in wäßriger Lösung *Z. Phys. Chem. (N. F)*. **1954**, *1*, 340.

(33) Eigen, M. Proton Transfer, Acid-Base Catalysis, and Enzymatic Hydrolysis. Part I: Elementary Processes *Angew. Chemie Int. Ed. English* **1964**, *3*, 1.

(34) Schmitt, U. W.; Voth, G. A. Multistate empirical valence bond model for proton transport in water *J. Phys. Chem. B* **1998**, *102*, 5547.

(35) Biswas, R.; Tse, Y. L. S.; Tokmakoff, A.; Voth, G. A. Role of Presolvation and Anharmonicity in Aqueous Phase Hydrated Proton Solvation and Transport *J. Phys. Chem. B* **2016**, *120*, 1793.

(36) Daly, C. A.; Streacker, L. M.; Sun, Y.; Pattenaude, S. R.; Hassanali, A. A.; Petersen, P. B.; Corcelli, S. A.; Ben-Amotz, D. Decomposition of the Experimental Raman and Infrared Spectra of Acidic Water into Proton, Special Pair, and Counterion Contributions *J. Phys. Chem. Lett.* **2017**, *8*, 5246.

(37) Carpenter, W. B.; Fournier, J. A.; Lewis, N. H. C.; Tokmakoff, A. Picosecond Proton Transfer Kinetics in Water Revealed with Ultrafast IR Spectroscopy *J. Phys. Chem. B* **2018**, *122*, 2792.

(38) Duong, C. H.; Gorlova, O.; Yang, N.; Kelleher, P. J.; Johnson, M. A.; McCoy, A. B.; Yu, Q.; Bowman, J. M. Disentangling the Complex Vibrational Spectrum of the Protonated Water Trimer, H^+ $(H_2 O)_3$, with Two-Color IR-IR Photodissociation of the Bare Ion and Anharmonic VSCF/VCI Theory *J. Phys. Chem. Lett.* **2017**, *8*, 3782.

(39) Yu, Q.; Bowman, J. M. Communication: VSCF/VCI vibrational spectroscopy of $H_7O_3^+$ and $H_9O_4^+$ using high-level, many-body potential energy surface and dipole moment surfaces *J. Chem. Phys.* **2017**, *146*, 121102.

(40) Huang, X.; Braams, B. J.; Bowman, J. M. Ab initio potential energy and dipole moment surfaces for $H_5O_2^+$ *J. Chem. Phys.* **2005**, *122*, 044308.

(41) Qu, C.; Yu, Q.; Bowman, J. M. Permutationally Invariant Potential Energy Surfaces *Annu. Rev. Phys. Chem.* **2018**, *69*, 151.

(42) Heindel, J. P.; Yu, Q.; Bowman, J. M.; Xantheas, S. S. Benchmark Electronic Structure Calculations for $H_3O^+(H_2O)_n$, n = 0-5, Clusters and Tests of an Existing 1,2,3-Body Potential Energy Surface with a New 4-Body Correction *J. Chem. Theory Comput.* **2018**, *14*, 4553.

(43) Yu, Q.; Bowman, J. M. Classical, Thermostated Ring Polymer, and Quantum VSCF/VCI Calculations of IR Spectra of $H_7O_3^+$ and $H_9O_4^+$ (Eigen) and Comparison with Experiment *J. Phys. Chem. A* **2019**, *123*, 1399.

(44) Wang, Y.; Bowman, J. M. Ab initio potential and dipole moment surfaces for water. II. Local-monomer calculations of the infrared spectra of water clusters *J. Chem. Phys.* **2011**, *134*, 154510.

(45) Liu, H.; Wang, Y.; Bowman, J. M. Quantum calculations of intramolecular IR spectra of ice models using ab initio potential and dipole moment surfaces *J. Phys. Chem. Lett.* **2012**, *3*, 3671.

(46) Liu, H.; Wang, Y.; Bowman, J. M. Quantum calculations of the IR spectrum of liquid water using ab initio and model potential and dipole moment surfaces and comparison with experiment *J. Chem. Phys.* **2015**, *142*, 194502.

(47) Liu, H.; Wang, Y.; Bowman, J. M. Quantum Local Monomer IR Spectrum of Liquid D_2O at 300 K from 0 to 4000 cm^{-1} Is in Near-Quantitative Agreement with Experiment *J. Phys. Chem. B* **2016**, *120*, 2824.

(48) De Marco, L.; Carpenter, W.; Liu, H.; Biswas, R.; Bowman, J. M.; Tokmakoff, A. Differences in the Vibrational Dynamics of H_2O and D_2O: Observation of Symmetric and Antisymmetric Stretching Vibrations in Heavy Water *J. Phys. Chem. Lett.* **2016**, *7*, 1769.

(49) Wu, Y.; Tepper, H. L.; Voth, G. A. Flexible simple point-charge water model with improved liquid-state properties *J. Chem. Phys.* **2006**, *124*, 024503.

(50) Tuckerman, M.; Laasonen, K.; Sprik, M.; Parrinello, M. Ab Initio Molecular Dynamics Simulation of the Solvation and Transport of H3O+ and OH- Ions in Water *J. Phys. Chem.* **1995**, *99*, 5749.

(51) Markovitch, O.; Chen, H.; Izvekov, S.; Paesani, F.; Voth, G. A.; Agmon, N. Special pair dance and partner selection: elementary steps in proton transport in liquid water. *J. Phys. Chem. B* **2008**, *112*, 9456.

(52) Bowman, J. M.; Carter, S.; Huang, X. MULTIMODE: A code to calculate rovibrational energies of polyatomic molecules *Int. Rev. Phys. Chem.* **2003**, *22*, 533.

(53) Esser, T. K.; Knorke, H.; Asmis, K. R.; Schöllkopf, W.; Yu, Q.; Qu, C.; Bowman, J. M.; Kaledin, M. Deconstructing Prominent Bands in the Terahertz Spectra of $H_7O_3^+$ and $H_9O_4^+$: Intermolecular Modes in Eigen Clusters *J. Phys. Chem. Lett.* **2018**, *9*, 798.

(54) Napoli, J. A.; Marsalek, O.; Markland, T. E. Decoding the spectroscopic features and time scales of aqueous proton defects *J. Chem. Phys.* **2018**, *148*, 222833.

(55) Xu, J.; Zhang, Y.; Voth, G. A. Infrared spectrum of the hydrated proton in water *J. Phys. Chem. Lett.* **2011**, *2*, 81.

(56) Houston, P. L.; Van Hoozen, B. L.; Qu, C.; Yu, Q.; Bowman, J. M. Teaching vibrational spectra to assign themselves *Faraday Discuss.* **2018**, *212*, 65.

(57) Yu, Q.; Bowman, J. M. How the Zundel ($H_5O_2^+$) Potential Can Be Used to Predict the Proton Stretch and Bend Frequencies of Larger Protonated Water Clusters *J. Phys. Chem. Lett.* **2016**, *7*, 5259.

(58) Marx, D. Proton Transfer 200 Years after von Grotthuss: Insights from Ab Initio Simulations *Chem. Phys. Chem* **2006**, *7*, 1848.

(59) Swanson, J. M. J.; Simons, J. Role of Charge Transfer in the Structure and Dynamics of the Hydrated Proton *J. Phys. Chem. B* **2009**, *113*, 5149.

(60) Boyer, M. A.; Marsalek, O.; Heindel, J. P.; Markland, T. E.; McCoy, A. B.; Xantheas, S. S. Beyond Badger's Rule: The Origins and Generality of the Structure–Spectra Relationship of Aqueous Hydrogen Bonds *J. Phys. Chem. Lett.* **2019**, *10*, 918.

(61) Lewis, N. H. C.; Fournier, J. A.; Carpenter, W. B.; Tokmakoff, A. Direct Observation of Ion Pairing in Aqueous Nitric Acid Using 2D Infrared Spectroscopy *J. Phys. Chem. B* **2018**, *123*, 225.

Chapter 7

Decoding the 2D IR Spectrum of the Aqueous Proton with High-Level VSCF/VCI Calculations

7.1 Abstract

The aqueous proton is a common and long-studied species in chemistry, yet there is currently intense interest devoted to understanding its hydration structure and transport dynamics. Typically described in terms of two limiting structures observed in gas-phase clusters, the Zundel $H_5O_2^+$ and Eigen $H_9O_4^+$ ions, the aqueous structure is less clear due to the heterogeneity of hydrogen bonding environments and room-temperature structural fluctuations in water. The linear infrared spectrum, which reports on structural configurations, is challenging to interpret because it appears as a continuum of absorption, and the underlying vibrational modes are strongly anharmonically coupled to each other. Recent two-dimensional infrared (2D IR) experiments presented strong evidence for asymmetric Zundel-like motifs in solution, but true structure-spectrum correlations are missing and complicated by the anharmonicity of the system. In this study, we employ high-level VSCF/VCI calculations to demonstrate that the 2D IR spectrum reports on a broad distribution of geometric configurations of the aqueous proton. We find that the diagonal 2D IR spectrum around 1200 cm^{-1} is dominated by the proton stretch vibrations of Zundel-like and intermediate geometries, broadened by the heterogeneity of aqueous configurations. There is a wide distribution of multidimensional potential shapes for the proton stretching vibration with varying degrees of potential asymmetry and confinement. Finally, we

find specific cross peak patterns due to aqueous Zundel-like species. These studies provide clarity on highly debated spectral assignments and stringent spectroscopic benchmarks for future simulations.

7.2 Introduction

The aqueous proton is one of the cornerstone entities in aqueous chemistry. Beyond standard acid-base chemistry,[1,2] the aqueous proton also plays a key role in catalysis,[3–5] biological energy conversion,[6,7] and hydrogen fuel cell technology.[8,9] Yet despite its importance, a clear molecular description of the aqueous proton has remained elusive for over a century due to the complexity of the proton's hydration structures and transport in solution.[2,10–15] Ultrafast fluctuations of the hydrogen bond (H-bond) network in liquid water[16–18] and the low barriers separating different proton hydration configurations are responsible for the complexity of the problem.[19–21] Experimental determination of the distribution of proton hydration configurations would be invaluable as a foundation for studying proton transport in experiments and simulations.

The aqueous proton has been described in terms of two gas-phase structural motifs, the Eigen[11] and Zundel[12] cations. In the Eigen cation $H_9O_4^+$, a central hydronium ion is tightly H-bonded to three equivalent waters, whereas the Zundel cation $H_5O_2^+$ consists of a central excess proton equally solvated by two flanking waters. These two gas-phase species are typically invoked to refer to $H^+(aq)$,[22,23] but the wide variety of aqueous H-bonding configurations in the liquid phase suggest that there is a distribution of $H^+(aq)$ hydration configurations,[24,25] breaking the symmetries inherent to the Eigen and Zundel complexes. While some simulations have described aqueous proton structure as a distribution with Eigen and Zundel motifs as limits,[17,24] other studies have concluded that the predominant configurations can be described as either all Zundel-like[22,26,27] or all Eigen-like.[19,23]

Infrared spectroscopy provides a stringent benchmark to measure molecular configurations[14,18,28–32] owing to its sensitivity to the nuclear potential, but modeling the infrared spectrum of the aqueous proton has proven to be challenging due to the extreme anharmonicities of the nuclear potential.[33–35] This challenge has spurred the development of highly precise quantum mechanical methods such as the multiconfiguration time-dependent Hartree (MCTDH)[33,34] and vibrational self-consistent field/virtual state configuration interaction (VSCF/VCI) methods[35–37] to calculate the IR spectrum of gas-phase protonated water clusters. The highly accurate IR spectra from these techniques have been invaluable for disentangling the behavior of highly mixed anharmonic modes in gas-phase clusters.[33,34,36,38,39] Due to the expense of these techniques, fully quantum mechanical calculations on high-dimensional potential energy surfaces have been limited to small, cold gas-phase clusters $H^+(H_2O)_n$, where $n < 21$.[35,36,39,40]

Analysis of the aqueous proton IR absorption spectrum is particularly challenging because it appears as a continuum spanning 1000-3000 cm^{-1}.[25,41,42] Molecular dynamics simulations have reproduced the aqueous proton continuum using the Fourier transform of the dipole autocorrelation function,[41,43–45] but this approach has only recently been employed for decomposing the spectrum by Eigen-like or Zundel-like configurations.[45] To examine the spectral signatures of different aqueous proton configurations, some of us recently analyzed the harmonic IR spectra of thousands of aqueous proton clusters generated from aqueous multi-state empirical valence bond (MS-EVB) simulations.[42] While this approach illuminated spectral contributions due to hydration symmetry with reliable statistics, it came at the cost of accuracy from the harmonic approximation.

In Chapter 6, we improved upon those harmonic calculations by employing high-level VSCF/VCI calculations on an ensemble of 800 configurations from MS-EVB simulations.[38] To calculate the anharmonic IR spectra of these clusters, we employed the local monomer

approximation,[46] where we chose a "special pair" local monomer $H^+(H_2O)_2$ whose spectrum was calculated fully quantum mechanically in an environment of four static solvating water molecules. As a result, we were able to achieve a much more reliable decomposition of the linear IR spectrum and address several controversies in feature assignment. In particular, we were able to reliably distinguish features arising from Eigen-like, Zundel-like, and intermediate geometries.

The linear IR spectrum of $H^+(aq)$ provides a limited amount of information due to the high spectral congestion of the continuum and multiple types of broadening. To address these issues, recent nonlinear IR spectroscopic studies of the aqueous proton have provided a wealth of new data that requires further interpretation. The 2D IR spectrum reduces spectral congestion by spreading out the IR response over two frequency axes, distinguishes homogeneous and inhomogeneous spectral broadening mechanisms, and identifies anharmonically coupled pairs of modes in the form of off-diagonal cross peaks.[47–49] The three ultrashort IR pulses used in the experiment provide a 100-fs time resolution and access to higher-lying excited states such as overtones and combination bands.[47] All of these features make a 2D IR spectrum a highly stringent observable for modeling the nuclear potential and distribution of configurations.

A burst of 2D IR experiments in the last few years has provided key insights towards characterizing aqueous proton configurations. For instance, direct evidence of aqueous Zundel-like configurations was established via a cross peak between the flanking water stretching and bending modes at 3200 cm^{-1} and 1750 cm^{-1}, respectively.[50] Measurement of the 2D IR spectrum along the diagonal at 1200 cm^{-1} revealed an excited state absorption (ESA) at higher frequency than the ground state bleach (GSB), providing undeniable evidence of shared protons tightly confined by two flanking waters in Zundel-like configurations.[22] Finally, recent 2D IR spectra at multiple key diagonal and off-diagonal regions across the mid-IR displayed cross peaks between

all vibrational features, suggesting the coupled vibrations all belong to a single species with a broad distribution of structures in solution, rather than distinct Eigen and Zundel configurations.[51] The 2D IR spectrum was most consistent with a distribution of asymmetric Zundel-like vibrational potentials where the excess proton feels the effects of confinement between two waters, but a connection between potential shape and molecular geometry is missing.

Even with the strengths of 2D IR spectroscopy, the substantial anharmonicity of the nuclear potential has hampered a straightforward analysis of the nonlinear spectroscopic data. For instance, a clear relationship between proton stretch frequencies and geometric coordinates of the aqueous proton complex has not been determined like in water or other aqueous solutions.[28,52] Additionally, the proton stretching vibration of Zundel-like configurations and the umbrella motion of Eigen-like configurations are both resonant at approximately 1200 cm^{-1},[31,38] which introduces ambiguity into the previous interpretation of the 2D IR spectrum. Finally, the polarization relationships between 2D IR features have not yet been connected to relative orientations between vibrational transition dipoles. With an establishment of spectrum-structure relationships, the 2D IR spectrum could be employed as a constraint on possible configurations and inform simulations of the aqueous proton.

To address the above challenges, we have employed anharmonic, high-level VSCF/VCI calculations to analyze the 2D IR spectrum of the aqueous proton. The previous calculations on 800 $[H^+(H_2O)_2](H_2O)_4$ clusters (Chapter 6) include frequency and dipole information for all of the excited states accessed in the 2D IR measurement, so they provide an opportunity to test our previous assignments. In the static limit, the 2D IR spectrum can be equated with a two-dimensional conditional probability frequency distribution function of vibrational frequencies, describing the spectrum of infrared transitions that can be detected given that a fundamental

vibrational transition has been excited. We first present such 2D conditional probability spectral distributions for single configurations of the gas-phase 6-Zundel and 6-Eigen protonated water hexamers, which serve as limiting cases for the distribution of structures seen in the aqueous phase. We then present 2D conditional probability spectra for Zundel-like, Eigen-like, and intermediate aqueous configurations. An analysis of the proton stretch vibrations is presented for interpreting the 2D IR diagonal region around 1200 cm^{-1}, followed by an analysis of the off-diagonal cross peaks due to Zundel-like configurations. These spectral assignments provide a rigorous foundation for structural interpretation of 2D IR spectroscopy of protonated water complexes.

7.3 Calculated Anharmonic Spectra of Gas-phase $H^+(H_2O)_6$ Clusters

7.3.1 Anharmonicity and Coupling in Two-dimensional Conditional Frequency Probability Distributions

We begin with calculated conditional frequency probability distributions for the 6-Zundel and 6-Eigen gas-phase hexamers to highlight the impact of anharmonicity on their characteristic spectral features and illustrate the expected 2D IR features associated with these structures. The conditional probability frequency distributions $P_{\mathrm{Fund}}(\omega_3|\omega_1)$ and $P_{\mathrm{Exc}}(\omega_3|\omega_1)$ represent the spectrally weighted expectation values of detecting a frequency ω_3 given excitation of a fundamental transition at ω_1,[53,54] and are defined here as

$$P_{\mathrm{Fund}}\left(\omega_3\middle|\omega_1\right)=\left\langle\sum_{a,b}\mu_{a0}^2\mu_{b0}^2\delta\left(\omega_1-\omega_{a0}\right)\delta\left(\omega_3-\omega_{b0}\right)\right\rangle \tag{7.1a}$$

$$P_{\mathrm{Exc}}\left(\omega_3\middle|\omega_1\right)=-\left\langle\sum_{a,f}\mu_{a0}^2\mu_{fa}^2\delta\left(\omega_1-\omega_{a0}\right)\delta\left(\omega_3-\omega_{fa}\right)\right\rangle. \tag{7.1b}$$

These distributions are expressed in terms of angular transition frequency ω_{fi} associated with the excitation from $|i\rangle \rightarrow |f\rangle$ with corresponding transition dipole vectors $\bar{\mu}_{fi}$. In Eq. 7.1a, the

summation over *a* and *b* refer to singly excited (one-quantum) states, whereas in Eq. 7.1b the index *a* refers to a singly-excited state and *f* can be a singly-excited or higher-lying excited state with energy up to 6775 cm^{-1}. $P_{Exc}(\omega_3|\omega_1)$ is primarily represented by excitations into two-quantum states such as overtones and combination bands, but the strong anharmonicity of the system allows excitation from one-quantum states into other one-quantum states or higher-lying excited states such as three-quantum states. The intensity of each feature is captured by the product of μ_{fi}^2 terms. Angular brackets denote ensemble averaging over calculations on many static clusters.

The sum of Eqs. 7.1a and 7.1b is closely related to the static limit of the 2D IR spectrum for these clusters, with no contribution to the line shapes from vibrational dynamics. $P_{Fund}(\omega_3|\omega_1)$ represents the positive bleach of fundamental transitions in 2D IR spectra, while $P_{Exc}(\omega_3|\omega_1)$ represents the negative excited state absorptions between the first excited state $|a\rangle$ and the final excited state $|f\rangle$. These spectral densities are calculated from the coupled eigenstates from the clusters, and are not derived from third-order response function calculations. As such, these surfaces resemble absorptive 2D IR spectra, but do not arise from a response function calculation or a sum over Liouville pathways. The set of accessible excited states from a collection of *N* fundamental transitions include $N(N+1)/2$ overtones and combination bands, which behave more anharmonically and are more strongly mixed than the fundamentals. As a result, the usual harmonic approximation does not hold, i.e. the μ_{21} and μ_{10} transition dipoles are not necessarily spatially aligned and the intensity ratio $\mu_{21}^2/\mu_{10}^2 \neq 2$. The large collection of excited states and breakdown of harmonic rules result in many features in $P_{Exc}(\omega_3|\omega_1)$ that appear dispersed along ω_3.

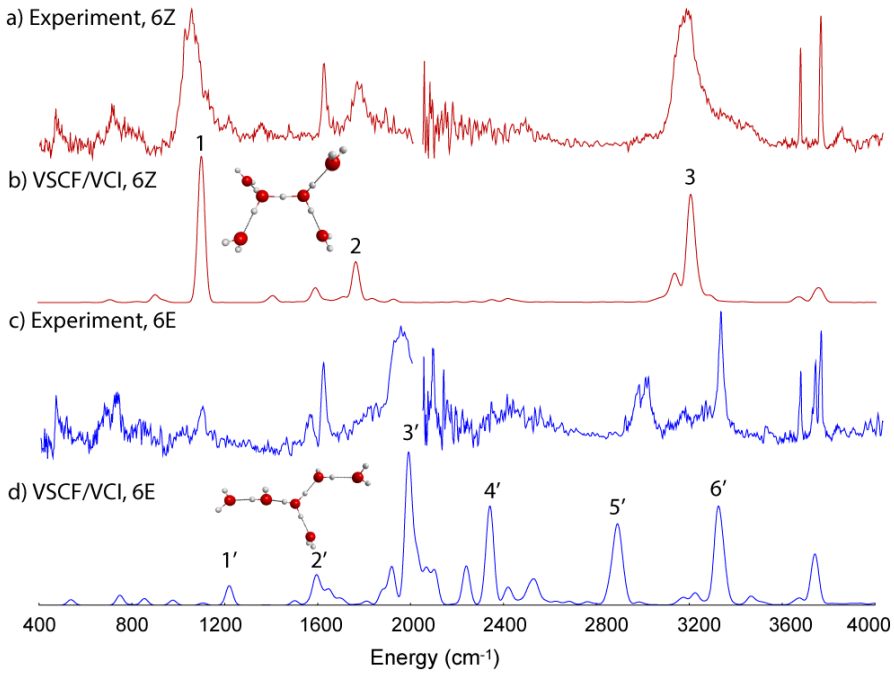

Figure 7.1: Vibrational spectra of (a)-(b) the 6-Zundel and (c)-(d) 6-Eigen protonated water hexamers from IR-IR double-resonance photodissociation experiments (Ref. 32) and VSCF/VCI calculations. Peaks in the calculated spectra are broadened with 20 cm^{-1} Gaussians. This figure is adapted from Fig. 6.2.

The 6-Zundel isomer consists of a symmetric "Zundel" core with four solvating waters. Its absorption spectrum consists of three characteristic peaks in the VSCF/VCI calculated spectrum (Fig. 7.1): an intense peak at 1102 cm^{-1} from the asymmetric stretching motion of the central proton (Peak 1), a peak at 1765 cm^{-1} (Peak 2) from the concerted bending motion of the two flanking waters in the Zundel core, and an intense and broad doublet peaked at 3128 and 3207 cm^{-1} (Peak 3) due to symmetric and antisymmetric O–H stretch normal modes of the two waters flanking the central proton, respectively. $P_{\mathrm{Fund}}(\omega_3|\omega_1)$ for the 6-Zundel cluster (Fig. 7.2a) displays a distinct coupling pattern between these peaks spread across the mid-IR. For example, the off-diagonal Peaks 4, 5, and 6 arise from anharmonic coupling between the proton stretch, flanking bend, and flanking stretches, and analogous downhill cross peaks 7,8, and 9 appear across the diagonal. The

proton stretch-associated cross peaks are particularly bright, which distinguishes the Zundel spectral pattern.

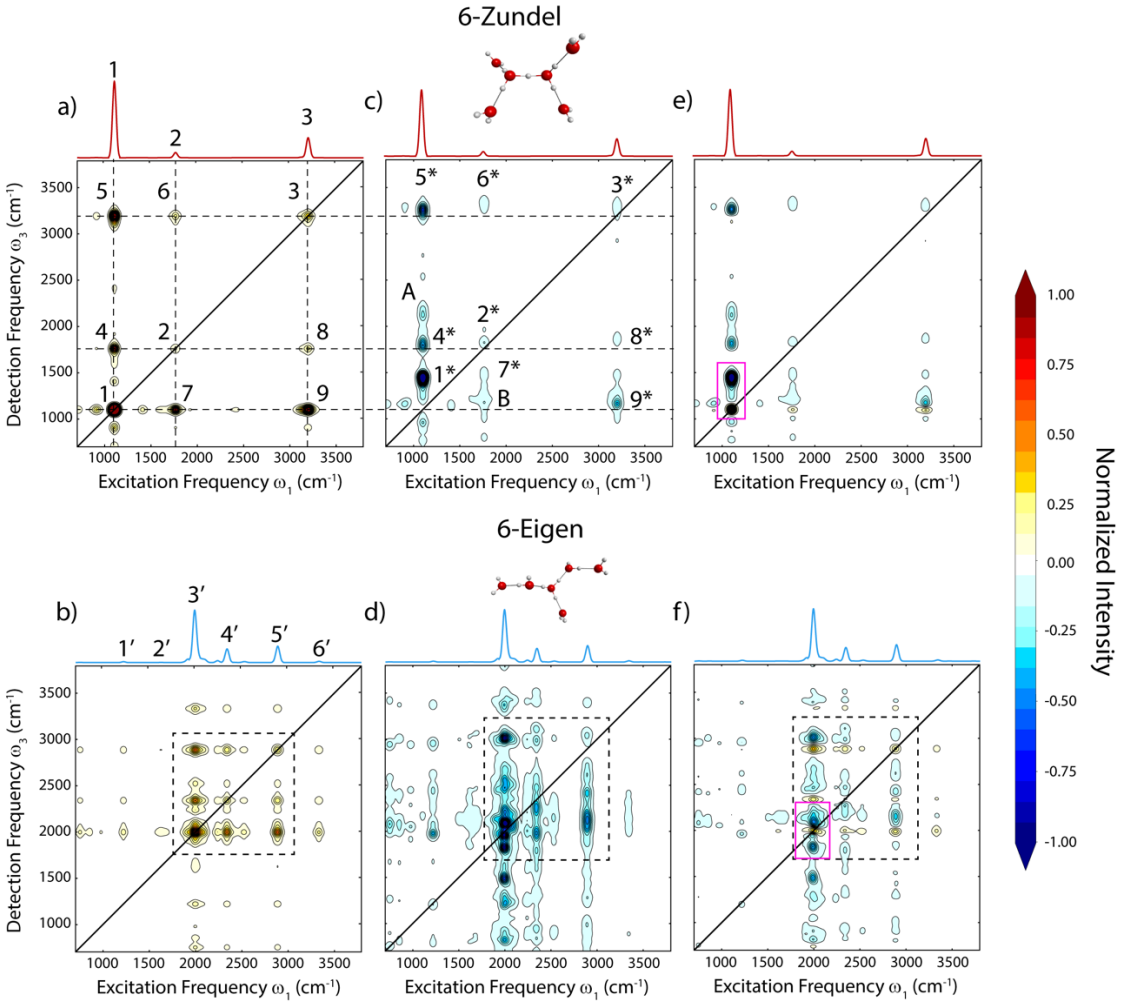

Figure 7.2: Conditional frequency probability distributions for the 6-Zundel and 6-Eigen protonated water hexamers. (a) $P_{\mathrm{Fund}}(\omega_3|\omega_1)$ of the 6-Z hexamer. The cross peaks with numerical labels are assigned in the text. (b) $P_{\mathrm{Fund}}(\omega_3|\omega_1)$ for the 6-Eigen hexamer. (c) $P_{\mathrm{Exc}}(\omega_3|\omega_1)$ for the excited state absorptions of the 6-Zundel isomer, with numerical labels corresponding to the overtones and combination bands that arise from the respective features in panel (a). (d) $P_{\mathrm{Exc}}(\omega_3|\omega_1)$ for the 6-Eigen isomer. (e)-(f) Combined surfaces $P_{\mathrm{Fund}}(\omega_3|\omega_1)+P_{\mathrm{Exc}}(\omega_3|\omega_1)$ for the Zundel and Eigen hexamers. Magenta boxes in (e) and (f) outline the proton stretch regions examined in Fig. 7.2. Above each conditional probability surface is the slice along the diagonal with quartic transition dipole scaling. Peaks presented here are broadened with two-dimensional Gaussians with 20 cm^{-1} bandwidth full width at half-maximum (FWHM).

The 6-Eigen cluster shows a different spectral pattern from the 6-Zundel species. This isomer can be described as an Eigen species $H_3O^+(H_2O)_3$ with two waters forming an incomplete second hydration shell around the central hydronium. This arrangement introduces asymmetry in the solvation environment of the hydronium compared to the Eigen cation $H_9O_4^+$. Its linear IR spectrum (Fig. 7.1d) includes three intense peaks at 1991, 2345, and 2893 cm^{-1} (Peaks 3'-5', respectively) from the three local O–H stretches of the central hydronium, in order from strongest to weakest H-bonds. The lowest frequency O–H stretch participates in what is known as the "special pair" of the hydronium and its closest first-shell water. In the 6-E complex, the special pair first-shell water donates a H-bond to a second shell water. The intermediate-frequency O–H stretch involves another branch with first and second shell waters, whereas the high-frequency O–H stretch donates to the first-shell water without a second shell water. The hydronium umbrella and in-plane bending modes appear as weak features at 1209 cm^{-1} and 1619 cm^{-1} (Peak 1' and 2', respectively). The $P_{\mathrm{Fund}}(\omega_3|\omega_1)$ distribution (Fig. 7.2b) reveals a high cross peak density between 2000 and 3300 cm^{-1} along both axes (inside dashed box in Fig. 7.2b).

The $P_{\mathrm{Exc}}(\omega_3|\omega_1)$ distributions demonstrate which excited states are accessible from the fundamental transitions in the 6-Zundel and 6-Eigen clusters. For the 6-Zundel cluster, the main peaks are associated with overtones or combination bands that arise from the couplings between the fundamental modes in the 6-Zundel cluster. As a result, $P_{\mathrm{Exc}}(\omega_3|\omega_1)$ displays a similar pattern to $P_{\mathrm{Fund}}(\omega_3|\omega_1)$, but with frequency shifts due to the anharmonicity of the nuclear potential. While $P_{\mathrm{Fund}}(\omega_3|\omega_1)$ is symmetric across the diagonal, $P_{\mathrm{Exc}}(\omega_3|\omega_1)$ necessarily loses that symmetry since excitations into two-quantum states are dependent on the initially accessed one-quantum state. Most anharmonic ESAs are lower in frequency than the GSB,[47,55] but the ESAs of all of the 6-Zundel vibrations appear above the diagonal. This is readily observed in the combined

$P_{\text{Fund}}(\omega_3|\omega_1)+P_{\text{Exc}}(\omega_3|\omega_1)$ surface in Fig. 7.2e which is the closest available match to the 2D IR spectrum and includes the interference of positive and negative features. Combination bands between the proton stretch, flanking bends, and flanking stretches are accessed off the diagonals as Peaks 4*-9*. In the 6-Eigen cluster (Fig. 7.2d), there is a high density of excited states between 2000-3000 cm^{-1} and forms a similar box pattern like the fundamentals in Fig. 7.2b. However, assignments of these features are challenging because there is strong anharmonic mixing between overtones and combination bands. For example, the ESA at $(\omega_1, \omega_3) = (2000\ cm^{-1}, 2080\ cm^{-1})$ arises from the excitation from the special pair O–H stretch to a combination band involving the special pair O–H stretch overtone and another combination band between the hydronium umbrella mode and hydronium libration.

There are some features about the $P_{\text{Exc}}(\omega_3|\omega_1)$ distributions that are less intuitive than for the fundamental distributions due to the large anharmonicities in these clusters. For both clusters, the intensities of the features in $P_{\text{Exc}}(\omega_3|\omega_1)$ differ from their counterparts across the diagonal, which is one indication of electrical anharmonicity in these clusters and the large manifold of the accessible excited states. Here, excitation of the proton stretch amplifies the intensities of other excited-state transitions, compared to the reverse excitation order. Many ESA peaks also appear elongated over hundreds of wavenumbers along ω_3 because of excitations into various combination bands and overtones. The proton stretch and flanking bend modes in the 6-Zundel cluster display substantial anharmonic character: the μ_{21} transition dipoles are 9° and 7° misaligned, respectively, from the corresponding μ_{10} vectors, and the intensity ratios μ_{21}^2/μ_{10}^2 are 0.286 and 0.310, respectively, instead of the expected value of 2 for harmonic transition dipoles. Finally, harmonically forbidden direct excitations from the proton stretch and flanking bend into the flanking stretch fundamental are present in Fig. 7.2c as Peaks A and B, respectively.

7.3.2 Proton Stretch Potential Shapes in Gas-phase $H^+(H_2O)_6$ Clusters

To study the hydrated proton clusters in more detail, we next analyze the vibrational frequencies assigned to the asymmetric proton stretch in 6-Z and special pair O–H stretch in 6-E since the proton stretch has been shown to shift dramatically as a function of hydration in gas-phase clusters.[30,56] As in Chapter 6, we describe the vibrations in each cluster in a harmonic basis, assigning the proton stretch normal mode to the mode that showed the most displacement of the local monomer central proton. The anharmonic proton stretch eigenstate was selected as the vibration with the largest squared VCI coefficient in the proton stretch normal mode coordinate.[38] The anharmonicity pattern of the fundamental (ω_{10}) and excited state (ω_{12}) transitions can be used to categorize the nuclear potential. In a harmonic system, the frequency ratio $\gamma = \omega_{21} / \omega_{10} = 1.0$ arises from the parabolic nuclear potential. We therefore classify anharmonic potentials as *superharmonic* if the transition frequency ratio $\gamma = \omega_{21} / \omega_{10} > 1$, or *subharmonic* if $\gamma < 1$. An example of a superharmonic potential shape is the quartic potential in one coordinate $V(r) = \chi r^4$, where $\gamma = 1.33$. γ is a similar measure to the anharmonicity parameter $\Delta = \omega_{21} - \omega_{10}$ but is inherently referenced to the magnitude of ω_{10}. While assigning a potential to the single number γ ignores many details, it is practical because it is directly connected to experimental observables and can be calculated from an arbitrary potential shape.

The $\omega_{21} > \omega_{10}$ anharmonicity pattern (Fig. 7.3a) of the 6-Zundel proton stretch provides indication of its superharmonic potential shape. For illustrative purposes, we show the slice of the 6-Zundel nuclear potential along the proton stretch normal mode coordinate in Fig. 7.3b. The potential shape consists of a relatively flat bottom with steep, confining walls on both sides compared to the harmonic oscillator, which raises the energy of the second excited state. For the 6-Zundel proton stretch, $\gamma = 1.324$. By contrast, the ESA frequency of the 6-Eigen special pair O–

H stretch at 1991 cm^{-1} is slightly less than its respective fundamental transitions (Fig. 7.3c-d), such that $\gamma < 1$. Interestingly, there is no "pure" O–H stretch overtone in the 6-Eigen hexamer because the overtones are highly mixed with other excited states. There are also multiple combination bands that mix with the overtone, as seen above the 6-Eigen proton stretch fundamental (Fig. 7.3c). Importantly, the proton stretch potentials shown in Fig. 7.3 are one-dimensional slices on a multidimensional potential energy surface which couples the proton stretch to other degrees of freedom such as bending and O···O extension.

We previously analyzed the proton stretch 2D frequency spacing and line shape in terms of an asymmetric Zundel-like quartic potential shape in one dimension in terms of the proton stretch normal mode coordinate r:[51]

$$V(r) = \chi r^4 - \kappa r^2 + \beta r. \tag{7.2}$$

We found that the quartic confinement coefficient χ and the linear asymmetry β trend strongly with proton stretch frequencies, whereas the quadratic barrier term κ is small compared to the proton stretch zero-point energy. The magnitude of χ reflects the confinement of the shared proton between two flanking waters in the 6-Zundel hexamer. As a result, the potential shape pushes up the second excited-state energy. Increasing β drives up ω_{10} (as seen between 6-Zundel and 6-Eigen) while ω_{21} is not as strongly affected, resulting in a lower γ value in the 6-Eigen complex.

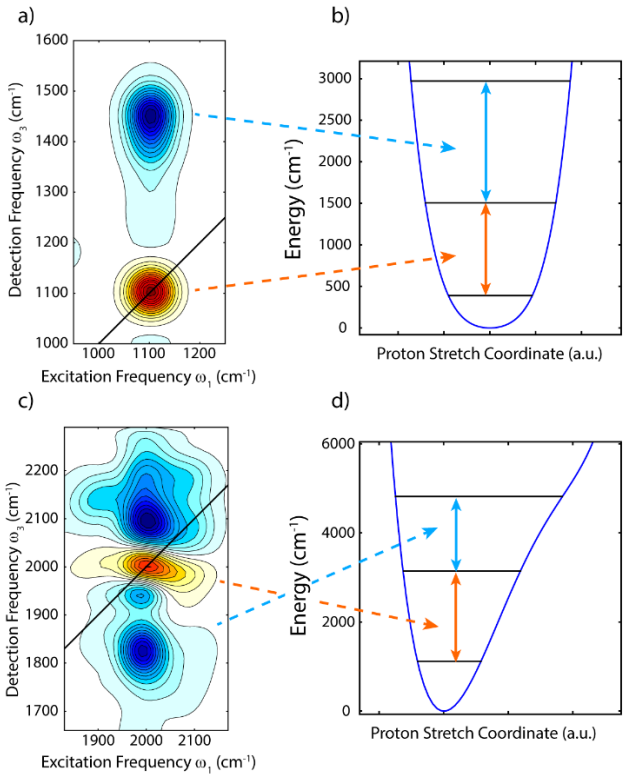

Figure 7.3: (a) 6-Zundel proton stretch fundamental (orange) and excited state absorption (blue) from the conditional frequency probability distributions. (b) The one-dimensional potential energy slice along the proton stretch coordinate with fundamental and excited-state transitions indicated as energy level gaps. (c) 6-Eigen hydronium O–H stretch fundamentals and excited state absorptions. The ESA above the fundamental comes from a combination band between the hydronium special pair O–H stretch and an umbrella/libration combination band. (d) The one-dimensional potential energy slice along the coordinate of the lowest frequency hydronium O–H stretch with indicated energy gaps. Peaks presented here are broadened with two-dimensional Gaussians with 20 cm^{-1} bandwidth FWHM.

7.3.3 Orientational Correlations in Gas-phase $H^+(H_2O)_6$ Clusters

Orientational information between two transition dipoles $\bar{\mu}_1$ and $\bar{\mu}_2$ can be obtained from polarization-resolved experiments by measuring the 2D anisotropy $r(\omega_1,\omega_3) = 0.4\left\langle P_2\left[\hat{\mu}_1(\omega_1)\cdot\hat{\mu}_2(\omega_3)\right]\right\rangle$, where P_2 is the second Legendre polynomial, circumflexes over the dipoles indicate unit vectors, and the angular brackets denote ensemble averaging in isotropic media. For two parallel transition dipoles, r = 0.4 whereas two perpendicular dipoles produce an anisotropy of r = –0.2. Here, we calculated the polarization-resolved parallel and

perpendicular surfaces similarly to the $P_{\mathrm{Fund}}(\omega_3|\omega_1)$ and $P_{\mathrm{Exc}}(\omega_3|\omega_1)$ surfaces in Eqs. 7.1a and 7.1b, including orientational correlation prefactors $Y_{\parallel,\perp}(\theta)$:

$$P_{\mathrm{Fund},\parallel}\left(\omega_3\middle|\omega_1\right)=\left\langle\sum_{a,b}Y_{\parallel}(\theta)\mu_{a0}^2\mu_{b0}^2\delta\left(\omega_1-\omega_{a0}\right)\delta\left(\omega_3-\omega_{b0}\right)\right\rangle \tag{7.3a}$$

$$P_{\mathrm{Fund},\perp}\left(\omega_3\middle|\omega_1\right)=\left\langle\sum_{a,b}Y_{\perp}(\theta)\mu_{a0}^2\mu_{b0}^2\delta\left(\omega_1-\omega_{a0}\right)\delta\left(\omega_3-\omega_{b0}\right)\right\rangle \tag{7.3b}$$

$$P_{\mathrm{Exc},\parallel}\left(\omega_3\middle|\omega_1\right)=-\left\langle\sum_{a,f}Y_{\parallel}(\theta)\mu_{a0}^2\mu_{fa}^2\delta\left(\omega_1-\omega_{a0}\right)\delta\left(\omega_3-\omega_{fa}\right)\right\rangle \tag{7.3c}$$

$$P_{\mathrm{Fund},\perp}\left(\omega_3\middle|\omega_1\right)=-\left\langle\sum_{a,f}Y_{\perp}(\theta)\mu_{a0}^2\mu_{fa}^2\delta\left(\omega_1-\omega_{a0}\right)\delta\left(\omega_3-\omega_{fa}\right)\right\rangle, \tag{7.3d}$$

where $Y_{\parallel}(\theta)=\frac{1}{15}\left(1+2\cos^2\theta\right)$, $Y_{\perp}(\theta)=\frac{1}{15}\left(2-\cos^2\theta\right)$, and $\theta=\hat{\mu}_1(\omega_1)\cdot\hat{\mu}_2(\omega_3)$. [57] With polarization-resolved surfaces $P_{\parallel}$ and $P_{\perp}$, the 2D anisotropy can be calculated from the parallel and perpendicular probability surfaces as

$$r(\omega_1,\omega_3)=\frac{P_{\parallel}-P_{\perp}}{P_{\parallel}+2P_{\perp}}. \tag{7.4}$$

The 2D anisotropy can be calculated for $P_{\mathrm{Fund}}(\omega_3|\omega_1)$, $P_{\mathrm{Exc}}(\omega_3|\omega_1)$, or the combined surface $P_{\mathrm{Fund}}(\omega_3\,|\,\omega_1)+P_{\mathrm{Exc}}(\omega_3\,|\,\omega_1)$. For the combined surface, it is important to calculate the combined $P_{\mathrm{Fund},\parallel}(\omega_3\,|\,\omega_1)+P_{\mathrm{Exc},\parallel}(\omega_3\,|\,\omega_1)$ and $P_{\mathrm{Fund},\perp}(\omega_3\,|\,\omega_1)+P_{\mathrm{Exc},\perp}(\omega_3\,|\,\omega_1)$ surfaces separately before calculating anisotropy in order to properly account for interference between positive and negative features.

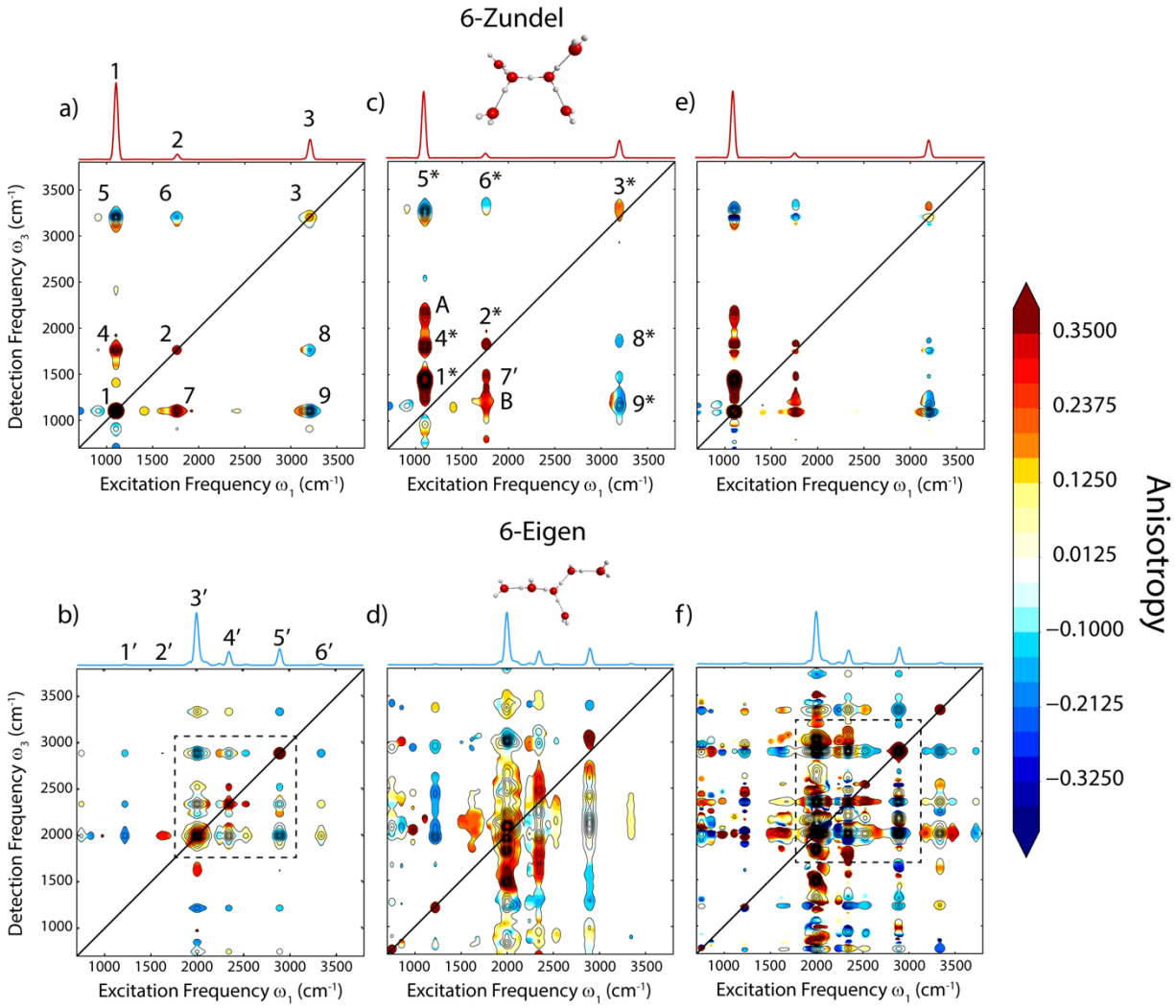

Figure 7.4: (a)-(b) 2D anisotropy surfaces for the fundamental transitions in the (a) 6-Zundel and (b) 6-Eigen isomers. (c)-(d) Excited state 2D anisotropy for the (c) 6-Zundel and (d) 6-Eigen clusters. (e)-(f) 2D anisotropy surfaces for the combined surfaces. Contours and peak labels presented here are the same as in Fig. 7.1. Anisotropy values are only shown in regions with at least 5% of the maximum intensity in each spectrum.

The 2D anisotropy surfaces for the 6-Zundel and 6-Eigen clusters display distinct anisotropy patterns that further distinguish these two clusters. In the 6-Zundel cluster (Fig. 7.4a), the anisotropies of diagonal Peaks 1 and 2 are both 0.4, since the modes along the diagonal are parallel with themselves. However, the anisotropy of Peak 3 is less than 0.4, likely due to interference of anisotropies between symmetric and antisymmetric flanking stretches. The 2D anisotropies of the

cross peaks encode the relative orientations between two vibrational modes. For instance, the anisotropy of Peak 4 is near 0.4, indicating that strongly coupled proton stretch and flanking bend modes are roughly parallel to each other, as expected from symmetry considerations. Peak 5 shows regions of both positive and negative anisotropy, indicating that the proton stretch is parallel to the symmetric stretch (3128 cm^{-1}) and perpendicular to the asymmetric flanking O–H stretch (3207 cm^{-1}). The 2D anisotropy plot for the 6-Eigen complex (Fig. 7.4b) demonstrates highly varying orientational information between the hydronium O–H stretches. Along the diagonal, each stretch displays an anisotropy of 0.4, but the anisotropies of their cross peaks are close to zero or negative, reflecting the large angles between them. On the other hand, the stretch-umbrella cross peaks all show anisotropy of –0.2, which is consistent with the out-of-plane transition dipole of the umbrella bend. The 2D anisotropy patterns of the 6-Zundel and 6-Eigen $P_{Exc}(\omega_3|\omega_1)$ and combined 2D anisotropy surfaces (Figs. 7.4c-f) are also similar to those for the Zundel and Eigen fundamental surfaces.

7.4 Vibrational Spectroscopy of Aqueous Proton Geometries

7.4.1 Conditional Frequency Probability Distributions and 2D Anisotropy Surfaces of Aqueous Structural Ensembles

To analyze the conditional probability frequency distributions of aqueous proton configurations, we calculated the anharmonic IR spectral densities for the $H^+(H_2O)_2$ local monomers within 800 $H^+(H_2O)_6$ clusters drawn from MS-EVB configurations and analyzed them relating geometric and spectral characteristics. We previously found that $\langle R_{OH} \rangle$, the quantum expectation value of the distance between the shared excess proton and its nearest oxygen, strongly correlates with the stretch frequency of the excess proton. We also found that grouping clusters based on $\langle R_{OH} \rangle$ produced distinct spectra that resembled the 6-Zundel and 6-Eigen gas-phase clusters in the extreme limits. In this vein, we analyze structurally averaged spectra by grouping

clusters into three groups: Zundel-like where $\langle R_{OH} \rangle > 1.14$ Å, Eigen-like ($\langle R_{OH} \rangle < 1.07$ Å), and intermediate ($1.07 Å < \langle R_{OH} \rangle < 1.14$ Å). These cutoffs represent one standard deviation away from the median $\langle R_{OH} \rangle$ value (1.11 Å), and different choices of cutoffs do not qualitatively change the analysis. In Chapter 6, we found a roughly linear correlation between $\langle R_{OH} \rangle$ and the proton sharing parameter $\langle \delta R_{OH} \rangle$.[38] For reference, the $\langle R_{OH} \rangle > 1.14$ Å roughly corresponds to $\langle \delta R_{OH} \rangle < 0.15$ Å, and $\langle R_{OH} \rangle < 1.07$ Å roughly corresponds to $\langle \delta R_{OH} \rangle > 0.30$, consistent with previous definitions of Zundel-like and Eigen-like geometries.[42,58] For each of these configurations, distributions of $\langle R_{OO} \rangle$ distances are broad and significantly overlap, but the median values shift from 2.38 Å, 2.41 Å, and 2.43 Å for Zundel-like, intermediate, and Eigen-like configurations, respectively.

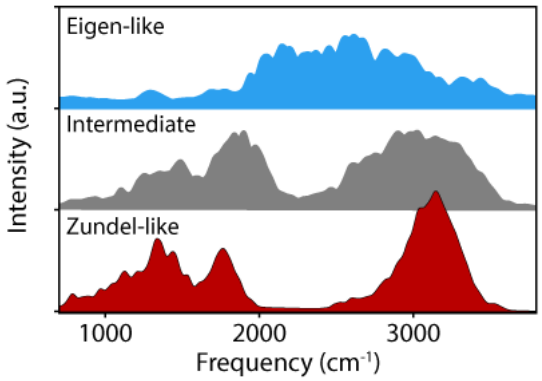

Figure 7.5: Calculated linear spectral densities of $H^+(H_2O)_2$ local monomers from 800 aqueous configurations. Spectra are normalized by the number of constituent clusters.

For Zundel-like configurations, the linear spectral density (Fig. 7.5) resembles that of the 6-Zundel gas-phase cluster (Fig. 7.1a) with three features peaked at 1300 cm^{-1}, 1800 cm^{-1}, and 3100 cm^{-1} and correspond to the proton stretch, flanking water bends, and flanking O–H stretches in aqueous configurations, respectively. On the other end of the distribution, the aqueous Eigen-like spectrum has features that resemble the gas-phase 6-Eigen spectrum: a weak umbrella mode at 1300 cm^{-1} and a broad band of hydronium and first-shell water O–H stretches spanning 2000-3500 cm^{-1}. The spectrum of intermediate configurations displays three bands like the Zundel-like

configurations, but are substantially broadened and contribute to the continuum of absorption between 2000 and 3000 cm^{-1} like the Eigen-like geometries. The relative populations of Zundel-like and Eigen-like configurations sampled may not be exactly representative of the bulk,[38] so spectral densities and two-dimensional conditional probability surfaces are all presented normalized by the number of clusters in each geometric grouping. Between the three groups, the integrated intensity of the normalized Zundel-like spectral density is highest, whereas the intermediate spectral density is approximately 96% as intense and Eigen-like configurations are approximately 85% as intense. Because the Eigen-like features are spread over one broad frequency range instead of appearing in three peaks, the maximum intensity is somewhat weaker than the maximum in the Zundel-like spectral density.

In Fig. 7.6a, we present the conditional probability frequency distribution of fundamental transitions in primarily Zundel-like clusters. We observe a diagonally symmetric distribution with features that retain the character of the peaks in the 6-Zundel $P_{\mathrm{Fund}}(\omega_3|\omega_1)$ surface (Fig. 7.2a). The diagonal region between 1100-1500 cm^{-1} arises from the fundamental transitions of the proton stretching modes, and is the most intense feature of the conditional frequency distribution. There is also a clear cross peak pattern between the proton stretch, flanking bend, and flanking stretch. The intermediate $P_{\mathrm{Fund}}(\omega_3|\omega_1)$ (Fig. 7.6b) displays many of the trends of the Zundel-like distribution, but the line shapes are generally broader. On the other extreme, the Eigen-like complexes show a $P_{\mathrm{Fund}}(\omega_3|\omega_1)$ pattern (Fig. 7.6e) that forms a box between 2000 and 3000 cm^{-1} like the gas-phase 6-Eigen complex.

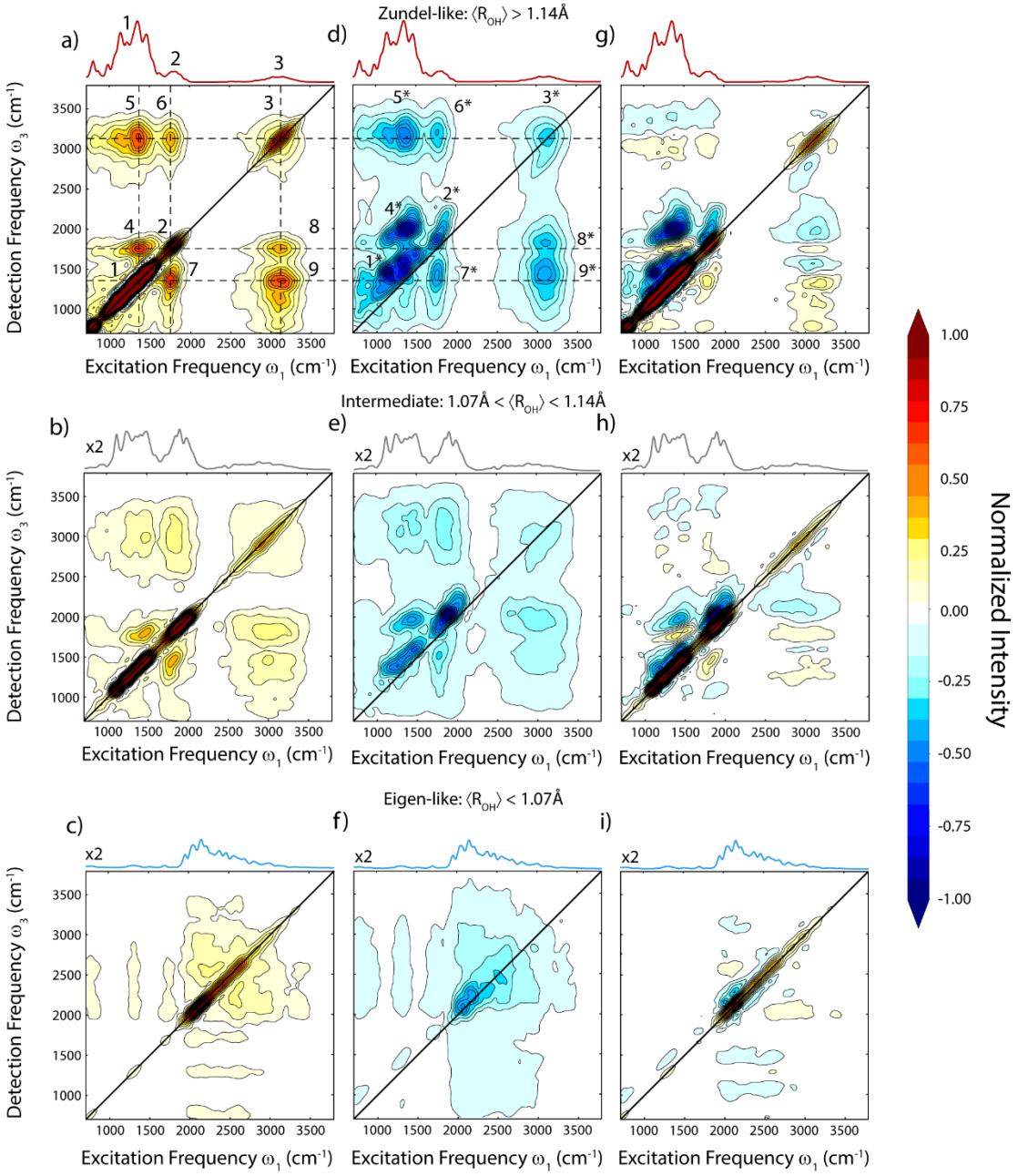

Figure 7.6: (a)-(c) Conditional frequency probability distributions $P_{\mathrm{Fund}}(\omega_3|\omega_1)$ of the (a) Zundel-like, (b) intermediate, and (c) Eigen-like configurations. The diagonal slices are shown above each surface with quartic transition dipole scaling. The cross peaks with numerical labels are assigned in the text. (d)-(f) Conditional frequency probability distributions $P_{\mathrm{Exc}}(\omega_3|\omega_1)$ of the (d) Zundel-like, (e) intermediate, and (f) Eigen-like configurations with numerical labels in (e) corresponding to the overtones and combination bands that arise from the respective features in panel (a). (g)-(i) Combined distributions for Zundel-like, Eigen-like, and intermediate complexes. All surfaces have been averaged to account for number of clusters in each group and share a common normalization factor. Surfaces have also been smoothed by third-order Savitzky-Golay filters along each axis over a breadth of 250 cm^{-1}.

The ESA conditional frequency distributions $P_{Exc}(\omega_3|\omega_1)$ are presented in Figs. 7.6d-f. For Zundel-like configurations (Fig. 7.6d), the stretch and bend ESAs (Peaks 1* and 2*, respectively) appear above the diagonal like in the 6-Zundel cluster, whereas the flanking O–H stretch ESAs (Peak 3*) appear along the diagonal and red-shifted compared to the gas phase. The proton stretch ESA and proton stretch/flanking bend combination band (Peak 4*) both display diagonal elongation, which indicates inhomogeneous broadening in their line shapes. The intermediate ESA $P_{Exc}(\omega_3|\omega_1)$ retains the same features (Fig. 7.6e), but the overtone near 2000 cm^{-1} is more intense due to the presence of blue-shifted proton stretch vibrations. Two-quantum transitions are also present in these surfaces, but are less distinct than in the gas phase (Fig. 7.2c). The Eigen-like excited-state spectral density (Fig. 7.6f) displays the same high spectral density between (ω_1, ω_3) = (2000-3000 cm^{-1}, 2000-3000 cm^{-1}) like in the $P_{Fund}(\omega_3|\omega_1)$ for Eigen-like configurations. As a result, there is significant destructive overlap in the combined surface for Eigen-like clusters, resulting in low probability amplitude across both dimensions in the mid-IR (Fig. 7.6i).

The 2D anisotropies (Fig. 7.7) in these groupings mirror those of the gas-phase clusters, which reinforces their separation by Zundel-like and Eigen-like character. For Zundel-like and intermediate configurations (Figs. 7.7a-b), Peaks 4 and 7 show high positive anisotropy ($r \approx 0.25$), while the cross peaks to the flanking stretches (Peaks 5, 6, 8, 9) display a primarily negative anisotropy. In the Eigen-like sub-ensemble, the 2D anisotropy pattern varies significantly between 2000-3000 cm^{-1}, but the cross peaks between the O–H stretches and the umbrella modes are consistently negative. For all three types of configurations, the ESA 2D anisotropies (Figs. 7.7d-f) all show similar trends as in the fundamental 2D anisotropy surfaces. For the combined $P_{Fund}(\omega_3|\omega_1) + P_{Exc}(\omega_3|\omega_1)$ surfaces, the qualitative trends of positive and negative anisotropy are

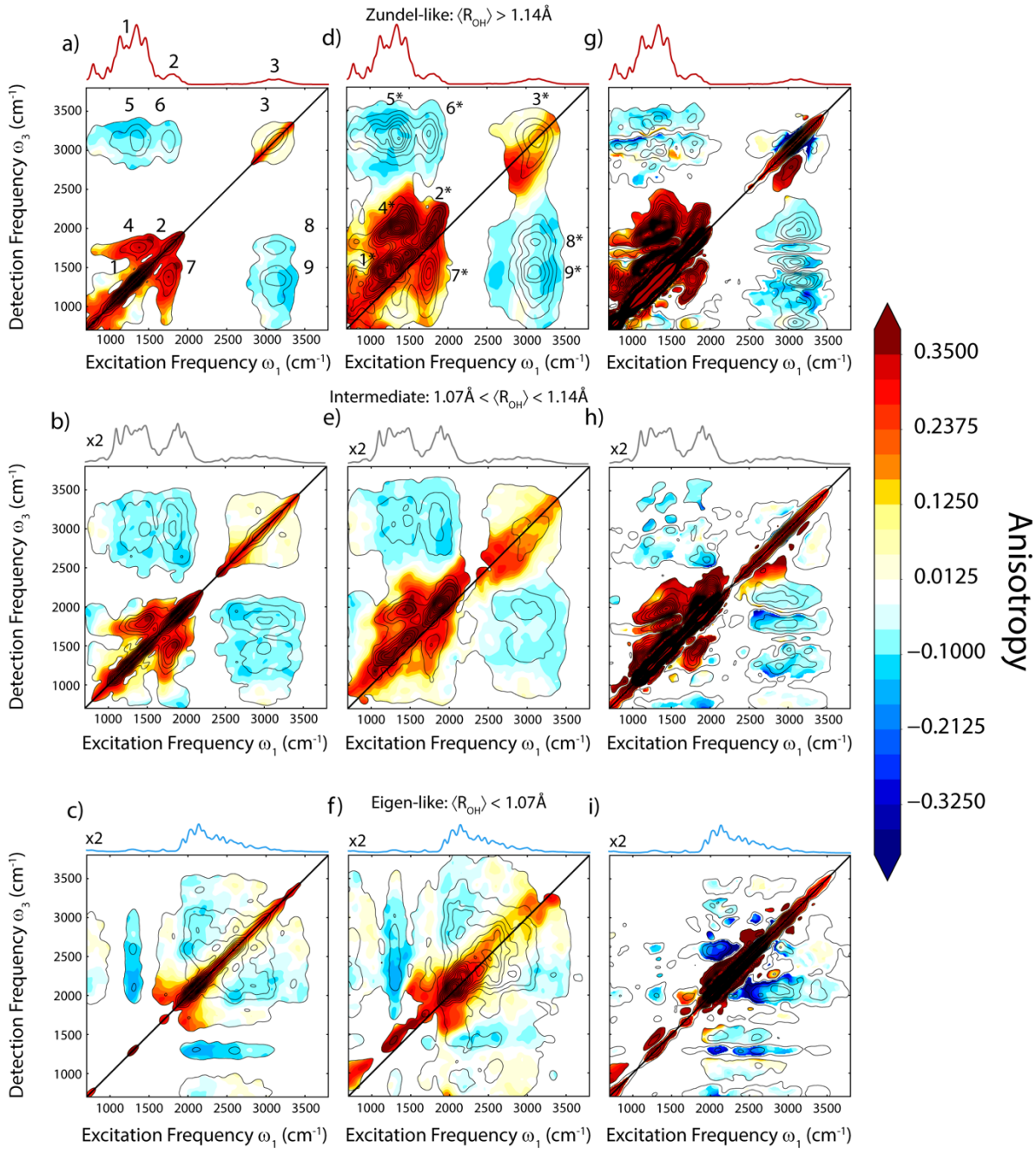

Figure 7.7: 2D anisotropy surfaces for three groups of cluster geometries. (a)-(c) Fundamental transition 2D anisotropies for (a) Zundel-like, (b) intermediate, and (c) Eigen-like configurations. (d)-(f) Excited state absorption 2D anisotropy surfaces for (d) Zundel-like, (e) intermediate, and (f) Eigen-like configurations. (g)-(i) 2D anisotropy surfaces for the combined features for (d) Zundel-like, (e) intermediate, and (f) Eigen-like configurations. Contours on 2D anisotropy surfaces are from their respective conditional probabilities and the anisotropy values are only presented in regions where the conditional probability is at least 5% of the maximum. Anisotropy surfaces have been smoothed by third-order Savitzky-Golay filters along each axis over a breadth of 250 cm^{-1}.

similar to the individual surfaces, but the effect of interference between positive and negative features results in actual anisotropy values beyond the usual limits of 0.4 and –0.2. To examine the connection between structures and spectra in more detail, we proceed to analyze the piece of the 2D IR spectrum pumped at 1200 cm^{-1}.

7.4.2 The Proton Stretch Vibration Reports on Geometries of the Aqueous Proton Complex

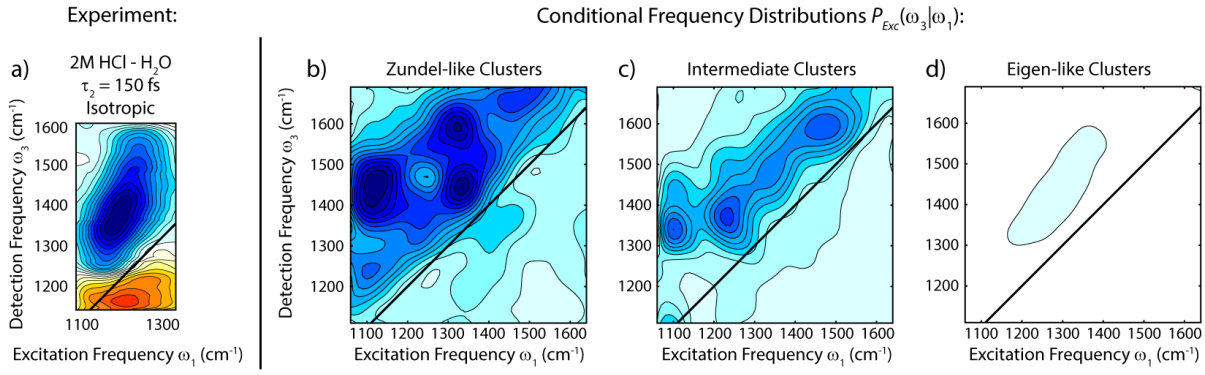

Figure 7.8: (a) Experimental isotropic 2D IR spectrum of 2M HCl – H_2O in the proton stretch diagonal region from Ref. 51. (b)-(d) Conditional frequency probability distributions $P_{\mathrm{Exc}}(\omega_3|\omega_1)$ for (b) Zundel-like, (c) intermediate, and (d) Eigen-like clusters. In (b)-(d), each distribution is presented with the same normalization constant and corrected for the number of clusters, so that amplitudes reflect nonlinear intensities.

Analyzing the 2D diagonal region between 1000-1600 cm^{-1} provides an opportunity to learn about the ensemble of Zundel-like and intermediate aqueous proton configurations. To demonstrate this, we present the experimental 2D IR spectrum of this region in Fig. 7.8a from Ref. 51. The ground state bleach lies along the diagonal, while the $|1\rangle \rightarrow |2\rangle$ ESA appears above the diagonal, centered at ω_3 = 1360 cm^{-1}. This doublet pattern demonstrates a peculiar anharmonicity, but is consistent with its assignment as the proton stretch in Zundel-like species.[22,51] In Fig. 7.8b-d, we find that the calculated $P_{\mathrm{Exc}}(\omega_3|\omega_1)$ distributions in this region for Zundel-like, intermediate, and Eigen-like clusters (Figs. 7.8b-d) share an ESA above the diagonal and also display diagonal elongation. For Zundel-like and intermediate clusters, the ESA is primarily due to the proton

stretch ω_{21} transition, whereas the ESA in Eigen-like clusters (Fig. 7.8d) arises from the ω_{21} transition of hydronium umbrella mode, which has a much smaller transition dipole amplitude. When normalized by the number of clusters in each type of configuration, the Zundel-like and intermediate surfaces are on average significantly more intense than the Eigen-like clusters in this region.

The diagonally elongated probability densities of Figs. 7.8b and 7.8c indicate that there are frequency correlations within a large distribution of ω_{10} and ω_{21} transitions. To connect proton stretch frequencies to atomic displacements, we employed linear least-squares regression on ω_{10} and ω_{21} with collective geometric coordinates.[59] We began by optimizing the R^2 correlation coefficient between vibrational frequency and a mixed coordinate q modeled by a linear combination of quantum expectation values of local monomer atomic distances, H–O–H angles, and H–O–O–H dihedrals, allowing their weighting coefficients to float freely. We found that the two most significant parameters were the $\langle R_{OH} \rangle$ and $\langle R_{OO} \rangle$ distances, and therefore reoptimized the correlations on a reduced collective coordinate:

$$q_r = c_1 \langle R_{OH} \rangle + c_2 \langle R_{OO} \rangle, \tag{7.5}$$

where the absolute values of c_1 and c_2 were constrained to sum to one. We carried out this analysis separately for Zundel-like, Eigen-like, and intermediate cluster geometries.

Table 7.1 shows the retrieved c_1 and c_2 coefficients and the R^2 value for corresponding scatter plots in Fig. 7.9. We find that in Zundel-like configurations $\langle R_{OO} \rangle$ is a more influential predictor of ω_{10} than $\langle R_{OH} \rangle$, with $|c_1| = 0.40$ and $|c_2| = 0.60$, whereas in Eigen-like clusters the frequency trend is dominated by $\langle R_{OH} \rangle$ ($c_1 = 0.96$). As seen in Table 7.1 and Fig. 7.9d, c_1 and c_2 values are similar for ω_{10} and ω_{21} trends in each grouping, which points to frequency correlation between ω_{10} and ω_{21} and diagonal elongation in the surfaces in Fig. 7.8. Interestingly, the

frequency trends for the intermediate complexes are dominated by $\langle R_{OH} \rangle$, even though the spectral density of intermediate complexes more closely resembles that of the Zundel-like configurations (Fig. 7.5). This suggests that the intermediate complexes represent a turning point between two regimes dominated by $\langle R_{OH} \rangle$ and $\langle R_{OO} \rangle$. The influence of $\langle R_{OO} \rangle$ on proton stretch frequency in Zundel-like and intermediate configurations indicates that confinement from the flanking two waters significantly influences the shape of the proton stretch potential. However, because of the substantial overlap between proton stretch frequency distributions for Zundel-like and intermediate configurations, the broad distribution of ω_{10} and ω_{21} frequencies between ω_1 = 1000-1600 cm^{-1} reflects the spread of both $\langle R_{OO} \rangle$ and $\langle R_{OH} \rangle$ in Zundel-like and intermediate configurations.

Table 7.1: Coefficients c_1 and c_2 for relative fractions of $\langle R_{OH} \rangle$ and $\langle R_{OO} \rangle$, respectively, in the reduced collective coordinate q_r.

Cluster Type	**Transition**	c_1	c_2	R^2
Zundel-like	ω_{10}	0.40	0.60	0.540
	ω_{21}	0.34	0.66	0.432
Intermediate	ω_{10}	0.81	0.19	0.507
	ω_{21}	0.77	0.23	0.370
Eigen-like	ω_{10}	0.96	0.04	0.641
	ω_{21}	0.94	0.06	0.540

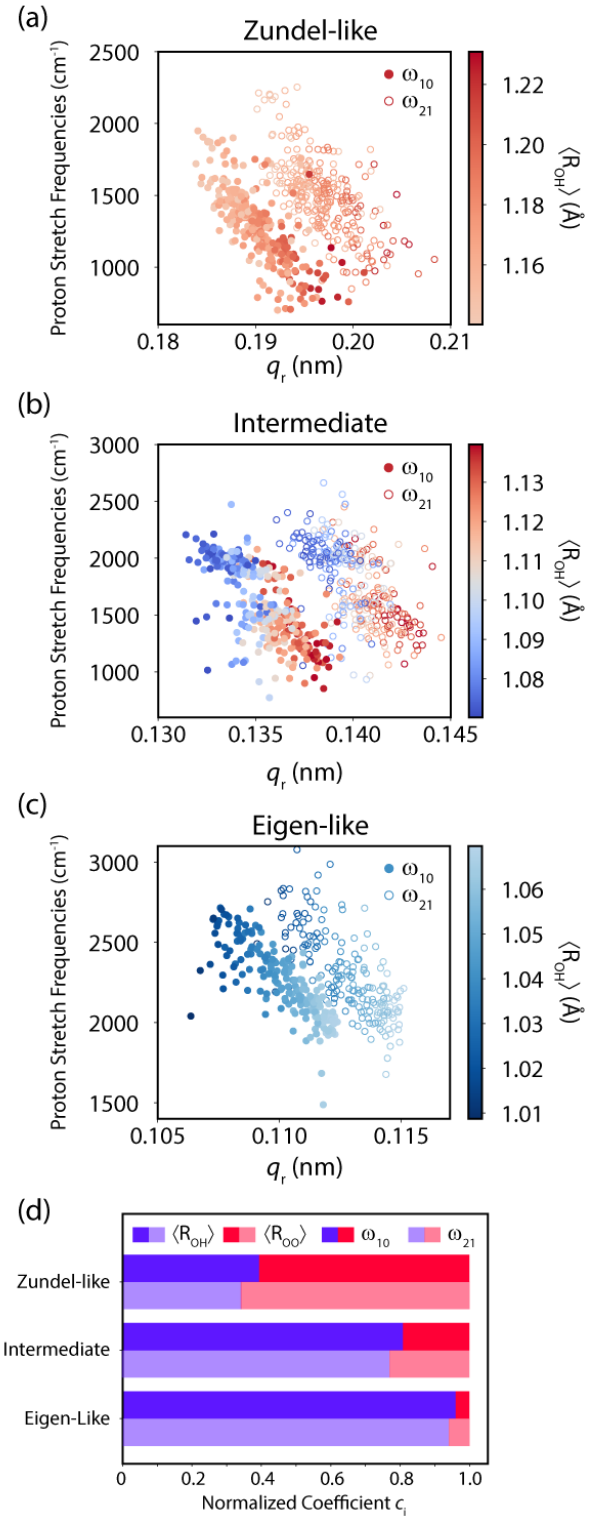

Figure 9: Reduced collective coordinate q_r versus proton stretch ω_{10} (closed circles) and ω_{21} (open circles) for (a) Zundel-like, (b) intermediate, and (c) Eigen-like clusters. Points are colored by the $\langle R_{OH} \rangle$ value for the given configuration. (d) Coefficients c_i for $\langle R_{OH} \rangle$ and $\langle R_{OO} \rangle$ in the reduced collective coordinate q_r for the three types of clusters.

While the ω_1 = 1000-1600 cm^{-1} region primarily reports on the heterogeneity of Zundel-like and intermediate distributions, trends across the entire mid-IR can be used as an experimental handle to characterize the heterogeneity of Eigen-like configurations. Fig 7.9c demonstrates that proton stretch ω_{10} spans almost 1000 cm^{-1} due to the $\langle R_{OH} \rangle$ range of approximately 0.06 Å in Eigen-like configurations. This is a relatively small distribution of values, particularly compared to the typical values of $\langle \delta R_{OH} \rangle$ (0.0-0.5 Å), underscoring the extreme sensitivity of the O–H stretch on bond length. Despite the extreme red-shifting of the special pair O–H stretch, the off-diagonal intensities in the $P_{Fund}(\omega_3|\omega_1)$ and $P_{Exc}(\omega_3|\omega_1)$ surfaces of Eigen-like clusters (Figs. 7.6c and 7.6f, respectively) demonstrate that all three of hydronium's O–H stretches are anharmonically coupled to each other. This implies that while the special pair H-bond is the primary determinant of special pair O–H frequency, the rest of the solvation environment will have some influence on special pair frequency as well.

7.4.3 Potential Energy Surfaces of the Proton Stretch Vibration

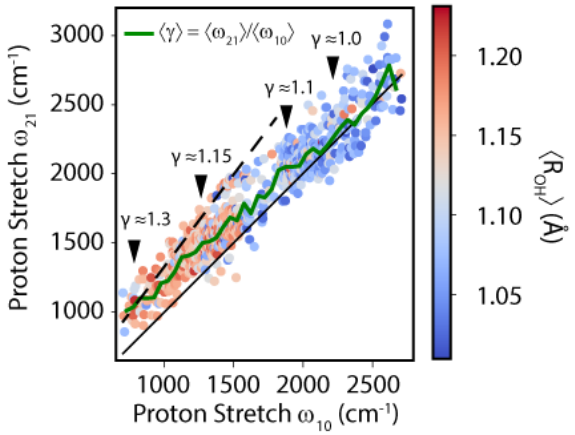

Figure 7.10. Scatter plot comparing proton stretch fundamentals ω_{10} and excited state ω_{21} transitions for all clusters. Points are colored by the $\langle R_{OH} \rangle$ value for the given configuration. The black dotted line represents where γ = 1.33 up to ω_{10} = 1800 cm^{-1}. The green line represents the average γ value taken over 50 cm^{-1} windows in ω_1.

As discussed in the previous section, the proton stretch frequency is a highly sensitive reporter of the configuration of the aqueous proton complex. In the static limit presented here, ω_{10} spans approximately 2000 cm^{-1}, spectrally separating configurations with different $\langle R_{OH} \rangle$ and $\langle R_{OO} \rangle$ values. We can compare the ω_{10} and ω_{21} values for each cluster to uncover trends in the proton stretch potential energy surface. To start, we present a scatter plot comparing proton stretch ω_{10} frequencies with their corresponding ω_{21} transitions (Fig. 7.10). As shown in the previous section, the ω_{10} transitions of Zundel-like and intermediate clusters overlap significantly and are distributed across 900-1600 cm^{-1}, whereas Eigen-like special pair O–H stretches are almost all above $\omega_{10} > 1600$ cm^{-1}. The ω_{21} transitions for the Zundel-like and intermediate clusters are almost all at higher frequency than their corresponding ω_{10} transitions, placing them above the diagonal in this plot. This is consistent with the surfaces shown in Figs. 7.8b and 7.8c for these two types of clusters. By averaging the ω_{21} values over 50 cm^{-1} intervals in ω_{10}, we can calculate a mean frequency ratio $\langle \gamma \rangle = \langle \omega_{21} \rangle / \langle \omega_{10} \rangle$. In Fig. 7.6a, $\langle \gamma \rangle \approx 1.3$ when $\omega_{10} < 1000$ cm^{-1}, and gradually reduces to $\langle \gamma \rangle \approx 1.15$ for $\omega_{10} \approx 1200$ cm^{-1}, in a range consistent with the experimental surface in Fig. 7.6a.[51] For Eigen-like clusters, the ω_{21} transitions are closer to their corresponding ω_{10} transitions approaching $\langle \gamma \rangle \approx 1$.

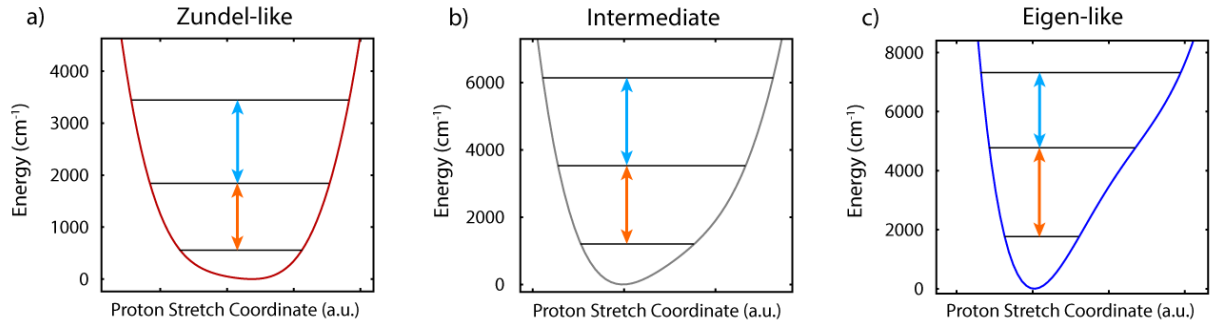

Figure 7.11. One-dimensional slices along the proton stretch normal mode coordinate from the multidimensional nuclear PES for representative (a) Zundel-like, (b) intermediate, and (c) Eigen-like clusters. Orange and blue arrows represent ω_{10} and ω_{21} energy gaps, respectively.

The above trends in frequency spacing derive from the shapes of the nuclear potential. Fig. 7.11 shows representative one-dimensional potential energy slices along the proton stretch normal mode coordinate defined in Section 7.3.2. The potential energy curve of the Zundel-like configuration (Fig. 7.11a) resembles the 6-Zundel potential energy curve in Fig. 7.3b, featuring a relatively flat bottom with steep walls and a mostly symmetric shape. These are the characteristics of a superharmonic potential shape, leading to the $\omega_{21} > \omega_{10}$ ($\gamma > 1$) relationship seen in Fig. 7.10. The potential of the intermediate complex (Fig. 7.11b) shows similar steep walls, but the bottom of the potential appears more asymmetric. Following the discussion of the relative effects of confinement and asymmetry in Section 7.3.2, the increase in asymmetry pushes up the ω_{10} transition, reducing γ to about 1.15. At the high-frequency extreme, the Eigen-like potential (Fig. 7.11c) displays a highly asymmetric shape much like the 6-Eigen potential (Fig. 7.3d) resulting in $\gamma < 1$.

While these potentials are representative for Zundel-like, Eigen-like, and intermediate configurations, there is some variation within each category. For each geometric group, one can find examples of flat-bottomed potentials, potentials with substantial asymmetry, and there are even a couple of cases of low-barrier double-welled potentials in each group. There are only a handful of such potentials in our ensemble, whereas the vast majority of complexes show single-well potential shapes along the proton stretch normal mode coordinate.

Each of the presented potentials are only slices in one dimension, but the full potential is multidimensional and involves coupling to other degrees of freedom. VSCF/VCI calculations reveal that quantitative calculation of proton stretch frequency requires at least four dimensions, whereas low-dimensional surfaces fail to reproduce frequency positions.[35,37,38] Anharmonic coupling with other modes influences the observed ω_{10}, ω_{21}, and γ in non-trivial ways, which could

explain the difficulty in achieving strong correlations between the proton stretch and geometric descriptors such as $\langle R_{OH} \rangle$ and $\langle R_{OO} \rangle$. Strong anharmonic mixing with other modes made identifying the proton stretch ambiguous in some cases. These issues could be alleviated by employing a similar analysis on a simpler strongly H-bonded aqueous system with clearly delineated vibrational modes. As a result, linear regression analyses correlating collective geometric coordinates with proton stretch potential characteristics like confinement or asymmetry did not yield quantitatively satisfactory correlations, even though the trends based on Eq. 7.2 were physically intuitive. Finally, the wide variability in one-dimensional potential energy cuts is amplified in two-dimensional surfaces, which complicates any systematic analysis of potential energy shape in multiple coordinates. This implies that the parameter γ is influenced by more than the potential shape in one dimension. Even though γ is a conceptually useful parameter, it cannot be connected quantitatively to potential shape.

There has been illuminating work demonstrating that the proton stretch is a function of many strongly coupled coordinates such as O···O stretching, flanking in-plane bending, and proton-involved low-frequency modes in Zundel-like and Eigen-like complexes.[33,34] The VSCF/VCI calculations are able to capture both of these aspects, but the accuracy is only achieved by applying quantum mechanical calculations on high-dimensional potential energy surfaces, each of which can be highly nonintuitive.[37] Zundel-like complexes exhibit strong mode mixing in particular, perhaps an effect of the smaller $\langle R_{OO} \rangle$ distances which would increase interactions between molecules in the complex. As configurations become more Eigen-like, proton stretch frequency trends more linearly with $\langle R_{OH} \rangle$ length. This suggests that coupling to other types of modes is less important to predict frequency, but as discussed in Section 7.4.2, there is still strong coupling between the three hydronium O–H oscillators.[35]

7.4.4 2D IR Cross Peaks Between Zundel-like Vibrations

The conditional frequency distributions presented in Fig. 7.6 display distinct cross peak patterns that distinguish spectral response from Eigen-like, Zundel-like, and intermediate geometries. For aqueous Zundel-like solutions, the off-diagonal features are relatively intense and tightly distributed in the four corners of the combined $P_{\mathrm{Fund}}(\omega_3|\omega_1) + P_{\mathrm{Exc}}(\omega_3|\omega_1)$ surface (Fig. 7.6g). Here, we examine two of these regions in more detail to interpret the response from experimental 2D IR spectra.

In Fig. 7.12a, the isotropic 2D IR spectrum of 2M HCl – H_2O at $(\omega_1, \omega_3) = (1200\ \mathrm{cm^{-1}}, 1750\ \mathrm{cm^{-1}})$ consists of a broad bleach spanning more than 250 $\mathrm{cm^{-1}}$ in the excitation dimension and approximately 150 $\mathrm{cm^{-1}}$ along the detection dimension. Additionally, there are narrow positive and negative bands below $\omega_3 = 1700\ \mathrm{cm^{-1}}$ due to the anharmonic coupling between high-frequency librational modes and bending modes in bulk water.[60] The bleach at $\omega_3 = 1750\ \mathrm{cm^{-1}}$ is joined by a negative feature centered at $\omega_3 = 1900\ \mathrm{cm^{-1}}$. The combined conditional probability surfaces from VSCF/VCI calculations (Fig. 7.12b) indicate that the most intense response originates from Zundel-like geometries with some contribution from intermediate configurations. This comparison confirms our previous assignment[51] that the cross peak doublet arises from coupling between the shared proton stretch and concerted flanking bend in Zundel-like configurations.

Closer inspection of these surfaces reveals orientational and frequency correlations between the proton stretch and flanking bend modes. The parallel polarization preference in the experimental spectrum[51] and calculated 2D anisotropy surfaces (Fig. 7.7g) reveal that these two modes have roughly parallel transition dipoles, implying that the concerted flanking bend dipole lies along the shared O···O axis and has asymmetric normal mode character. Additionally, the calculated conditional frequency probability surface (Fig. 7.12b) displays diagonal elongation of

bleach and induced absorptions, indicative of correlated frequencies with the excited proton stretching mode. Inspection of the individual $P_{\mathrm{Fund}}(\omega_3|\omega_1)$ and $P_{\mathrm{Exc}}(\omega_3|\omega_1)$ surfaces in Figs. 7.6a and 7.6d reveals that while there is some diagonal elongation of the bleach feature, the majority of the diagonal elongation is due to the frequency correlation in the two ESA features flanking the bleach. This frequency correlation is not as strongly present in the experimental spectrum, however, which suggests fast frequency fluctuations within 150 fs.

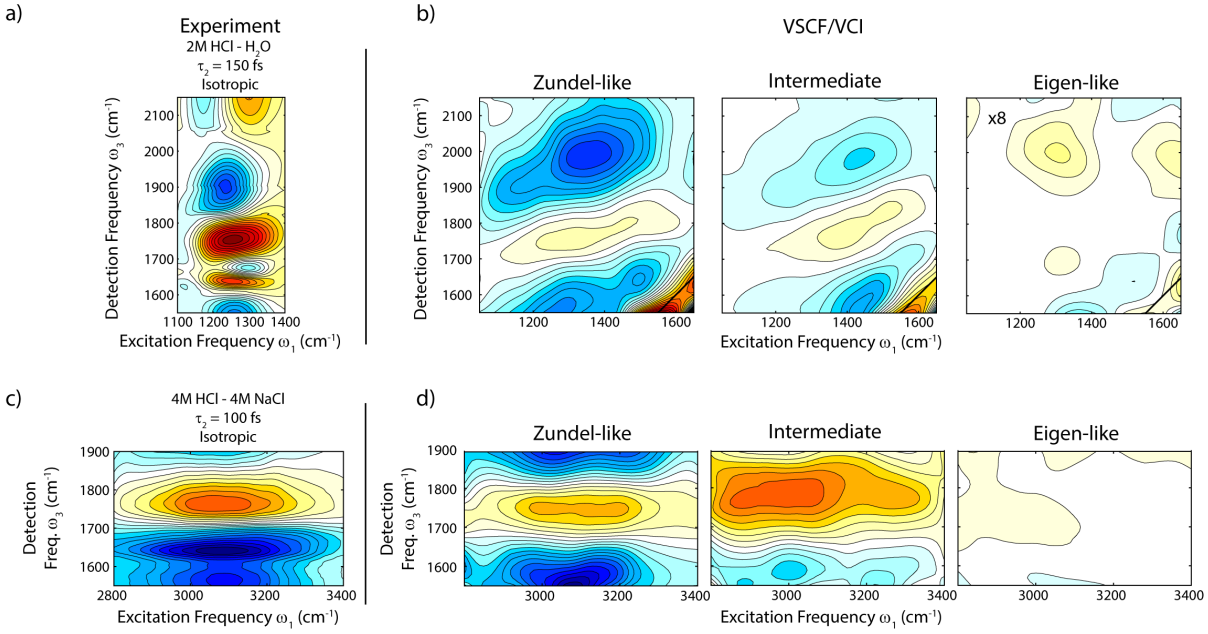

Figure 7.12. (a) Experimental isotropic 2D IR spectrum of 2M HCl – H_2O at (ω_1, ω_3) = (1200 cm^{-1}, 1750 cm^{-1}) from Ref. 51. (b) Combined conditional frequency probability distributions $P_{\mathrm{Fund}}(\omega_3|\omega_1) + P_{\mathrm{Exc}}(\omega_3|\omega_1)$ for the three geometric groups, corrected for number of clusters and presented on the same scale. (c) Experimental isotropic 2D IR spectrum of 4M HCl – 4M NaCl at (ω_1, ω_3) = (3100 cm^{-1}, 1750 cm^{-1}) from Ref. 51, with accompanying (d) combined conditional frequency distributions in this region, corrected for number of clusters and presented on the same scale.

Another region of interest is in the cross peak in the (ω_1, ω_3) = (3200 cm^{-1}, 1750 cm^{-1}) region (Fig. 7.12c), which was previously measured as the first experimental evidence for the Zundel species in solution.[50] This cross peak is reproduced in the conditional probability distribution for Zundel-like configurations (Fig. 7.12d), reinforcing this assignment as a cross peak between the Zundel flanking stretches and flanking bends. The negative features flanking the

bleach in the conditional probability distribution are due to excitations from the flanking stretch into the flanking stretch/flanking bend and flanking stretch/shared proton stretch combination bands. These are also expected in the experimental 2D IR spectrum, but this region also contains an intense negative background due to the strongly anharmonic water O–H stretch ESA which spans ω_3 = 1500-3000 cm^{-1}.[61]

In contrast to the clear cross peaks of Zundel-like configurations, the 2D IR features from Eigen-like geometries are less noticeable. Inspecting the $P_{\text{Fund}}(\omega_3|\omega_1)$ and $P_{\text{Exc}}(\omega_3|\omega_1)$ surfaces separately (Figs 7.6c and 7.6f, respectively) suggests that there are broad features due to coupling with the Eigen-like stretch continuum, but the combined surface (Fig. 7.6i) reveals that these features destructively overlap. For example, if one examined the $P_{\text{Fund}}(\omega_3|\omega_1)$ surface alone, it would appear that the cross peak between the Eigen umbrella and O–H stretch modes should be apparent at $(\omega_1, \omega_3) = (1200\ \text{cm}^{-1},\ 2000\text{-}2800\ \text{cm}^{-1})$, but this cross peak disappears when overlapped with the $P_{\text{Exc}}(\omega_3|\omega_1)$ surface. This is inconsistent with the presence of a cross peak bleach in the experimental 2D IR spectrum in this region.[51] One possibility is that the bleach and ESA overlap and destructively interfere in experiment. This would imply that the bleach is overall more intense than the induced absorption, which could be justified by reduced ESA transition dipole or larger breadth of allowable ESA transitions due to the anharmonicity of the system.

The difference between the calculated and experimental surfaces in this region means that there are a few possible assignments for this cross peak. Previously, some of us measured a cross peak between the 1200 cm^{-1} and 2500 cm^{-1} features with perpendicular polarization preference, which was used to assign the 2000-3000 cm^{-1} region as flanking O–H stretches of Zundel-like species.[51] However, the calculated linear spectral density and two-dimensional conditional frequency probability distribution point to this region belonging to Eigen-like geometries. Assuming static

configurations in solution, this would suggest that there should not be a cross peak between Eigen-like and Zundel-like geometries.

7.4.5 Possible Fluctuations Between Configurations

The VSCF/VCI calculations on clusters pulled from MS-EVB snapshots capture the broad distributions of structural parameters like $\langle R_{OH} \rangle$ and $\langle R_{OO} \rangle$, but do not account for solution fluctuation dynamics. These distributions arise from thermal fluctuations at room temperature, the low or non-existent barrier for the proton to rattle between water molecules,[24,25] and the quantum delocalization of the excess proton with finite zero-point energy.[20] Even in classical MS-EVB simulations, Eigen-like configurations are stabilized compared to Zundel-like configurations by only ~0.8 kcal/mol,[62] which means that the excess proton can experience a wide distribution of local environments at room temperature. This breadth in configurations underscores the importance of considering the ensemble of aqueous proton structures as a distribution, rather than characterizing it only as the Eigen and Zundel species that represent the limits of this distribution.

Within this broad distribution, simulations suggest that there are fast geometric fluctuations on the sub-100 fs timescale. Multiple simulations have found sub-100fs proton position fluctuations, including phenomena known as proton rattling[63] and the special pair dance.[23] These both impact the instantaneous values of $\langle R_{OH} \rangle$ and $\langle \delta R_{OH} \rangle$ which have been used to characterize complexes as Eigen-like or Zundel-like. Recent *ab initio* simulations of the excess proton found that δR_{OH} quickly decorrelates on a sub-100 fs timescale,[44] which suggests that $\langle R_{OH} \rangle$ also decorrelates rapidly. This implies that while $\langle R_{OH} \rangle$ is spectrally sensitive to instantaneous configuration, this vibration likely will not be sensitive to dynamics associated with slower processes like irreversible proton transfer, which occurs on a 1-2 ps timescale.[64,65] Additionally, the fast and large-amplitude fluctuation of $\langle R_{OH} \rangle$ implies that homogeneous broadening is likely a significant component of the

linear and nonlinear spectra that cannot be captured with the current VSCF/VCI calculations. Indeed this is the reason that diagonal GSB features in our calculated spectra, which are by definition perfectly correlated, are not useful in comparing to experiments with massively broadened spectral features. This plays a particularly large role in interpreting Eigen-like clusters in the 2000-3000 cm^{-1} window.

These rapid nuclear fluctuations of the excess proton in an essentially barrier-free potential would imply that the standard adiabatic assumptions for interpreting the spectroscopy are not valid. For instance, the sub-100 fs structural interconversions would occur on a timescale comparable to the vibrational period of the proton stretch mode (~25 fs). This would imply that the electronic and nuclear degrees of freedom that determine anharmonic coupling are also evolving on the timescale of the vibrational period. This could play an important role in shaping cross peaks between Eigen-like, intermediate, and Zundel-like spectral features at early waiting times. These vibrational non-adiabatic dynamics are known to efficiently dissipate energy in aqueous medium through collective low-frequency modes,[66,67] and these effects are sure to influence the environment around the excess proton. Sub-Å positional fluctuations of the solvent atoms, which usually are accounted for in models for vibrational lineshape broadening, can induce large configurational changes on the characteristic length scale of the excess proton. These factors imply that static configurations can be misleading as true representations of the aqueous system, despite the access to nuclear anharmonicities.

Because of the essentially zero-barrier proton fluctuations, there may be more appropriate geometric coordinates to consider when addressing the interconversion between Zundel-like and Eigen-like geometries. For instance, R_{OO} has been used to discriminate Eigen-like and Zundel-like configurations in simulations,[24] and this coordinate is expected to fluctuate on a 100 fs timescale,

as suggested by time-domain THz results.[68] Even then, if Eigen-like and Zundel-like configurations interconvert on this timescale, there may be a configurational correlation on a ps timescale due to the constraints imposed by the solvation environment. Some of us have measured a 2.5 ps anisotropy decay timescale for the Zundel-like bending modes due to Grotthuss proton transfer,[65,69] which suggests that fs-timescale fluctuations do not totally scramble aqueous proton configurations.

One limitation of analyzing an ensemble of static configurations is the inability to characterize the excess proton ensemble in a dynamical sense. From one perspective, some studies advocate that the aqueous proton complex is fundamentally Zundel-like, and deviations from the symmetric potential shape come from fast, large amplitude electric field fluctuations.[12,22,25] On the other hand, many studies continue to describe the aqueous proton as a fundamentally hydronium-like or Eigen-like species with large fluctuations in geometry due to solvation dynamics.[23,63,68,70,71] Each of these conceptions of the aqueous proton can produce the broad distribution of $\langle R_{OH} \rangle$ and $\langle R_{OO} \rangle$ values that we observed in our study, and perhaps the most appropriate description so far comes from early simulation studies describing it as a "fluxional complex" or a dynamic, strongly bonded, and persistent "special pair".[24]

7.5 Conclusion

We have presented an analysis of two-dimensional conditional frequency probability distributions generated from anharmonic vibrational calculations on gas-phase $H^+(H_2O)_6$ clusters and 800 aqueous proton configurations, which can be used to interpret the 2D IR spectrum of the aqueous proton in the static limit. The gas-phase clusters provide single-structure model systems to interpret how their anharmonic potential energy surface is reflected in two-dimensional conditional frequency probability distributions for transitions between 0-6800 cm^{-1}. By grouping

clusters based on Zundel-like, Eigen-like and intermediate geometric sub-ensembles according to $\langle R_{OH} \rangle$ values, we uncover trends in vibrational frequencies, relative orientations, and potential shape. The vibrational modes of the aqueous proton complex are sensitive reporters of instantaneous geometric configuration, particularly the expectation value of excess proton-oxygen distance $\langle R_{OH} \rangle$ and $\langle R_{OO} \rangle$ for Zundel-like configurations.

Analysis of the $P_{Fund}(\omega_3|\omega_1)$ and $P_{Exc}(\omega_3|\omega_1)$ surfaces assists in connecting the spectroscopy to potential shape. Qualitatively, as the potential asymmetry increases and the confinement decreases, the potential becomes more Eigen-like and the frequency ratio γ can take on values less than one. The extreme asymmetry narrows the potential around the zero point and first excited states, shifting ω_{10} to greater than 1700 cm^{-1}. This means that the 2D IR spectrum at excitation frequencies below ω_{10} = 1700 cm^{-1} is primarily sampling the Zundel-like and intermediate sub-ensemble of configurations. Moreover, from Fig. 7.6, the Zundel-like vibrations appear more intense than the broad response from Eigen-like clusters. Additionally, the spectral response from intermediate geometric configurations resembles that of the Zundel-like clusters. Both of these factors suggest that IR spectroscopy more easily detects Zundel-like spectroscopic features over Eigen-like response, especially with the μ^4 scaling in nonlinear experiments.

Comparing calculated 2D probability distributions with experimental 2D spectra indicates that that the majority of the clearly resolved experimental features correlate with Zundel-like configurations and, to a lesser extent, intermediate configurations. However, in experiments there are broad and featureless signatures in the spectral window 2000-2800 cm^{-1} which are better explained in terms of Eigen-like configuration. These features have cross-peaks to other resonances which are consistent with Zundel-like and intermediate configurations. As a result, it is possible that fluctuations between a distribution of configurations including Eigen-like,

intermediate, and Zundel-like configurations will best describe experimental 2D IR spectra. Given the lack of important dynamical effects in our calculations, and possible uncertainties in experimental spectra (such as water background subtraction), our conclusions must be viewed one step forward in the aqueous proton problem through a continuing advance of theoretical and experimental methods.

7.6 References

(1) Oxtoby, D. W.; Gillis, H. P.; Butler, L. J. *Principles of Modern Chemistry*, 8th ed.; Cengage Learning: Boston, MA, 2016.

(2) Agmon, N.; Bakker, H. J.; Campen, R. K.; Henchman, R. H.; Pohl, P.; Roke, S.; Thämer, M.; Hassanali, A. Protons and Hydroxide Ions in Aqueous Systems *Chem. Rev.* **2016**, *116*, 7642.

(3) Eigen, M. Proton Transfer, Acid-Base Catalysis, and Enzymatic Hydrolysis. Part I: Elementary Processes *Angew. Chemie Int. Ed. English* **1964**, *3*, 1.

(4) Whipple, D. T.; Kenis, P. J. A. Prospects of CO_2 Utilization via Direct Heterogeneous Electrochemical Reduction *J. Phys. Chem. Lett.* **2010**, *1*, 3451.

(5) Graves, C.; Ebbesen, S. D.; Mogensen, M.; Lackner, K. S. Sustainable hydrocarbon fuels by recycling CO_2 and H_2O with renewable or nuclear energy *Renew. Sustain. Energy Rev.* **2011**, *15*, 1.

(6) Taraphder, S.; Maupin, C. M.; Swanson, J. M. J.; Voth, G. A. Coupling Protein Dynamics with Proton Transport in Human Carbonic Anhydrase II *J. Phys. Chem. B* **2016**, *120*, 8389.

(7) Watkins, L. C.; Liang, R.; Swanson, J. M. J.; DeGrado, W. F.; Voth, G. A. Proton-Induced Conformational and Hydration Dynamics in the Influenza A M2 Channel *J. Am. Chem. Soc.* **2019**, *141*, 11667.

(8) Yan, L.; Hu, Y.; Zhang, X.; Yue, B. Applications of NMR Techniques in the Development and Operation of Proton Exchange Membrane Fuel Cells *Annu. Reports NMR Spectrosc.* **2016**, *88*, 149.

(9) Moilanen, D. E.; Spry, D. B.; Fayer, M. D. Water dynamics and proton transfer in nafion fuel cell membranes. *Langmuir* **2008**, *24*, 3690.

(10) Bernal, J. D.; Fowler, R. H. A theory of water and ionic solution, with particular reference to hydrogen and hydroxyl ions *J. Chem. Phys.* **1933**, *1*, 515.

(11) Wicke, E.; Eigen, M.; Ackermann, T. Über den Zustand des Protons (Hydroniumions) in wäßriger Lösung *Z. Phys. Chem. (N. F)*. **1954**, *1*, 340.

(12) Zundel, G.; Metzger, H. Energiebänder der tunnelnden Überschuß-Protonen in flüssigen Säuren. Eine IR-spektroskopische Untersuchung der Natur der Gruppierungen $H_5O_2^+$ *Z. Phys. Chem.* **1968**, *58*, 225.

(13) Okumura, M.; Yeh, L. I.; Myers, J. D.; Lee, Y. T. Infrared spectra of the solvated hydronium ion: Vibrational predissociation spectroscopy of mass-selected H3O+.cntdot.(H2O)n.cntdot.(H2)m *J. Phys. Chem.* **1990**, *94*, 3416.

(14) Schwarz, H. A. Gas phase infrared spectra of oxonium hydrate ions from 2 to 5 μ *J. Chem. Phys.* **1977**, *67*, 5525.

(15) Stoyanov, E. S.; Stoyanova, I. V.; Reed, C. A. The Structure of the Hydrogen Ion (H_{aq}^+) in Water *J. Am. Chem. Soc.* **2010**, *132*, 1484.

(16) Chandra, A.; Tuckerman, M. E.; Marx, D. Connecting solvation shell structure to proton transport kinetics in hydrogen-bonded networks via population correlation functions *Phys. Rev. Lett.* **2007**, *99*, 145901.

(17) Tuckerman, M.; Laasonen, K.; Sprik, M.; Parrinello, M. Ab Initio Molecular Dynamics Simulation of the Solvation and Transport of H3O+ and OH- Ions in Water *J. Phys. Chem.* **1995**, *99*, 5749.

(18) Fecko, C. J.; Eaves, J. D.; Loparo, J. J.; Tokmakoff, A.; Geissler, P. L. Ultrafast Hydrogen-Bond Dynamics in the Infrared Spectroscopy of Water. *Science* **2003**, *301*, 1698.

(19) Lapid, H.; Agmon, N.; Petersen, M. K.; Voth, G. A. A bond-order analysis of the mechanism for hydrated proton mobility in liquid water *J. Chem. Phys.* **2005**, *122*, 014506.

(20) Giberti, F.; Hassanali, A. A.; Ceriotti, M.; Parrinello, M. The Role of Quantum Effects on Structural and Electronic Fluctuations in Neat and Charged Water *J. Phys. Chem. B* **2014**, *118*, 13226.

(21) Roy, S.; Schenter, G. K.; Napoli, J. A.; Baer, M. D.; Markland, T. E.; Mundy, C. J. Resolving Heterogeneous Dynamics of Excess Protons in Aqueous Solution with Rate Theory *J. Phys. Chem. B* **2020**, acs. jpcb.0c02649.

(22) Dahms, F.; Fingerhut, B. P.; Nibbering, E. T. J.; Pines, E.; Elsaesser, T. Large-amplitude transfer motion of hydrated excess protons mapped by ultrafast 2D IR spectroscopy *Science* **2017**, *357*, 491.

(23) Markovitch, O.; Chen, H.; Izvekov, S.; Paesani, F.; Voth, G. A.; Agmon, N. Special pair dance and partner selection: elementary steps in proton transport in liquid water. *J. Phys. Chem. B* **2008**, *112*, 9456.

(24) Marx, D.; Tuckerman, M. E.; Hutter, J.; Parrinello, M. The nature of the hydrated excess proton in water *Nature* **1999**, *397*, 601.

(25) Daly, C. A.; Streacker, L. M.; Sun, Y.; Pattenaude, S. R.; Hassanali, A. A.; Petersen, P. B.; Corcelli, S. A.; Ben-Amotz, D. Decomposition of the Experimental Raman and Infrared Spectra of Acidic Water into Proton, Special Pair, and Counterion Contributions *J. Phys. Chem. Lett.* **2017**, *8*, 5246.

(26) Dahms, F.; Costard, R.; Pines, E.; Fingerhut, B. P.; Nibbering, E. T. J.; Elsaesser, T. The Hydrated Excess Proton in the Zundel Cation $H_5O_2^+$: The Role of Ultrafast Solvent Fluctuations *Angew. Chemie - Int. Ed.* **2016**, *55*, 10600.

(27) Xu, Z.-H.; Meuwly, M. Multistate Reactive Molecular Dynamics Simulations of Proton Diffusion in Water Clusters and in the Bulk *J. Phys. Chem. B* **2019**, *123*, 9846.

(28) Eaves, J. D.; Tokmakoff, A.; Geissler, P. L. Electric Field Fluctuations Drive Vibrational Dephasing in Water. *J. Phys. Chem. A* **2005**, *109*, 9424.

(29) Asmis, K. R.; Pivonka, N. L.; Santambrogio, G.; Brümmer, M.; Kaposta, C.; Neumark, D. M.; Wöste, L. Gas-phase infrared spectrum of the protonated water dimer. *Science* **2003**, *299*, 1375.

(30) Fournier, J. A.; Wolke, C. T.; Johnson, M. A.; Odbadrakh, T. T.; Jordan, K. D.; Kathmann, S. M.; Xantheas, S. S. Snapshots of Proton Accommodation at a Microscopic Water Surface: Understanding the Vibrational Spectral Signatures of the Charge Defect in Cryogenically Cooled $H^+(H_2O)_{n=2–28}$ Clusters *J. Phys. Chem. A* **2015**, *119*, 9425.

(31) Headrick, J. M.; Diken, E. G.; Walters, R. S.; Hammer, N. I.; Christie, R. A.; Cui, J.; Myshakin, E. M.; Duncan, M. A.; Johnson, M. A.; Jordan, K. D. Spectral Signatures of Hydrated Proton Vibrations in Water Clusters *Science* **2005**, *308*, 1765.

(32) Heine, N.; Fagiani, M. R.; Rossi, M.; Wende, T.; Berden, G.; Blum, V.; Asmis, K. R. Isomer-Selective Detection of Hydrogen-Bond Vibrations in the Protonated Water Hexamer *J. Am. Chem. Soc.* **2013**, *135*, 8266.

(33) Vendrell, O.; Gatti, F.; Meyer, H.-D. Full dimensional (15-dimensional) quantum-dynamical simulation of the protonated water dimer. II. Infrared spectrum and vibrational dynamics *J. Chem. Phys.* **2007**, *127*, 184303.

(34) Vendrell, O.; Gatti, F.; Lauvergnat, D.; Meyer, H.-D. Full-dimensional (15-dimensional) quantum-dynamical simulation of the protonated water dimer. I. Hamiltonian setup and analysis of the ground vibrational state *J. Chem. Phys.* **2007**, *127*, 184302.

(35) Yu, Q.; Bowman, J. M. Communication: VSCF/VCI vibrational spectroscopy of $H_7O_3^+$ and $H_9O_4^+$ using high-level, many-body potential energy surface and dipole moment surfaces *J. Chem. Phys.* **2017**, *146*, 121102.

(36) Yu, Q.; Bowman, J. M. High-Level Quantum Calculations of the IR Spectra of the Eigen,

Zundel, and Ring Isomers of $H^+(H_2O)_4$ Find a Single Match to Experiment *J. Am. Chem. Soc.* **2017**, *139*, 10984.

(37) Chen, Q.; Bowman, J. M. Quantum approaches to vibrational dynamics and spectroscopy: Is ease of interpretation sacrificed as rigor increases? *Phys. Chem. Chem. Phys.* **2018**.

(38) Yu, Q.; Carpenter, W. B.; Lewis, N. H. C.; Tokmakoff, A.; Bowman, J. M. High-Level VSCF/VCI Calculations Decode the Vibrational Spectrum of the Aqueous Proton *J. Phys. Chem. B* **2019**, *123*, 7214.

(39) Yu, Q.; Bowman, J. M. Tracking Hydronium/Water Stretches in Magic $H_3O^+(H_2O)_{20}$ Clusters through High-level Quantum VSCF/VCI Calculations *J. Phys. Chem. A* **2020**, *124*, 1167.

(40) Duong, C. H.; Gorlova, O.; Yang, N.; Kelleher, P. J.; Johnson, M. A.; McCoy, A. B.; Yu, Q.; Bowman, J. M. Disentangling the Complex Vibrational Spectrum of the Protonated Water Trimer, $H^+ (H_2 O)_3$, with Two-Color IR-IR Photodissociation of the Bare Ion and Anharmonic VSCF/VCI Theory *J. Phys. Chem. Lett.* **2017**, *8*, 3782.

(41) Kim, J.; Schmitt, U. W.; Gruetzmacher, J. A.; Voth, G. A.; Scherer, N. E. The vibrational spectrum of the hydrated proton: Comparison of experiment, simulation, and normal mode analysis *J. Chem. Phys.* **2002**, *116*, 737.

(42) Biswas, R.; Carpenter, W.; Fournier, J. A.; Voth, G. A.; Tokmakoff, A. IR spectral assignments for the hydrated excess proton in liquid water *J. Chem. Phys.* **2017**, *146*, 154507.

(43) Xu, J.; Zhang, Y.; Voth, G. A. Infrared spectrum of the hydrated proton in water *J. Phys. Chem. Lett.* **2011**, *2*, 81.

(44) Napoli, J. A.; Marsalek, O.; Markland, T. E. Decoding the spectroscopic features and time scales of aqueous proton defects *J. Chem. Phys.* **2018**, *148*, 222833.

(45) Li, C.; Swanson, J. M. J. Understanding and Tracking the Excess Proton in Ab initio Simulations; Insights from IR Spectra *J. Phys. Chem. B* **2020**, acs. jpcb.0c03615.

(46) Liu, H.; Wang, Y.; Bowman, J. M. Quantum Local Monomer IR Spectrum of Liquid D_2O at 300 K from 0 to 4000 cm^{-1} Is in Near-Quantitative Agreement with Experiment *J. Phys. Chem. B* **2016**, *120*, 2824.

(47) Khalil, M.; Demirdöven, N.; Tokmakoff, A. Coherent 2D IR Spectroscopy: Molecular Structure and Dynamics in Solution. *J. Phys. Chem. A* **2003**, *107*, 5258.

(48) Rubtsov, I. V; Kumar, K.; Hochstrasser, R. M. Dual-Frequency 2D IR Photon Echo of a Hydrogen Bond *Chem. Phys. Lett.* **2005**, *402*, 439.

(49) Asbury, J. B.; Steinel, T.; Kwak, K.; Corcelli, S. A.; Lawrence, C. P.; Skinner, J. L.; Fayer, M. D. Dynamics of water probed with vibrational echo correlation spectroscopy. *J.*

Chem. Phys. **2004**, *121*, 12431.

(50) Thämer, M.; De Marco, L.; Ramasesha, K.; Mandal, A.; Tokmakoff, A. Ultrafast 2D IR spectroscopy of the excess proton in liquid water *Science* **2015**, *350*, 78.

(51) Fournier, J. A.; Carpenter, W. B.; Lewis, N. H. C.; Tokmakoff, A. Broadband 2D IR spectroscopy reveals dominant asymmetric $H_5O_2^+$ proton hydration structures in acid solutions *Nat. Chem.* **2018**, *10*, 932.

(52) Boyer, M. A.; Marsalek, O.; Heindel, J. P.; Markland, T. E.; McCoy, A. B.; Xantheas, S. S. Beyond Badger's Rule: The Origins and Generality of the Structure–Spectra Relationship of Aqueous Hydrogen Bonds *J. Phys. Chem. Lett.* **2019**, *10*, 918.

(53) Loparo, J. J.; Roberts, S. T.; Tokmakoff, A. Multidimensional infrared spectroscopy of water. I. Vibrational dynamics in two-dimensional IR line shapes. *J. Chem. Phys.* **2006**, *125*, 194521.

(54) Loparo, J. J.; Roberts, S. T.; Tokmakoff, A. Multidimensional infrared spectroscopy of water. II. Hydrogen bond switching dynamics. *J. Chem. Phys.* **2006**, *125*, 194522.

(55) Woutersen, S.; Hamm, P. Nonlinear Two-Dimensional Vibrational Spectroscopy of Peptides *J. Phys. Condens. Matter* **2002**, *14*, R1035.

(56) Shin, J.-W.; Hammer, N. I.; Diken, E. G.; Johnson, M. A.; Walters, R. S.; Jaeger, T. D.; Duncan, M. A.; Christie, R. A. Infrared Signature of Structures Associated with the $H^+(H_2O)_n$ (n= 6 to 27) Clusters *Science* **2004**, *304*, 1137.

(57) Golonzka, O.; Tokmakoff, A. Polarization-selective third-order spectroscopy of coupled vibronic states *J. Chem. Phys.* **2001**, *115*, 297.

(58) Swanson, J. M. J.; Simons, J. Role of Charge Transfer in the Structure and Dynamics of the Hydrated Proton *J. Phys. Chem. B* **2009**, *113*, 5149.

(59) McGibbon, R. T.; Beauchamp, K. A.; Harrigan, M. P.; Klein, C.; Swails, J. M.; Hernandez, C. X.; Schwantes, C. R.; Wang, L.-P.; Lane, T. J.; Pande, V. S. MDTraj: A Modern Open Library for the Analysis of Molecular Dynamics Trajectories *Biophys. J.* **2015**, *109*, 1528.

(60) Huse, N.; Ashihara, S.; Nibbering, E. T. J.; Elsaesser, T. Ultrafast vibrational relaxation of O–H bending and librational excitations in liquid H2O *Chem. Phys. Lett.* **2005**, *404*, 389.

(61) Ramasesha, K.; De Marco, L.; Mandal, A.; Tokmakoff, A. Water vibrations have strongly mixed intra- and intermolecular character *Nat. Chem.* **2013**, *5*, 935.

(62) Biswas, R.; Tse, Y. L. S.; Tokmakoff, A.; Voth, G. A. Role of Presolvation and Anharmonicity in Aqueous Phase Hydrated Proton Solvation and Transport *J. Phys. Chem. B* **2016**, *120*, 1793.

(63) Berkelbach, T. C.; Lee, H. S.; Tuckerman, M. E. Concerted Hydrogen-Bond Dynamics in the Transport Mechanism of the Hydrated Proton: A First-Principles Molecular Dynamics Study *Phys. Rev. Lett.* **2009**, *103*, 238302.

(64) Yuan, R.; Napoli, J. A.; Yan, C.; Marsalek, O.; Markland, T. E.; Fayer, M. D. Tracking Aqueous Proton Transfer by Two-Dimensional Infrared Spectroscopy and ab Initio Molecular Dynamics Simulations *ACS Cent. Sci.* **2019**, *5*, 1269.

(65) Carpenter, W. B.; Lewis, N. H. C.; Fournier, J. A.; Tokmakoff, A. Entropic barriers in the kinetics of aqueous proton transfer *J. Chem. Phys.* **2019**, *151*, 034501.

(66) Hamm, P.; Stock, G. Vibrational conical intersections in the water dimer *Mol. Phys.* **2013**, *111*, 2046.

(67) De Marco, L.; Fournier, J. A.; Thämer, M.; Carpenter, W.; Tokmakoff, A. Anharmonic exciton dynamics and energy dissipation in liquid water from two-dimensional infrared spectroscopy *J. Chem. Phys.* **2016**, *145*, 094501.

(68) Decka, D.; Schwaab, G.; Havenith, M. A THz/FTIR fingerprint of the solvated proton: evidence for Eigen structure and Zundel dynamics. *Phys. Chem. Chem. Phys.* **2015**, *17*, 11898.

(69) Carpenter, W. B.; Fournier, J. A.; Lewis, N. H. C.; Tokmakoff, A. Picosecond Proton Transfer Kinetics in Water Revealed with Ultrafast IR Spectroscopy *J. Phys. Chem. B* **2018**, *122*, 2792.

(70) Fischer, S. A.; Dunlap, B. I.; Gunlycke, D. Correlated dynamics in aqueous proton diffusion *Chem. Sci.* **2018**, *9*, 7126.

(71) Chen, M.; Zheng, L.; Santra, B.; Ko, H.-Y.; DiStasio Jr, R. A.; Klein, M. L.; Car, R.; Wu, X. Hydroxide diffuses slower than hydronium in water because its solvated structure inhibits correlated proton transfer *Nat. Chem.* **2018**, *10*, 413.

Chapter 8

Entropic Barriers in the Kinetics of Aqueous Proton Transfer

The work presented in this chapter has been published and is reprinted with permission from:
Carpenter, W.B.; Lewis, N.H.C; Fournier, J.A. Tokmakoff, A. Entropic Barriers in the Kinetics of Aqueous Proton Transfer. *Journal of Chemical Physics* **2019**, *151* (3), 034501.

8.1 Abstract

Aqueous proton transport is uniquely rapid among aqueous processes, mediated by fluctuating hydrogen bond reorganization in liquid water. In a process known as Grotthuss diffusion, the excess charge diffuses primarily by sequential proton transfers between water molecules rather than standard Brownian motion, which explains the anomalously high electrical conductivity of acidic solutions. Employing ultrafast IR spectroscopy, we use the orientational anisotropy decay of the bending vibrations of the hydrated proton complex to study the picosecond aqueous proton transfer kinetics as a function of temperature, concentration, and counterion. We find that the orientational anisotropy decay exhibits Arrhenius behavior, with an apparent activation energy of 2.4 kcal/mol in 1M and 2M HCl. Interestingly, acidic solutions at high concentration with longer proton transfer timescales display corresponding decreases in activation

energy. We interpret this counterintuitive trend by considering the entropic and enthalpic contributions to the activation free energy for proton transfer. Halide counteranions at high concentrations impose entropic barriers to proton transfer in the form of constraints on the solution's collective H-bond fluctuations and obstruction of potential proton transfer pathways. The corresponding proton transfer barrier decreases due to weaker water-halide H-bonds in close proximity to the excess proton, but the entropic effects dominate and result in a net reduction of the proton transfer rate. We estimate the activation free energy for proton transfer as ~1.0 kcal/mol at 280 K.

8.2 Introduction

The excess proton is a key species in redox chemistry, where protonic charge transports over macroscopic distances in electrochemical devices,[1,2] biological channels,[3] and catalytic systems.[4] As an aqueous species, its motion is impacted by the fluctuating motions of water's hydrogen bond (H-bond) network. However, since the nineteenth century,[5] measurements of the diffusion of the excess proton revealed that its transport is anomalously rapid, almost five times faster than both the self-diffusion coefficient of water and the diffusion constants of alkali cations.[6] The framework for understanding such a rapid diffusion is described in terms of the Grotthuss mechanism, whereby net charge transport occurs through sequential transfers of individual protons. Reactive proton hops have been modeled in molecular dynamics (MD) simulations, ranging from classical reactive MS-EVB simulations[7,8] to *ab initio* simulations with classical[9] and quantized[10] hydrogen nuclei. Despite the demonstration of Grotthuss diffusion in simulations, a molecular-level understanding of aqueous proton transfer has yet to be experimentally verified.

The complexity of describing these dynamics is compounded by the differing views on the equilibrium structures that the aqueous proton can attain. The solution structure of the aqueous

proton is most commonly described as a hydronium ion H_3O^+, or as a hydronium with a tightly bound first solvation shell, $H_9O_4^+$, known as the Eigen complex.[11] On the other hand, the aqueous proton complex has been described as a proton equally shared between two waters, the Zundel complex, $H_5O_2^+$.[12] The Eigen and Zundel structural motifs can be prepared in cold gas-phase protonated water clusters, but the utility of these terms breaks down in liquid water since the solvation environment has large amplitude thermal fluctuations that break the symmetry of these complexes. Regardless, recent experimental studies emphasize the importance of a proton shared between a pair of flanking waters for describing spectroscopic findings,[13–15] and simulations that describe the aqueous proton species as hydronium-like also invoke language of a "special pair" of waters tightly coordinated around the excess proton.[8] Despite the growing evidence for a broadly two-water description, there is still debate on how to characterize the distribution of possible aqueous proton geometries.[13–15]

We recently collected two-dimensional infrared (2D IR) spectra of HCl solutions that provided evidence that the aqueous proton complex is composed of a proton tightly bound between two water molecules, a configuration we termed "Zundel-like".[16] With spectra spanning 1000-3000 cm^{-1} in excitation and detection frequencies, we found cross peaks between every main vibration at the earliest observable waiting time, implying that there is one dominant motif for the aqueous proton complex, rather than separate Eigen and Zundel complexes in solution. Furthermore, by exciting the asymmetric O-H-O stretching motions of the shared proton at 1200 cm^{-1}, we observed a 1→2 excited state absorption (ESA) at higher frequency than the 0→1 ground state bleach (GSB), indicating a proton stretching potential with steep walls bounding a single well, a clear signature of a Zundel-like complex. The vibrational potential shape does not directly imply that the aqueous proton complex is structurally a strictly symmetric Zundel species,

but the anomalous anharmonicity unequivocally demonstrates that the excess proton is confined by and strongly bound to a pair of flanking waters. Inhomogeneous broadening in both the GSB and ESA beyond the 200 fs lifetime of the aqueous proton stretch implies that the excess proton senses a distribution of microenvironments which persist at least 200 fs. Overall, we concluded that structures of the aqueous excess proton complex consist of persistent Zundel-like species as sensed by the nuclear potential, but the dynamics of this complex require further investigation.

Previous experimental studies of proton transfer have measured important kinetic quantities, spurring further investigation from theory and simulations. From polarographic studies of acidic aqueous solutions with varying concentrations of alkali halide salts,[17] it was determined that the majority of the proton diffusion coefficient arises from a Grotthuss component, and that the addition of salt reduces the magnitude of this component. From a spectroscopic perspective, ^{17}O NMR exchange studies in acidic and basic aqueous solutions concluded that the lifetime of a single hydronium H_3O^+ species is approximately 1.5 ps.[18] Temperature dependence of the related proton transfer rate exhibits Arrhenius behavior with an apparent barrier of 2.4-2.6 kcal/mol.[19–21] These results were synthesized to propose that hydrogen bond rupture in the second shell of hydronium drives the proton transfer process.[22] The proton transfer reaction was interpreted within an Eigen-Zundel-Eigen (E-Z-E) framework, where the Zundel complex serves as a transition state between two stable Eigen configurations. This theory was further studied with the aid of MS-EVB simulations,[7] which concluded that H-bond fluctuations which reduce the coordination of a first-shell water provide an opportunity for a proton to hop to the undercoordinated site. Temperature-dependent calculations of the proton diffusion coefficient obtained a barrier of 2.7 kcal/mol, which is only slightly larger than the value determined by the NMR experiments. *Ab initio* studies also

demonstrated that proton transfer occurs by fluctuation-induced undercoordination of a water adjacent to the hydronium,[9,23,24] naming the mechanism "presolvation."

These experimental and simulation studies have all interpreted proton transfer through Eigen-to-Eigen (E-E) or Eigen-Zundel-Eigen (E-Z-E) mechanisms, and considering the newer evidence for Zundel-like configurations, it is likely that important factors contributing to the mechanism are missing. As has been shown by multiple theoretical studies of aqueous proton transfer, there is a shallow local maximum in the reactive proton's nuclear potential between the two waters. However, the zero-point motion of the excess proton lies above this barrier,[10,14,25] and the amplitude of the maximum diminishes with decreasing oxygen separation.[25] Although this maximum in the potential has sometimes been called the "proton transfer barrier", it should be distinguished from the 2.4 kcal/mol free energy barrier along a collective coordinate that shifts the proton between two stable free-energy minima. Therefore, the rattling and quantum delocalization of the proton between two waters blurs the distinction between two adjacent hydronium species. Despite the recent evidence for persistent Zundel-like geometries in the liquid,[14–16,26] proton transfer between stable Zundel-like configurations has yet to receive attention as a potential proton transfer mechanism.

To study these dynamics, we recently used infrared transient absorption (TA) anisotropy decay to measure the orientational relaxation kinetics of the transition dipole moment of the bending modes of the hydrated excess proton complex, which we refer to as δ_{H^+}.[26] Supported by 2D IR spectroscopy,[16] the δ_{H^+} bending modes at approximately 1750 cm^{-1} were shown to be oriented roughly parallel to the O—O axis of the flanking waters, and TA anisotropy experiments measured δ_{H^+} reorientation kinetics on a 2.5 ps timescale. Because we measured reorientation on a timescale consistent with H-bond rearrangement in liquid water and we could rule out other processes such

as proton rattling,[27,28] we concluded that the anisotropy decay of δ_{H+} resulted from proton transfer events between Zundel-like configurations. Although those measurements are among the most direct observations of aqueous proton transfer kinetics to date, the orientational relaxation rate alone is insufficient to determine the mechanistic details of proton transfer, and processes determining the activation barrier remains to be determined. Furthermore, the influence of the counterion has not been carefully addressed in many proton transfer studies. At high concentration, anions significantly perforate the H-bond network, which may influence the possible paths that proton transfer may take.

To address questions about the mechanism of proton transport in water, we present a study of δ_{H+} reorientation as a function of temperature, acid concentration, ionic strength, and counterion identity. We measure a 2.4±0.2 kcal/mol barrier in 1-2M HCl solutions, which agrees with earlier studies of proton transfer. We find in high concentrations of HCl and in 2M HI that the timescale for proton transfer increases while the apparent activation barrier decreases below 2.0 kcal/mol, a counterintuitive trend that can be rationalized by considering entropic and enthalpic barriers that counterions place on the proton transfer process. We also find that the reorientation timescale grows monotonically with solution viscosity, but sublinearly. These findings all point to proton transfer driven by collective fluctuations of the solution's H-bond network, qualitatively consistent with a slightly modified presolvation mechanism observed in simulations.[23,29]

8.3 Methods

Experimental details pertaining to polarization-sensitive transient absorption (TA) spectra and polarization anisotropy decay are provided in Chapter 3. Samples were prepared using H_2O purified by reverse osmosis and ion exchange to 18 MΩ·cm resistivity (Millipore, *Milli-Q*). HCl solutions of concentrations of 1M−4M were prepared by serial dilution from a stock solution of

concentrated HCl (37% by mass, Sigma-Aldrich). To control for possible effects of the counterion, 2M HI was prepared also from concentrated solutions (57% by mass, *Sigma-Aldrich*). Control solutions of 1M, 2M, and 4M NaCl were prepared from the crystalline form (*Fisher*). Samples were held between two 200-μm thick CaF_2 windows (*Crystran*) with 3.6 μm Mylar spacers such that the absorbance of the H_2O bend was approximately 1 OD. 4M solutions were collected without a spacer due to large linear absorption from the bending modes of bulk water and the aqueous proton complex. FTIR measurements (*Bruker Tensor 27*) were taken with 1 mm CaF_2 windows and 6 μm Mylar sample spacers (Fig. S1 in the SI). Samples were held in a brass sample cell plumbed to a chiller (*Huber Ministat 125*) set from 5.0-55.0°C in steps of 10°C. Temperatures at the sample in the FTIR and transient absorption setups were measured with a thermocouple *(Phidgets)*, resulting in a sample temperature range of 8.1-50.0°C and 6.3-52.0°C, respectively.

Kinematic viscosity was measured with an Ubbelohde U-tube viscometer (*Cannon*) in a water bath with temperature control of ±1°C. Viscosity values were measured twice for each acid solution at each of the six temperatures, with differences less than 1% between measurements. Dynamic viscosities were determined by dividing measured kinematic viscosities with tabulated densities of HCl and HI solutions.[30,31]

8.4 Results

8.4.1 Infrared Spectroscopy of the Proton Hydration Bending Modes δ_{H^+}

In the FTIR spectrum of 2M HCl (Fig. 8.1), δ_{H^+} appears as a component of the "proton continuum" of IR absorption intensity around 1700-1800 cm^{-1}. After subtraction of the water background, it appears as a broad yet distinct feature centered at 1750 cm^{-1}, and as a depletion of the bulk water bend at 1650 cm^{-1}. We previously demonstrated with 2D IR spectroscopy that δ_{H^+} is a separate vibration from the bend of neutral water molecules (δ_{H2O}), most clearly shown as two

peaks on the diagonal of the 2D IR spectrum rather than a single inhomogeneously broadened feature[26] (Fig. 5.4). Our previous simulations of the IR spectrum of aqueous acid solutions concluded that the δ_{H+} resonance is composed of multiple types of HOH bending modes within the protonated water complex that are strongly mixed with each other and other vibrations of the complex, in a manner that depends on the varying geometries of the protonated water complex.[32]

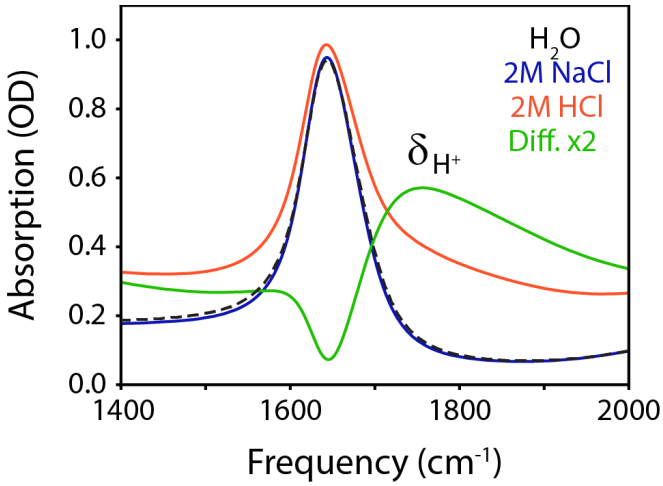

Figure 8.1: FTIR spectrum of H_2O (dashed black), 2M NaCl (blue), 2M HCl (red), and the 2M HCl–2M NaCl difference (green). The bending modes of hydrated proton complexes, δ_{H+}, are contained in the feature centered at 1750 cm^{-1}.

With this knowledge of the nature of the δ_{H+} band, we present the polarization-resolved transient absorption (TA) spectra of 2M NaCl and 2M HCl at 5˚C in Fig. 8.2. In 2M NaCl, the bleach of the H_2O bend δ_{H2O} ($\omega_3 = 1650$ cm^{-1}) decays within 200 fs in the parallel and perpendicular spectra (Figs. 8.2a and 8.2b) and the hot ground state (HGS) grows in with a 1 ps timescale. Briefly, the HGS represents the change in IR absorption that arises from deposition of vibrational energy from the excited H_2O bend into low-frequency modes. For δ_{H2O}, the HGS appears as an increase of absorption around 1630 cm^{-1}, flanked by an absorption loss around 1700 cm^{-1} which agrees with the narrowing and intensity gain of δ_{H2O} observed in 2M NaCl as temperature increases. While the TA spectrum of the bend HGS appears as a temperature-difference FTIR profile, it is a non-equilibrium signature that arises due to the effect of weakened

H-bonds on the system's vibrations (Chapter 4, Section 4.5.4). The parallel and perpendicular spectra of 2M NaCl appear nearly identical beyond 200 fs, consistent with the 80 fs TA anisotropy decay measured for the H_2O bend (Fig. 4.6).[33] This ultrafast anisotropy decay is due to the delocalized nature of the water bend, which allows fast excitation transfer and orientational scrambling between water bending modes. There is a clear window between ω_3 = 1720 cm^{-1} and ω_3 = 1820 cm^{-1} where signal from H_2O is weak.

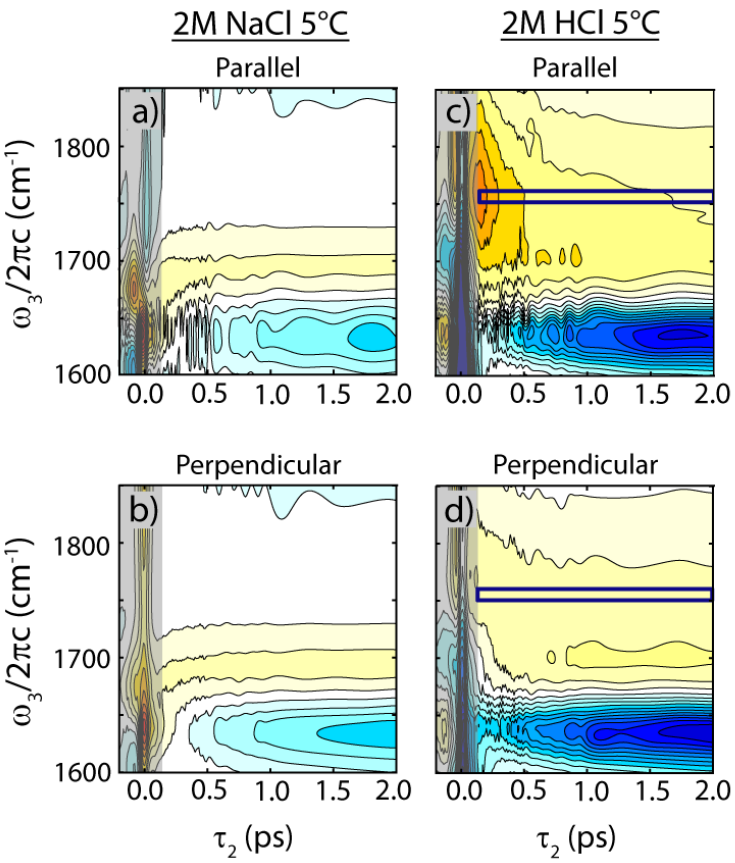

Figure 8.2: TA spectra of (a)-(b) 2M NaCl and (c)-(d) 2M HCl at 5˚C for various pump-probe polarization schemes. Bleaches are presented in orange, and induced absorptions are presented in blue. Surfaces are on a common normalization to the maximum amplitude of the isotropic 2M HCl spectrum at 10 ps. In all spectra, the signal at τ_2 = 0 fs and all ω_3 is instantaneous polarization response from the solution and the CaF_2 windows. Grayed out regions indicate waiting times before τ_2 = 200 fs, which are omitted from analysis. The colored boxes in (c) and (d) represent the frequency range ω_3 = 1750-1760 cm^{-1} analyzed in this study.

The parallel TA spectrum of 2M HCl at 5˚C (Fig. 8.2c) displays a prominent, broad bleach centered at ω_3 = 1750 cm^{-1}, arising from the bending vibrations of the hydrated proton complex (δ_{H+}).[13,26,32,34] Because of the clear frequency window in the 2M NaCl TA spectrum (Figs. 8.2a and 8.2b), the feature here arises solely from the hydrated excess proton. The amplitude of this feature is strongly polarization-dependent, as seen in the difference between the parallel and perpendicular surfaces (Figs. 8.2c and 8.2d, respectively). The δ_{H+} bleach in the parallel spectrum quickly relaxes within hundreds of fs, followed by a slower secondary decay within the first 2 ps. Even though the perpendicular surface does not display such a prominent bleach feature at early waiting time, both the parallel and perpendicular spectra of δ_{H+} reach a constant bleaching offset at late waiting times, corresponding to the hydrated proton's HGS signal. The isotropic 2D spectrum of δ_{H+} (Fig. 5.4) demonstrates similar fast decay of the early-time signal and slower rise of the HGS.

To quantify the dynamics of δ_{H+} excitations, we present the normalized isotropic and anisotropic TA traces at a detection frequency of ω_3 = 1750 cm^{-1}. In the isotropic spectrum, we correct for the long-time constant offset due to the HGS, $S_{Iso}(\infty)$, by normalizing it with the following expression

$$\Delta S_{Iso}(\tau_2) = \frac{S_{Iso}(\tau_2) - S_{Iso}(\infty)}{S_{Iso}(200\text{ fs}) - S_{Iso}(\infty)}, \tag{8.1}$$

For all TA traces in this study, we only analyze data beyond τ_2 = 200 fs due to residual nonresonant response from the sample windows. The isotropic trace in Fig. 8.3a demonstrates that the population relaxation of δ_{H+} follows exponential decay kinetics with a τ_{Iso} = 280 fs time constant. There is a small drop below S_{Iso} at τ_2 = 2 ps, which may result from a growing HGS signal, but its amplitude is too small compared to the noise to be reliably captured by a least-squares fit to a biexponential decay. In Fig. 8.3a, we also present the anisotropic trace, which persists more than

an order of magnitude beyond the δ_{H+} vibrational lifetime. The anisotropic trace is better fit by a biexponential decay with a fast timescale on the order of 200 fs and a slower, multi-ps decay such that the anisotropic trace is not fully decayed until 10 ps. For comparison, δ_{H2O} the anisotropy decay of δ_{H2O} in water (Fig. 4.6b) displays negligible anisotropic kinetics beyond 200 fs.

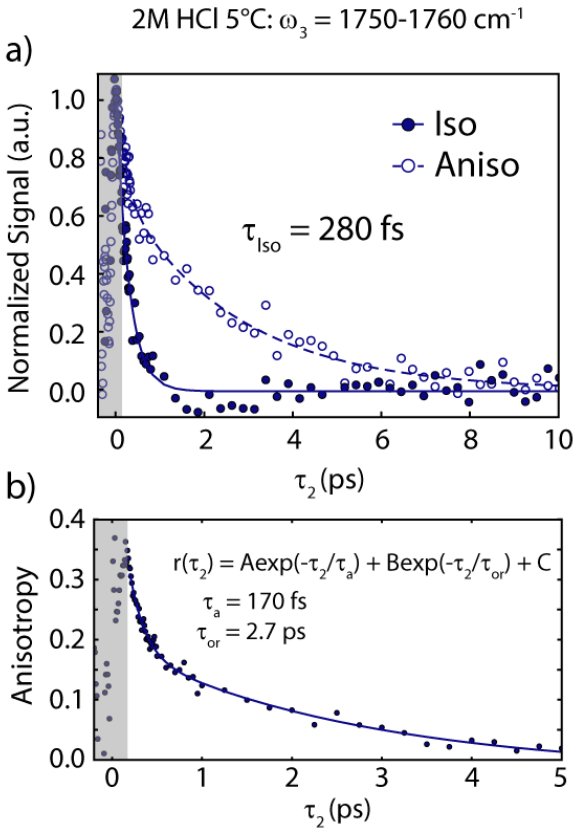

Figure 8.3. TA isotropic and anisotropic traces, and TA anisotropy of δ_{H+} in 2M HCl at 5˚C at ω_3 = 1750-1760 cm^{-1}. (a) Normalized isotropic and anisotropic TA traces from τ_2 = 200 fs to 10 ps, the latest measured waiting time. The isotropic trace is normalized and corrected for the hot ground state value at long waiting time according to Eq. 8.1. The anisotropic trace is normalized to the value at τ_2 = 200 fs, but not corrected for a long-time offset. (b) TA anisotropy decay after τ_2 = 200 fs, fit to a biexponential decay (solid line). Grayed regions denote waiting times excluded from analysis due to instrument response and interference from window nonresonant response. Together, these demonstrate that the anisotropic signal persists longer than the isotropic signal, but decays to zero by 10 ps.

The isotropic TA trace reports on vibrational population relaxation, and decays with a 280 fs decay timescale to a constant offset, similar to the vibrational relaxation of the H_2O bend

(Fig. 4.5).[33] We have previously examined the extent of delocalization of the bending modes of both the proton hydration complex[32] and water (Fig. 4.8),[33] revealing that both modes involve delocalization over approximately 20 atoms as a result of strong anharmonic coupling induced by the H-bond network. Even though the excess proton introduces a charge and H-bonding defect, the similar relaxation timescales, large anharmonicities, and delocalization of both bends suggest similar vibrational relaxation pathways to the H_2O bend in neutral water.[33,35] We propose, then, that bending excitations of the proton hydration complex rapidly relax within the manifold of bending vibrations of the complex and/or to strongly coupled adjacent water bends with the assistance of dissipation to other intermolecular degrees of freedom.

We next calculate the TA anisotropy decay $r(\tau_2)$ of δ_{H+} by taking the ratio of the anisotropic and isotropic TA traces (Fig. 8.3a) at 5°C after $\tau_2 = 200$ fs (Fig. 8.3b), which is well fit by a biexponential decay with fast and slow timescales of $\tau_a = 170$ fs and $\tau_{or} = 2.7$ ps, respectively. Near $\tau_2 = 0$ fs, the anisotropy is less than 0.4 because of the nonresonant polarization response of the CaF_2 windows[36] that interferes with early-time transient δ_{H+} signal. The 170 fs anisotropy timescale is too rapid for physical reorientation but could be consistent with an energy transfer mechanism or partial orientational relaxation due to solvent fluctuations, which we will further discuss below. On the other hand, the picosecond component is expected for H-bond exchange and physical reorientation. Anisotropy decay curves in 2M HI and HCl solutions of various concentrations exhibit similar biexponential relaxation behavior. As an independent way to quantify the anisotropy kinetics, we applied a simultaneous fit to the parallel and perpendicular traces at $\omega_3 = 1750$ cm^{-1}, which are consistent with the results from the anisotropy fit but assist in determining the uncertainty of the extracted timescales. We also collected the 2D IR anisotropy surfaces of δ_{H+} in 2M HCl (Fig. 5.5) for multiple waiting times between $\tau_2 = 100$ fs and $\tau_2 = 10$ ps

to demonstrate that the anisotropy of the neutral water bend δ_{H2O} vanishes by 200 fs and contributes only a small amount to the total anisotropy at $\omega_3 = 1750$ cm^{-1}.

The HGS, which arises from nonthermal energy deposition from the excited vibration into the coupled low-frequency, intermolecular modes of the solvent, grows in on a somewhat slower 800 fs timescale and persists beyond 100 ps.[33,37] Spectroscopically, the transient HGS signal can be considered a ground state bleach since it represents the depletion of molecules from the equilibrium state, and shifted into a kinetically "heated" ground state. Interestingly, we observe that the anisotropy relaxation of δ_{H+} is encoded in the HGS beyond the δ_{H+} lifetime. The persistence of anisotropic signal out to 10 ps is particularly unusual for an aqueous system because previous measurements of HGS signal had not detected polarization dependence within experimental signal-to-noise,[33,37–39] but HGS anisotropy was observed in hydroxide solutions.[40] For δ_{H+}, the presence of an anisotropic HGS signal reflects anisotropic energy deposition within the aqueous proton complex that are encoded into the HGS signal similar to the anisotropy encoded in conventional ground state bleach TA signals. This anisotropy is retained until vibrational or chemical dynamic processes fill this anisotropic "hole". By contrast, the common isotropic HGS signals reflect the fact that the anisotropy of initially excited modes decays much more rapidly than the approximately 800-fs rise of the HGS signal, which is the case in pure H_2O.[33,37,41] In 2D anisotropy measurements (Fig. 5.5), we observe that this persistent anisotropy is distributed relatively evenly across the entire δ_{H+} HGS spectrum. It appears, though, that in spectral regions which are primarily due to bulk water, such as at $\omega_3 = 1620$ cm^{-1} and $\tau_2 = 500$ fs, the overlap of large isotropic bulk HGS and δ_{H+} HGS results in a lower overall anisotropy.

In Fig. 8.4a, we illustrate the temperature dependence of the δ_{H+} anisotropy decay with curves from a few representative temperatures. Qualitatively, the amplitude of the fast anisotropy

decay component appears to diminish and the slow component decays more rapidly with increasing temperature (Fig. 8.4a). These observations are quantified in Figs. 8.4b and 8.4c. While the fast timescale τ_a is independent of temperature within experimental uncertainty, the slower timescale τ_{or} decreases with increasing temperature. The vibrational lifetime of δ_{H+} does not show a clear trend with temperature, however. As seen in Fig. 8.4c, the amplitude of the fast component slightly decreases (although this weak trend lies within the range of experimental uncertainty) and the slow component amplitude steadily grows in with increasing temperature until only the slow component is experimentally detectable at 52°C. However, for all temperatures the anisotropy values at τ_2 = 200 fs are consistently 0.34 ± 0.02.

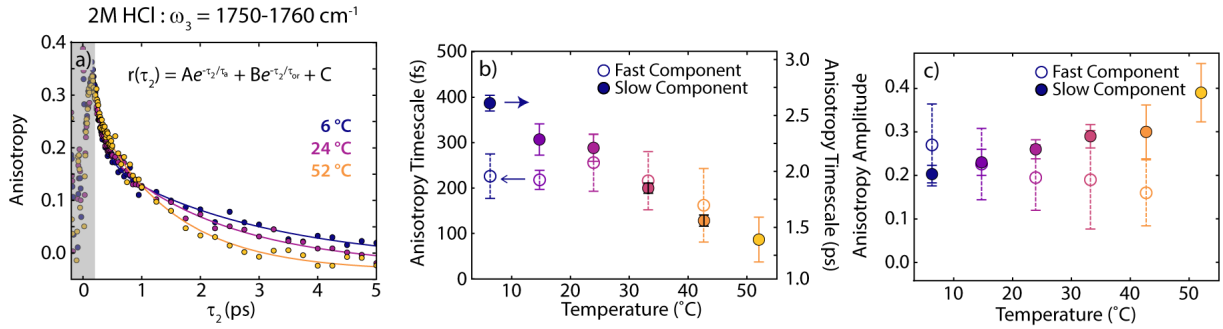

Figure 8.4. Temperature-dependent changes in the pump-probe anisotropy decay at ω_3 = 1750-1760 cm^{-1}. (a) Pump-probe anisotropy decays of 2M HCl at three representative temperatures across the temperature range used in this analysis. Grayed regions denote waiting times excluded from analysis due to instrument response and interference from window nonresonant response. (b) Fast (open circles, left vertical axis) and slow (closed circles, right vertical axis) timescales extracted by biexponential fits to the normalized anisotropy decays. The fast timescale at 52°C is omitted because the amplitude of the fast component was not experimentally significant within signal-to-noise. (c) Amplitudes of the two components of the anisotropy decay from 6-52°C. Error bars represent standard deviations in timescales and amplitudes determined from multiple measurements and two fitting procedures.

8.4.2 Dependence of the Slow Anisotropy Timescale on Temperature, Ionic Strength, and Solution Viscosity

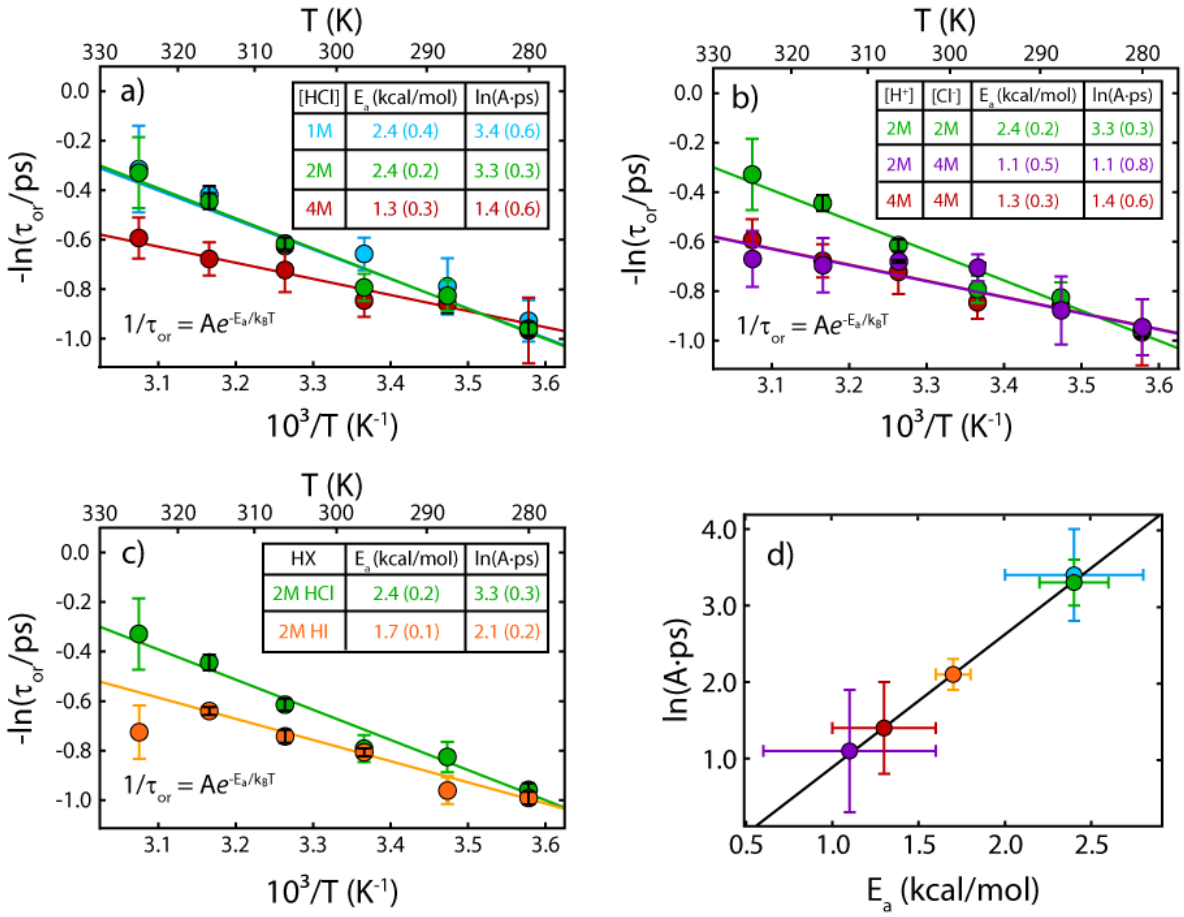

Figure 8.5. Arrhenius plots of the slow anisotropy timescale τ_{or} for δ_{H+} anisotropy decay. (a) 1M, 2M, and 4M HCl; (b) 2M HCl, 4M HCl, and 2M HCl/2M NaCl; (c) 2M HCl and 2M HI. (d) Correlation between activation energy E_a and rate prefactor A, where colors of the points indicate the corresponding solutions from (a)-(c). Error bars on timescales represent their standard deviations. Errors on the activation energy E_a and intercept are standard deviation errors on the fits determined by least-squares analysis.

Arrhenius plots for the slow timescale of the anisotropy decay in various acid solutions are presented in Fig. 8.5. For these solutions, the slow component displays Arrhenius behavior, $\tau_{or}^{-1} = Ae^{-E_a/k_BT}$, with low activation energies that vary with acid concentration and counterions. Beginning with the concentration dependence in Fig. 8.5a, in 1M and 2M HCl the timescales are

nearly identical within experimental uncertainty and they display apparent activation energies E_a = 2.4 ± 0.4 kcal/mol and 2.4 ± 0.2 kcal/mol, respectively. In 4M HCl solution, the anisotropy timescales are consistently slower for all temperatures, but the barrier decreases to 1.3 ± 0.3 kcal/mol. Slower anisotropy decays in higher-concentration solutions are consistent with the slowing of water reorientation in NaCl solutions observed with pump-probe anisotropy studies of NaCl in HOD/H_2O.[42] This behavior can be contrasted with previous studies on NaOH solutions that observed faster anisotropy decays with increasing concentration,[40] which may reflect a different interplay of anisotropy decay mechanisms and solvation dynamics around aqueous proton and hydroxide complexes.[43]

To test whether the decrease in E_a was due to acid concentration or chloride concentration, we measured a barrier for the anisotropy decay in a solution of 2M HCl/2M NaCl (Fig. 8.5b), agreeing with the timescales and the barrier in 4M HCl within experimental uncertainty. These results suggest that the anisotropy decay timescales and barrier depend on the concentration of the counterion in solution, more so than the concentration of $H^+(aq)$. The role of the anion is further reinforced by the results in 2M HI, where the substitution of the counterion slows down anisotropy timescales and lowers the activation barrier to 1.7 ± 0.1 kcal/mol (Fig. 8.5c).

Comparing all of the solutions studied we find a consistent and counterintuitive trend where solutions with lower activation barriers for δ_{H+} reorientation also have slower reorientation rates (Fig. 5D.3). Summarizing the temperature-dependent anisotropy results for all studied solutions, we find a linear relationship between the activation barriers of each solution with the natural logarithms of their pre-exponential factors (Fig. 8.5d), indicating competing trends in these two factors. Curiously, Fig. 8.5 shows that at approximately 280K the anisotropy timescales are independent of the solvent conditions we studied, and therefore the activation free energy is also.

The anisotropy decay activation energies in all solutions are low (on the order of 3-5 k_BT), and they are comparable to the barrier height of 3.7 kcal/mol for HOD reorientation in H_2O.[44] It is important to note, though, that the δ_{H+} reorientation barriers are consistently lower than the barrier in neat water, and the barriers are further reduced upon addition of ions to the solution. Since reorientation of bulk water molecules involves the concerted switching of multiple hydrogen bonds within the liquid,[45] it is also likely that the reorientation process of δ_{H+} is related to H-bond reorganization dynamics.

To further investigate the influence on liquid structural relaxation on the anisotropy decay, we tested whether the relationship between solution viscosity η and the slow anisotropy timescale τ_{or} follows the Stokes-Einstein-Debye (SED) equation, $\tau_{or} = \eta V_h/k_BT$, where V_h is the effective hydrodynamic volume. Viscosities of each of the solutions were measured as a function of temperature, and we plot all τ_{or} versus the corresponding η/T in Fig. 8.6. As a point of comparison, we also present the reorientation timescale of water molecules in bulk water measured using isotopically dilute HOD in H_2O[44] as a function of H_2O viscosity.[46] Water molecule reorientation and the viscosity in neutral water are observed to follow a linear trend, implying that they both depend on similar collective H-bond rearrangement dynamics of the liquid.[44,47–49]

Remarkably, for the HCl solutions, the orientational relaxation is significantly faster than for the anisotropy relaxation due to H-bond switching in the neat liquid. The δ_{H+} anisotropy timescale increases with solvent viscosity, from a value of ~1.3 ps (20% faster than bulk water) at low viscosity to a maximum value of ~2.5 ps at high viscosity. Qualitatively, this curvature tracks a viscosity scaling dependence of $\tau_{or} \sim \sqrt{\eta}$. 1M and 2M HCl solutions lie on the same trend curve, and the 2M HI trend exhibits similar curvature, although offset to lower viscosities and longer timescales. Comparing HCl and HI again illustrates a nonintuitive trend, in which the viscosity

and δ_{H+} orientational relaxation times at fixed temperature are negatively correlated, rather than the expected slowing of orientational relaxation in more viscous solutions.[17] The two separate trends provide evidence that the identity of the counterion, as a component of the solution, influences the δ_{H+} reorientation mechanism at high concentration.

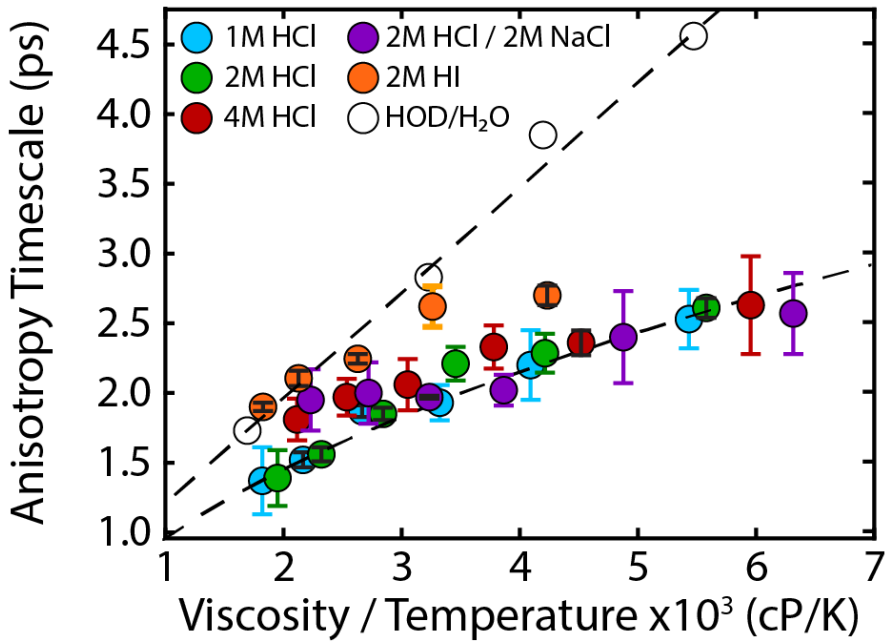

Figure 8.6. Stokes-Einstein-Debye plot of the slow δ_{H+} anisotropy decay timescale. Multiple points from the same solution originate from repeated measurements at different temperatures. Error bars in the timescales are standard deviations calculated from the measured values. Uncertainties in measured viscosities are within 1% of the mean values, and thus are not shown. HOD/H_2O anisotropy and H_2O viscosity data are from Refs. 38 and 39, respectively. Dashed lines correspond to linear and square-root fits to neat H_2O and 1-2M acid data, respectively.

8.5 Discussion

8.5.1 Relating Anistropy Decay to Proton Transfer

The TA anisotropy decay of the δ_{H+} transition dipole moment is well described by biexponential kinetics with a temperature-independent 200 fs timescale and a temperature-dependent timescale on the order of 2-3 ps (Fig. 8.4a). Anisotropy decays describe the loss of orientational alignment of the initial excitation, which in water and aqueous solutions are

commonly attributed either to physical reorientation of the transition dipole moment, or to energy transfer or excitonic coupling between quasi-degenerate transition dipole moments with different orientations. The 200 fs timescale is much faster than the structural relaxation of the liquid, and therefore inconsistent with molecular reorientation. As described previously, we do not expect that structural fluctuations around the aqueous proton such as O—O compression are significant enough to irreversibly alter the orientation of the bend dipole to a substantial degree.[26] Furthermore the timescale of the fast anisotropy decay component does not show a clear trend with temperature, and its amplitude decreases with increasing temperature. This is inconsistent with orientational fluctuations, whose amplitude is expected to increase with temperature.

It is more likely that the 200 fs anisotropy decay arises from energy transfer or excitonic coupling with other modes instead of reorientation of a single transition dipole. One can rule out intermolecular energy transfer to nearby hydrated proton complexes because the fast timescale shows no trend with HCl concentration. Because there is substantial non-zero anisotropy beyond a few hundred fs, the 200 fs anisotropy decay mechanism retains some orientational correlation, unlike in highly delocalized and excitonically coupled vibrations such as the O–H stretch or HOH bend in neat water.[33,37,50,51] The high anisotropy at τ_2 = 200 fs indicates that the δ_{H^+} excitation is more localized than the excitonic δ_{H2O} modes of the solvent. This suggests an anisotropy decay mechanism involving coupling within the aqueous proton complex. Given the multiple types bending vibrations resonant at 1750 cm^{-1} that vary with intermolecular configuration and are anharmonically mixed with the proton stretching modes,[32] excitation exchange between different bending vibrations within the same hydrated proton complex could then lead to partial loss of anisotropy. At present we believe this is the best explanation. A similar conclusion was also reached for a 200-fs anisotropy decay component seen in the TA kinetics of aqueous hydroxide

O–H stretches.[40] It remains unclear why the amplitude of the fast anisotropy component does not change significantly with increasing temperature.

Looking now at the slower activated kinetics, the picosecond anisotropy component reports on the reorientation of the hydrated proton complex as a result of proton transfer. From HCl concentration trends, we previously ruled out other anisotropy decay mechanisms such as intermolecular energy transfer and orientational diffusion of the protonated water complex without proton transfer.[26] The anisotropy relaxation time is also similar to the timescale for H-bond rearrangement in neat water, which is consistent with solvent reorganization playing a role in proton transfer.[7,22,23,29] Since the transition dipole moment of δ_{H+} aligns approximately parallel to the proton stretching mode (Figs. 5.12 and 5.17),[16] these observations indicate that the δ_{H+} anisotropy relaxation arises from proton transfer via Grotthuss diffusion in which the identity of the pair of flanking waters and the orientation of the proton stretching mode has changed. The 2.5 ps orientational relaxation timescale is similar to NMR measurements of 1.5 ps proton exchange times,[18,19] although we note that orientational and exchange kinetics are not directly comparable (Section 2.5.1).

In addition to the ps timescale, the activation energies presented here provide corroborating evidence that we measure proton transfer kinetics with the δ_{H+} anisotropy decay. The 2.4 kcal/mol activation barrier for δ_{H+} reorientation in 1M and 2M HCl has been obtained before in acidic solutions with NMR spectroscopy[18–20] (2.4-2.6 kcal/mol) and in simulations of excess charge diffusion (2.7 kcal/mol).[7] The similarity of barrier heights indicates a unifying origin.[44,52] As further evidence, δ_{H+} reorientation timescales in this study also increase with ionic strength, although with a much weaker dependence than bulk proton diffusion.[17] Altogether, the reorientation of δ_{H+} appears to be a reliable reporter of proton transfer kinetics. We note that there

is also a 2.7 kcal/mol process associated with H-bond dynamics in water and HCl solution that has been measured with optical Kerr effect (OKE) spectroscopy,[53] but the corresponding timescale is approximately 400 fs, which is inconsistent with predicted proton transfer timescales.[19,23]

8.5.2 Collective Solvent Dynamics Drive Proton Transfer

One may expect that the activation energy for aqueous proton transfer would be higher than that for H-bond reorganization in neat H_2O due to the strong, contracted H-bonds formed between the proton's hydration complex and its solvation environment,[24] but we find a barrier height that is at least 1 kcal/mol smaller. The viscosity-anisotropy trends demonstrate the different H-bonding motions that influence water H-bond exchange and proton transfer. At low viscosities, the proton transfer timescale in 1M and 2M HCl is comparable to the H-bond reorganization timescale in neat water, which suggests that proton transfer is driven by similar H-bonding rearrangement processes. However, at higher viscosities when the H-bond network becomes more rigid, proton transfer can occur almost twice as rapidly as water hydrogen bond reorganization. Additionally, the proton transfer timescale appears to plateau with increasing viscosity, which implies that proton transfer is less sensitive to the type of collective H-bond reorganization that is reported on in viscosity measurements. Regardless, the monotonic rise of the proton transfer anisotropy timescale with viscosity and a barrier on the same energy scale with H-bond reorganization in water points to a proton transfer process influenced by H-bond dynamics.

Aqueous H-bond rearrangement is highly collective, involving multiple molecules traversing different paths between configurations with varying barrier heights (~4-5 kT at 300 K).[54–57] Collective motions of neat liquid water have previously been observed by inherent structure analysis and Markov state modeling to explain the low barrier and non-Arrhenius behavior of H-bond reorganization in neat water.[54–56,58] Notably, it was also found that the timescales of H-bond

exchange do not necessarily correlate with the number of waters participating in the exchange, which implies that the fastest H-bonding fluctuations need not be the most localized. In the context of aqueous proton transfer, the sensitivity of the timescale and barrier on the identity of the halide anion at 2M suggests that this process involves H-bonding fluctuations spanning several water molecules, rather than just the water molecules in immediate proximity to the aqueous proton complex.

8.5.3 Entropic Penalties in the Proton Transfer Barrier

We find a counterintuitive trend that for solvent conditions that decrease the activation energy, the proton transfer rate correspondingly decreases. Our observed proton transfer rates do not follow common trends for kinetic salt effects or other dielectric properties of inert electrolyte solutions. The primary kinetic salt effect on ion reactions from Debye-Hückel theory predicts an increase of reaction rate with ionic strength,[59] which—although a weak trend—is opposite to what we observe. Also predicted is a decrease in rate with solvent dielectric constant as $(\epsilon_0 k_B T)^{-3/2}$ but the bulk dielectric constant of water decreases with increased ionic strength. Both of these factors would increase the rate with ionic strength by stabilizing electrostatic interactions between the transition complex and inert anions in solution. To explain our observations, it is important to consider other potential factors contributing to the proton transfer rate.

Qualitatively, we can interpret the trend with the Eyring equation for activated kinetics,

$$\tau_{or}^{-1} = k_0 e^{\Delta S^{\ddagger}/k_B} e^{-\Delta H^{\ddagger}/k_B T} \tag{8.2}$$

where $k_0 = k_B T/h$ for simple unimolecular processes but includes other factors such as the transmission coefficient κ. In this framework, relaxation times can increase even with a decrease in the activation enthalpy $\Delta H^{\ddagger}$ if there is a competing decrease in the activation entropy $\Delta S^{\ddagger}$.

Correlating the enthalpic and entropic terms of the Eyring equation with E_a and ln(A) of our Arrhenius analysis, these competing effects are apparent in the linear growth in Fig. 8.5d. Similarly, we observe that relaxation rates for all solutions are approximately the same at 280K, although the activation energies vary. Applying Eq. 8.2 gives an activation free energy at 280K of $\Delta G^{\ddagger}$ = 1.0 kcal/mol or 1.7 $k_B T$, and $\Delta S^{\ddagger}$ as roughly 1-5 cal/(mol·K) across the various solutions, decreasing with ionic strength. The values of $\Delta S^{\ddagger}$ are approximate because of the various possible terms in the pre-exponential for a solution-phase reaction, but the overall trend of decreasing activation entropy with ionic strength explains the decreasing proton transfer rate despite the reduction in the apparent barrier.

In solution there are multiple microscopic processes that would contribute to the decrease in the activation entropy. A significant contributor is the influence of the counteranions, which introduce local and global effects, according to simulation studies. On the local scale, the excluded volume created by solvated ions obstructs the approach of potential waters that could donate H-bonds to waters in the ions' solvation shells.[60] The significant presence of halide anions in solution also reduces translational degrees of freedom of the solvent molecules, which increases solution viscosity. While these effects have only a modest impact on water dynamics at low concentration, at high concentration the majority of waters are incorporated into the first two solvation shells of dissolved solutes. As a result of both local and global effects, excluded volume reduces the number of possible H-bonding configurations and H-bond exchange pathways. These decrease the activation entropies for H-bonding dynamics and also manifest as slowed down collective H-bonding fluctuations.

Applied to proton transfer, these effects are apparent in the lower prefactors obtained for the high-concentration chloride solutions (Fig. 8.5d). Global H-bonding defects and the local excluded

volume from counterions reduce the H-bond connectivity between waters, reducing the probability of successful proton transfer attempts by the Grotthuss mechanism. The local-scale H-bonding defects around counterions result in terminations of "water wires" at the anion and reduce the number of waters that are fully hydrated, which decrease the number of successful proton transfer events. Indeed, simulations of 4M HCl indicate that roughly 30% of chlorides are in contact with the water carrying the excess charge.[61] On top of this, global retardation of H-bonding fluctuations additionally slows down the frequency of proton transfer attempts. In HI solution, proton transfer rates are slower compared to equimolar HCl since iodide's larger solvation shells incorporates more water into its H-bonding defect. Our observations are in line with MS-EVB simulations of concentrated HCl and mixed HCl/NaCl solutions, where increased acid concentration and increased ionic strength impede proton migration.[62] These simulations suggest that ionic crowding reduces the likelihood of full hydration around the excess proton, but instead results in rattling between water molecules.

The diminished proton transfer activation enthalpies in high-concentration solutions likely arise from the collective effect of relatively weak H-bonding to the counteranions and their solvation waters. NMR studies of aqueous salt solutions estimate that the barrier to break a H-bond decreases as the acceptor changes from H_2O (3.5 kcal/mol) to Cl^- (3.3 kcal/mol) to I^- (2.7 kcal/mol).[63] Even though the strength of a single H-bond donated from a first shell water to the anion is only slightly less than a H-bond between two waters, it is possible that if a large fraction of waters are taken up by counterions, then collective H-bond motions involving multiple first-shell waters would require less energy to weaken the H-bonds necessary for successful proton transfer. Therefore, compared to 1M and 2M HCl, the activation enthalpy in 4M HCl would decrease, where proton and chloride solvation shells overlap. In 2M HI, where iodide retains

almost double the amount of first-shell waters compared to chloride, would also show a decreased proton transfer activation enthalpy.

8.5.4 Challenges and Hypothesized Picture of Proton Transfer Dynamics

There are still challenges associated with understanding proton transfer in water. In particular, H-bonding dynamics appear to manifest differently around the aqueous proton than in neat water, as seen with different barrier heights and timescale-viscosity trends. Clearly analyzing these H-bonding motions will be instrumental in providing context to coordinates predicted to drive proton transfer, such as O—O compression,[57] fluctuations in solvent electric field,[64,65] and H-bond imbalance.[7,66] Given the important role played by counterions, it will also still be necessary to better understand how collective H-bonding dynamics and barriers are perturbed in salt solutions.

Proton-anion pairing at high concentration may play a key role in proton transfer in high-concentration solutions, but its influence is unclear. In high-concentration solutions like 4M HCl, ion pairing likely alters the speciation of the aqueous excess proton compared to the bulk. Significant populations of proton-anion contact ion pairs have been observed in simulations and experiments in high-concentration HCl and HNO_3 solutions,[61,66,67] which have suggested a preference for asymmetric hydronium-like geometries next to the anion.[14,16] Altogether, possible alternative H-bonding topologies and Grotthuss diffusion pathways influence how measured proton transfer rates and barriers could be analyzed. The impact of these effects on the data in this study are unclear, however, because relatively longer timescales and lower barriers are present in 2M HI, which is a stronger acid and less likely to form ion pairs.

There is also still some ambiguity in the relationship between the timescale for δ_{H+} anisotropy decay and the proton transfer rate. Part of this stems from the variety of bending motions of the aqueous proton complex. The δ_{H+} band is relatively insensitive to the configuration of the aqueous

proton complex, and there are multiple bending vibrations in the 1750 cm^{-1} band within a given complex.[32] Furthermore, these modes delocalize over multiple molecules and strongly mix with other modes such as the proton stretch. A question is how much proton transfer reorients the hydrated proton complex and the associated δ_{H^+} transition dipole angle, which could form the basis for jump reorientation analysis such as has been done for water and ionic solutions.[68–70]

Even though atomistic characterization of the proton transfer process is ongoing, we can still infer new aspects about the mechanism and hypothesize a rough picture for proton transfer. The hydrated proton and its flanking pair of waters can be characterized by its distinctive H-bonding topology in which every H-bond to the solvent is donated.[9,66] Grotthuss diffusion can then be viewed as the structural diffusion that translocates the H-bonding anomaly through water hydrogen bond switching in its solvation shell. This picture is similar to the proposed "presolvation" mechanism for Grotthuss diffusion,[9,23] whereby proton transfer occurs by the donation of a H-bond to the aqueous proton complex and the concerted rupture of an accepted H-bond on an adjacent water. At high concentrations, counterions impose entropic penalties to this collective H-bond exchange process and obstruct possible pathways that lead to proton transfer. Combined with previous evidence for significant Zundel-like configurations in aqueous solution,[14–16,26] we hypothesize that the presolvation mechanism would involve proton transfer between two Zundel-like species where the identity of protonated $O\text{-}H^+\text{-}O$ triplet has migrated to a new pair of adjacent waters. However, more direct measurement of interchange between equilibrium structures will be necessary to determine which structures interconvert during proton transfer.

8.6 Conclusion

In this study, we have analyzed the temperature- and counterion-dependence of the anisotropy decay of the bending modes of proton hydration complexes to characterize the solvent-dependent

dynamics of aqueous proton transfer. We found that the anisotropy decay of δ_{H+} is well-modeled by a biexponential decay, corresponding to a fast (~200 fs) energy transfer process between bending modes within the same excess proton complex and a slower timescale (~2-3 ps) associated with reorientation due to proton transfer between Zundel-like species. In 1M and 2M HCl, the slower component shows Arrhenius behavior with an apparent activation energy of 2.4 kcal/mol, which is consistent with previous measurements of proton transfer and with collective H-bonding dynamics in water. We find that for solutions where the activation enthalpy decreases, there is a corresponding decrease in the overall proton transfer rate due to decrease in the activation entropy arising from the disruption of the solvent's H-bond network and obstruction of potential proton transfer pathways. We estimate the activation free energy at 280K as ~1.0 kcal/mol. There are many details about proton transfer dynamics that remain unclear, but recent progress analyzing potential collective reaction coordinates for H-bond exchange and proton transfer has stimulated vigorous study on this problem. Further experimental study of the proton transfer process will be invaluable for validating potential mechanisms and assembling a holistic picture for this process.

8.7 References

(1) Yan, L.; Hu, Y.; Zhang, X.; Yue, B. Applications of NMR Techniques in the Development and Operation of Proton Exchange Membrane Fuel Cells *Annu. Reports NMR Spectrosc.* **2016**, *88*, 149.

(2) Graves, C.; Ebbesen, S. D.; Mogensen, M.; Lackner, K. S. Sustainable hydrocarbon fuels by recycling CO_2 and H_2O with renewable or nuclear energy *Renew. Sustain. Energy Rev.* **2011**, *15*, 1.

(3) Khurana, E.; Dal Peraro, M.; DeVane, R.; Vemparala, S.; DeGrado, W. F.; Klein, M. L. Molecular dynamics calculations suggest a conduction mechanism for the M2 proton channel from influenza A virus. *Proc. Natl. Acad. Sci. U. S. A.* **2009**, *106*, 1069.

(4) Kaila, V. R. I.; Verkhovsky, M. I.; Wikström, M. Proton-Coupled Electron Transfer in Cytochrome Oxidase *Chem. Rev.* **2010**, *110*, 7062.

(5) Hittorf, W. On the migration of ions during electrolysis *Pogg. Ann.* **1853**, *89*, 177.

(6) Vanysek, P. *Ionic Conductivity and Diffusion at Infinite Dilution, Handbook of Chemistry and Physics*, 1992/1993.; CRC Press: Boca Raton, FL, 1992.

(7) Lapid, H.; Agmon, N.; Petersen, M. K.; Voth, G. A. A bond-order analysis of the mechanism for hydrated proton mobility in liquid water *J. Chem. Phys.* **2005**, *122*, 014506.

(8) Markovitch, O.; Chen, H.; Izvekov, S.; Paesani, F.; Voth, G. A.; Agmon, N. Special pair dance and partner selection: elementary steps in proton transport in liquid water. *J. Phys. Chem. B* **2008**, *112*, 9456.

(9) Marx, D.; Tuckerman, M. E.; Hutter, J.; Parrinello, M. The nature of the hydrated excess proton in water *Nature* **1999**, *397*, 601.

(10) Giberti, F.; Hassanali, A. A.; Ceriotti, M.; Parrinello, M. The Role of Quantum Effects on Structural and Electronic Fluctuations in Neat and Charged Water *J. Phys. Chem. B* **2014**, *118*, 13226.

(11) Wicke, E.; Eigen, M.; Ackermann, T. Über den Zustand des Protons (Hydroniumions) in wäßriger Lösung *Z. Phys. Chem. (N. F)*. **1954**, *1*, 340.

(12) Zundel, G.; Metzger, H. Energiebänder der tunnelnden Überschuß-Protonen in flüssigen Säuren. Eine IR-spektroskopische Untersuchung der Natur der Gruppierungen $H_5O_2^+$ *Z. Phys. Chem.* **1968**, *58*, 225.

(13) Dahms, F.; Costard, R.; Pines, E.; Fingerhut, B. P.; Nibbering, E. T. J.; Elsaesser, T. The Hydrated Excess Proton in the Zundel Cation $H_5O_2^+$: The Role of Ultrafast Solvent Fluctuations *Angew. Chemie - Int. Ed.* **2016**, *55*, 10600.

(14) Dahms, F.; Fingerhut, B. P.; Nibbering, E. T. J.; Pines, E.; Elsaesser, T. Large-amplitude transfer motion of hydrated excess protons mapped by ultrafast 2D IR spectroscopy *Science* **2017**, *357*, 491.

(15) Daly, C. A.; Streacker, L. M.; Sun, Y.; Pattenaude, S. R.; Hassanali, A. A.; Petersen, P. B.; Corcelli, S. A.; Ben-Amotz, D. Decomposition of the Experimental Raman and Infrared Spectra of Acidic Water into Proton, Special Pair, and Counterion Contributions *J. Phys. Chem. Lett.* **2017**, *8*, 5246.

(16) Fournier, J. A.; Carpenter, W. B.; Lewis, N. H. C.; Tokmakoff, A. Broadband 2D IR spectroscopy reveals dominant asymmetric $H_5O_2^+$ proton hydration structures in acid solutions *Nat. Chem.* **2018**, *10*, 932.

(17) Roberts, N. K.; Northey, H. L. Proton and deuteron mobility in normal and heavy water solutions of electrolytes *J. Chem. Soc. Faraday Trans. 1* **1974**, *70*, 253.

(18) Meiboom, S. Nuclear Magnetic Resonance Study of the Proton Transfer in Water *J. Chem. Phys.* **1961**, *34*, 375.

(19) Luz, Z.; Meiboom, S. The Activation Energies of Proton Transfer Reactions in Water *J. Am. Chem. Soc.* **1964**, *86*, 4768.

(20) Pfeifer, R.; Hertz, H. G. Activation Energies of the Proton-exchange Reactions in Water Measured with the 1 H-NMR Spin Echo Technique *Berichte Der Bunsengesellschaft Fur Phys. Chemie* **1990**, *94*, 1349.

(21) Loewenstein, A.; Szoke, A. The Activation Energies of Proton Transfer Reactions in Water *J. Am. Chem. Soc.* **1962**, *84*, 1151.

(22) Agmon, N. Hydrogen bonds, water rotation and proton mobility *J. Chim. Phys.* **1996**, *93*, 1714.

(23) Berkelbach, T. C.; Lee, H. S.; Tuckerman, M. E. Concerted Hydrogen-Bond Dynamics in the Transport Mechanism of the Hydrated Proton: A First-Principles Molecular Dynamics Study *Phys. Rev. Lett.* **2009**, *103*, 238302.

(24) Tse, Y. L. S.; Knight, C.; Voth, G. A. An analysis of hydrated proton diffusion in ab initio molecular dynamics *J. Chem. Phys.* **2015**, *142*, 014104.

(25) Marx, D. Proton Transfer 200 Years after von Grotthuss: Insights from Ab Initio Simulations *Chem. Phys. Chem* **2006**, *7*, 1848.

(26) Carpenter, W. B.; Fournier, J. A.; Lewis, N. H. C.; Tokmakoff, A. Picosecond Proton Transfer Kinetics in Water Revealed with Ultrafast IR Spectroscopy *J. Phys. Chem. B* **2018**, *122*, 2792.

(27) Steinel, T.; Asbury, J. B.; Corcelli, S. A.; Lawrence, C. P.; Skinner, J. L.; Fayer, M. D. Water dynamics: dependence on local structure probed with vibrational echo correlation spectroscopy *Chem. Phys. Lett.* **2004**, *386*, 295.

(28) Loparo, J.; Fecko, C.; Eaves, J.; Roberts, S.; Tokmakoff, A. Reorientational and Configurational Fluctuations in Water Observed on Molecular Length Scales. *Phys. Rev. B* **2004**, *70*, 180201.

(29) Biswas, R.; Tse, Y. L. S.; Tokmakoff, A.; Voth, G. A. Role of Presolvation and Anharmonicity in Aqueous Phase Hydrated Proton Solvation and Transport *J. Phys. Chem. B* **2016**, *120*, 1793.

(30) Perry, R. H.; Green, D. *Perry's Chemical Engineers' Handbook*, 6th ed.; McGraw-Hill: New York, 1984.

(31) Nishikata, E.; Ishii, T.; Ohta, T. Viscosities of aqueous hydrochloric acid solutions, and densities and viscosities of aqueous hydroiodic acid solutions *J. Chem. Eng. Data* **1981**, *26*, 254.

(32) Biswas, R.; Carpenter, W.; Fournier, J. A.; Voth, G. A.; Tokmakoff, A. IR spectral assignments for the hydrated excess proton in liquid water *J. Chem. Phys.* **2017**, *146*,

154507.

(33) Carpenter, W. B.; Fournier, J. A.; Biswas, R.; Voth, G. A.; Tokmakoff, A. Delocalization and stretch-bend mixing of the HOH bend in liquid water *J. Chem. Phys.* **2017**, *147*, 084503.

(34) Kalish, N. B.-M.; Shandalov, E.; Kharlanov, V.; Pines, D.; Pines, E. Apparent Stoichiometry of Water in Proton Hydration and Proton Dehydration Reactions in CH3CN/H2O Solutions **2011**.

(35) Petersen, J.; Møller, K. B.; Rey, R.; Hynes, J. T. Ultrafast Librational Relaxation of H_2O in Liquid Water *J. Phys. Chem. B* **2013**, *117*, 4541.

(36) Gardecki, J. A.; Constantine, S.; Zhou, Y.; Ziegler, L. D. Optical heterodyne detected spectrograms of ultrafast nonresonant electronic responses *J. Opt. Soc. Am. B* **2000**, *17*, 652.

(37) De Marco, L.; Fournier, J. A.; Thämer, M.; Carpenter, W.; Tokmakoff, A. Anharmonic exciton dynamics and energy dissipation in liquid water from two-dimensional infrared spectroscopy *J. Chem. Phys.* **2016**, *145*, 094501.

(38) Rezus, Y. L. A.; Bakker, H. J. Orientational dynamics of isotopically diluted H_2O and D_2O *J. Chem. Phys.* **2006**, *125*, 144512.

(39) Fournier, J. A.; Carpenter, W.; De Marco, L.; Tokmakoff, A. Interplay of Ion–Water and Water–Water Interactions within the Hydration Shells of Nitrate and Carbonate Directly Probed with 2D IR Spectroscopy *J. Am. Chem. Soc.* **2016**, *138*, 9634.

(40) Liu, L.; Hunger, J.; Bakker, H. J. Energy Relaxation Dynamics of the Hydration Complex of Hydroxide *J. Phys. Chem. A* **2011**, *115*, 14593.

(41) Paarmann, A.; Hayashi, T.; Mukamel, S.; Miller, R. J. D. Probing intermolecular couplings in liquid water with two-dimensional infrared photon echo spectroscopy *J. Chem. Phys.* **2008**, *128*, 191103.

(42) Post, S. T. van der; Bakker, H. J. The combined effect of cations and anions on the dynamics of water *Phys. Chem. Chem. Phys.* **2012**, *14*, 6280.

(43) Chen, M.; Zheng, L.; Santra, B.; Ko, H.-Y.; DiStasio Jr, R. A.; Klein, M. L.; Car, R.; Wu, X. Hydroxide diffuses slower than hydronium in water because its solvated structure inhibits correlated proton transfer *Nat. Chem.* **2018**, *10*, 413.

(44) Nicodemus, R. A.; Corcelli, S. A.; Skinner, J. L.; Tokmakoff, A. Collective Hydrogen Bond Reorganization in Water Studied with Temperature-Dependent Ultrafast Infrared Spectroscopy *J. Phys. Chem. B* **2011**, *115*, 5604.

(45) Roberts, S. T.; Ramasesha, K.; Tokmakoff, A. Structural Rearrangements in Water Viewed Through Two-Dimensional Infrared Spectroscopy. *Acc. Chem. Res.* **2009**, *42*,

1239.

(46) Kestin, J.; Sokolov, M.; Wakeham, W. A. Viscosity of Liquid Water in the Range -8C to 150C *J. Phys. Chem. Ref. Data* **1978**, *7*, 941.

(47) Shalit, A.; Ahmed, S.; Savolainen, J.; Hamm, P. Terahertz echoes reveal the inhomogeneity of aqueous salt solutions *Nat. Chem.* **2017**, *9*, 273.

(48) Heisler, I. A.; Mazur, K.; Meech, S. R. Low-Frequency Modes of Aqueous Alkali Halide Solutions: An Ultrafast Optical Kerr Effect Study *J. Phys. Chem. B* **2011**, *115*, 1863.

(49) Buchner, R.; Hefter, G. Interactions and dynamics in electrolyte solutions by dielectric spectroscopy *Phys. Chem. Chem. Phys.* **2009**, *11*, 8984.

(50) Ramasesha, K.; De Marco, L.; Mandal, A.; Tokmakoff, A. Water vibrations have strongly mixed intra- and intermolecular character *Nat. Chem.* **2013**, *5*, 935.

(51) Paarmann, A.; Hayashi, T.; Mukamel, S.; Miller, R. J. D. Nonlinear response of vibrational excitons: Simulating the two-dimensional infrared spectrum of liquid water *J. Chem. Phys.* **2009**, *130*, 204110.

(52) Giammanco, C. H.; Wong, D. B.; Fayer, M. D. Water dynamics in divalent and monovalent concentrated salt solutions. *J. Phys. Chem. B* **2012**, *116*, 13781.

(53) Foggi, P.; Bellini, M.; Kien, D. P.; Vercuque, I.; Righini, R. Relaxation dynamics of water and HCl aqueous solutions measured by time-resolved optical Kerr effect *J. Phys. Chem. A* **1997**, *101*, 7029.

(54) Tanaka, H.; Ohmine, I. Potential energy surfaces for water dynamics: Reaction coordinates, transition states, and normal mode analyses *J. Chem. Phys.* **1989**, *91*, 6318.

(55) Ohmine, I. Liquid Water Dynamics: Collective Motions, Fluctuation, and Relaxation *J. Phys. Chem.* **1995**, *99*, 6767.

(56) Ohmine, I.; Saito, S. Water Dynamics: Fluctuation, Relaxation, and Chemical Reactions in Hydrogen Bond Network Rearrangement *Acc. Chem. Res.* **1999**, *32*, 741.

(57) Hassanali, A.; Giberti, F.; Cuny, J.; Kühne, T. D.; Parrinello, M. Proton transfer through the water gossamer. *Proc. Natl. Acad. Sci. U. S. A.* **2013**, *110*, 13723.

(58) Schulz, R.; von Hansen, Y.; Daldrop, J. O.; Kappler, J.; Noé, F.; Netz, R. R. Collective hydrogen-bond rearrangement dynamics in liquid water *J. Chem. Phys.* **2018**, *149*, 244504.

(59) Glasstone, S.; Laidler, K. J.; Eyring, H. *The Theory of Rate Processes*; McGraw-Hill: New York, NY, 1941.

(60) Stirnemann, G.; Wernersson, E.; Jungwirth, P.; Laage, D. Mechanisms of acceleration and

retardation of water dynamics by ions. *J. Am. Chem. Soc.* **2013**, *135*, 11824.

(61) Baer, M. D.; Fulton, J. L.; Balasubramanian, M.; Schenter, G. K.; Mundy, C. J. Persistent Ion Pairing in Aqueous Hydrochloric Acid *J. Phys. Chem. B* **2014**, *118*, 7211.

(62) Xu, J.; Izvekov, S.; Voth, G. A. Structure and Dynamics of Concentrated Hydrochloric Acid Solutions *J. Phys. Chem. B* **2010**, *114*, 9555.

(63) Endom, L.; Hertz, H. G.; Thül, B.; Zeidler, M. D. A Microdynamic Model of Electrolyte Solutions as Derived from Nuclear Magnetic Relaxation and Self-Diffusion Data *Berichte Der Bunsengesellschaft Fur Phys. Chemie* **1967**, *71*, 1008.

(64) Geissler, P. L.; Dellago, C.; Chandler, D.; Hutter, J.; Parrinello, M. Autoionization in Liquid Water *Science* **2001**, *291*, 2121.

(65) Roberts, S. T.; Mandal, A.; Tokmakoff, A. Local and Collective Reaction Coordinates in the Transport of the Aqueous Hydroxide Ion *J. Phys. Chem. B* **2014**, *118*, 8062.

(66) Napoli, J. A.; Marsalek, O.; Markland, T. E. Decoding the spectroscopic features and time scales of aqueous proton defects *J. Chem. Phys.* **2018**, *148*, 222833.

(67) Lewis, N. H. C.; Fournier, J. A.; Carpenter, W. B.; Tokmakoff, A. Direct Observation of Ion Pairing in Aqueous Nitric Acid Using 2D Infrared Spectroscopy *J. Phys. Chem. B* **2018**, *123*, 225.

(68) Laage, D.; Hynes, J. T. A molecular jump mechanism of water reorientation *Science* **2006**, *311*, 832.

(69) Laage, D.; Hynes, J. T. On the Molecular Mechanism of Water Reorientation *J. Phys. Chem. B* **2008**, *112*, 14230.

(70) Ji, M.; Odelius, M.; Gaffney, K. J. Large angular jump mechanism observed for hydrogen bond exchange in aqueous perchlorate solution. *Science* **2010**, *328*, 1003.

Chapter 9

Summary and Outlook

9.1 Aqueous Proton Structure: Challenges Describing a Dynamic Complex

Over the last decades, many questions have been raised about the structural and dynamical nature of the aqueous excess proton. For instance, the aqueous proton has been described in terms of either the gas-phase Eigen or Zundel complexes even though it was recognized that the solvation environment removes the symmetry of the complex.[1–3] Recent simulations have introduced more nuanced pictures of the aqueous proton,[4,5] invoking concepts such as the "special pair" and "fluxional complex," but there were no direct experimental verifications of these ideas. The linear infrared (IR) spectrum is potentially a sensitive reporter on the nuclear configurations of the aqueous proton complex, but the absorption is continuous and the underlying vibrational modes are strongly mixed and anharmonic, preventing straightforward interpretation. Each of the assignments across the mid-IR have been interpreted in terms of both Zundel-like and Eigen-like vibrations without a clear way to come to a consensus.

The work in this thesis represents progress made towards answering some of these questions using infrared spectroscopy. First, with the aid of vibrational self-consistent field/ virtual state configuration interaction (VSCF/VCI) calculations, we made more reliable vibrational assignments of the linear IR spectrum in terms of a distribution instantaneous geometrical configurations (Chapter 6). Absorption at 1200 cm^{-1} is primarily due to the stretching motion of

the shared proton in Zundel-like and intermediate geometries, with a small contribution from Eigen-like umbrella modes. The Zundel like stretching mode is sensitive to both the quantum expectation value of the O–O distance $\langle R_{OO} \rangle$ and the O–H distance $\langle R_{OH} \rangle$ between the excess proton and the nearest oxygen. The 1750 cm^{-1} feature arises from multiple contributions presented here in order of decreasing intensity: the concerted flanking bending modes in Zundel-like configurations, vibrations of mixed stretching/bending character, high-frequency Zundel-like shared proton stretches, and stretching and bending modes of Eigen-like configurations. The continuous absorption between 2000-3000 cm^{-1} arises from hydronium O–H stretching modes of Eigen-like configurations, and the peak at 3100 cm^{-1} is due to the flanking O–H stretches in Zundel-like configurations. The linear IR spectrum is best modeled with a broad distribution of aqueous proton structures, with Eigen and Zundel geometries as idealized limits.

Two-dimensional infrared (2D IR) spectroscopy demonstrates the strong anharmonic coupling between all vibrational modes in Zundel-like and Eigen-like configurations, supporting a dynamic special pair conception of the aqueous excess proton (Chapter 7). The 2D IR spectrum of the Zundel-like proton stretching mode at 1200 cm^{-1} shows an inverted anharmonicity pattern, where the excited state absorption (ESA) lies above the ground state bleach in ω_3. This reflects the confinement of the shared proton between two waters in Zundel-like and intermediate complexes. The potential is also inherently asymmetric in shape, which is particularly pronounced in intermediate configurations. The cross peaks between all Zundel-like vibrations are well-described by the VSCF/VCI cluster calculations, whereas the response from Eigen-like vibrations is less well understood. The Zundel-like cross peaks include polarization information, which reveal that the shared proton stretch and flanking bending modes are aligned parallel to the special pair O···O axis, whereas the O–H flanking stretch modes are roughly perpendicular to this axis. The

experimental cross peak at (ω_1, ω_3) = (1200 cm^{-1}, 2400 cm^{-1}) between the Zundel and Eigen proton stretch modes is not reproduced in the VSCF/VCI calculations of the 2D spectral density, which points to vibrationally non-adiabatic, dynamical effects in the aqueous excess proton that cannot be captured by cluster-based calculations.

These experiments present evidence for a more sophisticated understanding of the structure and dynamics of the excess proton, but there are many unresolved details that will require further work. For example, even though the structure of the aqueous proton complex is best described as a distribution of configurations, current experiments have not been able to quantify relative populations with this distribution. Simulations with classical nuclei predict a relative stabilization of Eigen-like configurations on the order of 1 kcal/mol,[6,7] but quantum mechanical treatment of hydrogen nuclei diminishes the relevance of this barrier due to nuclear quantum effects.[8] The uncertainty in the simulated distribution of configurations led us to presenting average infrared response for the three different groupings, but the fast fluctuations within the distribution also demonstrate the limitations of using a cluster-based approach. To better understand the impact of ultrafast fluctuations on the IR spectrum, it is important to not only consider the multidimensional and anharmonic nature of the nuclear potential, but also how the potential and the resulting vibrational couplings fluctuate on the fs timescale.

In the process of these studies, it has become apparent that typical geometric descriptors such as δR_{OH} or R_{OH} are insufficient as the sole descriptors for a dynamical aqueous proton complex. Where they succeed is in their intuitive description and their ability to separate certain IR absorption regions. However, the sub-100 fs configurational fluctuations within a flat-bottomed potential mean result in rapid decorrelations in δR_{OH} and R_{OH} on the fastest timescales measurable by IR spectroscopy.[9] One could propose slower moving coordinates for describing the aqueous

proton complex such as R_{OO}, but this coordinate is predicted to decorrelate on an approximately 100 fs timescale,[10] which does not provide much longer of a time window. The 2.5 ps anisotropy timescale of the flanking bend modes suggests that there is some persistence to the aqueous proton configuration, subject to the arrangement of the solvation environment. Perhaps there are collective coordinates involving the solvent configuration that are more adept at capturing the average geometric parameters of an aqueous proton configuration, even if the fast degrees of freedom undergo large-amplitude fluctuations.

9.2 Proton Transfer Dynamics: Towards Molecular-level Detail

The anomalously high conductivity of acidic solutions is explained by the Grotthuss mechanism, but the molecular details of this process had only been examined in the last twenty-five years with simulations[4,11–13] with limited verification by experiment. These simulations have examined proton transfer with atomistic detail, but they have also reached different conclusions. Importantly, most of these analyses treat hydrogen nuclei classically, whereas some studies have stressed the role of nuclear quantum effects amplifying the rate of proton transport.[8,9] There remain many competing theories for the proton transfer mechanism, such as the Eigen-Zundel-Eigen and Zundel-Eigen-Zundel models, coherent burst-rest dynamics, and the pre-solvation mechanism.

This thesis presents transient absorption (TA) anisotropy experiments that provide the most direct experimental measurements of aqueous proton transfer to date (Chapter 8). The anisotropy at 1750 cm^{-1}, primarily reporting on Zundel-like flanking bending modes, decays biexponentially with a fast timescale on of approximately 200 fs and a slow timescale on the order of 2.5 ps. While the fast timescale likely reflects rapid energy transfer within the aqueous proton complex, the slow timescale reports on reorientation due to proton transfer events. The ps timescale grows with

increasing viscosity but displays non-Stokes-Einstein-Debye behavior, which may reflect the deviation of Grotthuss proton transport from standard hydrodynamic diffusion.

Arrhenius analysis reveals that in 1M and 2M HCl, the barrier for the anisotropy decay is 2.4 ± 0.2 kcal/mol, which matches previous measured values for the proton transfer barrier, obtained through conductivity[14] and NMR lineshape analyses.[15,16] The measured value of the barrier changes with solution composition, leading to the counterintuitive result that proton transfer slows down alongside a reduction of the activation barrier. The dependence of the dynamics on solution composition indicates that proton transfer occurs via collective H-bond reorganization events in water. Using transition state theory, this trend in rate can be rationalized in terms of competing effects from transition state entropy and enthalpy. The transition state enthalpy decreases with anion concentration due to relatively weaker H-bonds formed between water and counteranions compared to water-water H-bonds, which reduce the energy barrier of collective H-bond reorganization. The proton transfer rate also decreases due to an entropic penalty at high concentration, arising from anions obstructing proton transfer pathways and excluding volume from the H-bond network.

There are multiple lingering questions regarding using anisotropy decay to measure proton transfer kinetics. It is important to reiterate that for multiple reasons, the approximately 2.5 ps anisotropy decay timescale is not the mean proton transfer timescale. First, the anisotropy decay strictly reports on the total polarization response at 1750 cm^{-1}, which includes contributions from multiple types of vibrations, not just the Zundel-like bending modes. Additionally, the measured timescale reflects the decorrelation of the second Legendre polynomial of the dipole orientation, not the dipole TCF itself, which requires comparison to simulations to extract a quantitative value for the proton transfer timescale. Simulation analysis is also necessary for this measurement

because proton transfer likely induces reorientation by a large angular jump. In principle, experimental measurement of the average hopping angle involves measurements of the same process with multiple techniques sensitive to different correlation functions, but in practice this is challenging since these measurements are not necessarily directly comparable.

Beyond the uncertainties in interpreting what has been measured, these results still have not addressed the multiple theories for proton transfer posed by simulations, such as the Zundel-Eigen-Zundel, Eigen-Zundel-Eigen, the special pair dance, or the pre-solvation mechanism. Framed more concretely, these results do not observe the interconversion between stable reactant and product configurations with distinct free-energy minima. As a result, a reaction coordinate for aqueous proton transfer has not been determined. Interconversion between two stable H-bonding configurations with isotopically dilute mixtures of HOD in D_2O has been shown,[17,18] and possibly similar strategies could be employed in acidic solutions (discussed further below). These types of experiments can be connected to computational studies to assemble a more concrete picture of proton transfer.

Experiments with isotopically dilute H in DCl may be useful for tracking the coupling and dynamics of proton transfer without spectroscopic artifacts like energy transfer or sub-200 fs vibrational lifetimes. The FTIR spectrum of the dilute proton in DCl (Appendix 5B) is a starting point for designing such experiments. These measurements indicate that nonlinear experiments would likely be limited to above 2700 cm^{-1} to avoid interference from the strong DCl absorption continuum. Earlier two-color TA measurements found 120 fs and 800 fs decays in the isotropic response exciting at 2800 cm^{-1}, and detecting at 3400 cm^{-1}, which was interpreted as rapid Eigen-Zundel rattling.[19] It would be interesting to revisit this signal with 2D IR spectroscopy, incorporating excitation frequency resolution, anisotropy decay kinetics, and temperature

dependence. Additionally, pre-solvation studies predict that the O–H stretch of the H-bond donor to excess proton complex is resonant at 3700-3800 cm^{-1},[9] which is blue-shifted from bulk water due to the relative weakness of this H-bond. There may be a cross peak at (ω_1, ω_3) = (2800 cm^{-1}, 3800 cm^{-1}) due to coupling between this donor and the aqueous proton complex. This approach has been employed for the HOD 2D IR spectrum in NaOD,[20] revealing a Zundel-like transition state during proton transfer in basic solutions. Similar analyses across the O–H stretch in acid solutions might be useful for distinguishing stable states and transition states during the proton transfer process in acidic solutions.

There may also be some utility in studying isotopically pure DCl/D_2O solutions for proton transfer studies. The DCl IR spectrum also features continuous absorption, and the deuteron and proton transfer barriers are the same within error.[14,21] However, the zero-point energy of the excess deuteron is expected to be lower, which will affect the anharmonicity of the potential that is experienced by the deuteron. Therefore, there may be a kinetic isotope effect with regard to proton rattling due to its lower position in the potential well and its reduced quantum mechanical behavior. These would be particularly valuable for the deuteron stretch mode, which would be useful for making observations of the proton stretch potential closer to the minimum. This feature is expected to be resonant at 900 cm^{-1},[22] which is currently out of reach experimentally.

9.3 Experimental Progress and Challenges

This project was possible after developing tunable excitation sources down to 1200 cm^{-1}, but there is still work to do to investigate potential artifacts due to sample conditions. As described in Section 5.3.1, we have obtained different results in the lineshape for 2D IR features excited at 1250 cm^{-1}, but the analyses presented in this thesis are not affected since they only involved

frequency positions and polarization relationships. These distortions are likely due to the early implementation of 1 mm CaF_2 windows, which are highly dispersive below 1300 cm^{-1}. We have also used 0.2 mm CaF_2 windows and diamond windows, which are less dispersive but still have issues at 1200 cm^{-1} and 1800 cm^{-1}, respectively. The development of flat jet technology holds the promise of preparing samples as thin as a few microns without the need for windows, but will require some effort to effectively incorporate it into the experiment.

The development of broadband IR laser technology can enable collecting the full 2D IR spectrum with a single excitation source. Current pulses are limited to approximately 300-400 cm^{-1} in bandwidth, with 50 fs FWHM temporal pulse width, whereas the acid continuum spans more than 2000 cm^{-1} and certain proton dynamics take place on the tens of fs timescale. Preliminary work in the group has achieved a promising broadband excitation source based on OPA in GaSe, which can deliver pulses of >10 μJ spanning the entire mid-IR. The Fourier limit for these pulses is approximately 20 fs, but a pulsewidth of 100 fs has been measured so far, likely due to known angular dispersion issues. For all experiments, dispersion due to transmission through material is a constant issue which is more difficult to manage with broadband pump pulses, further underscoring the potential benefits of implementing a flat jet sample configuration.

9.4 Conclusion

The results and analysis presented in this thesis support predictions that the aqueous proton is a dynamical species, shaped by the fluctuations of the surrounding solvation environment. These studies not only provide a more accurate molecular picture for this complex, but demonstrate the power of nonlinear spectroscopy for studying this problem. There is more work to do to understand the mechanism and reaction coordinate for proton transfer mechanism in water, which may be

achieved with a concerted effort from experimental and computational studies. The methods employed here provide a framework for studying hydrated protons in a wide variety of systems, such as in fuel cell membranes and biological proton channels. Research is already underway in our group to study excess protons in the nanoscale pores of zeolite materials. While the bulk and nano-confined systems show clear differences, we have found some shared behavior which has facilitated systematic study of the proton-in-zeolite system. Further effort in this direction will not only improve our understanding of nano-confined protonated systems, but may reveal new fascinating details about bulk aqueous acid solutions as well.

9.5 References

(1) Zundel, G.; Metzger, H. Energiebänder der tunnelnden Überschuß-Protonen in flüssigen Säuren. Eine IR-spektroskopische Untersuchung der Natur der Gruppierungen $H_5O_2^+$ *Z. Phys. Chem.* **1968**, *58*, 225.

(2) Daly, C. A.; Streacker, L. M.; Sun, Y.; Pattenaude, S. R.; Hassanali, A. A.; Petersen, P. B.; Corcelli, S. A.; Ben-Amotz, D. Decomposition of the Experimental Raman and Infrared Spectra of Acidic Water into Proton, Special Pair, and Counterion Contributions *J. Phys. Chem. Lett.* **2017**, *8*, 5246.

(3) Markovitch, O.; Chen, H.; Izvekov, S.; Paesani, F.; Voth, G. A.; Agmon, N. Special pair dance and partner selection: elementary steps in proton transport in liquid water. *J. Phys. Chem. B* **2008**, *112*, 9456.

(4) Tuckerman, M.; Laasonen, K.; Sprik, M.; Parrinello, M. Ab Initio Molecular Dynamics Simulation of the Solvation and Transport of H3O+ and OH- Ions in Water *J. Phys. Chem.* **1995**, *99*, 5749.

(5) Marx, D.; Tuckerman, M. E.; Hutter, J.; Parrinello, M. The nature of the hydrated excess proton in water *Nature* **1999**, *397*, 601.

(6) Biswas, R.; Tse, Y. L. S.; Tokmakoff, A.; Voth, G. A. Role of Presolvation and Anharmonicity in Aqueous Phase Hydrated Proton Solvation and Transport *J. Phys. Chem. B* **2016**, *120*, 1793.

(7) Roy, S.; Schenter, G. K.; Napoli, J. A.; Baer, M. D.; Markland, T. E.; Mundy, C. J. Resolving Heterogeneous Dynamics of Excess Protons in Aqueous Solution with Rate Theory *J. Phys. Chem. B* **2020**, acs. jpcb.0c02649.

(8) Giberti, F.; Hassanali, A. A.; Ceriotti, M.; Parrinello, M. The Role of Quantum Effects on Structural and Electronic Fluctuations in Neat and Charged Water *J. Phys. Chem. B* **2014**, *118*, 13226.

(9) Napoli, J. A.; Marsalek, O.; Markland, T. E. Decoding the spectroscopic features and time scales of aqueous proton defects *J. Chem. Phys.* **2018**, *148*, 222833.

(10) Decka, D.; Schwaab, G.; Havenith, M. A THz/FTIR fingerprint of the solvated proton: evidence for Eigen structure and Zundel dynamics. *Phys. Chem. Chem. Phys.* **2015**, *17*, 11898.

(11) Marx, D. Proton Transfer 200 Years after von Grotthuss: Insights from Ab Initio Simulations *Chem. Phys. Chem* **2006**, *7*, 1848.

(12) Day, T. J. F.; Schmitt, U. W.; Voth, G. A. The mechanism of hydrated proton transport in water *J. Am. Chem. Soc.* **2000**, *122*, 12027.

(13) Berkelbach, T. C.; Lee, H. S.; Tuckerman, M. E. Concerted Hydrogen-Bond Dynamics in the Transport Mechanism of the Hydrated Proton: A First-Principles Molecular Dynamics Study *Phys. Rev. Lett.* **2009**, *103*, 238302.

(14) Gierer, A.; Wirtz, K. Proton and deuteron transfer over hydrogen bridges as cause of conductivity effects *J. Phys. Chem.* **1952**, *56*, 914.

(15) Luz, Z.; Meiboom, S. The Activation Energies of Proton Transfer Reactions in Water *J. Am. Chem. Soc.* **1964**, *86*, 4768.

(16) Loewenstein, A.; Szoke, A. The Activation Energies of Proton Transfer Reactions in Water *J. Am. Chem. Soc.* **1962**, *84*, 1151.

(17) Eaves, J. D.; Loparo, J. J.; Fecko, C. J.; Roberts, S. T.; Tokmakoff, A.; Geissler, P. L. Hydrogen Bonds in Liquid Water are Broken Only Fleetingly. *Proc. Natl. Acad. Sci. U. S. A.* **2005**, *102*, 13019.

(18) Roberts, S. T.; Ramasesha, K.; Tokmakoff, A. Structural Rearrangements in Water Viewed Through Two-Dimensional Infrared Spectroscopy. *Acc. Chem. Res.* **2009**, *42*, 1239.

(19) Woutersen, S.; Bakker, H. J. Ultrafast Vibrational and Structural Dynamics of the Proton in Liquid Water *Phys. Rev. Lett.* **2006**, *96*, 138305.

(20) Roberts, S. T.; Petersen, P. B.; Ramasesha, K.; Tokmakoff, A.; Ufimtsev, I. S.; Martinez, T. J. Observation of a Zundel-like transition state during proton transfer in aqueous hydroxide solutions. *Proc. Natl. Acad. Sci. U. S. A.* **2009**, *106*, 15154.

(21) Gierer, A.; Wirtz, K. Anomalous Mobility of H^+ and OH^- Ions *J. Chem. Phys.* **1949**, *17*, 745.

(22) Vendrell, O.; Gatti, F.; Meyer, H.-D. Full dimensional (15-dimensional) quantum-dynamical simulation of the protonated water dimer. II. Infrared spectrum and vibrational dynamics *J. Chem. Phys.* **2007**, *127*, 184303.